Design, Techno-Economic Assessment, and Comparison of Clean Hydrogen Production/Utilization Technologies Based on High-Temperature Solar Thermal Energy

by

Amir Reza Razmi

A thesis submitted in partial fulfilment of the requirements for the degree of

Doctor of Philosophy

Department of Mechanical Engineering

University of Alberta

Abstract

The transition to a sustainable and low-carbon energy future significantly depends on the development of economically viable and environmentally sustainable hydrogen production pathways. Achieving an optimal balance between economic feasibility and environmental impact remains a formidable challenge within the hydrogen sector, particularly in large-scale applications. Concentrated solar power (CSP), with its superior efficiency over other renewable sources, offers immense yet almost underexplored potential for high-temperature, solar-driven hydrogen production. This thesis is dedicated to exploring the integration of CSP in water electrolysis and methane pyrolysis, advancing novel design proposals to enhance these solar-powered processes. Through a comprehensive comparative analysis, the research highlights each method's unique advantages and constraints, revealing their roles in fostering a resilient hydrogen economy. Moreover, the thesis investigates the potential of hydrogen storage and hydrogen-based combined heat and power (CHP) systems for sustainable energy management, with a focused analysis on their implementation across the University of Alberta, Alberta, and Canada. This work aims to lay a foundation for next-generation solar-driven hydrogen technologies and integrated energy solutions, contributing to the broader decarbonization and sustainability goals.

First, a comprehensive assessment is presented, including innovative designs and evaluation of high-temperature solar thermal field integration with proton exchange membrane electrolyzers (PEME), solid oxide electrolyzer cells (SOEC), and methane pyrolysis. Through comparative evaluation of low- and high-temperature water electrolysis technologies, it was determined that the SOEC integration with high-temperature solar thermal field yields a high exergy efficiency of 74%, with payback periods of less than two years in reversible operation. However, despite

selecting an optimal working fluid to enhance the operational efficiency of the solar unit and conducting a thorough techno-economic optimization, the exergy efficiency of the CSP-PEM configuration remained constrained to approximately 18%, with an associated cost rate of $492 per hour. Additionally, the results indicated a promising round-trip efficiency (RTE) of 49.8% and a levelized cost of hydrogen (LCOH) of $1.93/kg for the proposed novel design, which employs molten salt as a thermal transfer medium between high-temperature solar thermal fields and methane pyrolysis. An exploration of hydrogen incentives in the U.S. and Canada for clean hydrogen production indicates that the LCOH could be reduced to as low as $1.28/kg for solar-based methane pyrolysis through the U.S. incentives. These findings propose a promising economic pathway for solar-driven hydrogen production.

Next, a comprehensive techno-economic assessment was conducted to compare solar-based molten salt methane pyrolysis (SMSMP) and solar-based solid oxide electrolyzer cell (SSOEC) systems across five geographically diverse cities—Edmonton, San Antonio, Auckland, Seville, and Lyon. The SSOEC system, driven by both electrical and thermal energy, demonstrated a significantly higher hydrogen output at equivalent solar capacities, achieving an RTE of 75.2%, compared to 40.6% for SMSMP. Despite this, SMSMP achieved a lower LCOH at $2.83/kg, outperforming SSOEC's LCOH of $5.34/kg, making SMSMP more cost-effective in regions with moderate to high solar potential. Conversely, SSOEC's configuration proved more favourable in areas with lower solar availability, with its cost-effectiveness influenced by regional grid carbon intensity and electricity pricing. Even with anticipated declines in renewable infrastructure costs, SSOEC's LCOH is unlikely to match SMSMP or meet the target of $1/kg, highlighting the need for government support mechanisms, such as clean hydrogen tax credits, to enhance the economic feasibility of SSOEC systems.

In addition, a comparative case study examines SOFC-based CHP and hydrogen internal combustion engine (HICE-based CHP) systems using operational data from the University of Alberta. Despite higher capital and operational costs for SOFC-based CHP, its potential for superior long-term performance and sustainability exceeds that of HICE-CHP, which is limited by direct nitrogen oxides (NOx) emissions. Finally, this thesis evaluates the potential of SOFC-CHP systems for Alberta and Canada, forecasting market impact, job creation, and greenhouse gas (GHG) reduction potential. Results indicate significant benefits, with projected GHG reductions of 7.8 million tons in Canada's commercial sector and 1.7 million tons in Alberta by 2050, alongside substantial job creation and a potential Canadian market size reaching $15 billion. This thesis thus positions SOFC-based CHP as the favorable choice for sustainable energy management as the technology matures, underscoring the potential of high-temperature solar thermal integration and SOFC technology for a resilient hydrogen economy.

Preface

This thesis is an original work by Amir Reza Razmi. The research was conducted at the University of Alberta Energy Mechatronics Lab (EML) led by Prof. Mahdi Shahbakhti. The content of each chapter is either fully or partially based on published or submitted papers in peer-reviewed Journals, conferences, and book chapters [1–7]. As the lead author, I made substantial contributions to all the peer-reviewed published papers referenced throughout this thesis. The contributions of co-authors in each paper are listed below:

In Chapter 1 [1], Shakiba Sharifi, Dr. Ehsan Gholamian, and Prof. Ahmad Arabkoohsar contributed through insightful discussions on literature review and concept of "Green Hydrogen" book chapter.

In Chapter 2 [2], Seyed Mojtaba Alirahmi, Mohammad Hossein Nabat and Dr. Ehsanolah Assareh provided valuable insights regarding the modeling and optimization of the designed system.

In Chapter 3-6 [3–7], Dr. Amir Reza Hanifi contributed to the conceptualization and insightful discussions on the investigation of the designed systems.

Acknowledgements

First and foremost, I would like to extend my deepest gratitude to my supervisor, Prof. Mahdi Shahbakhti, for his dedication and profound expertise, which have greatly influenced my growth over the past four years. His mentorship has been invaluable to the completion of this work.

I am also sincerely grateful to Dr. Amir Reza Hanifi and Prof. Ahmad Arabkoohsar for their significant contributions as members of my supervisory committee. Their insights and guidance have been essential in shaping the direction and success of my work.

A special thank you goes to my wife, Shakiba, for her steadfast support of my academic and professional ambitions. Her love, care, and encouragement at every stage have been fundamental to my accomplishments. I am also profoundly appreciative of my family for their constant encouragement and unwavering belief in my abilities throughout this academic journey. Their support has been a source of strength and motivation.

I extend my gratitude to Michael Versteege for providing the campus data of the University of Alberta and welcoming me as a student representative on the Master Energy Plan Committee of the University of Alberta. I also wish to express my heartfelt thanks to my friends and colleagues at the University of Alberta for their friendship and unwavering support throughout this journey.

Finally, I would like to express my sincere gratitude for the financial support provided by the Natural Sciences and Engineering Research Council of Canada (NSERC), Alberta Innovates, and the University of Alberta Future Energy Systems (FES). I also wish to acknowledge the Government of Alberta and the University of Alberta for awarding me the Alberta Graduate Excellence Scholarship (AGES) for the 2023-2024 academic year. Your support has been instrumental in furthering my research and academic pursuits.

Table of contents

Abstract ..... **ii**

Preface ..... **v**

Acknowledgements ..... **vi**

List of tables ..... **xv**

List of figures ..... **xx**

List of abbreviations and acronyms ..... **xl**

Chapter 1: Introduction and Background **2**

1.1 Solar energy 2

1.2 Energy storage 3

1.3 Hydrogen energy 5

1.3.1 Hydrogen production 7

1.3.1.1 Water electrolysis 10

1.3.1.1.1 Proton exchange membrane (PEM) electrolyzer 10

1.3.1.1.2 Alkaline water electrolyzer (AWE) 12

1.3.1.1.3 Solid oxide electrolyzer (SOEC) 13

1.3.1.2 Methane pyrolysis 14

1.3.2 Hydrogen storage 16

1.3.3 Hydrogen safety 17

1.3.4 Hydrogen utilization 17

1.4 Literature review 19

1.4.1 Solar based PEM electrolyzer and fuel cell 21

1.4.2 Solar based SOEC and SOFC 24

1.4.3 Solar based methane pyrolysis 28

1.4.4 Solar based SOEC vs solar-based methane pyrolysis 32

1.4.5 Potential of hydrogen-based CHPs and their comparison 36

1.5 Problem identification and proposed solutions 41

1.6 Thesis contributions for the identified gaps in the literature 43

1.6.1 Solar-based PEM electrolyzer and fuel cell 43

1.6.2 Solar based SOEC and SOFC 44

1.6.3 Solar based methane pyrolysis 45

1.6.4 Solar based SOEC vs solar based methane pyrolysis 47

1.6.5 Potential of hydrogen-based CHPs and their comparison 48

1.7 Thesis outline 49

Chapter 2: Design and Techno-Economic Analysis of a Novel Solar-Based Proton Exchange Membrane Electrolyzer and Fuel Cell System 53

2.1 System description 54
2.1.1 Baseload 54
2.1.2 Peak loads 55
2.2 System modelling 56
2.2.1 Energy analysis 58
2.2.1.1 Parabolic trough collector 58
2.2.1.2 Steam Rankine cycle 59
2.2.1.3 Thermoelectric generator 59
2.2.1.4 PEM electrolyzer 60
2.2.1.5 PEM fuel cell 62
2.2.2 Exergy analysis 66
2.2.3 Exergoeconomic analysis 68
2.2.4 Performance criteria 70
2.3 Results and discussions 70
2.3.1 Model validation 71
2.3.2 Multi-objective optimization 72
2.3.2.1 Artificial neural network model validation 74
2.3.2.2 Optimization results 75
2.3.3 Sensitivity analysis 81

2.3.3.1 Direct normal irradiance 81

2.3.3.2 Charging and discharging time 82

2.3.3.3 Fuel cell temperature 84

2.4 Summary of chapter 86

2.5 Uncertainty consideration 88

Chapter 3: Design and Techno-Economic Analysis of a Novel Solar-Based Solid Oxide Electrolyzer and Fuel Cells System 89

3.1 System description 90

3.2 System modelling 92

3.2.1 Energy analysis 95

3.2.1.1 Heliostat solar unit 96

3.2.1.2 Solid oxide electrolyzer 100

3.2.1.3 Solid oxide fuel cell 104

3.2.1.4 Kalina cycle 105

3.2.1.5 District heating 105

3.2.2 Exergy analysis 106

3.2.3 Performance criteria 107

3.2.4 Economic analysis 107

3.3 Result and discussion 109

3.3.1 Model validation 109

3.3.2 Steady-state modelling 111

3.3.3 Parametric analysis 116

3.4 Case study 123

3.5 Summary of chapter 130

3.6 Uncertainty consideration 132

Chapter 4: Design and Techno-Economic Analysis of a Novel Solar-Based Methane Pyrolysis in Molten Salt System 133

4.1 System description 134

4.2 Mathematical modelling 136

4.2.1 System modelling 137

4.2.1.1 Heliostat solar unit 137

4.2.1.2 High-temperature thermal energy storage 142

4.2.1.3 Methane pyrolysis in molten salt 142

4.2.2 Economic analysis 146

4.2.3 Performance and economic criteria 147

4.3 Results and discussion 148

4.3.1 Model validation 148

4.3.2 Modelling results 150

4.3.3 Parametric analysis 154

4.4 Summary of chapter 168

4.5 Uncertainty consideration 169

Chapter 5: Techno-Economic Comparison of Solar-Based Solid Oxide Electrolyzer with Solar-Based Methane Pyrolysis 172

5.1 System description 173

5.2 Results and discussion 177

5.2.1 Validation of models 177

5.2.2 Modelling results 179

5.2.3 Parametric analysis 184

5.2.4 Case studies 190

5.2.4.1 Case study selection 190

5.2.4.2 Hydrogen production by case studies 192

5.3 Summary of chapter 202

5.4 Uncertainty consideration 204

Chapter 6: Hydrogen-Based Combined Heat and Power Systems 205

6.1 System description 206

6.1.1 Hydrogen-based CHPs for the University of Alberta 206

6.1.1.1 Methodology 211

6.1.2 Residential and commercial CHPs for Alberta and Canada 214

6.2 Results and discussion 216

6.2.1 University of Alberta 216

6.2.1.1 Basic strategy 218

6.2.1.2 Refined strategy 220

6.2.2 Alberta 228

6.2.2.1 Case studies for heat-to-power ratio of SOFC 229

6.2.2.2 Residential CHPs in Alberta 238

6.2.2.3 Commercial CHPs in Alberta 243

6.2.3 Canada 247

6.2.3.1 Residential CHPs in Canada 247

6.2.3.2 Commercial CHPs in Canada 251

6.3 Summary of chapter 255

6.4 Uncertainty consideration 257

Chapter 7: Conclusions 259

7.1 Solar-based water electrolysis and methane pyrolysis methods 259

7.2 Comparison of different technologies and case studies 261

7.3 Future work 264

References 266

Appendix A: Ph.D. Publications 287

Appendix B: Thesis Files 290

List of tables

Table 1.1: Specifications of some common energy storage systems based on the data from references [12,18]. 5

Table 1.2: Comparison of the properties of molten salt and molten metal [86]. 15

Table 2.1: Design conditions and input values for the proposed system subsystems. 56

Table 2.2: Exergy destruction formula for the subsystems and equipment. 67

Table 2.3: Capital cost functions for estimation price of the proposed system components [193,211–213]. 69

Table 2.4: Cost balance and auxiliary formula for the components of the reference system. 70

Table 2.5: Specifications of the proposed thermal oils [218]. 73

Table 2.6: Decision variables and their range for optimization. 74

Table 2.7: Specifications of TOPSIS points of different oils. 75

Table 2.8: Thermodynamic and exergoeconomic characteristics of solar cycle currents for the optimal point of Dowtherm A. 77

Table 2.9: Results of thermodynamic and exergoeconomic analysis based on the optimal conditions with Dowtherm A oil. 78

Table 3.1: Design conditions of different units for the modeling of the proposed system. 92

Table 3.2: Capital cost functions of different units and components [191,225,248]. 108

Table 3.3: Comparison of the present model with the respective articles [220,251]..... 110

Table 3.4: Thermodynamic properties of different streams of the proposed hybrid system. 111

Table 3.5: Summary of important thermodynamic results of the proposed system. 112

Table 3.6: Hourly electricity prices ($/kWh) for different seasons in Los Angeles, California [253]. 126

Table 4.1: Input values and assumptions for modeling of various components and cycles. 136

Table 4.2: Capital cost equation of each component in its reference year [31,210,255,256,263]. CEPCI: chemical engineering plant cost index. 147

Table 4.3: Validation of the modelling results for different units with their corresponding papers in literature. 149

Table 4.4: Thermodynamic properties and molar composition of each stream in Figure 4.1. .. 150

Table 4.5: Overview of key calculated parameters for the proposed cycle (Figure 4.1). 151

Table 4.6: Clean hydrogen production tax incentives of §45V for the United States [264,265]. 161

Table 4.7: Clean hydrogen production tax incentives for Canada [266,267]. 161

Table 5.1: Design parameters and assumptions of different equipment and systems..... 176

Table 5.2: Validation of the model for heliostat solar field [254]. 177

Table 5.3: Properties and molar fraction of different streams of the SMSMP (Figure 5.1). 179

Table 5.4: Properties of different streams of the SSOEC (Figure 5.2). 179

Table 5.5: A summary of significant findings for the SMSMP and SSOEC units. 180

Table 5.6: Summary of the techno-economic results for the five case studies. 200

Table 6.1. Critical parameters of the SOFC- and HICE-based CHPs and advanced air-source heat pumps. 212

Table 6.2. The monthly average ambient temperature and COP of the heat pump for operation in the city of Edmonton. 214

Table 6.3. Properties of the proposed residential CHP based on the SOFC with a base capacity of 5 kW in 2035. 215

Table 6.4. Properties of the proposed commercial CHP based on the SOFC with a base capacity of 100 kW in 2030. 215

Table 6.5. Key metrics of the designed CHPs along with the university requirements. All the economic values are in USD. 224

Table 6.6. A summary of heat and electricity consumption with corresponding heat to power ratio for the houses. 236

Table 6.7. Operating range of the SOFC-based CHP. 237

Table 6.8: Assumptions used to calculate the technical, economic, and environmental impacts of residential CHP installations with 5 kW capacity in Alberta. 239

Table 6.9: Space Heating Secondary Energy Use and GHG Emissions by Building Type in Alberta[1] 239

Table 6.10: A summary of important results for residential CHP installations with 5 kW capacity in Alberta. 240

Table 6.11: Project assumptions used to calculate the technical, economic, and environmental impacts of commercial CHP installations with 100 kW capacity in Alberta. 243

Table 6.12: Secondary energy use and GHG emissions of commercial sectors by energy source in Alberta[1] 244

Table 6.13: A summary of important results for commercial CHP installations with 100 kW capacity in Alberta. 245

Table 6.14: Assumptions used to calculate the technical, economic, and environmental impacts of residential CHP installations with 5 kW capacity in Canada. 248

Table 6.15: A summary of important results for residential CHP installations with 5 kW capacity in Canada. 249

Table 6.16: Assumptions used to calculate the technical, economic, and environmental impacts of commercial CHP installations with 100 kW capacity in Canada. 251

Table 6.17: Secondary energy use and GHG emissions of commercial sectors by energy source in Canada[1] 252

Table 6.18: A summary of important results for commercial CHP installations with 100 kW capacity in Canada. 253

List of figures

Figure 1.1: Capacity and discharge time of common types of energy storage systems using the data from references [13,14]. 3

Figure 1.2: Four main phases of hydrogen storage. 6

Figure 1.3: Hydrogen production cost and life-cycle carbon intensity of the main hydrogen production methods [5-17]. SMR: Steam methane reforming, ATR: Autothermal reforming, CCS: carbon capture and storage/sequestration, and RE: renewable energy. 8

Figure 1.4: Schematic of a PEM electrolyzer [1]. 11

Figure 1.5: Schematic of the alkaline water electrolyzer [1]. 12

Figure 1.6: Schematic of the solid oxide electrolyzer [1]. 13

Figure 1.7: Hydrogen storage methods [87]. 16

Figure 1.8: The use of hydrogen for local heat and power production [91]. 18

Figure 1.9: Hydrogen-fired boiler [92]. 19

Figure 1.10: Internal hydrogen combustion engine for heat and power generation [93]. 19

Figure 1.11: Graphical review of the literature for the combination of the PTC with PEM electrolyzer/fuel cell and the novelties of the present work in Chapter 2 [2]. 23

Figure 1.12: Graphical literature review about the use of SOEC, SOFC, or combined SOEC and SOFC for hydrogen production/usage and presentation of the novelties of this study. SOEC: Solid oxide electrolyzer cell; SOFC: Solid oxide fuel cell; PEME: Proton exchange membrane electrolyzer; PTC: Parabolic trough collector; TES: Thermal energy storage; SDC: Solar dish collector; RTE: Round-trip efficiency; ERTE: Exergy round-trip efficiency. 26

Figure 1.13: The main studies in literature about methane pyrolysis in molten salt. HTES: High-temperature thermal energy storage. 28

Figure 1.14: Overview of the studies about solar-based methane pyrolysis and solar-based water electrolysis. CSP: Concentrated solar power, PEM: Proton exchange membrane, PV: Photovoltaic, SOEC: Solid oxide electrolyzer, TES: Thermal energy storage. 34

Figure 1.15. The plan of City of Edmonton to expand energy saving and GHG emission reduction for over 350,000 residential and 11 million ft^2 commercial sectors [177]. 39

Figure 1.16. The plan of City of Calgary to reduce community-wide GHG emissions to net zero by 2050 [178]. 40

Figure 1.17. Thesis outline along with the publication outcomes from this study. CHP: Combined Heat and Power, ERTE: Exergy Round Trip Efficiency, GHG: Greenhouse Gases, HICE: Hydrogen Internal Combustion Engine, PEM: Proton Exchange Membrane, RTE: Round Trip Efficiency, SOFC: Solid Oxide Fuel Cell. 49

Figure 2.1: General schematic of the new hybrid system based on PTC, SRC-TEG, PEME, and PEMFC. 54

Figure 2.2: Temperature-entropy qualitative diagram for the solar field and steam Rankine cycle (SRC). 56

Figure 2.3: Validation of (a) PEMFC, (b) PEME, (c) PTC subsystems. 71

Figure 2.4: Schematic diagram of the optimization process to determine optimum thermal oil from the five options shown in connection with optimizer. 73

Figure 2.5: Artificial neural network validation for Dowtherm A oil including a) Exergy efficiency (η_{ex}), b) Cost rate ($\dot{Z}$)..... 74

Figure 2.6: Distribution of Pareto frontier diagrams for five types of thermal oils based on the grey wolf optimization algorithm. 75

Figure 2.7: Ranking of TOPSIS points of each thermal oil. 76

Figure 2.8: Population dispersion for decision variables: a) T_2 , b) P_5 , c) ZT_M , and d) ΔT_{Pinch}^{Evap} . .. 77

Figure 2.9: Sankey exergy diagram for the PTC and SRC-TEG subsystems under optimal conditions, the values are in MW. 79

Figure 2.10: Exergoeconomic Sankey diagram for PTC and SRC-TEG subsystems under optimal conditions. 80

Figure 2.11: The cost rate of different subsystems and their percentage. 81

Figure 2.12: Impact of direct normal irradiance (DNI) on the ratio of excess hydrogen to the produced hydrogen (ETP), system power output, exergy efficiency, and product cost rates..... 82

Figure 2.13: The effect of discharge time and PEMFC power generation on the required excess hydrogen ratio. 83

Figure 2.14: Effect of charge time and amount of power input to PEME on the ratio of excess hydrogen required. 84

Figure 2.15: The effect of fuel cell temperature on current density and voltage under the PEMFC system. 85

Figure 2.16: Influence of fuel cell temperature on flow density and output power under PEMFC system. 86

Figure 3.1: Schematic diagram of the proposed system based on heliostat solar, SOEC, SOFC, and Kalina cycle for green hydrogen storage. 90

Figure 3.2: Flowchart of the system modeling process and the applied methodologies. 95

Figure 3.3: The validations of the SOEC and SOFC units with the measured data in the literature [249,250]. 110

Figure 3.4: Sankey exergy diagram of the proposed hybrid system. 114

Figure 3.5: Capital costs of different units and components and their contribution to total capital cost. 115

Figure 3.6: The effect of direct normal irradiance and solar time on a) power consumption and generation of SOEC and SOFC, b) charge and discharge district heating capacities. 117

Figure 3.7: The effect of direct normal irradiance on a) hydrogen sale to the market and power consumption of hydrogen compressors at various solar times, b) RTE, ERTE, and heat absorption in the solar unit..... 118

Figure 3.8: The effect of current density and operating temperature of SOEC on a) power consumption and generation of SOEC and SOFC, b) RTE, ERTE. 119

Figure 3.9: The effect of current density and operating temperature of SOFC on a) power consumption and generation of SOEC and SOFC, b) RTE, ERTE. 121

Figure 3.10: The effect of a) compressed hydrogen pressure on RTE, ERTE, and charging district heating capacity, b) ammoniac concentration of the Kalina cycle on its exergy efficiency and power generation..... 122

Figure 3.11: Hourly direct normal irradiance at different months for the case study of Los Angeles, California, data is taken from Meteonorm software [252]. 124

Figure 3.12: a) Hourly DNI in different seasons b) Annual, seasonal, and monthly hydrogen production rate for the case study of Los Angeles, California, data is taken from Meteonorm software [252]. 125

Figure 3.13: System profit over time and payback period based on the percentage of hydrogen consumption in the SOFC to the produced hydrogen in the SOEC, HC: hydrogen consumption in the SOFC..... 127

Figure 3.14: System profit over time and payback period in different hydrogen sale prices of 2-6 $/kg at a) no hydrogen consumption b) 50% consumption of the produced hydrogen for peak shaving in the SOFC. 128

Figure 3.15: System profit over time and payback period in different discharge times based on 50% hydrogen consumption in the SOFC and hydrogen sale price of 2 $/kg. 130

Figure 4.1: Graphical illustration of the proposed innovative concept for turquoise hydrogen production based on molten salt bubble column reactor, heliostat solar field, and HTES. HE: Heat exchange, Comp: Compressor, HTES: High-temperature thermal energy storage, P: Pump, PSA: Pressure swing adsorption..... 134

Figure 4.2: The validation of the present model for methane pyrolysis with the experimental data of Kang et al [136]. 150

Figure 4.3:. Energy Sankey diagram of the proposed system during a) day and b) night. Com: Compressor, DH: District Heating, HE: Heat exchanger, Hel: Heliostat field, HTES: High-temperature thermal energy storage, Mix: Mixer, PSA: Pressure swing adsorption, Reac: Reactor, Rec: Receiver, ... 153

Figure 4.4: Capital costs of various elements and units and their impact on CAPEX with the grid electricity and renewable energy (RE) electricity sources. 154

Figure 4.5: The effect of direct normal irradiance (DNI) on system products and fuel flow rates. 155

Figure 4.6: The effect of methane conversion rate on system products and fuel flow rates. 156

Figure 4.7: The effect of average reactor temperature on methane conversion rate (MCR), system products, and fuel flow rates. 157

Figure 4.8: The effect of average reactor temperature on round-trip efficiency (RTE), exergy round-trip efficiency (ERTE), heat absorption and radiation losses in solar unit. 158

Figure 4.9: The effect of methane conversion rate on levelized cost of hydrogen (LCOH) and capital expenditure (CAPEX) at different direct normal irradiances (DNIs). 159

Figure 4.10: The effect of average reactor temperature on levelized cost of hydrogen (LCOH) and capital expenditure (CAPEX) at different carbon sale prices. 160

Figure 4.11: The effect of carbon sale price on the LCOH for solar-based methane pyrolysis with (a) grid electricity and (b) renewable energies. "W/" stands for "with". 162

Figure 4.12: The effect of methane purchase price on the LCOH for solar-based methane pyrolysis with (a) grid electricity and (b) renewable energies. "W/" stands for "with". 163

Figure 4.13: The effect of off-peak electricity price on the LCOH for solar-based methane pyrolysis with (a) grid electricity and (b) renewable energies. "W/" stands for "with". 165

Figure 4.14: The effect of system lifespan on the LCOH for solar-based methane pyrolysis with (a) grid electricity and (b) renewable energies. "W/" stands for "with". 166

Figure 4.15: The effect of cost reduction in renewable energy infrastructure on the LCOH for solar-based methane pyrolysis with (a) grid electricity and (b) renewable energies. "W/" stands for "with". 167

Figure 5.1:. Schematic diagram of the proposed novel design for turquoise hydrogen production based on heliostat solar field and molten salt-based methane pyrolysis. CMST: Cold molten salt tank, Comp: Compressor, DH: District heating, HE: Heat exchanger, HMST: Hot molten salt tank, P: Pump, PSA: Pressure swing adsorption. 174

Figure 5.2: Schematic diagram of the proposed design for green hydrogen production based on heliostat solar field and solid oxide water electrolysis. CMST: Cold molten salt tank, HE: Heat exchanger, HMST: Hot molten salt tank, P: Pump, SOEC: Solid oxide electrolyzer cell. 175

Figure 5.3: The validation of the proposed models for methane pyrolysis (Kang et al. [136]) and the SOEC (Ebbesen et al. [249])...... 178

Figure 5.4: Sankey diagrams for a) solar-based molten salt methane pyrolysis (SMSMP) and b) solar-based solid oxide electrolyzer cell (SSOEC). CMST: Cold molten salt tank, Comp: Compressor, DH: District Heating, HE: Heat exchanger, Hel: Heliostat field, HMST: Hot molten salt tank, Mix: Mixer, PSA: Pressure swing adsorption, React: Reactor, Rec: Receiver, SOEC: Solid oxide electrolyzer cell..... 182

Figure 5.5: Capital expenditure of a) solar-based molten salt methane pyrolysis (SMSMP), b) solar-based solid oxide electrolyzer cell (SSOEC).. 183

Figure 5.6: The effect of direct normal irradiance (DNI) on round trip efficiency (RTE) and levelized cost of hydrogen (LCOH) by solar-based molten salt methane pyrolysis and solid oxide electrolysis. 185

Figure 5.7: The effect of solar available time on the rate of hydrogen production and levelized cost of hydrogen (LCOH) by solar-based molten salt methane pyrolysis and solid oxide electrolysis. 186

Figure 5.8: The effect of the number of heliostat mirrors on the rate of hydrogen production and methane and water consumption by solar-based molten salt methane pyrolysis and solid oxide electrolysis. 187

Figure 5.9: The effect of methane price on levelized cost of hydrogen (LCOH) of solar-based molten salt methane pyrolysis and solid oxide electrolysis. 188

Figure 5.10: The effect of electricity price on levelized cost of hydrogen (LCOH) of solar-based molten salt methane pyrolysis and solid oxide electrolysis. 188

Figure 5.11: The effect of cost reduction in renewable energy infrastructure on levelized cost of hydrogen (LCOH) for solar-based molten salt methane pyrolysis and solid oxide electrolysis. 189

Figure 5.12: Selection of five case studies from fifty candidates all over the world with different solar direct normal irradiances (DNIs) and industrial methane prices (C_{CH_4}) [270][271–280]. 190

Figure 5.13: The spider chart presentation of the values of the major critical parameters for the five selected case studies [273–285]. 192

Figure 5.14. (a) Annual hourly direct normal irradiance (DNI) and b) annual, seasonal, and monthly hydrogen production by solar-based molten salt methane pyrolysis (SMSMP) and solar-based solid oxide electrolyzer cell (SSOEC) for the case study of Edmonton, Canada. 193

Figure 5.15. (a) Annual hourly direct normal irradiance (DNI) and b) annual, seasonal, and monthly hydrogen production by solar-based molten salt methane pyrolysis (SMSMP) and solar-based solid oxide electrolyzer cell (SSOEC) for the case study of of San Antonio, United States. 194

Figure 5.16. (a) Annual hourly direct normal irradiance (DNI) and b) annual, seasonal, and monthly hydrogen production by solar-based molten salt methane pyrolysis (SMSMP) and solar-based solid oxide electrolyzer cell (SSOEC) for the case study of Auckland, New Zealand..... 196

Figure 5.17. Annual, seasonal, and monthly hydrogen production by solar-based molten salt methane pyrolysis (SMSMP) and solar-based solid oxide electrolyzer cell (SSOEC) for the case study of Seville, Spain. 197

Figure 5.18. (a) Annual hourly direct normal irradiance (DNI) and b) annual, seasonal, and monthly hydrogen production by solar-based molten salt methane pyrolysis (SMSMP) and solar-based solid oxide electrolyzer cell (SSOEC) for the case study of Lyon, France. 198

Figure 5.19: A comparison of solar-based pyrolysis vs electrolysis preference based on methane and electricity prices for a) weak, b) average, and c) ideal solar conditions. 201

Figure 6.1. a) Schematic diagram of the main campus of the University of Alberta and the planned location for installing either b) solid oxide fuel cell (SOFC)-based combined heat and power (CHP) (FuelCell Energy [293]), or c) hydrogen fuelled internal combustion engine (HICE)-based CHP (2G Energy [93]) at the University of Alberta. 209

Figure 6.2. The average COP measurements for the advanced air-source heat pumps as a function of the ambient temperature [298]..... 210

Figure 6.3. Research methodology and strategies considered in the present study. CHP: combined heat and power, COP: coefficient of performance, SOFC: solid oxide fuel cell, UofA: University of Alberta. 211

Figure 6.4. Monthly energy consumption of the University of Alberta (UofA). The data is based on year 2019..... 216

Figure 6.5. Monthly heat-to-power ratio of the University of Alberta (UofA). The data is based on year 2019..... 217

Figure 6.6. a) Percentage of the operational load factor of the CHPs to meet the electricity demand of UofA **b)** Heat coverage percentage of UofA by the designed CHPs. 218

Figure 6.7. Monthly hydrogen demand of the SOFC-based and HICE-based CHPs to cover all the electricity demand of University of Alberta. 220

Figure 6.8. The operational load factor percentage to fully cover the heat and electricity demands of UofA by the designed SOFC-based and HICE-based CHPs..... 221

Figure 6.9. Monthly hydrogen demand of the SOFC-based and HICE-based CHPs to cover all the energy demand (electricity and heat) of University of Alberta. 223

Figure 6.10. The effect of the SOFC lifetime and CAPEX on the total annual costs of the SOFC-based CHP to cover the energy (electricity and heat) demand of UofA..... 227

Figure 6.11. A comparative diagram for the selection of the SOFC-based CHP or the HICE-based CHP for University of Alberta based on the future variations in the lifetime and CAPEX of the SOFC-based CHP. 228

Figure 6.12: Monthly gas and electricity consumption of a house in South Edmonton from July 2023 to June 2024. 231

Figure 6.13: Monthly heat to power ratio of the CHP for a house in South Edmonton from July 2023 to June 2024. 232

Figure 6.14: Monthly gas and electricity consumption of a house in West Edmonton from July 2023 to June 2024. 233

Figure 6.15: Monthly heat to power ratio of the CHP for a house in West Edmonton from July 2023 to June 2024. 234

Figure 6.16: Monthly gas and electricity consumption of a house in Central Edmonton from July 2023 to June 2024. 235

Figure 6.17: Monthly heat to power ratio of the CHP for a house in West Edmonton from July 2023 to June 2024. 236

Figure 6.18: (a) CHP market and annual maintenance costs per unit, (b) Total GHG emission reduction and monthly utility cost per unit, (c) Number of the available direct and indirect jobs, and (d) total number and CAPEX per unit, following implementation of the SOFC based CHPs with 5 kW capacity per household in residential sectors of Alberta during 2035-2050. 241

Figure 6.19: (a) CHP market and annual maintenance costs per unit, (b) Total GHG emission reduction and monthly utility cost per unit, (c) Number of the available direct and indirect jobs, and (d) total area and CAPEX per unit, following implementation of the SOFC based CHPs with 100 kW capacity per unit in commercial sectors of Alberta during 2030-2050. 246

Figure 6.20: (a) CHP market and annual maintenance costs per unit, (b) Total GHG emission reduction and monthly utility cost per unit, (c) Number of the available direct and indirect jobs, and (d) total number and CAPEX per unit, following implementation of the SOFC based CHPs with 5 kW capacity per household in residential sectors of Canada during 2035-2050. 250

Figure 6.21: (a) CHP market and annual maintenance costs per unit, (b) Total GHG emission reduction and monthly utility cost per unit, (c) Number of the available direct and indirect jobs, and (d) total area and CAPEX per unit, following implementation of the SOFC based CHPs with 100 kW capacity per unit in commercial sectors of Canada during 2030-2050. 254

List of symbols

0	Dead condition
$\boldsymbol{A}$	Area [m^2]
$\boldsymbol{A_a}$	Aperture area [m^2]
$\boldsymbol{A_{FC}}$	Active surface of the fuel cell [cm^2]
Abs	Absorbed
Act	Activation
Amb	Ambient
Ap	Aperture
An	Anode
$\boldsymbol{C}$	Concentration ratio [-]
$\boldsymbol{c}$	Cost per exergy unit [$/GJ]
Ca	Cathode
Cd	Conduction
ch	Charge
Con	Concentration
Cv	Convection
$\boldsymbol{C_{CH_4}}$	Instant methane concentration [-]
$\dot{\boldsymbol{C}}$	Cost rate of streams [$/h]

c_P	Cost rate of products [$/GJ]
d	Particle size [μm]
d_i	Inlet diameter of the receiver tube [m]
d_o	Outlet diameter of the receiver tube [m]
D	Membrane thickness [μm] & Diffusion coefficient [-]
dch	Discharge
DH	District heating
D_P	Depletion number [-]
$\$M$	Million dollars
eff	Effective
e_0	Specific exergy of each stream [kJ/kg]
e_j	Specific exergy of each stream [kJ/kg]
E	Activation energy [J/mol]
E_D	Exergy destruction [kWh]
$Ex_{D,x}$	Exergy destruction in component x [kWh]
Ex	Input exergy rate [kW]
F	Faraday constant [A.s/mol]
F_{CL}	Collector efficiency factor [-]

F_R	Heat removal factor [-]
Fr	View factor [-]
G_b	Solar radiation intensity [W/m^2]
g	Specific Gibbs free energy [kJ/kmol]
H	Height of the receiver aperture [m]
H_{im}	Immersed height of the column [m]
HHV	Higher heating value [kJ/kg]
h_x	Specific enthalpy at point x [kJ/kg]
hc	Convective heat transfer coefficient [W/m^2.K]
i	Interest rate [-]
I_{Sun}	DNI level [W/m^2]
in	Inlet
Ins	Insulation
j	Current density [A/m^2]
k	Coefficient of exchange current density [A/cm^2]
K	Thermal conductivity [W/m.K]
L	Thickness [cm]
L_{CL}	Single collector length [m]
LHV	Low heating value [kJ/kg, MJ/kg]

$\dot{m}_x$	Mass flow rate at point x [kg/s]
MS	Molten salt
N_x	Number of components x [-]
n	Number of electrons [-]
n_{cell}	Numeral of cells in a fuel cell stack [-]
$n_{CL,P}$	Number of collectors in parallels [-]
$n_{CL,S}$	Number of collectors in series [-]
Nu	Nusselt number
o	Outside
ohm	Ohmic
out	Outlet
Ph	Physical
Pr	Prandtl number
P_x	Pressure at point x [kPa, bar]
P_j^0	Partial pressure of component j [bar]
$\dot{Q}$	Heat transfer rate [kW]
r	Radius [µm]
r_{CH_4}	Rate of reaction [-]
R	Universal gas constant [kJ/kmol.K]

R^2	Coefficient of determination
Re	Reynolds number
Rad	Radiation
Rec	Receiver
Rc,ap	Receiver aperture
Rc,sur	Receiver surface
Ref	Reflection
S	Isentropic
s_x	Specific entropy at point x [kJ/kg.K]
t	Time [hr]
T_x	Temperature at point x [K]
TPB	Triple phase boundaries
U_a	Air utilization factor [-]
U_f	Fuel utilization factor [-]
U_L	Collector heat loss coefficient [-]
U_s	Steam utilization factor [-]
V	Voltage [V]
V_0	Reversible potential [V]
v_b	Rise velocity of bubbles [m/s]

V_i	Volume of the storage tank [m^3]
V_{Wind}	Speed of the wind [m/s]
W	Width of the receiver aperture [m]
$\dot{W}$	Power consumption/generation [kW]
x	Hydrogen consumption rate in the SOFC [mol/s]
X	Concentration [-]
X_{Ave}	Average length of grain contact [μm]
Y	Net cash flow [$]
Z	Capital cost [$]
α	Reflectivity coefficient of the receiver surface [-]
β	Annual operating hour
δ	Thickness [m]
ε	Electrode's porosity [%]
ΔG	Gibbs free energy change
ε_{CH_4}	Fractional alternation in gas volume [-]
ε_W	Emissivity coefficient of the receiver surface [-]
γ	Vapor consumption in the SOEC [-]
λ	Water contents [-]
ϕ_K	Maintenance factor [-]

τ	Residence time [s] & Tortuosity [-]
τ_C	Transmissivity of the cover glazing
τ_P	Effective transmissivity of the parabolic trough collector
η	Efficiency [%]
μ	Dynamic viscosity [kg/m.s]
ρ	Density [kg/m^3] & Electrical resistivity [Ω.cm]
σ	Stefan–Boltzmann constant [W/m^2.K^4]

List of abbreviations and acronyms

ANN	Artificial Neural Network
ATR	Authothermal Reforming
AWE	Alkaline Water Electrolyzer
BES	Battery Energy Srorage
CAES	Compressed Air Energy Stoarge
CAPEX	Capital Expenditure
CCS	Carbon Capture and Storage/Sequestration
CCHP	Combined Cooling, Heating, and Power
CEPCI	Chemical Engineering Plant Cost Index
CH_4	Methane
CHP	Combined Heat and Power
CMS	Cold Molten Salt
CMST	Cold Molten Salt Tank
CO_2	Carbon Dioxide
Comp	Compressor
COP	Coefficient of Performance
CRF	Capital Recovery Factor

CSP	Concentrated Solar Power
DC	Direct Current
DH	District Heating
DNI	Direct Normal Irradiance
DOE	Department of Energy
EES	Engineering Equation Solver
ERTE	Exergy Round Trip Efficiency
ETP	Excess to Produced Hydrogen
EV	Expansion Valve
Gen	Generator
GHG	Greenhouse gas
GWO	Grey Wolf Optimization
HE	Heat Exchanger
HES	Hydrogen Energy Storage
HICE	Hydrogen Internal Combustion Engine
HMS	Hot Molten Salt
HMS	Hot Molten Salt Tank
HTES	High Temperature Thermal Energy Storage
LCOH	Levelized Cost of Hydrogen

MCFC	Molten Carbonate Fuel Cell
MCR	Methane Conversion Rate
Mix	Mixer
NO_x	Nitrogen Oxide
NPV	Net Present Value
P	Pump
PEM	Proton Exchange Membrane
PEME	Proton Exchange Membrane Electrolyzer
PEMFC	Proton Exchange Membrane Fuel Cell
PHES	Pumped Hydro Energy Storage
PSA	Pressure Swing Adsorption
PTC	Parabolic Through Collector
PV	Photovoltaic
RE	Renewable Energy
RTE	Round Trip Efficiency
Sep	Seperator
SDC	Solar Dish Collector
SMR	Steam Methane Reforming
SMSMP	Solar-based Molten Salt Methane Pyrolysis

SOEC	Solid Oxide Electrolyzer
SOFC	Solid Oxide Fuel Cell
SRC	Steam Rankine Cycle
SSOEC	Solar-based Solid Oxide Electrolyzer Cell
TEG	Thermoelectric Generator
TES	Thermal Energy Storage
TOPSIS	Technique for Order of Preference by Similarity to Ideal Solution
Tur	Turbine
UofA	University of Alberta
W/	With

PART I: Introduction and Literature Review

Chapter 1: Introduction and Background[1]

1.1 Solar energy

Solar energy has become one of the most widely adopted forms of renewable energy globally, due to its scalability, ease of installation, and numerous inherent advantages [8]. However, it faces significant limitations when it comes to providing a continuous, stable, and reliable power supply. Solar power generation is inherently intermittent, being available only during daylight hours, and its output can be highly variable due to factors such as cloud cover and reduced energy levels when the sun is low on the horizon. This intermittency, coupled with the mismatch between energy production and electricity demand on distribution grids, presents a critical challenge to the widespread adoption of sustainable energies [9]. One promising solution to address this issue is the integration of energy storage systems, which can store surplus energy generated during periods of high solar output and release it during times of peak demand. By enabling a more balanced and reliable energy supply, storage technologies play a pivotal role in stabilizing electricity grids and promoting the broader use of renewable energy [10]. In addition, among the various solar-based technologies, concentrated solar power (CSP) is particularly noteworthy for its ability to deliver higher power capacities. CSP systems offer better economic feasibility for larger-scale installations, making them an attractive option for utility-scale power generation. As a result, the combination of energy storage technologies with high-temperature solar thermal energy has garnered significant attention in recent years, particularly in the context of grid-scale energy storage solutions that are capable of meeting the growing demand for clean, reliable energy [2,3].

[1] This chapter is partially based on [1–7].

1.2 Energy storage

There are various types of energy storage technologies that exist at different scales including electrical, electrochemical, mechanical, thermal, and chemical. These systems can be categorized into short-term (several seconds to minutes), medium-term (several minutes to hours), and long-term (several hours to days and months) according to discharge time [11]. Short- and medium-term energy storage systems can compensate for output fluctuations in just a few hours, while long-term energy storage technologies can bridge the gap in a matter of weeks to months [12]. Figure 1.1 illustrates different available energy storage technologies based on their storage capacity and discharge time.

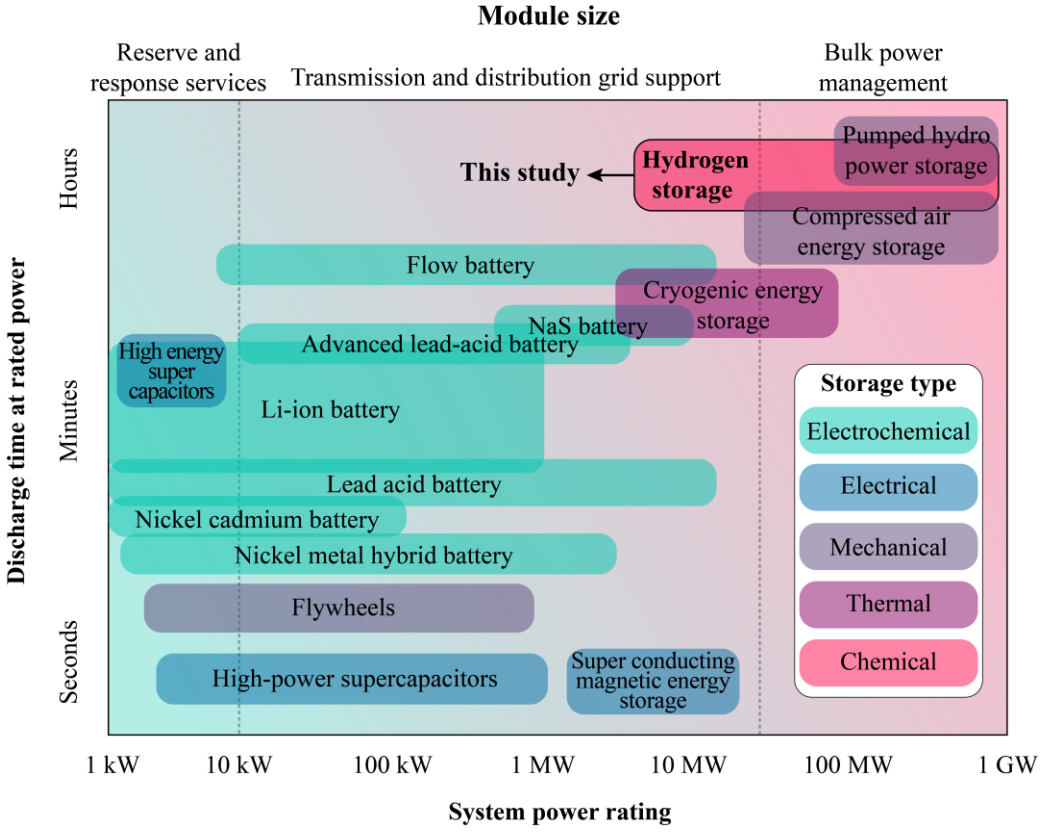

Figure 1.1: Capacity and discharge time of common types of energy storage systems using the data from references [13,14].

Battery energy storage systems (i.e., Lead-acid, Lithium-ion, Nickel-cadmium, Sodium-sulfur, Redox flow, and Hybrid flow) are mostly used as short-term and medium-term storage systems [15]. These systems in terms of power and energy density, size, portability, and rapid response are used for emergency power devices and also for power quality improvement (voltage and frequency adjustment) on grid [12]. Although batteries have high nominal efficiencies, their overall performance is 50-55% in grid support programs [16]. This poor performance is due to the need for cooling, parasitic loads in power conversion systems, and their self-discharge characteristics. Furthermore, batteries can cause environmental pollutions at the end of their lifetime due to the use of heavy and toxic metals such as sodium, cadmium, and lead in their construction. The production of lithium batteries requires high energy with a carbon footprint, and in large scales, it is associated with resource depletion, global warming, biological toxicity, and human health problems [14,16]. Another major drawback of batteries for large scale applications is that each battery has a fixed storage capacity. On the other hand, the extra generated power of renewable energies, which is mostly used as the source for charging of large-scale energy storage systems, is variable and needs a more flexible energy storage system than the batteries [16].

In addition to batteries, mechanical energy storage systems such as pumped hydro and compressed air are the other alternatives for large-scale energy storage. These systems are mature and have been developed for many years; however, owing to their dependency on the topology of the installed region, their applications are limited to specific geographical conditions. Due to slightly increased geographical adaptability, research and development of hydrogen energy storage have been recently accelerated to be hybridized with renewable energies [16]. Unlike fixed battery storage, hydrogen is more flexible and can be produced with as much as extra power as is available in the grid. It also has a high calorific value compared to petroleum products and if combined with

fuel cells, it will not emit pollutant gases [17]. Table 1.1 also presents more detailed information about the important specifications of various types of energy storage systems.

Table 1.1: Specifications of some common energy storage systems based on the data from references [12,18].

Energy storage system	Power rating (MW)	Energy density (Wh/kg)	Power density (W/kg)	Storage duration	Self-discharge per day	Discharge time	Response time	Life time (Years)	Impact on environment
PHES	100-5000	0.5-1.5	--	hrs-months	Very small	1-24 hr+	1-2 min	40-60	Substantial, massive zones of natural landscapes are needed.
CAES	5-300	30-60	--	hrs-months	Small	1-24 hr+	1-2 min	20-40	Emissions from the burn of hydrocarbons.
HES	0-50	80-10,000	500+	hrs-months	0	Secs-24 hr+	Secs-mins	5-15	Insignificant, because a by-product is water.
Lead Acid BES	0-20	30-50	75-300	Mins-days	0.1-0.3%	Secs-hrs	Secs	5-15	Lead is so toxic and polluting for soil and water.
NiCd BES	0-40	50-75	150-300	Mins-days	0.2-0.6%	Secs-hrs	Secs	10-20	Cadmium is poisonous and hazardous for health and environment.
Sodium-Sulfur BES	0.05-8	150-240	150-230	Secs-hrs	20%	Secs-hrs	Secs	10-15	Substantial, because the liquid sodium can react with water in the environment.
Lithium BES	0-0.01	75-200	150-315	Mins-days	0.1-0.3%	Mins-hrs	Secs	5-15	Relatively low, affects generally via emissions in cell production.

1.3 Hydrogen energy

As the first element on the periodic table, hydrogen is known as the most abundant, simplest, and lightest component in the universe. It can be found in water and organic composites and has the greatest energy per mass among fuels [19]. Paracelsus from Switzerland explored that the reaction between sulphuric acid and iron resulted in the gas formation in the 16th century [20]. Then, in the

17th century, Myelin stated that hydrogen can burn. Robert Boyle could produce hydrogen by a reaction of iron filings and dilute acids in 1761. Then, in 1776, Henry Cavendish recognized that hydrogen is an exceptional substance and due to critical discoveries that he reported in his article he is known as the explorer of hydrogen [21]. In 1788, Antoine Lavoisier called this element "hydrogen" from a Greek root of "hydro" meaning water. In 1800, Nicholson and Carlisle produced hydrogen by means of a water electrolyzer for the first time. In 1839, the first hydrogen-powered fuel cell was developed by William Robert Grove [21]. Hydrogen-based energy systems include four phases of production, storage, safety, and utilization, as shown in Figure 1.2 [21]. These phases are explained in the following:

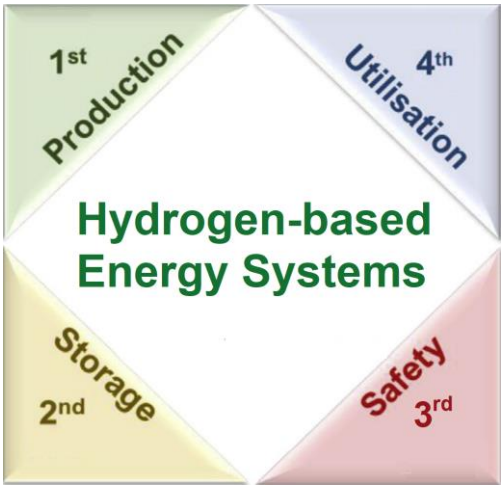

Figure 1.2: Four main phases of hydrogen storage.

The utilization of hydrogen as one of the most important clean energy carriers has garnered substantial interest across diverse applications in recent years [22]. This heightened interest aligns notably with the worldwide urgency to mitigate carbon emissions by 2050 [23]. Despite advancements in advocating for hydrogen as a sustainable energy carrier, the concurrent achievement of economically viable and clean hydrogen remains a significant challenge [24]. In response, the United States Department of Energy (DOE) set a hydrogen initiative in 2021, known

as the “Hydrogen Shot”, with the objective to reach a clean hydrogen production cost of 1 \$/kg H_2 within a decade [25]. This initiative reflects a persistent need to enhancing the affordability and availability of this crucial energy source, which can lead to expansion of hydrogen economy and economic benefits for the US and other countries [25]. It is projected that a reduction in the hydrogen cost will lead to advancement in different sectors of the hydrogen value chain [25].

1.3.1 Hydrogen production

Currently, the predominant method for global hydrogen production is steam methane reforming (SMR) due to its competitive hydrogen production cost (1-1.6 \$/kgH_2) [26]. However, as shown in Figure 1.3, the high life-cycle carbon footprint associated with this process (7-13 kgCO_2/kgH_2) makes it inappropriate for large-scale production. Although the introduction of the autothermal reforming (ATR) method reduced the life-cycle carbon intensity of hydrogen production by natural gas, its environmental footprint remains significant [26]. An alternative approach to curb carbon emissions in hydrogen production methods based on natural gas feedstock involves integrating carbon capture and storage/sequestration (CCS) units with the existing SMR and ATR infrastructure, known as blue hydrogen. This approach can reduce the life-cycle carbon intensity to about 2.5-7 kgCO_2/kgH_2, albeit at the expense of marginal growth in hydrogen cost, approximately 0.5 \$/kgH_2 [26–29]. Nevertheless, logistical challenges such as transportation and the need for dedicated carbon sequestration sites, coupled with potential leakage issues, pose significant challenges to its widespread adoption [27].

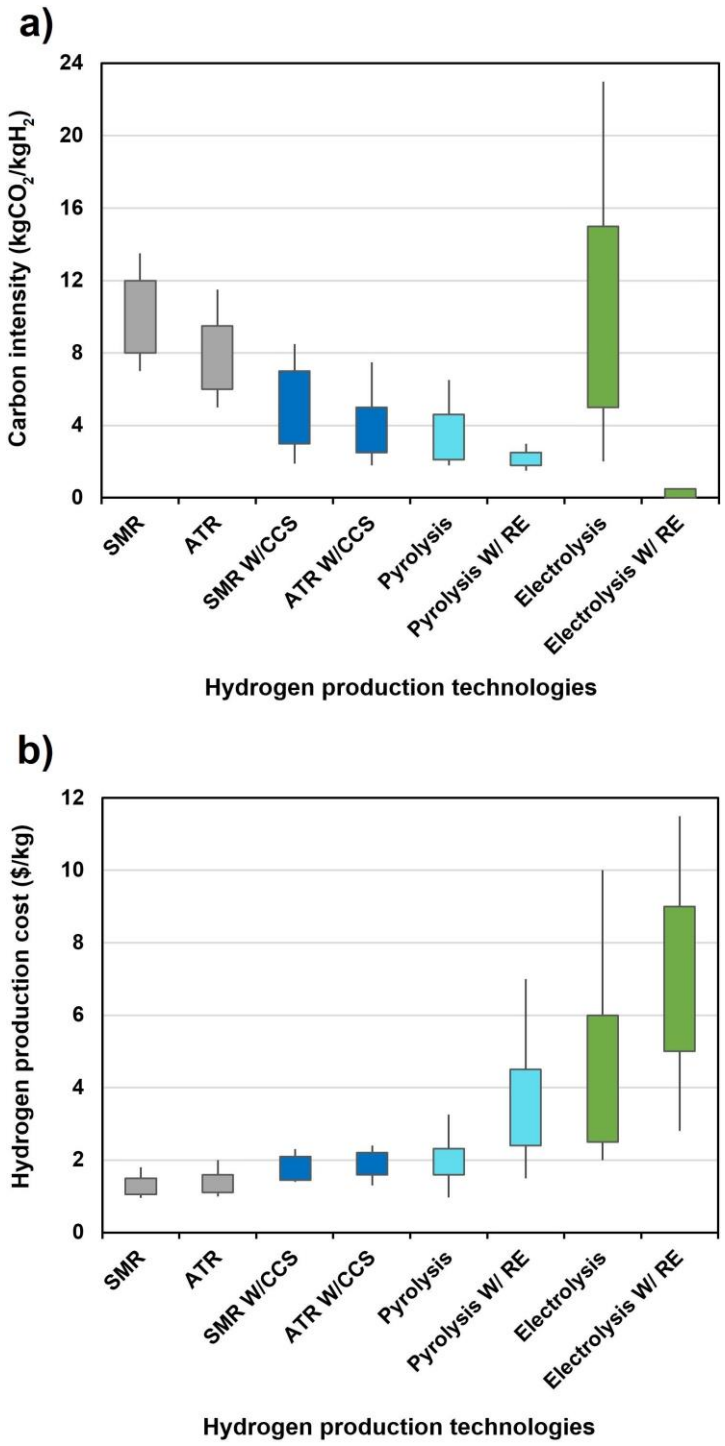

Figure 1.3: Hydrogen production cost and life-cycle carbon intensity of the main hydrogen production methods [5-17]. SMR: Steam methane reforming, ATR: Autothermal reforming, CCS: carbon capture and storage/sequestration, and RE: renewable energy.

Methane pyrolysis is considered to be a powerful competitor to traditional methane reforming methods from both economic and environmental standpoints [30]. Its remarkably low electricity consumption, coupled with zero direct emissions, results in a hydrogen production cost ranging from 1.3-3.4 $/kg$H_2$ [31,32] and a life-cycle carbon intensity spanning from 2.1-4.6 kgCO_2/kgH_2 [26,33]. Integration of methane pyrolysis with renewable energy sources further improves its attraction, yielding even lower life-cycle carbon intensity levels, between 1.8-2.5 kgCO_2/kgH_2, and subsequent hydrogen prices ranging from 2.4 to 4.5 $/kg$H_2$ [30,34,35]. Notably, there is an opportunity for further cost reductions of about 1 $/kg$H_2$ by the development of the carbon market as a byproduct of methane pyrolysis [30,32].

Another appealing approach to hydrogen production is water electrolysis. Its primary drawbacks are the high demands for electricity and water [29]. So, its economic feasibility and carbon intensity heavily depend on the sources of electricity used [29]. If grid electricity is utilized, both the cost and carbon footprint of hydrogen production are linked to the price and carbon emissions of the electricity grid [36]. On the other hand, leveraging renewable energies as the main electricity source results in hydrogen with an exceptionally reduced life-cycle carbon footprint, normally below 0.5 kgCO_2/kgH_2 [29,37]. Nonetheless, the significant initial investments required for renewable energy installations result in increased hydrogen production costs ranging from 5 to 9 $/kg$H_2$ in the electrolysis process. This highlights the need to balance environmental sustainability with economic concerns in developing clean hydrogen production solutions [26,27,36,38].

1.3.1.1 Water electrolysis

During the electrolysis process, liquid water is separated into its elementary components under the influence of electricity, for which a detailed modelling procedure is presented in the next section. Water electrolysis, because of the ability to benefit from renewable energies and renewable H_2O, as well as producing pure hydrogen, is a popular approach for hydrogen production. It is also capable of using the direct current (DC) power of some of such renewable energy units such as solar PV panels, etc. Moreover, water electrolysis has other benefits including high cell efficiency and great pure hydrogen production rate, which are special advantages to make hydrogen a potential energy carrier and an energy storage method [39]. Today, only 4% of total global hydrogen is produced by water electrolysis, but that is expected to significantly increase in the coming years with the new initiatives due to the urgent needs for that and the above-mentioned advantages for that [40,41].

1.3.1.1.1 Proton exchange membrane (PEM) electrolyzer

PEM technology is one of the popular methods for hydrogen production. In a PEM electrolyzer, water is separated into hydrogen and oxygen during an electrochemical reaction, where hydrogen and oxygen are produced at the cathode and anode, respectively. Water is pumped to the anode, splitting into oxygen (O_2), protons (H^+), and electrons (e^-). The produced protons are moved to the cathode by passing through the proton conductive membrane and the electrons are taken from the anode side using an external power circuit to provide the required cell voltage of the reaction. Finally, the electrons and protons are joined for hydrogen production at the cathode. Common materials for PEM electrolyzers include titanium for bipolar plates, platinum-group metals (e.g., platinum, iridium) for catalysts, and Nafion membranes as the electrolyte [42]. A schematic of what happens in the PEM electrolyzer is displayed in Figure 1.4.

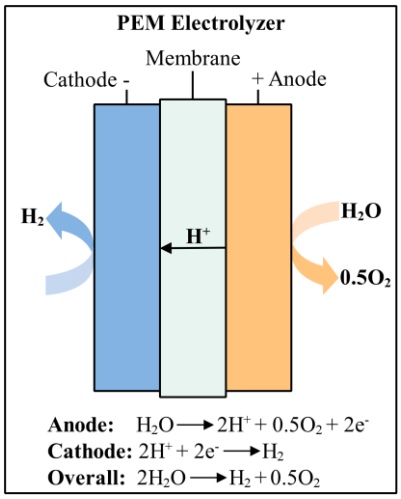

Figure 1.4: Schematic of a PEM electrolyzer [1].

Considering its ability for operation at higher current densities and quick response to dynamic operations, PEM technology has attracted much attention in recent years. The first PEM technology was introduced in the 1960s by two chemists in General Electric Company. Then, it was developed more to be used in NASA'S Gemini spaceflight [43]. It was also developed further in 1966 to overcome the weaknesses in comparison to the alkaline electrolyzer [44]. In PEM water electrolyzers, polysulfonated membranes (generally Nafion and Fumapem) are utilized as the electrolyte (proton conductor) [45,46]. The PEM electrolyzers have a lot of benefits including high efficiency, high proton conductivity and current density, fast response, low thickness, low permeability, operation at high pressure and low temperature (20-80 °C), compact design, etc. [47–49]. From the environmental perspective, PEM electrolyzer is considered a top choice because of its ability for ultrapure hydrogen production [49]. The other special characteristic of the PEM is its easy balancing, making it a favourable choice for industrial uses. However, the PEM electrolyzer has a major drawback of high investment and maintenance costs, which limits the applications of the PEM electrolyzer. Therefore, many studies have focused on developing low-price PEM electrolyzers to enhance their penetration into the commercial markets [50–54].

1.3.1.1.2 Alkaline water electrolyzer (AWE)

AWE was first presented by Troostwijk and Diemann in 1789 and was developed and used for many commercial applications even on large scales (MWh) globally [55–57]. Like the PEM electrolyzer, AWE works at low temperatures (30-100℃) by using the electrolytes with an aqueous solution (KOH/NaOH) and a concentration of 20-30%. The major drawbacks of the AWE are low efficiency, operation with low pressure, and restricted current density (<400 mA/cm^2) [58–61]. The details of phenomena that happen in an AWE are shown in Figure 1.5. AWEs typically use nickel-based catalysts, stainless steel or nickel-coated steel for electrodes, and a liquid electrolyte composed of potassium hydroxide. Firstly, at the cathode side of the AWE, two molecules of the solution are broken into two hydroxyl ions (OH^-) and one hydrogen (H_2). The generated hydrogen is removed from the cathode side to re-integrate in a gas form and the OH^-, using the power circuit, moves between the anode and cathode sides over a porous diaphragm to the anode, where being split into half molecule of O_2 and an H_2O molecule. Finally, the oxygen is re-integrated to the electrode surface and release as hydrogen [42,61].

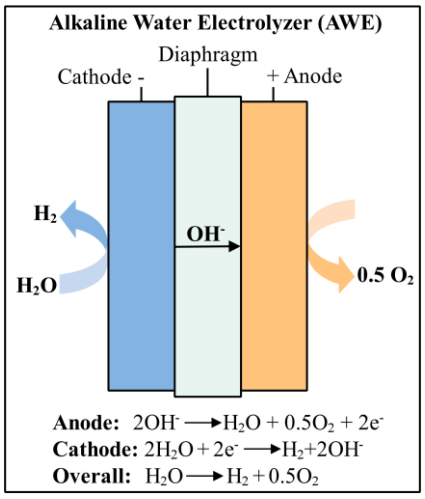

Figure 1.5: Schematic of the alkaline water electrolyzer [1].

1.3.1.1.3 Solid oxide electrolyzer (SOEC)

After the introduction of the PEM and AWE, the SOEC was introduced by Donitz and Erdle in 1980s [55,62]. In recent years, the SOEC has attracted great attention due to its ability to produce pure hydrogen with high efficiency [63]. Unlike the PEM and AWE, the SOEC is a high-temperature water electrolyzer, which operates at a temperature range of 600-900 ℃ with higher efficiency, and water is injected into it as steam. Generally, the O^{2-} conductors that have been made up of nickel/yttria stabilized zirconia are utilized in the SOEC. The SOEC commonly use ceramic materials like yttria-stabilized zirconia (YSZ) as the electrolyte, nickel-based cermet for the fuel electrode, and lanthanum strontium manganite (LSM) for the oxygen electrode. In addition, with further development of this technology in recent years, some ceramic proton conducting materials are used in the SOEC systems as well. These materials improve the efficiency because of their greater ionic conductivity in comparison with the O^{2-} conductors [64]. Like the PEM and AWE, the SOEC has its special disadvantages, the most important of which are the degradation and lack of stability [65]. The schematic of an SOEC is presented in Figure 1.6.

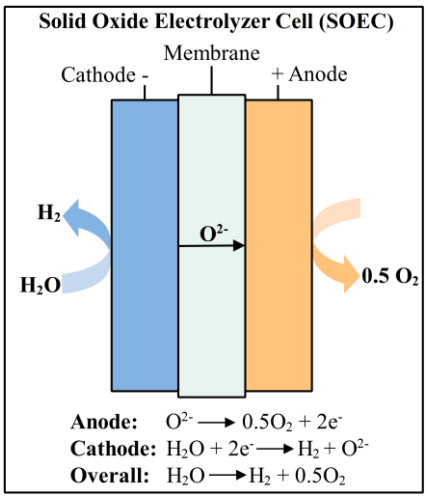

Figure 1.6: Schematic of the solid oxide electrolyzer [1].

1.3.1.2 Methane pyrolysis

In methane pyrolysis reaction, methane cracks into hydrogen and solid carbon and the process avoids the production of carbon dioxide (CO_2). This process produces several types of carbon as a by-product, including carbon black, graphitic carbon, carbon nanotubes, carbon nanofibers, etc., which vary based on the process conditions and catalysts used [66]. The produced carbon can be effectively separated and sold as a by-product to be used in different applications. For example, carbon black has uses such as in tire and steel industries, concrete, soil, direct carbon fuel cells, etc. [66]. Nevertheless, non-catalytic methane pyrolysis requires elevated operating temperatures (>1200°C), leading to economically unfavourable hydrogen production [67]. To establish a cost-competitive hydrogen production process through methane pyrolysis, it is imperative to identify an effective catalyst and design a reaction environment characterized by lower temperatures, high conversion rates, and a streamlined process for solid carbon removal [68,69]. Extensive research has been conducted on solid transition metals as effective catalysts [70–73]; however, their susceptibility to deactivation through coking is a significant challenge. Reactivation of the catalyst can be achieved through carbon gasification with O_2 [74], H_2O [75], or CO_2 [76], albeit at the expense of undesirable CO_2 emissions. Alternatively, coke removal through acid treatment is deemed prohibitively expensive [77].

An effective new strategy to prevent deactivation by coke involves subjecting methane to a liquid catalyst, wherein the catalyst surface undergoes continuous renewal [78]. In this regard, methane pyrolysis in molten media emerges as a prospective alternative for facilitating the industrial-scale expansion of turquoise hydrogen production [79]. This process takes place in a bubble column high-temperature reactor [80]. High thermal conductivity and density of molten

media facilitate the attainment of elevated temperatures and enable the continuing separation of carbon, thereby enhancing operational feasibility [81]. In addition, the utilization of molten media provides the opportunity to catalyze the process in sustained and continuous long-term operations [82].

Two primary categories of molten media utilized in methane pyrolysis are molten metal, which includes various alloys, and molten salt. As listed in Table 1.2, molten metals exhibit a sole advantage over molten salts, due to their higher catalytic activity [82]. Despite molten salts serving as comparatively weaker catalysts for cracking, their economic advantage over metals and lower density resulting from heightened intermolecular interactions make them a more cost-effective and volumetrically efficient choice for methane pyrolysis [83]. Consequently, the utilization of molten salts has the potential to lower the investment costs associated with the methane cracking process [84]. Furthermore, carbon contaminated with salt presents a more facile purification process, as the salt is readily flushable through dissolution in water [85]. Notably, salts exhibit low vapor pressure, thereby mitigating salt evaporation—a phenomenon responsible for carbon contamination and substantial melting losses [86]. Additionally, the comparatively lower melting point of salts, as opposed to metals, decreases the energy demands of the process, consequently enhancing the feasibility of large-scale implementation [86].

Table 1.2: Comparison of the properties of molten salt and molten metal [86].

Properties	Molten metal	Molten salt
Cost	High	Low
Catalytic activity	High	Moderate
Carbon purification	Complicated	Easy
Vapor pressure	High	Low
Melting point	High	Low

1.3.2 Hydrogen storage

After hydrogen production, hydrogen storage is the next step which is done by various methods, as shown in Figure 1.7.

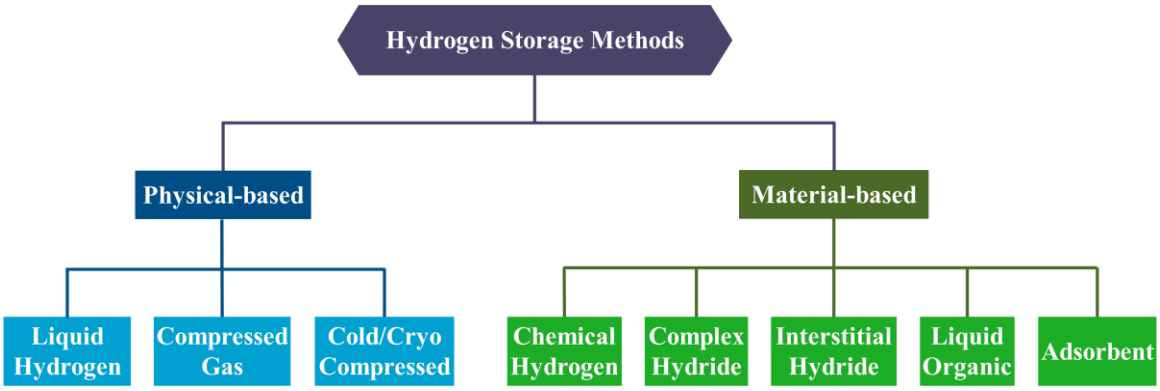

Figure 1.7: Hydrogen storage methods [87].

Physical hydrogen storage is the most common method, in which hydrogen can be supplied as either liquid or gas forms. Hydrogen storage in the gas phase needs special storage tanks with the capability of enduring very high pressures ranging from 350 to 700 bar. For hydrogen storage in the liquid form, considering the extremely low boiling point of hydrogen (-252.87 ℃) at the ambient pressure, cryogenic temperatures are required. The other ways for hydrogen storage are absorption (inside solids) and adsorption (surfaces of solids). Most of the existing hydrogen storage units use large-volume vessels that are able to supply hydrogen in gaseous form. This is not a matter for stationary uses, where the high volume of compressed gas tanks is not a challenge. But, the story is completely different for mobile and automotive hydrogen storage applications, where the hydrogen storage volume should be as low as possible. Therefore, to meet this requirement, research and development of storing hydrogen in special materials have attracted great attention. Currently, the metal hydride, sorbent material, and chemical storage of hydrogen are some of the available options to be used for hydrogen storage especially in automotive

applications [88,89]. However, most of them are not economical at the present. For more information on material-based hydrogen storage, you can refer to reference [90].

1.3.3 Hydrogen safety

Like other fuels, hydrogen does have a degree of danger; hence, safety parameters should be taken into consideration to avoid the presence of three combustion elements: ignition, oxidant, and fuel. Fortunately, hydrogen is non-toxic and much lighter than air, dissipating quickly in case of leakage. Actually, the major danger happens when a confined room is filled out with an unnoticed leakage, which can cause ignition and explosion. Moreover, hydrogen has some special characteristics that need extra engineering monitoring to guarantee its safety. For example, hydrogen can flame in a wide concentration range (4-75%) and needs very low ignition energy (10% of gasoline). Also, its embrittlement and corrosion properties in case of leakage need special attention to the selection of suitable materials [43].

1.3.4 Hydrogen utilization

Naturally, on the production side, as long as the used electricity for hydrogen generation is the excess production of renewable plants, it is perfectly in line with sustainability roadmaps. For the application part, the produced clean hydrogen can be used for a variety of applications compatible with sustainability purposes. This includes using hydrogen as the feed source of fuel cells for power generation in stationary and mobile units, using hydrogen as a boosting source of conventional combustion processes, injecting that into natural gas distribution pipelines to enhance the heating value of the gas and better sustainability, direct combustion of hydrogen for heat or cogeneration of heat and power, etc. Figure 1.8 shows a typical way of hydrogen use where it is transferred to the residential sector to be used in fuel cells as combined heat and power production

units or burned in hydrogen burners for heat supply and hot water production [91]. Another example of such typical applications is hydrogen-powered domestic boilers, as shown in Figure 1.9, recently introduced to the market [92]. In addition, as shown in Figure 1.10, CHP systems can also utilize hydrogen internal combustion engines (HICE) for the co-generation of heat and electricity. HICEs operate similarly to traditional internal combustion engines, but they use hydrogen as the primary fuel, emitting water vapor as the main byproduct, which significantly reduces carbon emissions. These systems offer flexibility in fuel type, as some can run on a blend of hydrogen and other fuels, making them a transitional solution in the energy transition towards full decarbonization [93]. However, despite the advantages, HICE-based CHPs also have certain drawbacks. One of the key concerns is the production of nitrogen oxides (NOx) due to the high combustion temperatures, which can contribute to air pollution and necessitate the use of additional emission control technologies. Additionally, the overall efficiency of HICE systems is generally lower compared to fuel cell-based CHPs, meaning more fuel is required to produce the same amount of energy [94]. While HICE technology benefits from existing engine infrastructure, the need for NOx mitigation and lower efficiency may reduce its competitiveness in the long term compared to other hydrogen-powered systems like fuel cells [95].

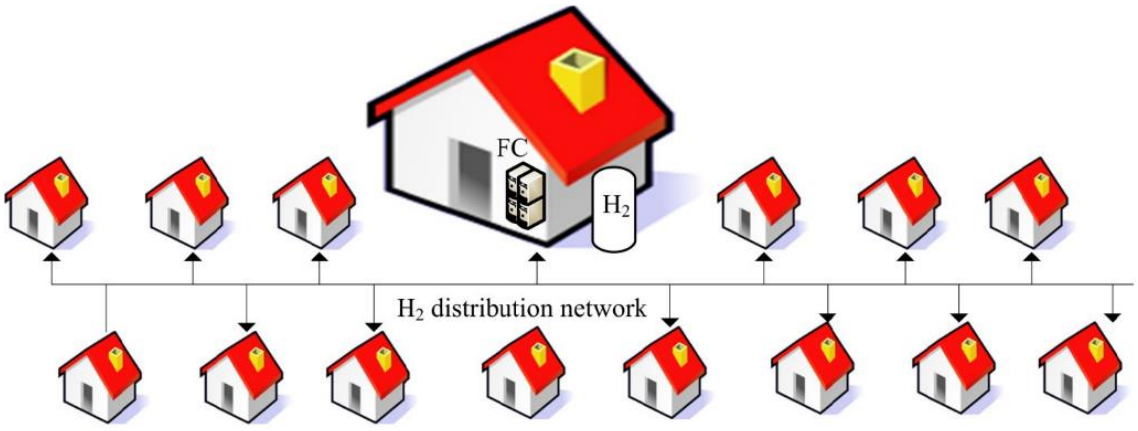

Figure 1.8: The use of hydrogen for local heat and power production [91].

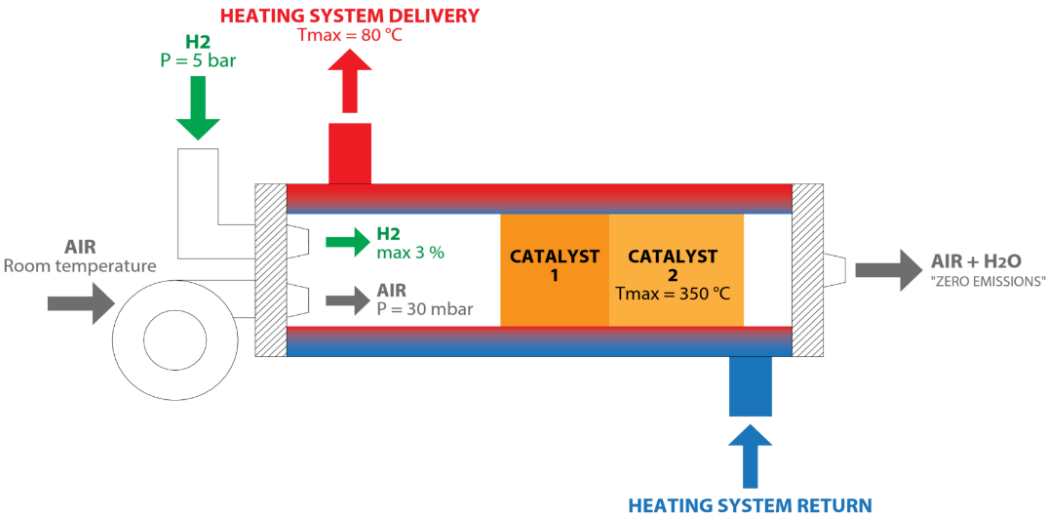

Figure 1.9: Hydrogen-fired boiler [92].

Figure 1.10: Internal hydrogen combustion engine for heat and power generation [93].

1.4 Literature review

The synthesis of renewables and hydrogen production represents a symbiotic relationship, with renewables offering emission-free pathways to generate hydrogen, and hydrogen, in reciprocation, providing a means for renewables to ensure reliable power generation [23]. While upfront costs

associated with renewable energies may exceed those of conventional sources, ongoing technological innovations and escalating demand within the energy industry drive down prices [96]. Furthermore, the environmental benefits offset these initial expenses. Considering these factors collectively, the upcoming integration of hydrogen and renewable energies holds significant promise for the future [97]. Within the spectrum of renewable energy resources, solar energy has distinguished itself as the most abundant source [98]. As a result, solar-driven hydrogen production has emerged as a leading candidate for sustainable energy solutions [98]. Given its scalability and environmental benefits, high-temperature solar thermal energy was selected as the primary renewable energy source for this thesis.

For the selection of electrolyzers, after evaluating various electrolyzer technologies, including PEM, AWE, and SOEC, the decision was made to focus on PEM and SOEC was based on their superior operational characteristics. The AWEs, while more established and less costly, were not selected due to their slower response times, lower current density, and challenges in operating efficiently at variable power inputs—making them less suitable for dynamic renewable energy systems. Therefore, PEM electrolyzers were chosen as the preferred low-temperature option due to their rapid response times and high efficiency when paired with intermittent renewable energy sources, such as solar and wind. Their compact design, ability to operate at higher current densities, and simpler system integration further strengthened their selection. SOECs, on the other hand, were chosen for high-temperature operations due to their exceptional electrical efficiency and the potential for co-electrolysis, which enables the simultaneous production of hydrogen and valuable synthetic fuels. This combination of PEM and SOEC technologies provides a versatile and efficient approach to hydrogen production, optimized for low and high-temperature applications.

The integration of high-temperature solar thermal energy with molten salt pyrolysis offers a more efficient and feasible solution for methane pyrolysis compared to other methods. This approach leverages molten salt as a shared operating fluid in both methane pyrolysis and heliostat solar technologies, providing a cost-effective pathway to low-carbon hydrogen production. The renewable, carbon-free heat from high-temperature solar field reduces energy input, while molten salts, with their excellent thermal capacity and stability, ensure efficient heat transfer for consistent methane conversion into hydrogen and solid carbon without CO_2 emissions. In contrast, alternative methods like plasma or catalytic pyrolysis are less suitable for large-scale use due to higher energy demands and infrastructure complexity. On the other hand, maximizing the efficiency of hydrogen utilization in energy production represents a critical aspect of the hydrogen value chain. Hence, a comprehensive comparison of various hydrogen-based CHP systems for power generation across different case studies will also be conducted.

The literature review of solar-based hydrogen production via water electrolysis and methane pyrolysis, along with a detailed comparison of these methods and an analysis of various hydrogen-based CHP systems across different case studies, will be discussed in the followings sections:

1.4.1 Solar based PEM electrolyzer and fuel cell

Solar and wind fields, due to their easy installation and maturity, are the most commonly used types of renewable energies [16]. Among various solar-based technologies, parabolic through collector (PTC) is considered an attractive choice for higher power capacities because of its better economic feasibility in larger installations. That is why the combination of hydrogen storage technology (by means of PEME and PEMFC for production and usage) with the PTC, has attracted much attention for grid-scale energy storage in recent years. Indeed, hybridizing a PTC with PEME and organic Rankine cycle was introduced by Yuksel [99] for the production of hydrogen,

electricity, and cooling capacity. In this work [99], authors could achieve a hydrogen production rate of around 0.1 kg/h. The important studies about the combination of the PTC with PEME and PEMFC are categorized into five groups, as shown in Figure 1.11. Group (I) relates to the thermodynamic and economic analysis of this combination. In this regard, Chitsaz et al. [100] analyzed the possibility of integrating PEME with PEMFC from thermodynamic and exergoeconomic standpoints. They found that the cost rate of power generation by the PEMFC is around 0.001 $/s. Chen et al. [101] proposed a multi-generation system based on PEME, PEMFC, PTC, and dual Rankine cycle for coincident production of hydrogen, power, heat, and hot water. They reached a maximum energy efficiency of 82% and concluded that the highest exergy destruction happens in the PEMFC. Assareh et al. [102] designed and simulated a solar-powered combined cooling, heating, and power (CCHP) system based on PEME and PEMFC. Then, by optimizing the results, the energy and exergy efficiencies of the CCHP system improved by 22.3 and 8.6%, respectively. Group (II) includes some studies that have focused on dynamic modelling of the solar unit and the design of a proportional integral controller for stabilizing the input current to the PEME [103–105]. There are also two review articles to further study of the benefits and challenges of the solar-powered PEME/PEMFC in hybrid concepts at very detailed standpoint. These studies are considered as group (III) in Figure 1.11 [106,107]. Group (IV) includes the experimental works that have analyzed the feasibility of hydrogen storage by means of solar energy and PEME for later use in a PEMFC for peak shaving applications [108–110]. To elaborate on the specific merits of the solar-based hydrogen storage for peak shaving applications, several case studies have analyzed real uses in different locations. These studies are categorized as group (V) in Figure 1.11. For instance, Ahmadi et al. [111] analyzed the performance of a solar-powered PEME coupled with a PEMFC from the transient thermodynamic viewpoint for remote CCHP

application in Toronto, Canada. They achieved the total energy and exergy efficiencies of 29% and 36%, respectively. Keshavarzzadeh et al. [17] proposed a hybrid system based on PEME, PEMFC, PTC, absorption chiller, and organic Rankine cycle for the case study of Tehran, Iran. Performing thermodynamic and economic analyses, as well as a multi-objective optimization, the authors in [17] reached an optimum cost rate of 0.058 $/s for their proposed system. De and Ganguly [112] proposed a hybrid concept including PTC, photovoltaic, PEME, PEMFC to provide thermal and electricity demands of a standalone multi-commodity cold storage system. By performing thermodynamic, economic, and environmental investigations for the climate of Kolkata, India, the authors in [112] concluded that installing such a system reduces carbon dioxide emission 350 tons/year with a payback period of seven years.

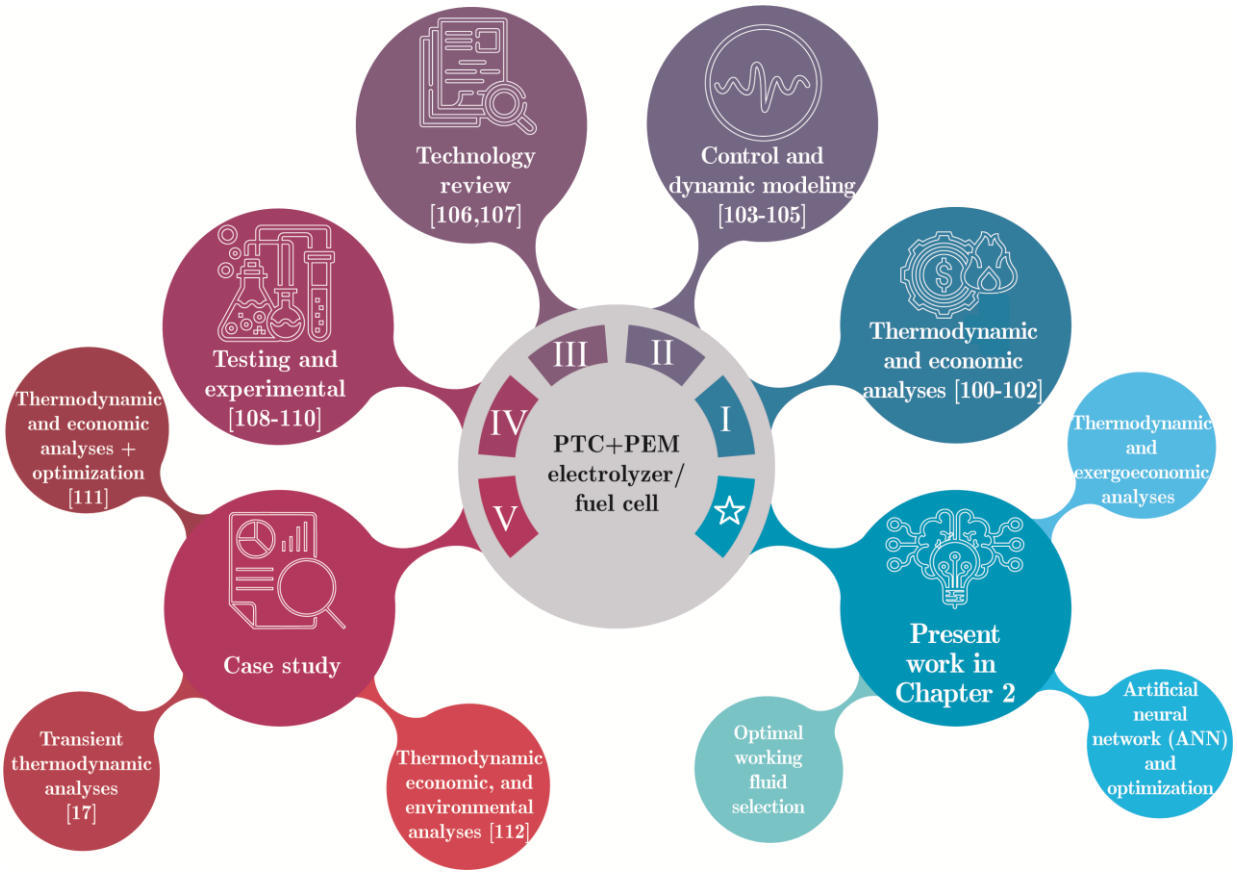

Figure 1.11: Graphical review of the literature for the combination of the PTC with PEM electrolyzer/fuel cell and the novelties of the present work in Chapter 2 [2].

1.4.2 Solar based SOEC and SOFC

An additional strategy to reduce the overall cost of green hydrogen production is employing advanced efficient electrolysis technologies to convert power to hydrogen with optimal efficiency [113]. In this regard, solid oxide electrolyzer cell (SOEC) has emerged as a promising technology for stationary and large-scale hydrogen production due to its high efficiency [114]. Compared to other alternatives such as alkaline and polymer electrolyte membrane (PEM) electrolyzers, SOEC has several advantages: First of all, it operates at high temperatures (over 700 °C), which provides faster reaction rates and higher efficiencies of up to 80% [115]. This is feasible since high temperatures reduce the activation energy for electrochemical reactions, improving efficiency by the reduced energy losses [116]. Secondly, SOECs are capable of producing high-purity hydrogen, expanding the range of applications for the produced hydrogen [117]. In addition, SOECs have a longer lifespan and high durability in comparison to other electrolyzers because of their solid-state design [118]. Finally, SOECs can efficiently operate at varying loads and adapt to intermittent power generation [119]. This allows SOECs to be easily integrated with renewable energy sources such as solar and wind for green hydrogen production [120]. Overall, given the aforementioned advantages, SOECs have the potential to play a pivotal role in facilitating the global transition towards a low-carbon economy [120].

In recent years, several studies have evaluated the feasibility of using SOEC for hydrogen production and storage. As shown in Figure 1.12, Nasser et al. [121] proposed a techno-economic analysis of hydrogen production by using SOEC and PEM electrolyzers with waste heat recovery from the cement industry integrated with the Rankine cycle. They concluded that SOEC produces more hydrogen with higher efficiency than PEM electrolyzer in all conditions and temperatures. For instance, SOEC produced 37 kg/hr of hydrogen with a total system efficiency of 23.8%, while

the PEM electrolyzer produced 27.4 kg/hr of hydrogen with an overall system efficiency of 14.45%. In addition, the minimum hydrogen production cost for SOEC and PEM electrolyzers were 0.88 and 1.55 $/kg, correspondingly. Wang et al. [122] introduced a hybrid hydrogen storage system based on SOEC driven by solar photovoltaic (PV) and solar dish collector (SDC). They also used molten carbonate fuel cell (MCFC) for conversion of the stored hydrogen to power during peak demand times. The proposed system was found to be capable of producing 3.9 kg/day of hydrogen with electrical and round-trip efficiencies of 33.6% and 59.1%, respectively. Mohammadi et al. [123] proposed a novel design for hydrogen production by using the SOEC, powered by PTC and thermal energy storage (TES). They could reach an exergy efficiency of 26.8% and a levelized cost of 4.43 $/kg for the produced hydrogen at optimal conditions.

The SOFC is a reversible mode of SOEC and similarly operates at higher temperatures with higher reaction rates and conversion efficiency in comparison to other types of fuel cells. The fuel flexibility (hydrogen and hydrocarbons) of SOFC makes it an ideal choice for power generation by using a variety of available fuels for stationary applications. Many studies have substantiated the use of SOFC for power generation during periods of high demand. For instance, Yilmaz et al. [124] proposed an innovative schematic for hydrogen production based on a PEM electrolyzer. According to their design, a portion of the produced hydrogen was stored as compressed hydrogen for later use in SOFC for power generation during peak times, and the remaining hydrogen was converted to ammonia for sale. Considering a waste heat recovery unit, they achieved overall energy and exergy efficiencies of 61% and 57%, respectively. Zheng et al. [125] proposed and investigated a multi-generation system, including PTC, PEM electrolyzer, TES, and SOFC, which operates with an efficiency of 67.5%. Performing economic analysis, they concluded that the PEM electrolyzer is the most expensive component of their hybrid system and determined that the

system has a payback period of over 9 years. Wang et al. [126] proposed a novel solar-powered reforming unit for methanol production that incorporates a SOFC to generate power during peak times using the stored methanol as fuel. They achieved a maximum energy efficiency of 93% and 48% in summer and winter, respectively.

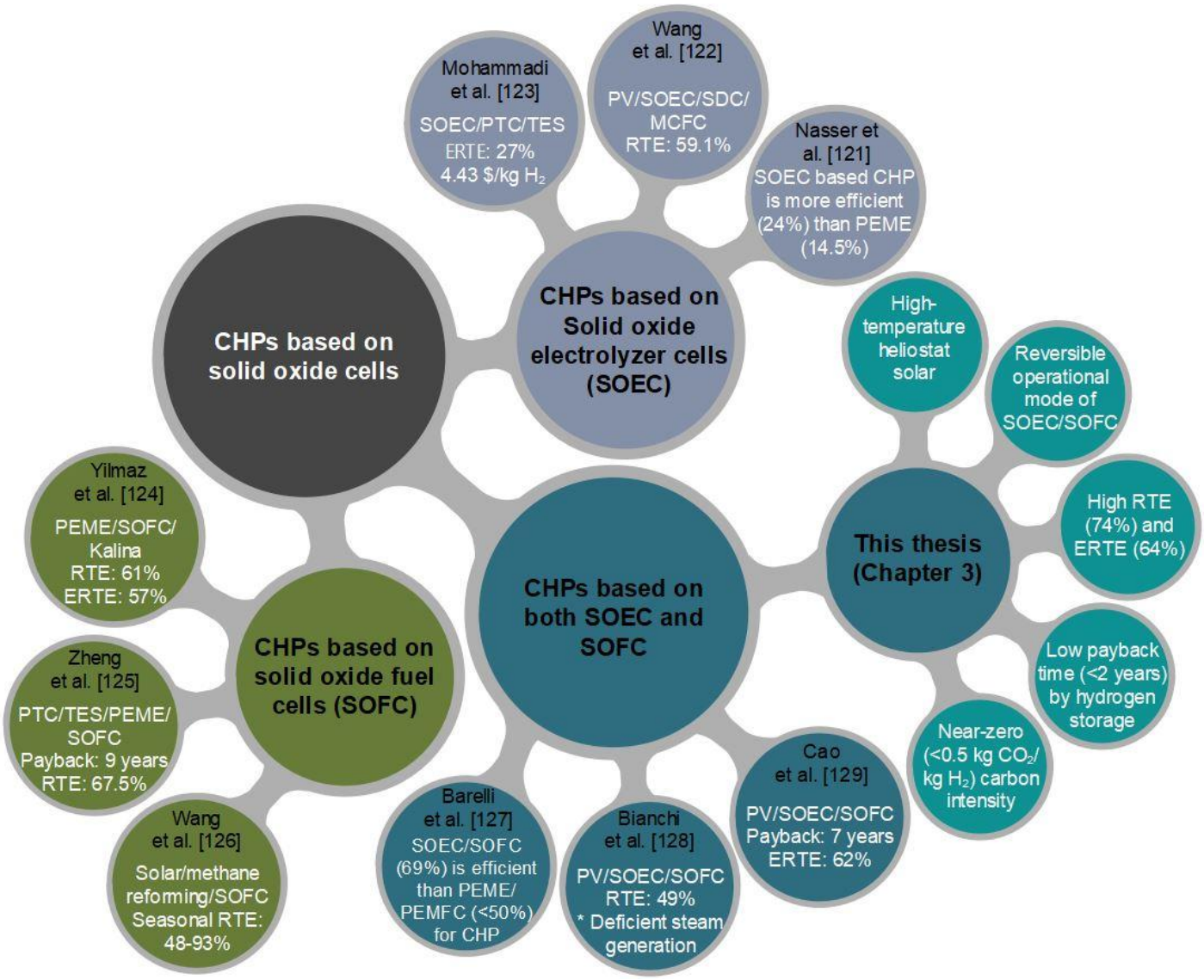

Figure 1.12: Graphical literature review about the use of SOEC, SOFC, or combined SOEC and SOFC for hydrogen production/usage and presentation of the novelties of this study. SOEC: Solid oxide electrolyzer cell; SOFC: Solid oxide fuel cell; PEME: Proton exchange membrane electrolyzer; PTC: Parabolic trough collector; TES: Thermal energy storage; SDC: Solar dish collector; RTE: Round-trip efficiency; ERTE: Exergy round-trip efficiency.

The recent studies have highlighted the simultaneous use of SOEC and SOFC for efficient hydrogen and power generation during off-peak and peak times. In addition, considering their operation in different periods, reversible SOEC/SOFC can be a promising solution to decrease the extra capital and operating costs associated with their stand-alone operation. In this regard, Barelli et al. [127] studied the effect of fuel utilization factor and anodic off-gas recirculation for hydrogen-fuelled SOFC for its application as reversible solid oxide technology. Based on the adjustments of these factors, they achieved an energy conversion efficiency of 68.6% which is remarkably higher than the best PEM performance recorded in the literature. Bianchi et al. [128] proposed an algorithm for the use of reversible solid oxide cells with a PV power plant for efficient balancing of the mismatch between power generation and demand at different times. They tested their proposed algorithm for two case studies in summer and winter to reach the best management strategy by minimizing the transition between SOEC and SOFC modes to reduce the cell degradation rate. They achieved an average round trip efficiency (RTE) of 49%, concluding that the significant power consumption required for steam generation in the SOEC is a substantial obstacle to achieving higher RTE. Cao et al. [129] proposed a hybrid system based on solar PV, SOEC, and SOFC for hydrogen storage applications. Performing a comprehensive investigation, they concluded that producing hydrogen at levels exceeding double the amount required by SOFC is not a cost-effective strategy. In addition, through the optimization of system operation, they reached an optimum exergy efficiency of 62%, a total cost rate of 1.3 $/hr, and a payback period of 7 years.

It is anticipated that through further development of SOEC, the price of green hydrogen will be lower than the average price of hydrogen production through steam methane reforming by the year 2035 [130]. In addition, benefiting the potential of hydrogen storage by using reversible solid

oxide technology will further economize green hydrogen production [128]. Given the high operating temperature of the reversible solid oxide technology in both electrolysis and fuel cell modes, its integration with high-temperature solar thermal energy systems can signify a promising concept to reach a better temperature balance between the units to improve overall efficiency. However, no study has considered the combination of reversible solid oxide cells with high-temperature heliostat solar field.

1.4.3 Solar based methane pyrolysis

Given the increasing demand for hydrogen, there has been considerable focus on the research and development of methane pyrolysis in molten salts in recent years, as illustrated in Figure 1.13.

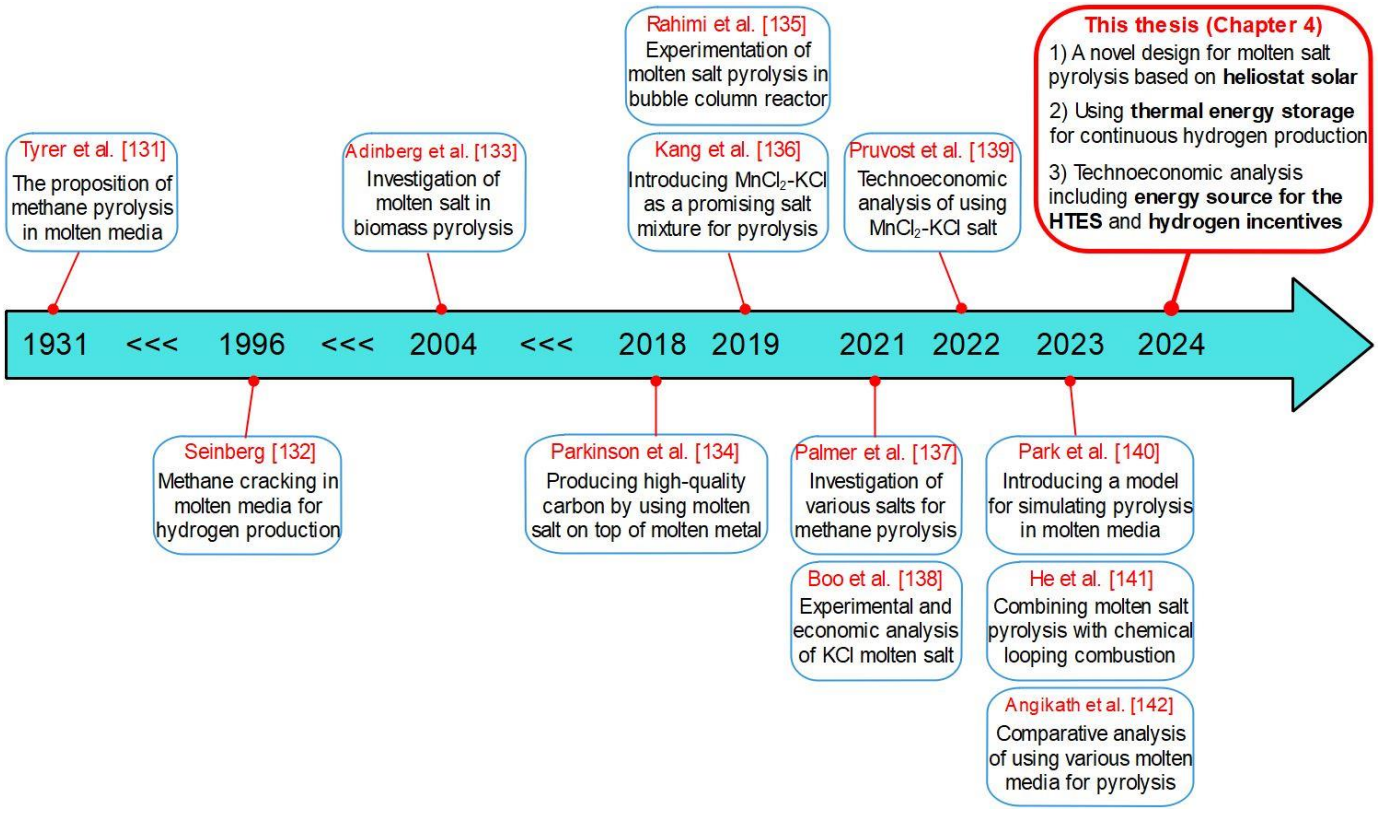

Figure 1.13: The main studies in literature about methane pyrolysis in molten salt. HTES: High-temperature thermal energy storage.

The initial proposition of the methane decomposition process within molten media was introduced by Tyrer in 1931 [131]. At a temperature of 1000°C, methane was introduced to molten iron to undergo decomposition into hydrogen and carbon. The expectation was that carbon would dissolve into the molten iron and form a floating layer on its surface. For a long period, this approach remained unexplored and no substantial investigations on methane pyrolysis in molten media were undertaken until the 1990s.

A fundamental advancement in this domain emerged through the research conducted by Steinberg in 1996, focusing on the environmentally-friendly methanol synthesis [132]. This innovative method utilized hydrogen, generated through methane cracking in molten tin, and CO_2 captured from power plants as key reactants. The study concluded that the Carnol process held the potential to significantly reduce CO_2 emissions while enhancing economic viability through the sale of the resulting carbon. In 2004, Adinberg et al. [133] investigated the viability of employing molten salt in biomass pyrolysis. Their findings substantiate that the incorporation of molten salt effectively reduces the required activation energy for the process, resulting in a noticeable enhancement in the conversion rate from initial biomass to syngas.

Prior to 2018, there were very limited investigations on the methane pyrolysis in molten salt; however, this year marked the commencement of significant advancements to this particular domain. Parkinson et al. [134] employed a multi-layer system by introducing molten salt atop molten metal to facilitate the continuous collection of carbon at the salt surface, thereby preventing impurities in downstream flow. Conducting a techno-economic analysis, they determined that the incorporation of molten salt, resulting in the production of high-quality carbon byproduct, positions methane pyrolysis as a significant competitor against SMR. Rahimi et al. [135]

conducted experimental investigations on methane pyrolysis within a bubble column reactor. The reactor comprised a catalyst layer of molten alloy and an additional molten salt layer floating on the metal surface to eliminate contaminants from the carbon product. Their findings indicated that the introduction of molten salt as a secondary phase above the catalytic molten metal alters the structure of the resulting carbon, yielding a solid carbon product with metal contaminants comprising less than 0.1 wt%. Kang et al. [136] conducted experimental investigations on the utilization of a catalyst comprising a mixture of $MnCl_2$-KCl salts for methane pyrolysis within a bubble column, reaching promising results. Through varying the molar ratio of the mixtures, they observed that the highest methane conversion occurred in the molten $MnCl_2$-KCl mixture at a molar ratio of 67:33. Furthermore, this mixture exhibited the lowest reported activation energy among molten catalysts, surpassing even that of solid carbon catalysts. Notably, the use of $MnCl_2$-KCl mixture as a molten salt for methane pyrolysis offers additional advantages, including a 99% hydrogen selectivity, the production of high-quality carbon, and its facile separation. Palmer et al. [137] examined methane pyrolysis across various molten salts, including NaCl, NaBr, KBr, and KCl. Their findings led to the determination that KCl stands out as the optimal selection due to several advantageous factors, including a lower operating temperature and a higher methane conversion rate (MCR). Moreover, the study revealed that the MCR remains consistent in the presence of accumulating carbon particles within the reactor over time. Boo et al. [138] conducted a comprehensive study including both experimental and economic analyses of methane pyrolysis within a bubble column reactor containing KCl molten salt. Their experimental findings demonstrated no catalytic deactivation during a continuous operation of 40 hours. Through optimized operational parameters that minimized KCl loss and maximized carbon revenue (450 \$/ton), they achieved a hydrogen production cost of 2.13 \$/kgH_2, which is comparable to

SMR/ATR with CCS. Pruvost et al. [139] conducted a comprehensive techno-economic evaluation of molten salt pyrolysis utilizing $MnCl_2$-KCl, with a focus on its medium- and long-term viability. The study systematically examined various parameters, including reactor temperature, MCR, and operating pressure. They concluded that to achieve a competitive price for blue hydrogen, the produced carbon should be priced at 400 €/ton. Their findings underscored the considerable potential of molten salt pyrolysis, advocating for further research efforts directed toward demonstrating and scaling up this technology. Park et al. [140] introduced a numerical model designed for simulating methane pyrolysis within the bubble column reactor, applicable to both molten metal and molten salt. Validating their modelling results with the experimental data of Kang et al. [136] for $MnCl_2$-KCl molten salt, they achieved a high degree of accuracy in their simulations. The proposed model holds significant importance in optimizing reactor performance and facilitating scale-up processes for turquoise hydrogen production. He et al. [141] proposed an innovative configuration by integrating molten salt methane pyrolysis with chemical looping combustion, and subsequently conducted a comprehensive techno-economic analysis. Considering a high MCR of 85% in a reactor temperature of 1050 ℃ and carbon sale price of 300 $/ton, they estimated a levelized cost of hydrogen (LCOH) of 1.12 $/kg$H_2$, which is 33% and 52% lower than LCOH of SMR and SMR W/CCS. Angikath et al. [142] conducted a techno-economic assessment and comparative analysis of methane pyrolysis in various molten media, including $Ni_{0.27}Bi_{0.73}$, Ga, and KCl-$MnCl_2$ (33:67), in comparison with alternative technologies. Their findings indicated that molten pyrolysis surpasses solid catalyzed pyrolysis in terms of efficiency, resulting in lower hydrogen production costs attributed to faster kinetics. In addition, the molten salt medium (KCl-$MnCl_2$) emerged as the most cost-effective plant process due to its economically advantageous procurement cost, while molten metal ($Ni_{0.27}Bi_{0.73}$) was identified as the most viable option for

sustained long-term operation. Comparing with proton exchange membrane electrolysis (PEME), they found that methane pyrolysis requires 21% of the energy required for green hydrogen production by PEME.

1.4.4 Solar based SOEC vs solar-based methane pyrolysis

As shown in Figure 1.14, the original concept of solar-based pyrolysis was first introduced by Antal et al. in 1983 [143]. Their experimentation with biomass feedstock led to the conclusion that the use of concentrated solar energy can be a promising approach for renewable-based pyrolysis. In 2005, Abanades et al. [144] pioneered the development and testing of the primary laboratory-scale high-temperature solar thermal-based reactor, aimed at turquoise hydrogen production without catalyst employment. Utilizing a solar concentrator with a diameter of 1.5 m, they achieved a methane conversion rate (MCR) of 20%. Subsequently, through refinement of the nozzle geometry to optimize the fluid-wall reaction surface area and gas residence time, the same group enhanced their initial concept, achieving an MCR of 90% [145]. Additionally, Abanades et al. [146] demonstrated the capability to attain an MCR of 99% at a temperature of 1880 K through a double-walled reactor tube of thermal plasma or four double-walled tubes in parallel to receive concentrated solar radiation in a cavity receiver. Subsequently, in 2011, Parada et al. [147] proposed a numerical simulation of a tubular solar reactor for methane pyrolysis, noting a significant decrease in methane concentration within the reaction cavity when temperatures exceeded 1500 K. To reduce the operating temperature of the reactor, Paxman et al. [79] proposed an experimental and theoretical approach to solar-based methane pyrolysis utilizing molten media in 2014. They achieved an MCR of 69% employing molten metal (Sn) for methane pyrolysis at a temperature of 1373 K. Abanades et al. [148] also developed and tested a solar-based methane pyrolysis system with continuous carbon-based catalyst injection in a tube-type reactor in 2015.

Their findings revealed that maximizing the MCR involves elevating the temperature to 1623 K while reducing the gas flow rate to enhance residence time (exceeding 100 ms). Presenting a perspective of hydrogen generation through solar-driven methane pyrolysis, Boretti [149] showed that the process holds promise as the primary method for hydrogen production in the regions abundant in both natural gas and solar resources. He highlighted its potential to achieve a cost of less than 1 $/kg$H_2$ by 2030. Msheik et al. [150] advanced an experimental analysis comparing solar-powered methane pyrolysis conducted in gas-phase versus molten media. The conclusions revealed that while the MCR in molten media is comparatively lower than that observed in the gas phase, the facilitation of carbon separation and the generation of high-quality carbon within molten media possess the potential to notably enhance the economic viability of methane pyrolysis. Abuseada et al. [151] introduced a roll-to-roll process as a scalable method for continuous solar-driven thermal methane pyrolysis in 2023. Employing a parabolic dish collector, they achieved production rates of 6.7 and 17 g/h for hydrogen and carbon, respectively, with a solar-to-chemical efficiency of 3.75% during laboratory-scale experimentation. More recently, the authors introduced a pioneering approach to solar-based methane pyrolysis, circulating molten salt between solar and pyrolysis units [4]. Additionally, they integrated a high-temperature thermal energy storage mechanism to maintain continuous operation during times when solar energy is not available. Through a thorough technoeconomic evaluation, incorporating clean hydrogen tax incentives, they determined that the target set forth by the US hydrogen shot initiative (achieving hydrogen production at 1 $/kg$H_2$) could be realized through a 20% reduction in costs related to renewable energy infrastructure, combined with the utilization of the US hydrogen tax incentives.

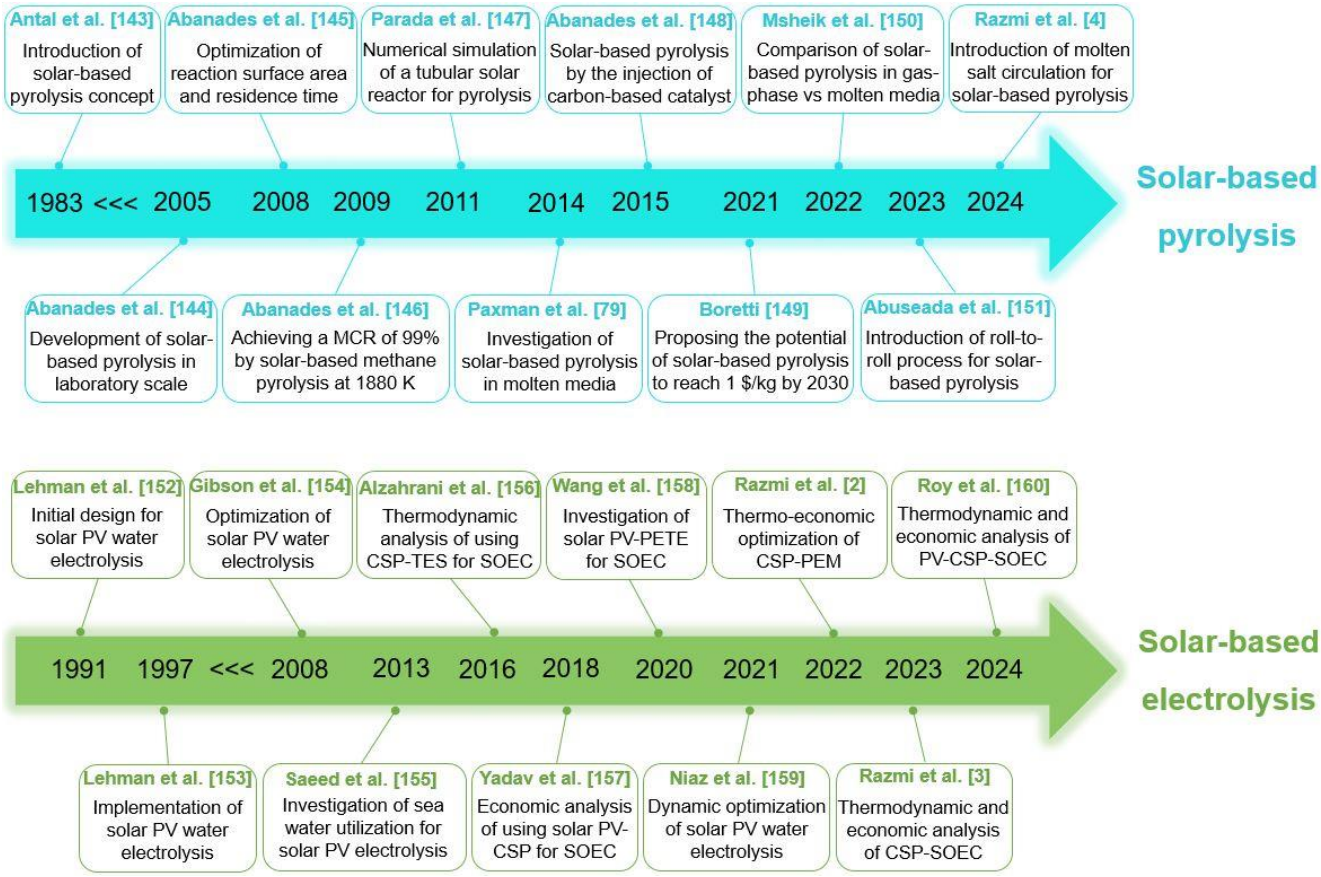

Figure 1.14: Overview of the studies about solar-based methane pyrolysis and solar-based water electrolysis. CSP: Concentrated solar power, PEM: Proton exchange membrane, PV: Photovoltaic, SOEC: Solid oxide electrolyzer, TES: Thermal energy storage.

The initial design for a laboratory-scale solar photovoltaic (PV) based water electrolysis was presented by Lehman et al. in 1991 [152]. Subsequently, in 1997, Lehman et al. [153] documented the successful implementation of their system, achieving a total electrolyzer efficiency of 76.7%, a PV efficiency of 8.1%, and a hydrogen generation efficiency of 6.2%. Building upon this foundation, Gibson et al. [154] performed an optimization of solar PV-based green hydrogen production in 2008, elevating the optimized hydrogen production efficiency to 12%. Recognizing the significant water demand inherent in electrolysis processes, Saeed et al. [155] explored the viability of utilizing seawater for solar PV-based green hydrogen production in 2013. Their findings revealed that the percentage of hydrogen recovery from the feed mixture can vary between

15 to 95%, depending on factors such as the hydrogen content in the feed and the membrane temperature. Alzahrani et al. [156] employed concentrated solar power (CSP) and thermal energy storage (TES) to facilitate green hydrogen production via solid oxide electrolyzer cell (SOEC). Through thermodynamic analysis, they achieved an energy efficiency of 56.8% for heat and hydrogen production. Yadav et al. [157] conducted an economic assessment of green hydrogen production utilizing a combination of solar PV, CSP, and SOEC units. Their calculations projected a levelized cost of hydrogen (LCOH) of 6.5 $/kg by 2030, with a prospective reduction to 3 $/kg contingent upon a decrease in SOEC cost to 330 $/kW and PV cost to 200 $/kW. Wang et al. [158] introduced an innovative approach to green hydrogen production, integrating solar PV, photon-enhanced thermionic emission cell, and SOEC. Achieving an energy efficiency of 77%, their research underscored the remarkable potential of solar-driven hydrogen production. Niaz et al. [159] conducted a dynamic optimization study of solar-based green hydrogen production, yielding a notable 24.6% increase in annual hydrogen output with a 39% reduction in startup occurrences. This highlights the importance of uninterrupted solar-based hydrogen production. In authors' prior works, Razmi et al. [2,3], they proposed a comprehensive investigation of green hydrogen production based on the combination of high-temperature solar thermal energy with both proton exchange membrane (PEM) electrolyzer [2] and the SOEC [3]. Their findings indicated superior techno-economic viability for hydrogen production via SOEC, boasting an overall round-trip efficiency of approximately 74% and a competitive LCOH of 2.75 $/kg$H_2$ [3]. Roy et al. [160] presented a comprehensive analysis including thermodynamic and economic aspects of green hydrogen production. Their study employed a combination of solar PV, CSP, and SOEC, culminating in an optimized LCOH of 1.02 $/kg$H_2$ under optimal operating conditions.

1.4.5 Potential of hydrogen-based CHPs and their comparison

The transition towards sustainable energy management in the commercial and residential sectors is becoming increasingly critical to meet decarbonization goals, improve energy efficiency, and reduce reliance on fossil fuels. Among various solutions, hydrogen-based CHP systems offer a promising solution by providing a dual-function approach: a) simultaneous generation of electricity and heat, b) Utilizing hydrogen as a clean energy carrier. These systems not only support a reduced carbon footprint, but also enhance energy efficiency, making hydrogen-based CHP systems an ideal fit for diverse building energy needs [161].

Among the available hydrogen-based CHP systems, SOFC-based CHP holds particular promise due to its high efficiency, fuel flexibility, and adaptability to various applications. SOFC-based CHPs operate at high temperatures, which enables them to achieve superior efficiency by converting chemical energy directly into electricity and capturing heat as a by-product [162]. This captured heat can be utilized for space heating, hot water, or other thermal requirements, which is particularly beneficial in cold climates or high-demand settings. By offering decentralized energy production, SOFC-based CHP systems significantly reduce transmission losses and contribute to grid stability, making them an effective tool for advancing sustainable energy management in both commercial and residential sectors [3,163].

In recent years, several studies have highlighted the potential of SOFC-based CHPs for different applications. Marocco et al. [164] analyzed the environmental impact of using SOFC-based CHPs in commercial buildings, focusing on their emissions performance under varying grid carbon intensities. Considering the unavailability of low carbon hydrogen, they found that even natural gas-fed SOFC systems become environmentally advantageous, in terms of CO_2 emissions,

when grid carbon intensity exceeds approximately 300 gCO_2/kWh. Gandiglio et al. [165] evaluated the long-term performance and emissions of commercial-scale SOFC modules (10–60 kW) installed in European non-residential buildings, operating over thousands of hours. With system-level electrical efficiencies of 51%–61% and thermal efficiencies of 18%–28%, they found that, given near-continuous operation with minimal on/off cycling, SOFC-based CHPs offer a best-in-class solution for decentralized power generation in the tens to hundreds of kW range. Alns et al. [166] investigated the feasibility of installing SOFC-based CHP systems in commercial buildings in Qatar and Kuwait. Their findings indicate that SOFC-based CHP can achieve substantial emissions reductions, with up to 30% for CO_2, 90% for NO_x, and 90% for SO_2. Additionally, they estimated payback periods of 11 years for Qatar and 7.8 years for Kuwait, highlighting the economic viability of SOFC technology in the commercial sectors of these regions. Roy et al. [167] conducted a study on the feasibility of using hydrogen as a clean energy source for residential consumers in the UK via a low-carbon energy hub. They compared two configurations: a SOFC-based CHP system and a SOFC–heat pump (HP) integrated CHP system, each powered by natural gas and hydrogen. Using actual electricity and heating demand data from a UK residential cluster, they found that the hydrogen-fuelled SOFC-CHP system achieved a higher energy efficiency of 92.12% compared to 66.98% for the natural gas-fuelled system. Economically, the SOFC–HP system was more viable, with a hydrogen-powered levelized cost of energy (LCOE) of £0.2984 per kWh. Their environmental assessment also indicated that the natural gas-powered SOFC system had levelized CO_2 emissions of 0.308 kg/kWh, while the SOFC–HP system reduced emissions to 0.213 kg/kWh.

Hydrogen internal combustion engine (HICE)-based CHPs present a cost-effective alternative to SOFC-based CHP systems. While HICE-based CHPs generally exhibit lower electrical

efficiency (less than 40%) and can generate some NO_x emissions, they provide a viable solution for applications where economic factors and higher heat demands outweigh the need for high electrical efficiency [168]. From an economic standpoint, HICE-based systems are typically less capital-intensive due to the long historical development of combustion engines and simpler manufacturing processes and lower material costs compared to SOFC systems, which require high-temperature ceramic materials and advanced control mechanisms [169]. This makes HICE-based CHPs particularly suitable for sectors that prioritize cost-effective solutions with less emphasis on maximizing electrical output. Moreover, HICE-CHPs offer operational flexibility in applications with predominant thermal loads, making them ideal for environments where the primary requirement is to meet significant heat demand [170]. This characteristic aligns well with sectors such as industrial facilities, district heating, and residential applications that require more heat generation than electricity [171]. However, while NO_x emissions from HICEs remain a challenge, ongoing advancements in exhaust after-treatment technologies, including selective catalytic reduction and exhaust gas recirculation, are increasingly enabling emission reductions [172,173].

The development of hydrogen-based CHPs holds paramount importance for Canada and specially Alberta, which has historically been a significant contributor to Canada's greenhouse gas emissions due to its reliance on fossil fuels [174]. Hydrogen-based CHP systems can not only provide a consistent and clean source of electricity but also generate heat for commercial and residential units, addressing the heating issue in frigid winters [175]. It offers advantages such as reduced greenhouse gas emissions, utilization of abundant hydrogen resources, energy security, improved air quality, job creation, increased energy efficiency, grid stability, remote applications, technology leadership, and compliance with environmental regulations, making it a promising solution for both environmental and economic sustainability in the region [176].

In this regard, the City of Edmonton has set an ambitious target to reduce community-based GHG emissions by 50% from 2005 levels by the year 2030 [177]. This commitment aligns completely with the strategic initiative to enhance local heat power generation by the SOFC-based CHPs in both commercial and residential sectors. In addition to the GHG reduction goal, the plan includes generating 10% of Edmonton's total electricity consumption locally. This local generation strategy supports the objectives for sustainable energy development and aligns with the city's broader environmental goals [177].

As shown in Figure 1.15, the scope of these energy-saving and GHG emission reduction plans is extensive. It is projected that over 350,000 residential units and 11 million square feet of commercial space in Edmonton will be included by these initiatives [177]. These measures will not only contribute significantly to reducing the city's carbon footprint but also foster energy independence and resilience within the community. By integrating local power generation, Edmonton can leverage renewable energy sources, reduce reliance on external power grids, and enhance the overall sustainability of its energy infrastructure [177].

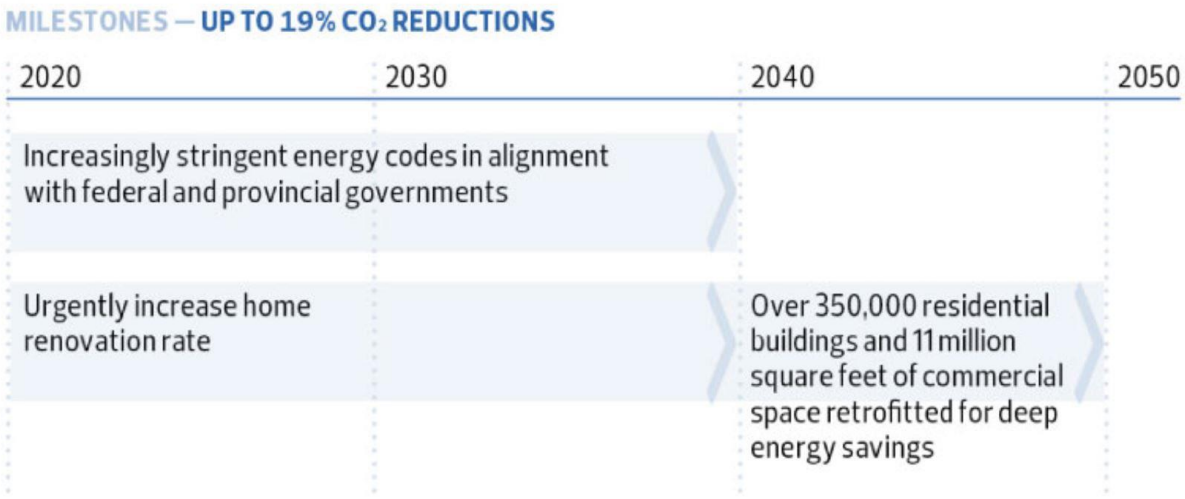

Figure 1.15. The plan of City of Edmonton to expand energy saving and GHG emission reduction for over 350,000 residential and 11 million ft^2 commercial sectors [177].

Similarly, as shown in Figure 1.16, the City of Calgary has planned to achieve net zero GHG emissions in all sectors, including residential and commercial buildings [178]. These initiatives further highlight the critical role of efficient, standalone, and clean CHP systems in meeting the energy demands of various sectors through innovative, economically viable, and sustainable approaches.

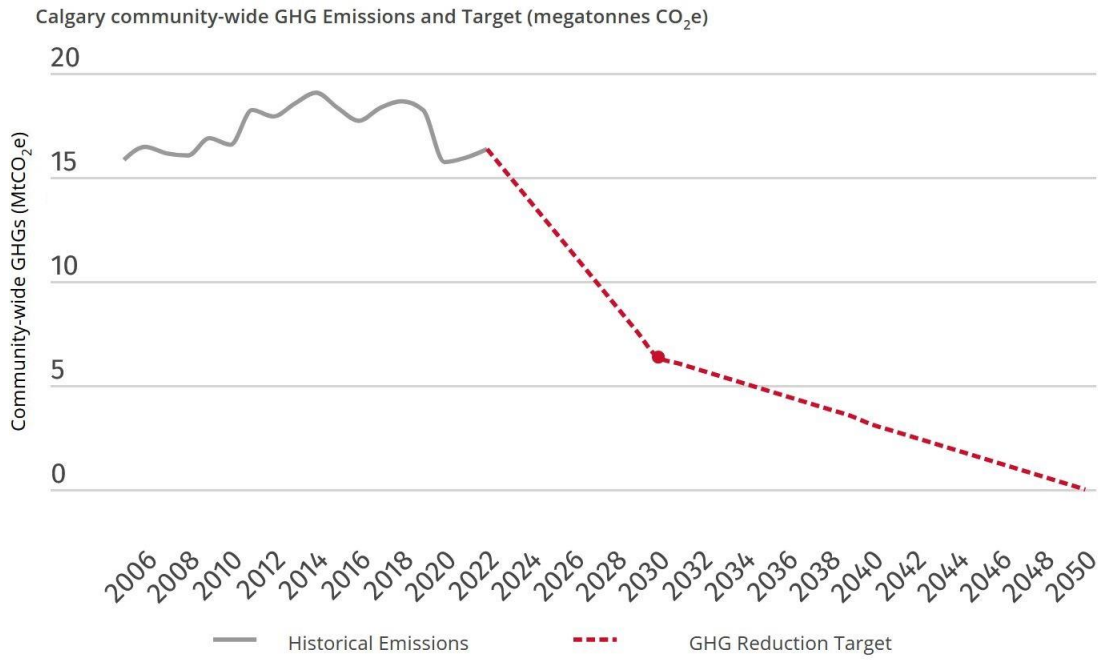

Figure 1.16. The plan of City of Calgary to reduce community-wide GHG emissions to net zero by 2050 [178].

University of Alberta (UofA) is also strategically advancing its energy management framework to foster sustainability, focusing on the integration of cutting-edge clean technologies. Central to the university's Master Energy Plan is a robust commitment to improving energy efficiency, reducing GHG emissions, and ensuring the campus's energy demands are met through a diverse range of innovative solutions. This plan emphasizes the increased use of renewable energy sources and the exploration of hydrogen technologies, aimed at reducing dependency on traditional fossil fuels, thus contributing to Alberta's energy transition.

1.5 Problem identification and proposed solutions

Research on clean and economic hydrogen production plays a pivotal role in addressing the pressing challenges in this era, such as climate change and the transition to sustainable energy systems. By advancing the understanding of efficient and environmentally friendly methods for producing hydrogen, research efforts enable the widespread adoption of this clean fuel and contribute to a greener and more sustainable future. The importance of research in this area lies in unlocking breakthrough technologies and innovative processes that can make hydrogen production both *cleaner* and *more economically viable*. Currently, a significant portion of hydrogen is derived from fossil fuels, leading to carbon dioxide emissions and environmental degradation. By exploring alternative pathways, such as electrolysis and pyrolysis powered by renewable energy sources, cost-effective and sustainable methods for hydrogen generation can be developed.

It is anticipated that through further development of high-temperature clean hydrogen production systems, the price of green hydrogen will be lower than the average price of hydrogen production through SMR by the year 2035 [130]. In addition, benefiting the potential of hydrogen storage by using reversible electrolysis/fuel cell will further economize green hydrogen production [128]. According to the literature review, very few studies have considered the combination of high-temperature solar thermal energy with reversible PEME/PEMFC and reversible solid oxide cells. Furthermore, despite the favourable prospects associated with utilizing a shared operating fluid for high-temperature solar thermal and methane pyrolysis (molten salt), this significant aspect has yet to be investigated in the literature. The main hypothesis of this thesis is to explore the potential of utilizing the thermal energy from concentrated solar fields to power water electrolysis and methane pyrolysis systems, potentially enhancing the overall efficiency, sustainability, and

economic feasibility of these processes. Based on the literature, **the main research gaps** for solar-based hydrogen production are:

- There is a lack of feasibility studies examining high-temperature solar thermal-based hydrogen production using PEME, a highly developed water electrolysis technology. Such research is imperative to enhance overall efficiency and attain economically viable hydrogen production.
- Despite recent advancements in the development of solid oxide cells for reversible operations and the potential for achieving a favourable temperature balance with high-temperature solar thermal energy, no study to date has explored the integration of solid oxide cells with a high-temperature solar thermal field. This represents a notable gap in the existing research literature and calls for further investigation to fully leverage the synergistic benefits of this promising combination.
- Despite the significant potential and favourable conditions for utilizing the same operating fluid (molten salt) in methane pyrolysis and heliostat solar technologies, there remains a notable absence of studies exploring the coupling of these two approaches to achieve economically viable hydrogen production with low carbon intensity. This unexplored combination holds considerable promise for advancing sustainable hydrogen production and merits further investigation in the field.
- No studies have been conducted to investigate the potential of energy storage technologies in facilitating continuous, full-time operation of solar-based methane pyrolysis systems. Given the constant availability of methane resources throughout day and night, this critical knowledge gap highlights the need to explore viable solutions

for uninterrupted system operation, thereby enhancing the economic feasibility and overall viability of the process.

- There is a notable absence of a comparative study between high-temperature hydrogen production technologies with low carbon intensity (solid oxide electrolysis and methane pyrolysis) to determine their respective suitability in diverse locations with varying resource availabilities. Such a study is imperative to provide valuable insights into the optimal choice of technology for different geographic and resource contexts.

1.6 Thesis contributions for the identified gaps in the literature

A summary of the main contributions of this thesis are:

1.6.1 Solar-based PEM electrolyzer and fuel cell

There is a lack of studies about the potential of integrating the PEM electrolyzers and fuel cells with high-temperature solar thermal fields. This represents a significant gap in the current research, as such a combination could potentially offer enhanced system efficiency and improved thermal management by leveraging the synergies between PEM technology and concentrated solar energy. Exploring this innovative integration could unlock new pathways for optimizing renewable energy systems and advancing the decarbonization of energy-intensive sectors. The Chapter 2 of thesis aims to address the existing gap in the literature for assessing the feasibility of using a combination of a PTC with a coupled PEME/PEMFC for grid-scale and long-term energy storage to power the grid during on-peak times. The main new contributions are:

- Introducing an environmentally-friendly design based on PTC, PEME, and PEMFC for hydrogen energy storage with the aim of peak power demand shaving;

- A comprehensive and parametric analysis of the proposed system from the energy, exergy, and exergoeconomic (3E) viewpoints;
- Comparing five different types of thermal oil as the operating fluid in the solar unit and selecting the optimal option by using a combination of artificial neural network (ANN) with grey wolf optimization (GWO) algorithms to provide a trade-off between exergy efficiency and total cost rate;
- Providing detailed exergy and exergoeconomic Sankey diagrams under optimal conditions to address the sources of exergy destruction and cost rates.

The content of this study has been comprehensively detailed and presented in Chapter 2. This chapter provides a thorough exploration of the key findings, methodologies, and analyses, ensuring a complete and structured presentation of the research outcomes.

1.6.2 Solar based SOEC and SOFC

Due to the high operating temperatures of reversible solid oxide technology in both electrolysis and fuel cell modes, its integration with high-temperature solar thermal energy systems presents a promising approach for achieving better thermal synergy between the components, thereby enhancing overall system efficiency. However, no studies have yet explored the potential combination of reversible solid oxide cells with a high-temperature heliostat solar thermal field. To bridge the existing gap in the literature and provide a viable solution, Chapter 3 of this thesis presents an innovative and environmentally-friendly concept for green hydrogen production, storage, and utilization for power and heat production. The primary objective is to utilize solar thermal energy to supply the necessary heat for raising the inlet gas temperature of the SOEC and SOFC systems, thereby minimizing electricity consumption to the greatest extent possible. The

contributions of the present study are outlined as follows:

- Proposing a novel design based on the hybridization of reversible solid oxide cells (SOEC and SOFC) with high-temperature heliostat solar thermal field for improving the RTE and ERTE of hydrogen production and utilization to 74% and 64% with near-zero carbon intensity;
- Conducting an investigation into the economic feasibility of utilizing green hydrogen storage for peak demand shaving (less than 2 years) in comparison to a stand-alone hydrogen production unit for direct sales in hydrogen markets (over 17 years);
- A thorough analysis of the proposed novel system from the energy, exergy, and economic (3E) points of view based on actual direct normal irradiance (DNI) and hourly electricity price for a real case study in the United States.

The content of this study is thoroughly detailed and fully presented in Chapter 3. This chapter offers an in-depth examination of the key findings, methodologies, and analyses, ensuring a well-organized and comprehensive presentation of the research results.

1.6.3 Solar based methane pyrolysis

Despite the recent advancements about methane pyrolysis in molten salt, there remains a lack of studies exploring its integration with REs. Considering the significant potential and unique opportunity for utilizing the same operating fluid (molten salt) in methane pyrolysis and heliostat solar technologies, combining these two technologies holds promise for achieving economically viable hydrogen production with low carbon intensity. This unexplored combination holds considerable promise for advancing sustainable turquoise hydrogen production and merits further

investigation in the field. In addition, no studies have been conducted to investigate the potential of energy storage technologies in facilitating continuous and full-time operation of methane pyrolysis systems. Given the constant availability of methane resources throughout day and night, this critical knowledge gap highlights the need to explore viable solutions for uninterrupted system operation, thereby enhancing the economic feasibility and overall viability of the process. The main new contributions of Chapter 4 are:

- Proposing an innovative concept for the combination of methane pyrolysis with high-temperature heliostat solar thermal unit to produce turquoise hydrogen with the lowest carbon intensity (~2 $kgCO_2/kgH_2$).
- Investigating the potential of implementing high-temperature thermal energy storage (HTES) to ensure uninterrupted and sustained operation of the proposed system, during periods of solar energy unavailability, to enhance the economic feasibility of the system.
- Initiating an assessment of the financial viability of turquoise hydrogen production, examining the feasibility of utilizing grid electricity versus solar renewable energy sources as the inputs for the HTES.
- Conducting a comprehensive techno-economic assessment of the proposed system, incorporating critical parameters and accounting for carbon credits from both the United States and Canada.

A comprehensive presentation of this study's content, featuring an in-depth analysis of the key findings and methodologies employed throughout the research will be presented in Chapter 4.

1.6.4 Solar based SOEC vs solar based methane pyrolysis

High-temperature solar thermal-driven hydrogen production is predicted to make a substantial contribution to the ongoing transition towards clean hydrogen production. Despite recent advancements in this domain, a thorough comparison between high-temperature solar thermal-based hydrogen production, utilizing pyrolysis and electrolysis methods, projected as future pioneering techniques, is notably absent in the existing literature. This gap represents a significant opportunity to progress and identify appropriate solar-based hydrogen production technologies for various conditions, necessitating further investigation in this domain. Consequently, this thesis presents a comprehensive comparative analysis between two innovative approaches: heliostat solar-driven hydrogen production via methane pyrolysis and water electrolysis. To enhance the economic viability of both systems, they are designed for uninterrupted operation throughout the day and night. The primary contributions of this study are:

- Conducting a comprehensive comparative techno-economic analysis between solar-based molten salt methane pyrolysis (SMSMP) and solar-based solid oxide electrolyzer cell (SSOEC).
- Proposing an innovative design for the SMSMP combined with sensible TES for uninterrupted operation during solar unavailability.
- Investigating the potential of implementing the SMSMP and the SSOEC for five case studies with different geographical locations, solar conditions, and natural gas and electricity prices.
- Analyzing the technical and economic performance of the proposed systems under dynamic solar conditions, realistic electricity, and natural gas prices.

A detailed presentation of the comparison of the SMSMP and SSOEC, including parametric analysis of novel cycles and several case studies for different cities all over the world will be presented in Chapter 5.

1.6.5 Potential of hydrogen-based CHPs and their comparison

In addition to advancements in clean hydrogen production technologies, hydrogen-based energy management would play a crucial role in the transition to sustainable energy systems in the near future. Therefore, developing robust hydrogen-based energy management systems can optimize the supply chain, ensure energy security, and provide grid stability. The final chapter of this thesis is dedicated to evaluating the potential of hydrogen-based CHPs across various case studies, including those at the UofA, Alberta, and Canada. The objective is to provide projections for the potential of hydrogen-based CHP systems, thereby facilitating informed decision-making for energy policies and sustainable development initiatives across different sectors and regions. The primary contributions of this chapter include:

- Conducting a comprehensive comparison between SOFC- and HICE-based CHP systems for the energy management of UofA to support the university's ambitious Master Energy Plan towards transition to a have sustainable campus. By evaluating the efficiency, economic viability, and environmental impacts of both systems, the study will provide insights to inform strategic decisions, enhance energy utilization, and contribute to the university's sustainability goals.
- Conducting an investigation into the potential of SOFC-based CHP systems in the commercial and residential sectors of Alberta and Canada. The study will encompass market penetration forecasts, variations in capital and operational maintenance costs, the identification of opportunities for GHG emission reductions, and the potential for job

creation in Alberta and Canada over time, highlighting the socio-economic benefits associated with the adoption of SOFC technology.

1.7 Thesis outline

This thesis is organized into four main parts that are described in seven chapters. The four parts and chapters within each part are schematically shown in Figure 1.17.

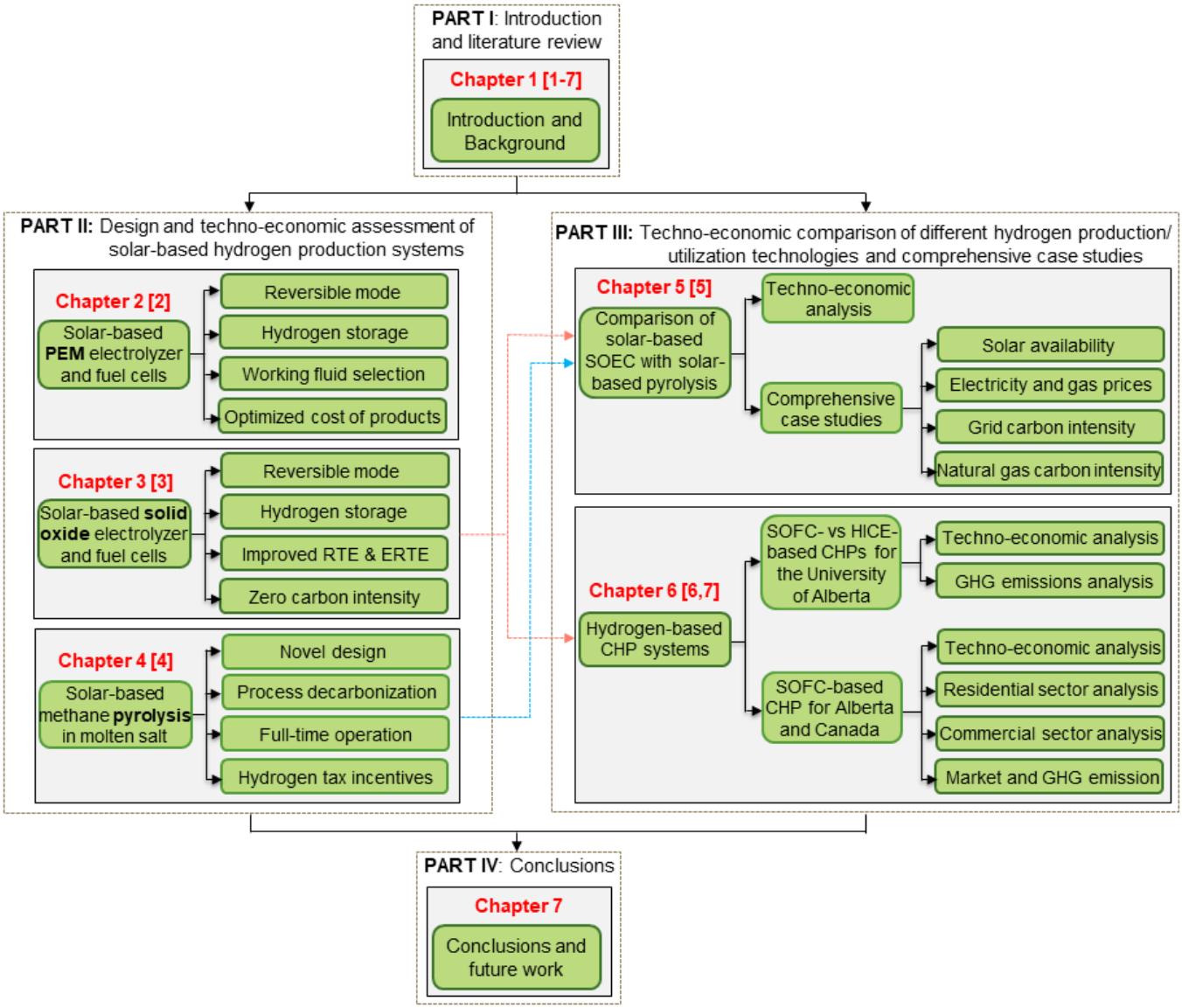

Figure 1.17. Thesis outline along with the publication outcomes from this study. CHP: Combined Heat and Power, ERTE: Exergy Round Trip Efficiency, GHG: Greenhouse Gases, HICE: Hydrogen Internal Combustion Engine, PEM: Proton Exchange Membrane, RTE: Round Trip Efficiency, SOFC: Solid Oxide Fuel Cell.

The main parts and chapters of this thesis are as follows:

- **PART I: Introduction and Literature Review**

  - ✓ **Chapter 1** provides introduction, background, literature review, problem identification, and main contributions of this thesis.

- **PART II: Techno-Economic Analysis of Different Technologies**

  - ✓ **Chapter 2** presents a novel design for solar-based PEM electrolyzer and fuel cell and comprehensive techno-economic analysis and optimization.

  - ✓ **Chapter 3** proposes an innovative solar-based solid oxide cell with reversible operation as electrolyzer and fuel cell, a comprehensive techno-economic analysis, and case study.

  - ✓ **Chapter 4** provides a novel design for solar-based methane pyrolysis in molten salt, techno-economic analysis, incorporating critical parameters and accounting for clean hydrogen tax incentives from both the United States and Canada.

- **PART III: Techno-Economic Comparison of Technologies and Case Studies**

  - ✓ **Chapter 5** provides a comprehensive techno-economic comparison of solar-based solid oxide electrolysis and solar-based methane pyrolysis, followed by a detailed case study for five cities all over the world by considering all the critical factors.

  - ✓ **Chapter 6** provides a techno-economic comparison between HICE- and SOFC-based CHPs for the University of Alberta, followed by a techno-economic analysis for

development of SOFC-based CHP in commercial and residential sectors of Alberta and Canada.

- **PART IV: Conclusions**

  - ✓ **Chapter 7** provides a summary of conclusions of this thesis and suggestions for future work.

PART 2: Novel Designs and Comprehensive Investigation of Different Solar-based Hydrogen Production Technologies

Chapter 2: Design and Techno-Economic Analysis of a Novel Solar-Based Proton Exchange Membrane Electrolyzer and Fuel Cell System[1]

With the continuous penetration of renewable energy plants into energy markets and their surplus power generation during off-peak periods, the need for utility-scale energy storage technologies is globally prioritized. Among the existing large-scale energy storage technologies, hydrogen storage has appeared as a powerful alternative due to its environmental benefits and the ability to store a large amount of energy for several hours to months. The major objective of the proposed research is to introduce a novel configuration of green hydrogen production for power generation during peak demand periods. In this regard, an innovative hybridization of a solar unit based on a parabolic trough collector with a proton-exchange membrane electrolyzer and a fuel cell is introduced and analyzed from the thermodynamic and exergoeconomic perspectives. Moreover, a sensitivity analysis and a multi-objective optimization based on the combination of neural network and grey wolf optimization algorithms are conducted to select the best working fluid of the solar unit and ideal operating conditions according to the minimum cost rate and the maximum exergy efficiency. The results indicate that Dowtherm^{TM} A synthetic oil is the best working fluid, and the proposed system can generate 9, 14.9, and 20.1 MW of power during off-, mid-, and on-peak times, respectively. The results also show that the proposed system operates with an exergy efficiency of 17.6%, a cost rate of 492.4 $/hr, and a levelized cost of electricity of 62.6 $/MWh under the optimal conditions.

[1] This chapter is based on [2].

2.1 System description

A graphical diagram of the proposed hybrid system is demonstrated in Figure 2.1. This system consists of four central subsystems: PTC, steam Rankine cycle (SRC)-thermoelectric generator (TEG), PEME, and PEMFC. As already mentioned, one of the main features of the present system is the power production and storage with the least environmental impact. Due to the fact that the electricity demand in the network is not the same at different times, the performance of the proposed system is described in two phases: baseload and peak load.

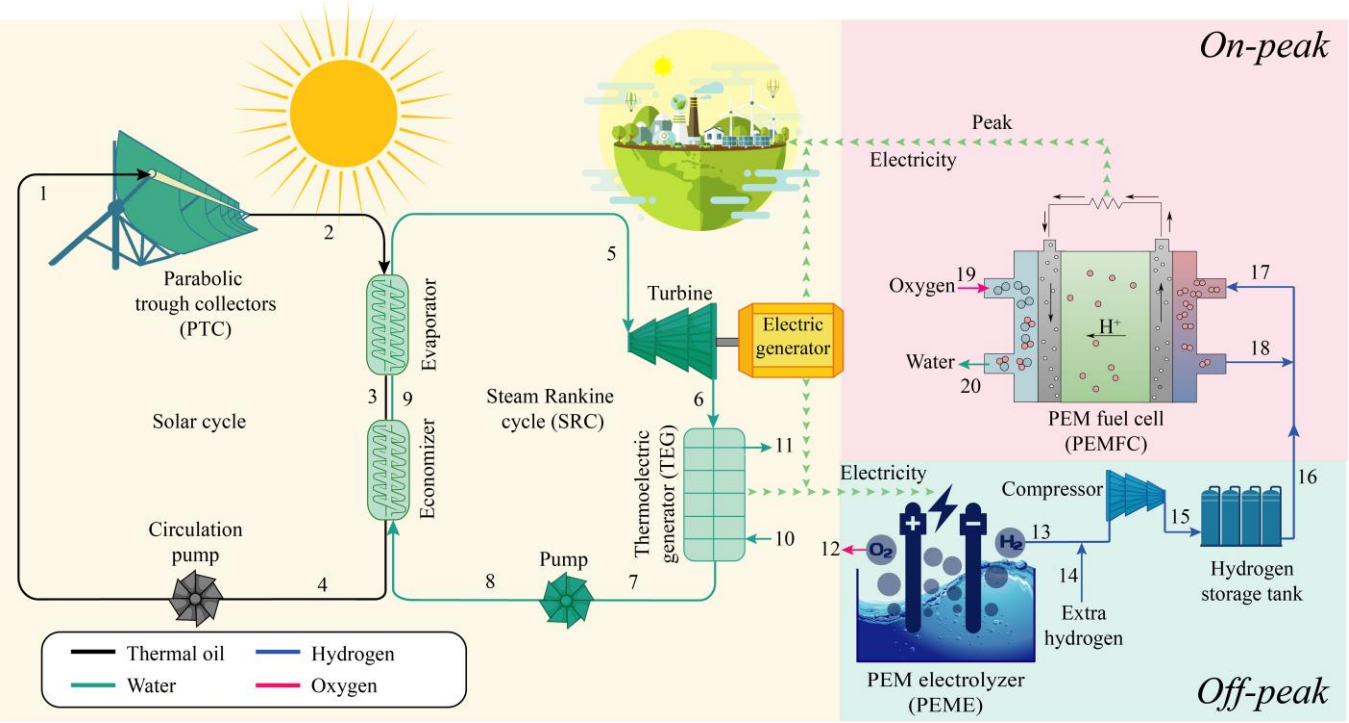

Figure 2.1: General schematic of the new hybrid system based on PTC, SRC-TEG, PEME, and PEMFC.

2.1.1 Baseload

The main part of the proposed system generates the base load of the grid. This section includes two subsystems of parabolic trough collector (PTC) and steam Rankine cycle-thermoelectric generator (SRC-TEG). The reasons behind using TEG for waste heat recovery are its simple

structure and avoid adding more complexity to the proposed system, being environmentally-friendly, low production cost, and high scalability [179]. As the sun rises, the sun's radiation is reflected and concentrated by the parabolic collectors on the oil flow through the center of the collectors. The passing oil temperature is increased by absorbing heat, exiting the collector at a high temperature (states 1 and 2). The hot oil then enters the evaporator and economizer (states 2 and 3) and heats the working fluid of the SRC.

In the SRC-TEG subsystem, water first enters the pump as a saturated liquid (state 7). High-pressure water is pumped into the evaporator and economizer (state 8). The water temperature rises as it passes through the economizer and evaporator and enters the turbine as saturated steam (state 5). The inlet steam expands inside the turbine and exits at low pressure (state 6). The output stream from the turbine enters the TEG to recover the heat with usable energy density. Indeed, the TEG not only helps to change the water vapor phase, but also generates excess power by capturing the heat of the water vapor. Finally, the water exits the TEG as saturated liquid and re-enters the pump and this cycle is completed (state 7).

2.1.2 Peak loads

The consumed power during the day can be divided into three parts: off-, mid- and on-peak. During off-peak times, the additional power generated by the SRC and TEG is given to the PEME. The electrolyzer converts water flow into hydrogen and oxygen by the flow of electricity (states 12 and 13). The produced hydrogen is compressed for later use by a compressor and stored in the tank (state 15). During on-peak times, the supplied hydrogen is exploited to run the PEMFC (states 16-18). Reacting with oxygen inside the fuel cell, power and water are produced as the system products (states 19 and 20). Finally, the power generated by the PEMFC is transmitted to the grid

for peak shaving and load levelling. To better understand the performance of the SRC, a precise quantitative temperature-entropy (T-S) diagram is shown in Figure 2.2.

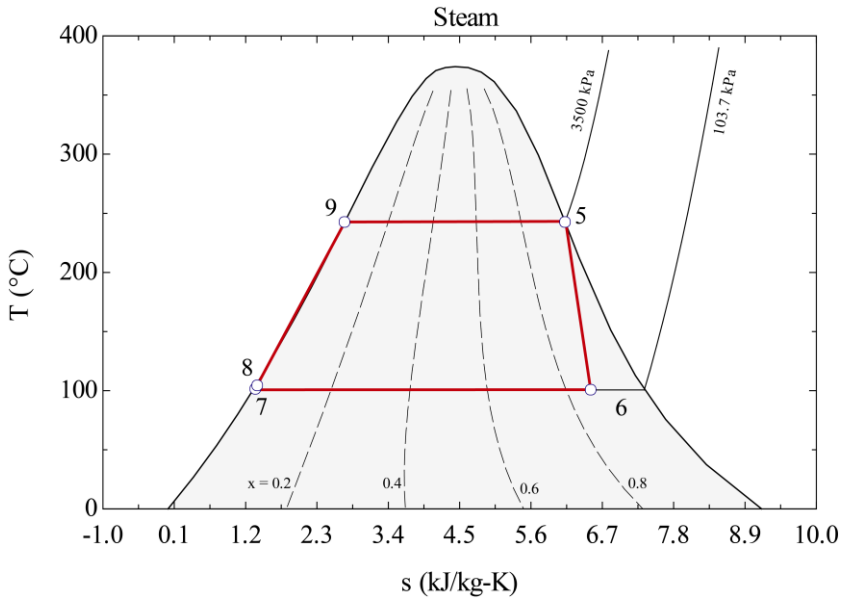

Figure 2.2: Temperature-entropy qualitative diagram for the solar field and steam Rankine cycle (SRC).

2.2 System modelling

In order to provide a comprehensive evaluation of system performance, a precise investigation of the proposed system based on energy, exergy, and exergoeconomic assessments are done according to the design conditions and initial values listed in Table 2.1.

Table 2.1: Design conditions and input values for the proposed system subsystems.

Subsystem	Parameter	Abbreviation	Value	Unit
PTC [180,181]	Absorptivity of receiver	α	0.96	-
	Collector heat loss coefficient	U_L	3.82	W/m^2.°C
	Correction factor for diffuse radiation	γ	0.95	-
	Effective transmissivity of PTC	τ_P	0.94	-
	Heat transfer coefficient inside the receiver	h_{fi}	300	W/m^2.°C
	Receiver inside diameter	$D_{i,r}$	0.066	m
	Receiver outside diameter	$D_{o,r}$	0.07	m
	Single collector length	L	12.27	m
	Single collector width	W	5.76	m
	Solar collectors area	$A_{a,p}$	100,000	m^2
	Sun period	t_{Sun}	11	hr
	Thermal conductivity of the receiver	K	16	W/m.°C

	Total solar radiation	G_b	850	W/m^2
	Transmissivity of the cover glazing	τ_C	0.96	-
PEME [182,183]	Activation energy for anode	$E_{act,a}$	76	kJ/mol
	Activation energy for cathode	$E_{act,c}$	18	kJ/mol
	Charging period	t_{Ch}	6	hr
	Faraday constant	F	96.486	C/mol
	Membrane thickness	D	100	μm
	Partial pressure of H_2	P_{H_2}	101.325	kPa
	Partial pressure of O_2	P_{O_2}	101.325	kPa
	PEME temperature	T_{PEM}	80	˚C
	Pre-exponential factor for anode	J_a^{ref}	1.7×10^5	A/m^2
	Pre-exponential factor for cathode	J_c^{ref}	4.6×10^3	A/m^2
	Water contents at the anode	λ_a	14	-
	Water contents at the cathode	λ_c	10	-
PEMFC [100,184–186]	Constant part of the resistance	R_c	0.0003	Ω
	Discharging period	t_{Dch}	3	hr
	Empirical constant	ψ	22	-
	Fuel utilization factor	U_F	0.85	-
	Heat of vaporization of water	$\overline{H}_V$	40644	J/mol
	Higher heating value of hydrogen	$\overline{HHV}_{H_2}$	285.55	kJ/mol
	Limiting current density of PEMFC	I_{FC}	1.5	A/cm^2
	Membrane thickness	l_m	0.00254	cm
	Numeral of cells in stack	n_{cell}	$13{,}000 \times 4$	-
	Numeral of electrons	n	2	-
	Operating temperature of PEMFC	T_{FC}	85	℃
	PEMFC active surface area	A_{FC}	232	cm^2
	PEMFC operating current density	i	0.5	A/cm^2
	Specific heat capacity of hydrogen	$\overline{Cp}_{H_2}$	28.86	J/mol.℃
	Specific heat capacity of nitrogen	$\overline{Cp}_{N_2}$	28.39	J/mol.℃
	Specific heat capacity of oxygen	$\overline{Cp}_{O_2}$	29.72	J/mol.℃
	Specific heat capacity of water	$\overline{Cp}_{H_2O}$	75.95	J/mol.℃
	Universal gas constant	R_u	8.314	kJ/kmol.℃
SRC [187]	Figure of merit coefficient	ZT_m	0.8	-
	Isentropic efficiency of SRC turbines	η_{Tur}	85	%
	Isentropic efficiency of SRC pump	η_{Pump}	80	%

2.2.1 Energy analysis

The following subsections provide the governing equations for modelling each unit from the first law of thermodynamics. The optimum sizing of each system component in Figure 2.1 is calculated based on the design conditions specified in Table 2.1 and the governing equations listed below.

2.2.1.1 Parabolic trough collector

The useful heat rate received by the collectors can be calculated as follows [180]:

$$\dot{Q}_u = n_{CL,P} \cdot n_{CL,S} \cdot F_R \cdot \left[\left(S_{AR} \cdot A_a \right) - \left(A_r \cdot U_L \cdot (T_{ri} - T_0) \right) \right] \tag{2.1}$$

where $n_{CL,S}$, $n_{CL,P}$, F_R and S_{AR} are the number of collectors in series and in parallel, heat removal factor, and absorbed solar radiation. Moreover, A_a, A_r, U_L, T_{ri}, and T_0 are area of the aperture, area of the receiver, collector heat loss coefficient, receiver inlet temperature, and ambient temperature, respectively. In this regard, S_{AR}, F_R and A_a can be defined as follows [99,182,188]:

$$S_{AR} = G_b \cdot \eta_r \tag{2.2}$$

$$\eta_r = \gamma \cdot \tau_C \cdot \tau_P \cdot \alpha \tag{2.3}$$

$$F_R = \frac{\dot{m}_{CL} \cdot C_{P,CL}}{A_r \cdot U_L} \cdot \left[1 - \exp\left(- \frac{A_r \cdot U_L \cdot F_{CL}}{\dot{m}_{CL} \cdot C_{P,CL}} \right) \right] \tag{2.4}$$

$$F_{CL} = \frac{1 \diagup U_L}{\frac{1}{U_L} + \frac{D_{o,r}}{h_{fi}} + \left(\frac{D_{o,r}}{2k} \cdot \ln \frac{D_{o,r}}{D_{i,r}} \right)} \tag{2.5}$$

$$A_a = L_{CL} \cdot (W - D_{o,r}) \tag{2.6}$$

where, η_r is the receiver efficiency.

2.2.1.2 Steam Rankine cycle

The rate of heat received by the economizer and evaporator can be calculated by [189,190]:

$$\dot{Q}_{Evap} = \dot{m}_9 \cdot \left(h_5 - h_9\right) = \dot{m}_2 \cdot \left(h_2 - h_3\right) \tag{2.7}$$

$$\dot{Q}_{Eco} = \dot{m}_8 \cdot \left(h_9 - h_8\right) = \dot{m}_3 \cdot \left(h_3 - h_4\right) \tag{2.8}$$

The isentropic efficiency and the amount of power generated by the steam turbine are equal to [191]:

$$\eta_{ST} = \frac{h_5 - h_6}{h_5 - h_{6,s}} \tag{2.9}$$

$$\dot{W}_{ST} = \dot{m}_5 \cdot \left(h_5 - h_6\right) \tag{2.10}$$

The power consumed by the pump ($\dot{W}_P$) can be found by taking the isentropic efficiency (η_P) into the consideration [192]:

$$\eta_P = \frac{h_{8,s} - h_7}{h_8 - h_7} \tag{2.11}$$

$$\dot{W}_P = \dot{m}_7 \cdot \left(h_8 - h_7\right) \tag{2.12}$$

2.2.1.3 Thermoelectric generator

Due to the fact that a great amount of heat is always wasted in the condenser, the TEG unit has replaced the conventional condensers. In fact, the residual heat of the steam cycle in the turbine exhaust is recovered by the TEG for further power generation. The equation of energy balance, efficiency, and production capacity by the TEG unit can be expressed as follows [193]:

$$\dot{m}_6 \cdot h_6 + \dot{m}_{10} \cdot h_{10} = \dot{m}_7 \cdot h_7 + \dot{m}_{11} \cdot h_{11} + \dot{W}_{TEG} \tag{2.13}$$

$$\eta_{TEG} = \eta_{Carnot} \frac{\sqrt{1+ZT_m} - 1}{\sqrt{1+ZT_m} + \frac{T_C}{T_H}} \tag{2.14}$$

$$\eta_{TEG} = \frac{\dot{W}_{TEG}}{\dot{m}_7 \cdot (h_8 - h_7)} \tag{2.15}$$

here, ZT_m is figure of merit coefficient and its value strongly influences the performance of the TEG system, so ZT_m is an important parameter in design of the TEG. The auxiliary equations are as follows [194]:

$$\eta_{Carnot} = 1 - \frac{T_C}{T_H} \tag{2.16}$$

$$T_H = \left(\frac{T_7 + T_{11}}{2} \right) \tag{2.17}$$

$$T_C = \left(\frac{T_6 + T_{10}}{2} \right) \tag{2.18}$$

here, T_H and T_C are the temperatures of the hot and cold sides, correspondingly.

2.2.1.4 PEM electrolyzer

The proton exchange membrane (PEM) electrolysis has been appeared as one of the most attractive methods for hydrogen production from water in recent years because of its insignificant maintenance costs and favourable environmental properties [195]. The chemical reactions in the PEME are as follows [196]:

Overall: $H_2O + Energy \longrightarrow H_2 + \frac{1}{2}O_2$ (2.19)

Cathode $2H^+ + 2e^- \longrightarrow H_2$ (2.20)

Anode: $H_2O \longrightarrow 2H^+ + 2e^- + \frac{1}{2}O_2$ (2.21)

Moreover, the overall energy needed for chemical reactions within the PEME can be determined as follows [197]:

$$\Delta H = \Delta G + T \cdot \Delta S \tag{2.22}$$

here, ΔG and $T \cdot \Delta S$ show the Gibbs free energy change and required heat energy. In addition, the amount of hydrogen rate produced is found by [198]:

$$\dot{N}_{H_2,out} = \frac{J}{2F} = \dot{N}_{H_2O,Reacted} \tag{2.23}$$

here, J and F are the current density and Faraday constant. In addition, the consumed electricity for generating hydrogen equals [199]:

$$Ex_{elect} = E_{elect} = J \cdot V \tag{2.24}$$

In Eq. (2.24), V represents the overpotential, which is defined by:

$$V = V_0 + V_{act,a} + V_{act,c} + V_{ohm} \tag{2.25}$$

According to the Nernst equation, V_0, $V_{act,a}$, $V_{act,c}$, and V_{ohm} are calculated as follows [183,198,200,201]:

$$V_0 = 1.229 - \left(8.5\times10^{-4}\cdot\left(T_{PEM} - 298\right)\right) \tag{2.26}$$

$$V_{act,i} = \frac{R_u \cdot T}{F}\cdot \sinh^{-1}\left(\frac{J}{2J_{0,i}}\right) = \frac{R_u \cdot T}{F}\cdot \ln\left[\frac{J}{2J_{0,i}} + \sqrt{\left(\frac{J}{2J_{0,i}}\right)^2 + 1}\right], \qquad i = a,c \tag{2.27}$$

$$J_{0,i} = J_i^{ref}\cdot \exp\left(-\frac{E_{act,i}}{R_u \cdot T}\right), \quad i = a,c \tag{2.28}$$

$$V_{ohm} = J\cdot\int_0^D \frac{dx}{\left(0.5139\left(\frac{\lambda_a - \lambda_c}{D}x + \lambda_c\right) - 0.326\right)\cdot \exp\left[1268\left(\frac{1}{303} - \frac{1}{T}\right)\right]} \tag{2.29}$$

2.2.1.5 PEM fuel cell

Similar to PEMEs, the applications of PEMFC have been substantially grown in recent years and a promising future can be predicted for this technology for power generation [202]. During on-peak times, to generate electricity for peak shaving, the stored hydrogen reacts with the air in the PEMFC, and power, heat, and water are produced based on the following equations [203]:

Overall: $$H_2 + \frac{1}{2}O_2 \longrightarrow H_2O + Energy \tag{2.30}$$

Cathode: $$2H^+ + 2e^- + \frac{1}{2}O_2 \longrightarrow H_2O \tag{2.31}$$

Anode: $$H_2 \longrightarrow 2H^+ + 2e^- \tag{2.32}$$

The maximum voltage produced by a cell or Nernst voltage can be obtained as follows [184]:

$$E_{\text{Nernst}} = \left[-\frac{\Delta G^0}{n \cdot F} + \frac{\Delta S}{n \cdot F} \cdot (T_{FC} - T_0) + \left(\frac{R_u \cdot T_{FC}}{n \cdot F} \cdot \ln\left(\frac{P_{O_2}^{0.5} \cdot P_{H_2}}{P_{H_2O}} \right) \right) \right]$$
$$= \left[1.229 - \left(0.85 \times 10^{-3} \cdot \left(T_{FC} - 298.15 \right) \right) + \left(\frac{R_u \cdot T_{FC}}{n \cdot F} \cdot \ln\left(\frac{P_{O_2}^{0.5} \cdot P_{H_2}}{P_{H_2O}} \right) \right) \right] \quad (2.33)$$

here, ΔG^0, n, F, and R_u are Gibbs free energy changes in the standard condition (-237.17 kJ/mol), the quantity of electrons moving through the electrochemical reactions, the Faraday constant, and the global gas constant, respectively. Furthermore, T_{FC} is the working temperature of the PEMFC in terms of Kelvin and P_J is the operative partial pressure of the reactant J, respectively. Losses in the fuel cell can be divided into three categories: loss of activation, concentration, and ohm. Activation losses (V_{act}) are associate with the onset of reactions that are considered as ignition sparks. Temperature, partial pressures, and the type of catalyst used on the electrodes are among the three parameters affecting the activation loss. A semi-empirical equation is used to calculate activation losses [17,185]:

$$V_{act} = 0.948 - \xi - \left(0.000076 \cdot T_{FC} \cdot \ln\left(C_{O_2} \right) \right) + \left(0.000193 \cdot T_{FC} \cdot \ln\left(I_{FC} \right) \right) \quad (2.34)$$

$$\xi = 4.38386 + 0.0002 \cdot \ln(A) - 5 \cdot \ln\left(C_{H_2} \right) \quad (2.35)$$

$$I_{FC} = i \cdot A_{FC} \quad (2.36)$$

$$C_{O_2} = \frac{P_{O_2}}{5.08 \cdot 10^6 \cdot \exp\left(-\frac{498}{T_{FC}} \right)} \quad (2.37)$$

$$C_{H_2} = 9.174 \cdot 10^{-7} \cdot \exp\left(-\frac{77}{T_{FC}} \right) \quad (2.38)$$

here, C_{O_2} and C_{H_2} are the oxygen and hydrogen concentrations at the membrane/cathode and anode/membrane interfaces, correspondingly. Moreover, I_{FC} and A_{FC} show the flow current from the cell and the active surface of the fuel cell, respectively. Concentration losses are the result of the fluctuations. Actually, the fluctuations cause a voltage drop across the input hydrogen concentration through the reactions on the surface of the electrode. To calculate the concentration losses, the following equation is used [100]:

$$V_{con} = -\frac{Ru \cdot T_{FC}}{n \cdot F} \cdot \ln\left(\frac{i_l}{i_l - i}\right) \tag{2.39}$$

here, i_l is the highest current density in PEMFC. Ohmic losses are caused by losses of electrical resistance in the fuel cell. This kind of resistance is common in all fuel cell equipment like ionic resistance in membranes, ionic and electron resistance in electrodes, and electronic resistance in bipolar plates and terminals. Based on the Ohmic law, Ohmic voltage is stated as [185,204]:

$$V_{ohm} = I_{FC} \cdot (R_m + R_C) \tag{2.40}$$

$$R_m = \frac{\rho_m \cdot l_m}{A} \tag{2.41}$$

$$\rho_m = \frac{181.6 \cdot \left(1 + 0.03 \cdot \left(\frac{i_{FC}}{A}\right) + \left(0.062 \cdot \left(\frac{T_{FC}}{303}\right)^2 \cdot \left(\frac{i_{FC}}{A}\right)^{2.5}\right)\right)}{\left(\psi - 0.6343 - \frac{3 \cdot i_{FC}}{A}\right) \cdot \exp\left(\frac{4.18 \cdot (T_{FC} - 303)}{T_{FC}}\right)} \tag{2.42}$$

here, R_C, R_m, l_m, and ρ_m are the constant part of the resistance for each cell, the resistance of the internal cell, the thickness of the membrane, and the membrane specific resistivity against the flow

of hydrated protons, respectively. In addition, ψ is an empirical constant. Finally, the output power of PEMFC and its voltage value according to the losses are obtained by:

$$V_{FC} = E_{Nernst} - V_{act} - V_{con} - V_{ohm} \tag{2.43}$$

$$W_{FC} = N_{cell} \cdot V_{FC} \cdot I \tag{2.44}$$

here, N_{cell} indicates the quantity of cells in the stack. According to the PEMFC electrochemical reactions, the molar rate equilibrium of the reactions can be defined as follows [100]:

$$\dot{n}_{H_2,in} = \frac{Z_z}{U_F} \tag{2.45}$$

$$\dot{n}_{H_2,out} = \dot{n}_{H_2,in} - Z_z \tag{2.46}$$

$$\dot{n}_{H_2,use} = \dot{n}_{H_2,in} - \dot{n}_{H_2,out} \tag{2.47}$$

$$\dot{n}_{O_2,in} = \frac{Z_z}{2 \cdot U_0} \tag{2.48}$$

$$\dot{n}_{O_2,out} = \dot{n}_{O_2,in} - \frac{Z_z}{2} \tag{2.49}$$

$$\dot{n}_{N_2,in} = \dot{n}_{N_2,out} = \frac{79}{21} \cdot \dot{n}_{O_2,in} \tag{2.50}$$

$$Z = \frac{N_{cell} \cdot i \cdot A}{2 \cdot F} \tag{2.51}$$

here, U_F and U_0 show the fuel and air utilization factor proportions. Moreover, Z_z is the amount of molar conversion during the total reaction at the fuel cell. Moreover, the amount of water produced in PEMFC is:

$$\dot{n}_{H_2O,generate} = N_{cell} \cdot \frac{I}{2 \cdot F} \tag{2.52}$$

According to the fuel cell energy balance relationship, the amount of heat generated can be defined as follows [185]:

$$\dot{Q}_{net} = \dot{Q}_{ch} - W_{FC} - \dot{Q}_{s,l} \tag{2.53}$$

$$\dot{Q}_{ch} = \dot{n}_{H_2,use} \cdot HHV \tag{2.54}$$

$$\begin{aligned} \dot{Q}_{s,l} = {} & Cp_{H_2} \cdot \left(\dot{n}_{H_2,out} \cdot T_{FC} - \dot{n}_{H_2,in} \cdot T_0 \right) + Cp_{O_2} \cdot \left(\dot{n}_{O_2,out} \cdot T_{FC} - \dot{n}_{O_2,in} \cdot T_0 \right) \\ & + Cp_{N_2} \cdot \left(\dot{n}_{N_2,out} \cdot T_{FC} - \dot{n}_{N_2,in} \cdot T_0 \right) + Cp_{H_2O} \cdot \dot{n}_{H_2O,generate} \cdot \left(T_{FC} - T_0 \right) \\ & + \dot{n}_{H_2O,generate} \cdot H_v \end{aligned} \tag{2.55}$$

here, $\dot{Q}_{ch}$ and $\dot{Q}_{s,l}$ are the chemical energy produced in the electrochemical reactions and the latent heat, respectively. Moreover, $C_{p_{H_2}}$, $C_{p_{O_2}}$, $C_{p_{N_2}}$, and $C_{p_{H_2O}}$ represent the specific heat capacity of oxygen, hydrogen, water, and nitrogen, respectively; and, H_v indicates the heat of evaporation of water. The electrical efficiency of the PEM fuel cell is found by:

$$\eta_{FC} = \frac{W_{FC}}{\dot{n}_{H_2,use} \cdot HHV} \tag{2.56}$$

2.2.2 Exergy analysis

Exergy represents the maximum work that can be done at each process of the system [205]. Considering the unavoidable irreversibilities in thermodynamic processes, each process leads to some exergy destruction [206]. Therefore, for modelling of thermodynamic systems, besides

examining the exchanged energy, the exchanged exergy in various processes should be examined as well. The exergy balance of each process is written as follows [207]:

$$\dot{E}x_Q + \sum \dot{E}x_{in} = \sum \dot{E}x_{out} + \dot{E}x_W + \dot{E}x_D \tag{2.57}$$

$$Ex_i = \dot{m} \cdot \left(\left(h_i - h_0 \right) - T_0 \cdot \left(s_i - s_0 \right) \right) \tag{2.58}$$

$$\dot{E}x_W = \dot{W} \tag{2.59}$$

$$\dot{E}x_Q = \dot{Q}_j \cdot \left(1 - \frac{T_0}{T_j} \right) \tag{2.60}$$

here, h and s present the specific enthalpy and entropy, respectively, and the subscripts i and 0 show the number of flows and the reference conditions. Exergy destruction formula for different equipment are listed in Table 2.2.

Table 2.2: Exergy destruction formula for the subsystems and equipment.

Components	Exergy destruction
PTC	$Ex_{D,PTC} = \left(\dot{E}x_1 + \dot{E}x_{Sun} - \dot{E}x_2 \right) \cdot t_{Sun}$
PTC pump	$Ex_{D,Pump}^{PTC} = \left(\dot{E}x_4 - \dot{E}x_1 + \dot{W}_{Pump}^{PTC} \right) \cdot t_{Sun}$
Evaporator	$Ex_{D,Evap} = \left(\dot{E}x_9 + \dot{E}x_2 - \dot{E}x_5 - \dot{E}x_3 \right) \cdot t_{Sun}$
Economizer	$Ex_{D,Eco} = \left(\dot{E}x_8 + \dot{E}x_3 - \dot{E}x_9 - \dot{E}x_4 \right) \cdot t_{Sun}$
Steam turbine	$Ex_{D,ST} = \left(\dot{E}x_5 - \dot{E}x_6 - \dot{W}_{ST} \right) \cdot t_{Sun}$
TEG	$Ex_{D,TEG} = \left(\dot{E}x_6 + \dot{E}x_{10} - \dot{E}x_7 - \dot{E}x_{11} - \dot{W}_{TEG} \right) \cdot t_{Sun}$
SRC pump	$Ex_{D,Pump}^{SRC} = \left(\dot{E}x_7 - \dot{E}x_8 + \dot{W}_{Pump}^{SRC} \right) \cdot t_{Sun}$
PEME	$Ex_{D,PEME} = \left(\dot{W}_{PEME} - \dot{E}x_{13} - \dot{E}x_{12} \right) \cdot t_{Ch}$
Hydrogen storage tank	$Ex_{D,HST} = \dot{E}x_{15} \cdot t_{Ch} - \dot{E}x_{16} \cdot t_{Dch}$
PEMFC	$Ex_{D,PEMFC} = \left(\dot{E}x_{17} + \dot{E}x_{19} - \dot{E}x_{20} - \dot{E}x_{18} - \dot{W}_{PEMFC} \right) \cdot t_{Dch}$

2.2.3 Exergoeconomic analysis

In energy systems, part of the transmitted exergy is always lost due to irreversibilities. Hence, exergy determines the true amount of thermodynamic effects. The system costs can be determined based on exergy and are denoted as exergoeconomic costs. In exergoeconomic analysis, the cost rate at the state and the final cost rate of products are determined [208]. In this regard, the cost balance equation is defined as follows [209]:

$$\sum\left(\dot{C}_j\right)_{K,in} + \dot{Z}_K = \sum\left(\dot{C}_j\right)_{K,out} \tag{2.61}$$

$$\dot{C}_j = c_j \cdot \dot{E}x_j \tag{2.62}$$

here, c_j and $\dot{E}x_j$ are the cost per unit of exergy ($/GJ) and exergy flow of j^{th} stream (kW), respectively. $\dot{Z}_K$ is the levelized cost in K^{th} component [210]:

$$\dot{Z}_K = \dot{Z}_{K,CI} + \dot{Z}_{K,OM} \tag{2.63}$$

here, $\dot{Z}_{K,CI}$ is the levelized capital investment and $\dot{Z}_{K,OM}$ represents the operating and maintenance costs of the k^{th} component. Therefore, $\dot{Z}_K$ can be found as follows:

$$\dot{Z}_{K,CI} = \frac{CRF \cdot Z_K}{\beta} \tag{2.64}$$

$$\dot{Z}_{K,OM} = \frac{\phi_K \cdot Z_K}{\beta} \tag{2.65}$$

here, Z_K is the purchasing cost of the component, β is the operating hours of the system during a year and ϕ_K indicates the operating and maintenance factor of the system, which is considered 1.06 (annually 6% of Z_K). Moreover, CRF is the capital recovery factor and is stated by [187]:

$$CRF = \frac{i_R(1+i_R)^{n_S}}{(1+i_R)^{n_S}-1} \tag{2.66}$$

here, i_R is the interest rate and n_S is the service year of the system. The investment cost functions of the equipment are given in Table 2.3.

Table 2.3: Capital cost functions for estimation price of the proposed system components [193,211–213].

Component	Capital cost function ($)
Condenser	$Z_{Cond} = 1773 \cdot \dot{m}_{Cond}$
Evaporator	$\mathrm{Z_{Evap}} = 276 \cdot \left(\mathrm{A_{Evap}}\right)^{0.88}$, $\mathrm{A_{Evap}} = \frac{\dot{\mathrm{Q}}_{\mathrm{Evap}}}{\mathrm{U_{Evap}} \cdot \Delta \mathrm{T_{in}}}$, $\mathrm{U_{Evap}} = 4.39\left(\mathrm{kW/m^2 \cdot K}\right)$
Heat exchanger	$Z_{Hex} = 12000 \cdot \left(\frac{A_{Hex}}{100}\right)^{0.6}$
PEME	$Z_{PEME} = 1000 \cdot \dot{W}_{PEME}$
PEMFC	$Z_{PEMFC} = 2500 \cdot \dot{W}_{PEMFC}$
PTC	$Z_{PTC} = 240 \cdot A_{PTC}$
Pump	$Z_{Pump} = 3500 \cdot \left(\dot{W}_{Pump}\right)^{0.41}$
TEG	$Z_{TEG} = 1500 \cdot \dot{W}_{TEG}$
Steam Turbine and generator	$Z_{ST} = 4750 \cdot \left(\dot{W}_{ST}\right)^{0.7} + 60 \cdot \left(\dot{W}_{ST}\right)^{0.95}$

Furthermore, this balance can be applied to update the purchase cost of the equipment [214]:

$$\text{Cost at present year} = \text{Original cost} \cdot \frac{\text{Cost index for the present year}}{\text{Cost index for the year of original cost}} \tag{2.67}$$

The economic and auxiliary formulas for each equipment are given in Table 2.4. Furthermore, the final cost rate of products and levelized cost of electricity (LCOE) by the proposed system are calculated as follows:

$$c_p = \frac{\dot{C}_{w,ST} + \dot{C}_{w,TEG} + \dot{C}^{SRC}_{Pump} + \dot{C}^{PTC}_{Pump} + \dot{C}_{w,PEMFC} + \dot{C}_{w,PEME}}{\dot{W}_{ST} + \dot{W}_{TEG} + \dot{W}_{PEMFC} - \dot{W}_{PEME} - \dot{W}^{SRC}_{Pump} - \dot{W}^{PTC}_{Pump}} \tag{2.68}$$

$$LCOE = \frac{24 c_p}{t_{off-peak}\dot{W}_{Net_{off-peak}} + t_{mid-peak}\dot{W}_{Net_{mid-peak}} + t_{on-peak}\dot{W}_{Net_{on-peak}}} \tag{2.69}$$

Table 2.4: Cost balance and auxiliary formula for the components of the reference system.

Component	Cost balance	Auxiliary equation
Hydrogen storage tank	$\dot{C}_{15} + \dot{Z}_{HST} = \dot{C}_{16}$	
Evaporator	$\dot{C}_9 + \dot{C}_2 + \dot{Z}_{Evap} = \dot{C}_5 + \dot{C}_3$	$c_2 = c_3$
Economizer	$\dot{C}_8 + \dot{C}_3 + \dot{Z}_{Eco} = \dot{C}_9 + \dot{C}_4$	$c_3 = c_4$
PEME	$\dot{C}_{W,PEME} + \dot{Z}_{PEME} = \dot{C}_{13}$	$c_{w,PEME} = c_{w,ST}$
PTC pump	$\dot{C}_4 + \dot{C}_{W,PTC,P} + \dot{Z}_{PTC,P} = \dot{C}_1$	$c_{w,PTC,P} = c_{w,ST}$
SRC pump	$\dot{C}_7 + \dot{C}_{W,SRC,P} + \dot{Z}_{SRC,P} = \dot{C}_8$	$c_{w,SRC,P} = c_{w,ST}$
PEMFC	$\dot{C}_{17} + \dot{C}_{19} + \dot{Z}_{PEMFC} = \dot{C}_{W,PEMFC} + \dot{C}_{19} + \dot{C}_{18}$	$c_{19} = 0$
PTC	$\dot{C}_{Sun} + \dot{C}_1 + \dot{Z}_{PTC} = \dot{C}_2$	$c_{Sun} = 0$
Steam turbine	$\dot{C}_5 + \dot{Z}_{ST} = \dot{C}_6 + \dot{C}_{W,ST}$	$c_5 = c_6$
TEG	$\dot{C}_6 + \dot{C}_{10} + \dot{Z}_{TEG} = \dot{C}_7 + \dot{C}_{11} + \dot{C}_{W,TEG}$	$c_6 = c_7$; $c_{10} = 0$

2.2.4 Performance criteria

Finally, the exergy efficiency of the base-load and peak-load can be expressed as follows:

$$\eta_{Ex} = \frac{\dot{W}_{ST} + \dot{W}_{TEG} - \dot{W}_{Pump}^{SRC} - \dot{W}_{Pump}^{PTC}}{\dot{E}x_{sun}} \tag{2.70}$$

2.3 Results and discussions

The proposed system is simulated by using MATLAB™ and Engineering Equation Solver (EES) software based on the design conditions (Table 2.1) and the methods mentioned in Section 2.2. In this regard, first, the simulated model is validated by the data from the literature. Then, using multi-objective optimization by the grey wolf algorithm, the optimal working conditions and the most suitable thermal oil for the proposed system are determined. The results of energy, exergy and exergoeconomic analyses are reported under optimal conditions. Lastly, performing parametric analysis, the impact of the substantial factors on the system performance is determined.

2.3.1 Model validation

The proposed system is a new power generation system that has not been investigated formerly; thus, the data achieved from the present model for each subsystem are separately verified by the correlated paper in the literature. The validation results are presented in Figure 2.3.

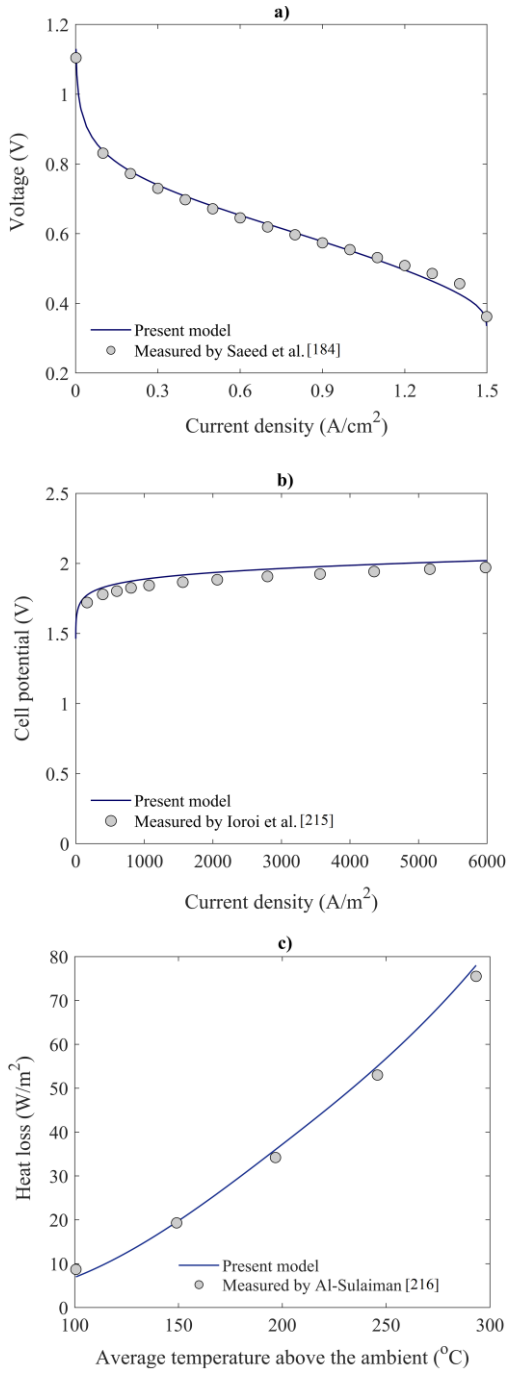

Figure 2.3: Validation of (a) PEMFC, (b) PEME, (c) PTC subsystems.

In this regard, simulation results of the PEMFC subsystem by Saeed et al. [184], the PEME subsystem by Ioroi et al. [215], and the solar PTC unit by Al-Sulaiman et al. [216] are compared. It is obvious that there is a sensible variance between the simulation and experimental data.

2.3.2 Multi-objective optimization

In the present work, a combination of artificial neural network (ANN) and grey wolf optimization (GWO) algorithms is used to evaluate and optimize the system performance. The GWO algorithm is prioritized to other alternatives due to several advantages such as (a) easy implementation owing to its simple structure, (b) low storage and computational requirements, (c) fast convergence, (d) no need for a large number of decision variables and control parameters, and (e) high stability [217]. Given that the optimization process is a time-consuming process, the results of the simulation are trained by using the ANN to reduce the simulation time from a few hours to a few minutes. In this regard, the energy, exergy, and exergoeconomic analyses of the proposed system with the developed model are repeated 700 times, and 700 random data sets are generated. Then, these data are passed to ANN to get the target functions. The objectives of the optimization are reducing the total cost rate ($\dot{Z}$) and improving the exergy efficiency (η_{ex}) of the referenced system as much as possible. After optimization, the technique for order of preference by similarity to ideal solution (TOPSIS) decision criterion is used to obtain the optimal amount and the most suitable thermal oil. To provide a comprehensive and optimal review of the reference system, the impact of five different types of thermal oils on the PTC subsystem is investigated. To better explain the goals and optimization method, a schematic diagram is given in Figure 2.4.

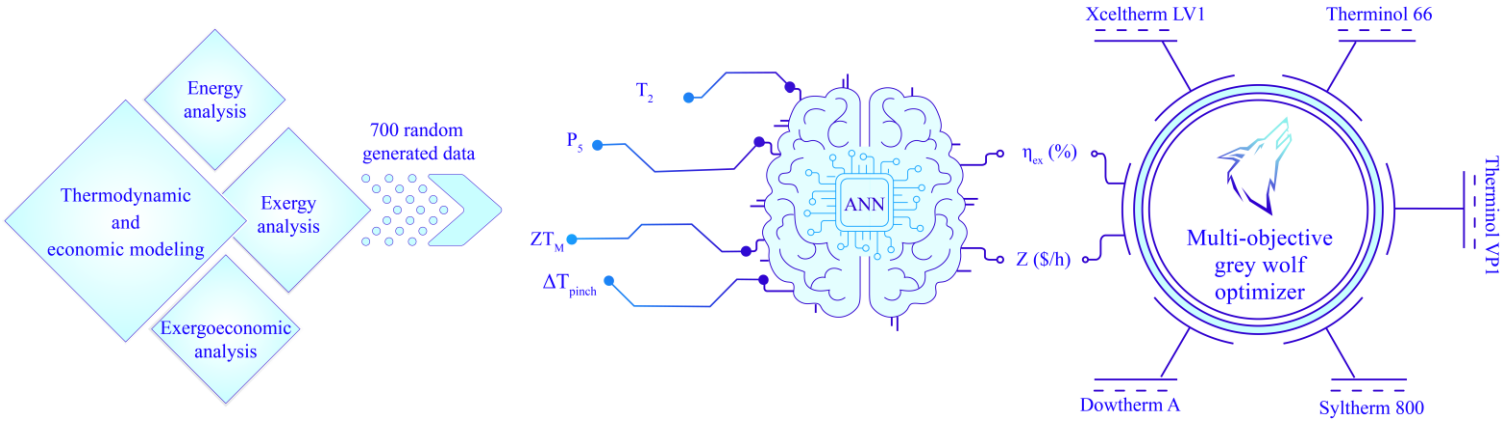

Figure 2.4: Schematic diagram of the optimization process to determine optimum thermal oil from the five options shown in connection with optimizer.

In general, thermal oils are available in different properties and costs. The two main parameters for oil selection are their operating temperature ranges in the solar cycle and heat transfer coefficients. Here, the effect of various thermal oils on the system performance is scrutinized in the present study. The properties of the proposed thermal oils are given in Table 2.5.

Table 2.5: Specifications of the proposed thermal oils [218].

Thermal oil	T_{Min} (°C)	T_{Max} (°C)	$C_P\left(J/kg\cdot K\right)$
Dowtherm A	12	400	1501
Syltherm 800	-60	400	1574
Therminol 66	-3	345	1475
Therminol VP1	12	400	1486
Xceltherm LV1	7	371	1519

Due to the use of ANN, the optimization time is remarkably reduced. As a result, optimization can be performed for different thermal oils by investing a reasonable time to select the most appropriate one based on the minimum total cost rate ($\dot{Z}$) and the maximum exergy efficiency (η_{ex}). The critical parameters of the system as optimization decision variables along with their minimum and maximum values are listed in Table 2.6.

Table 2.6: Decision variables and their range for optimization.

Parameter	Lower bound	Upper bound
T_2 (°C)	300	400, 371, 345
P_5 (kPa)	2000	3500
ΔT_{Pinch}^{Evap} (°C)	3	10
ZT_M	0.3	1.5

2.3.2.1 Artificial neural network model validation

To validate the ANN model, a coefficient of determination (R^2) for one of the studied oils (e.g., Dowtherm A oil) is used as shown in Figure 2.5. It is noted that the closer the value of R^2 is to one, the more accurate the ANN predictions are. As shown in Figure 2.5, the R^2 of the trained neural network model for exergy efficiency (η_{ex}) and the total cost rate ($\dot{Z}$) are 0.99992 and 0.99999, respectively, which confirms the high precision and consistency of the considered ANN model.

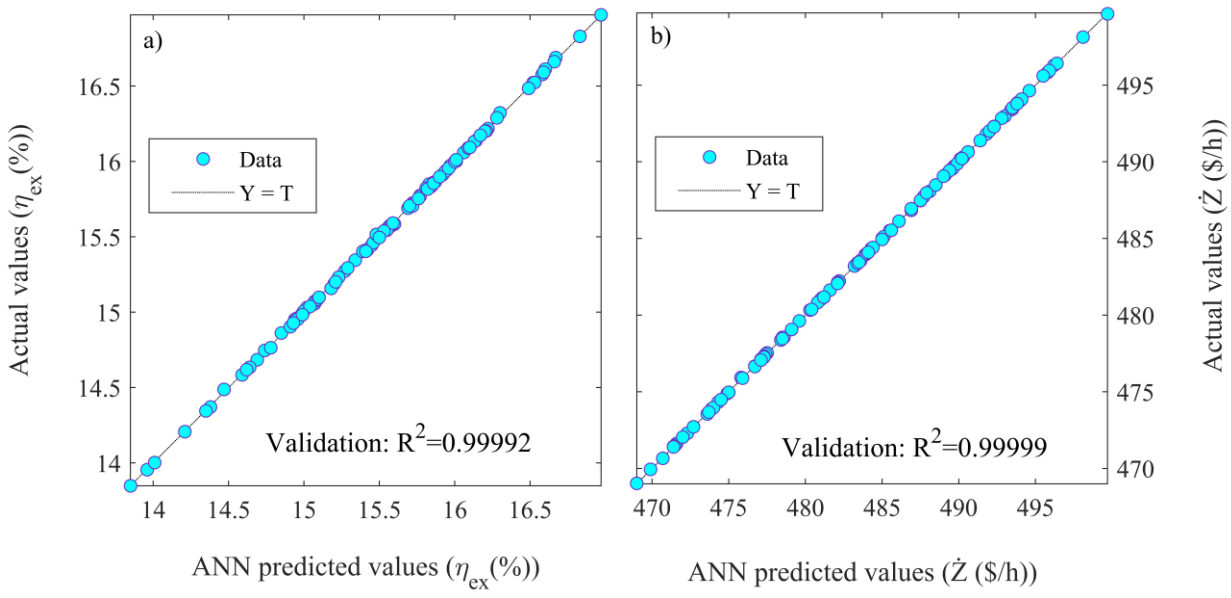

Figure 2.5: Artificial neural network validation for Dowtherm A oil including a) Exergy efficiency (η_{ex}), b) Cost rate ($\dot{Z}$).

2.3.2.2 Optimization results

Multi-criteria optimization results for five types of thermal oils are shown in Figure 2.6. It is noted that a solar collector area of 100,000 m^2 is considered for optimization.

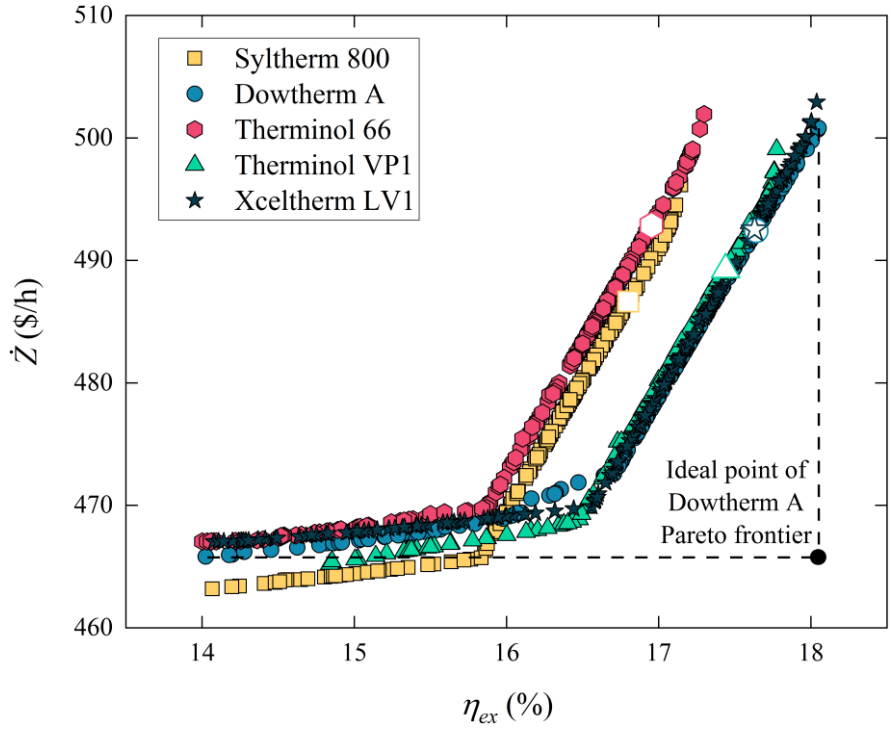

Figure 2.6: Distribution of Pareto frontier diagrams for five types of thermal oils based on the grey wolf optimization algorithm.

According to Figure 2.6, all the points in this figure can be considered as an optimal point; thus, the TOPSIS decision method is used to obtain the ideal point. The selected points are marked with white symbols by the TOPSIS criterion. The specifications of these points are given in Table 2.7.

Table 2.7: Specifications of TOPSIS points of different oils.

Thermal Oil	Design parameters				Objective functions	
	T_2 (°C)	P_5 (kPa)	ΔT_{Pinch}^{Evap} (°C)	ZT_M	η_{ex}	$\dot{Z}$ ($/h)
Dowtherm A	400	3500	8.81	1.06	17.64	492.42
Syltherm 800	400	3500	10.0	1.21	16.80	486.63
Therminol 66	345	3500	8.61	1.28	16.95	492.86
Therminol VP1	400	3500	10.0	1.49	17.44	489.25
Xceltherm LV1	371	3500	7.36	1.15	17.63	492.52

Since the behaviour of the five oils is similar in Figure 2.6, a separate figure (Figure 2.7) is demonstrated to provide a better understanding of their operation values and ranks. Based on the results, Dowtherm A oil has the best TOPSIS point and can be used as the most suitable thermal oil in the system.

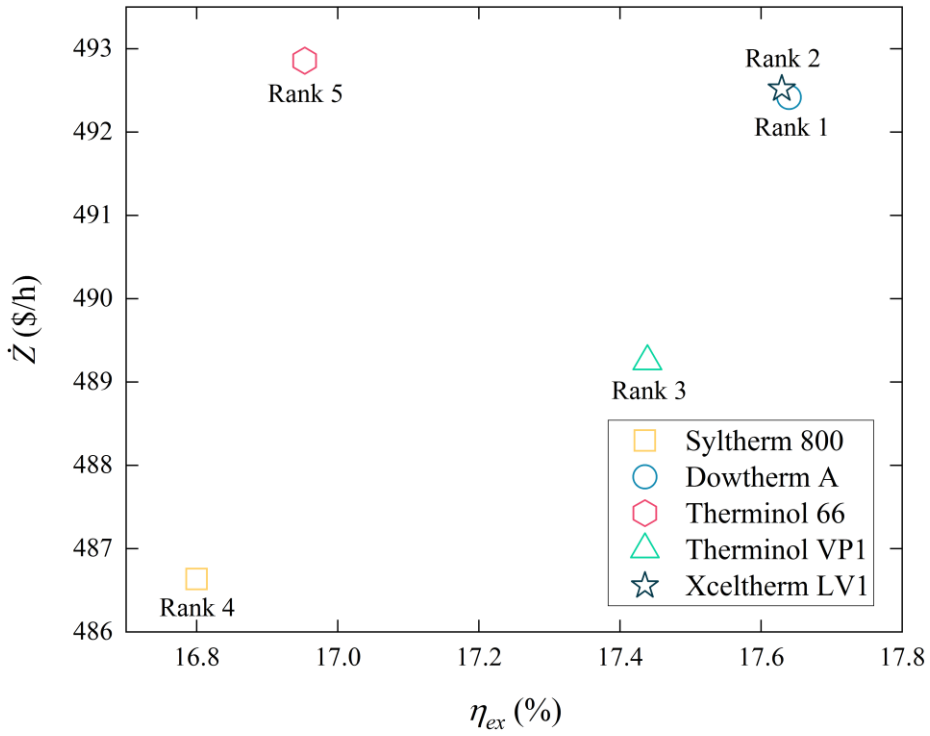

Figure 2.7: Ranking of TOPSIS points of each thermal oil.

For more clarification, the optimization population dispersion of Dowtherm A is shown in Figure 2.8. According to Figure 2.8 (a), most of the points are at the highest value for the collector outlet temperature, but due to the oil temperature limitation, it is not possible to increase more than the allowable value (the maximum allowable temperature of each oil is given in Table 2.5). In addition, the optimal point distribution for the inlet pressure of the steam turbine in Figure 2.8 (b) and the pinch point temperature difference at the evaporator in Figure 2.8 (d) are more focused on the end of the optimization interval. In this regard, the optimum pressure at the steam turbine inlet pressure is 3500 kPa and the optimal pinch point temperature difference in the evaporator is 10 ℃. But,

Figure 2.8 (c) shows that the optimal points of the figure of merit coefficient (ZT_M) are consistently distributed in the range of 0.3 to 1.5.

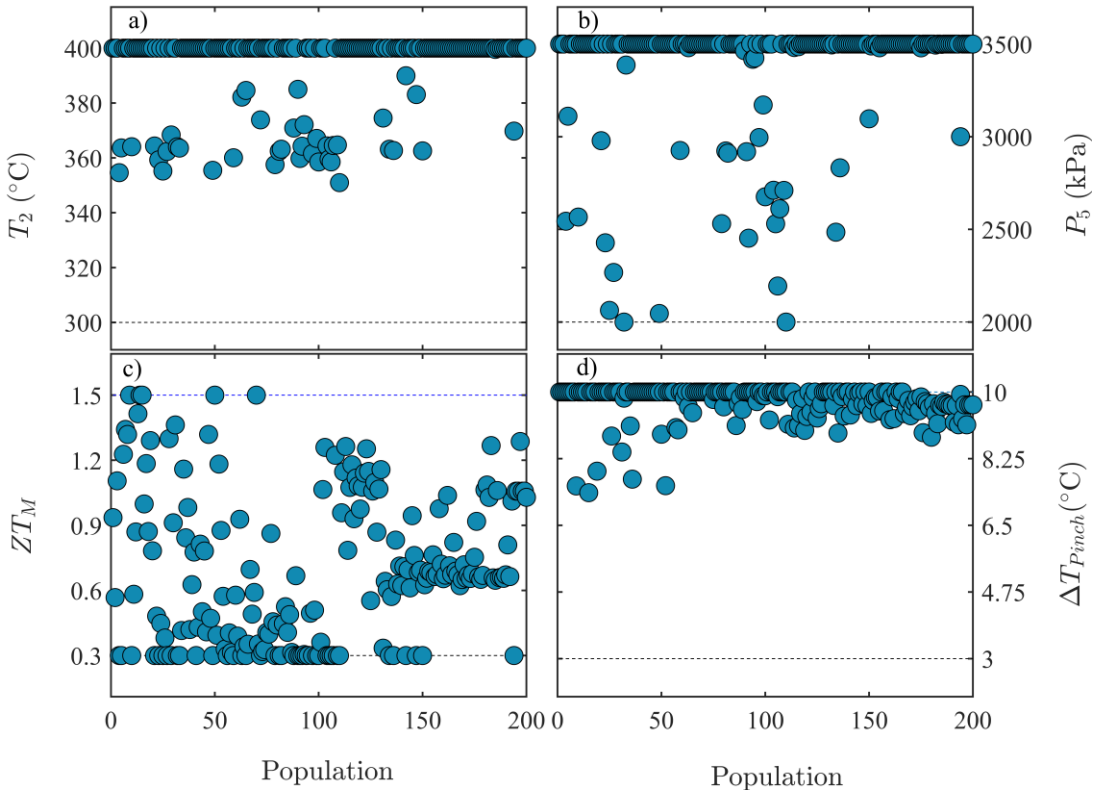

Figure 2.8: Population dispersion for decision variables: a) T_2, b) P_5, c) ZT_M, and d) ΔT_{Pinch}^{Evap}.

The thermodynamic and exergoeconomic characteristics of the reference system streams based on the optimal conditions are shown in Table 2.8. In addition, the results of thermodynamic and exergoeconomic analyses, using the governing equations presented in the section 2.2 and the optimal conditions specified, are tabulated in Table 2.9.

Table 2.8: Thermodynamic and exergoeconomic characteristics of solar cycle currents for the optimal point of Dowtherm A.

State	$\dot{m}(kg/s)$	$P(kPa)$	$T(°C)$	$h(kJ/kg)$	$s(kJ/kg\cdot K)$	$\dot{E}x(kJ/s)$	$c(\$/GJ)$	$\dot{C}(\$/h)$
0		101.3	25					
1	139.8	250	162.8	260.9	0.726	6110	3.452	75.92
2	139.8	250	400	811.4	1.722	41586	3.188	477.2
3	139.8	237.5	251.4	447.5	1.114	16022	3.188	183.9
4	139.8	225.6	162.3	260.9	0.7237	6200	3.188	71.15
5	29.02	3500	242.6	2803	6.124	28503	4.236	434.7

6	29.02	90	96.69	2321	6.45	11710	4.236	178.6
7	29.02	90	35	146.7	0.5051	20.17	4.236	0.3076
8	29.02	3500	35.18	150.5	0.5063	120	9.814	4.241
9	29.02	3500	242.6	1050	2.725	7026	5.032	127.3
10	1480	101.3	25	104.9	0.3672	0	0	0
11	1480	101.3	35	146.7	0.5051	1046	48.88	184

Table 2.9: Results of thermodynamic and exergoeconomic analysis based on the optimal conditions with Dowtherm A oil.

Parameter	Value	Unit
Circulation pump power	0.140	MW
Cost rate of products	492.42	$/h
Levelized cost of electricity	62.6	$/MWh
Economizer heat transfer rate	26.1	W
Evaporator heat transfer rate	50.9	MW
Mid peak power	14.9	MW
Off peak power	9.00	MW
On peak power	20.1	MW
Overall exergy efficiency	17.64	%
Ratio of excess hydrogen to the produced hydrogen	2.30	-
Steam pump power	0.11	MW
Steam turbine power	14.0	MW
TEG power	1.20	MW

To better understand the results of exergy and exergoeconomic analysis, Sankey diagrams for various components and streams of the system are given in Figure 2.9 and Figure 2.10. Figure 2.9 shows the exergy flow in the system, as well as the amount of exergy destruction that happens at each process. The thickness of the flows drawn in the Sankey diagram is proportional to the exergy values. Initially, 84.51 MW of solar radiation is received by the PTC collectors. Due to the significant exergy destruction in solar collectors, 41.59 MW of the input exergy is transferred to Dowtherm A thermal oil, and the rest of the input exergy (49.12 MW) is lost. The temperature difference between the sun and oil is the primary reason for exergy destruction in solar collectors.

In the following, the thermal oil transfers its heat to the steam by passing through the evaporator and economizer. Water vapor enters the turbine with an exergy rate of 28.50 MW and generates power through the expansion process. Exergy destruction in turbines, evaporators, and economizers are 2.57, 4.10, and 3 MW, respectively. Due to the fact that the output stream from the steam turbine has significant exergy, the TEG produces 1.2 MW of useful exergy by recovering the residual heat. In total, out of the 84.51 MW of exergy input by the sun, 15.17 MW is converted to power, and 68.29 MW is destructed. In addition, 1.05 MW of hot water is produced by the condenser. The most share of exergy destruction happened in the PTC solar collector, TEG thermoelectric, and evaporator, respectively.

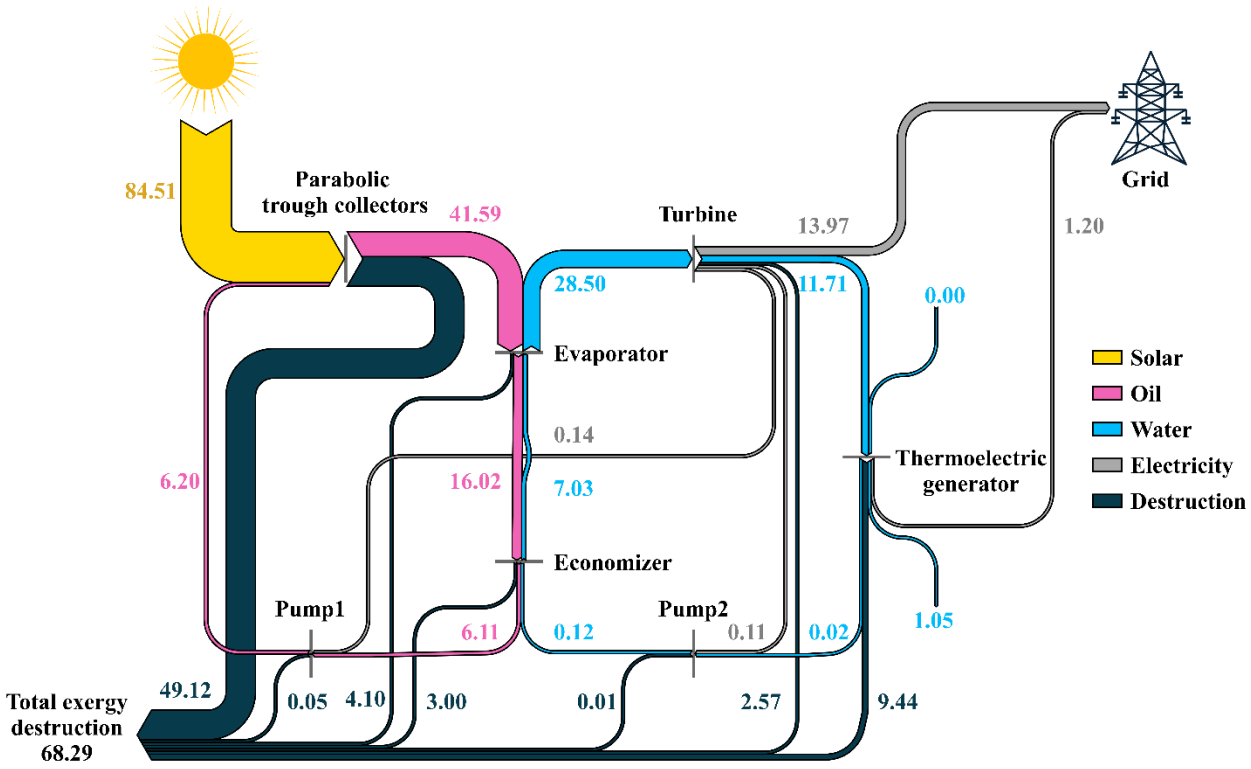

Figure 2.9: Sankey exergy diagram for the PTC and SRC-TEG subsystems under optimal conditions, the values are in MW.

Figure 2.10 shows the cost rates associated with the PTC and SRC-TEG subsystem streams. Due to the high cost of solar technology, 82% of total system costs are related to solar collectors.

Considering free access to solar radiation, its input cost rate is zero. Moreover, the output streams of the collector, evaporator, and turbine have the highest cost rates.

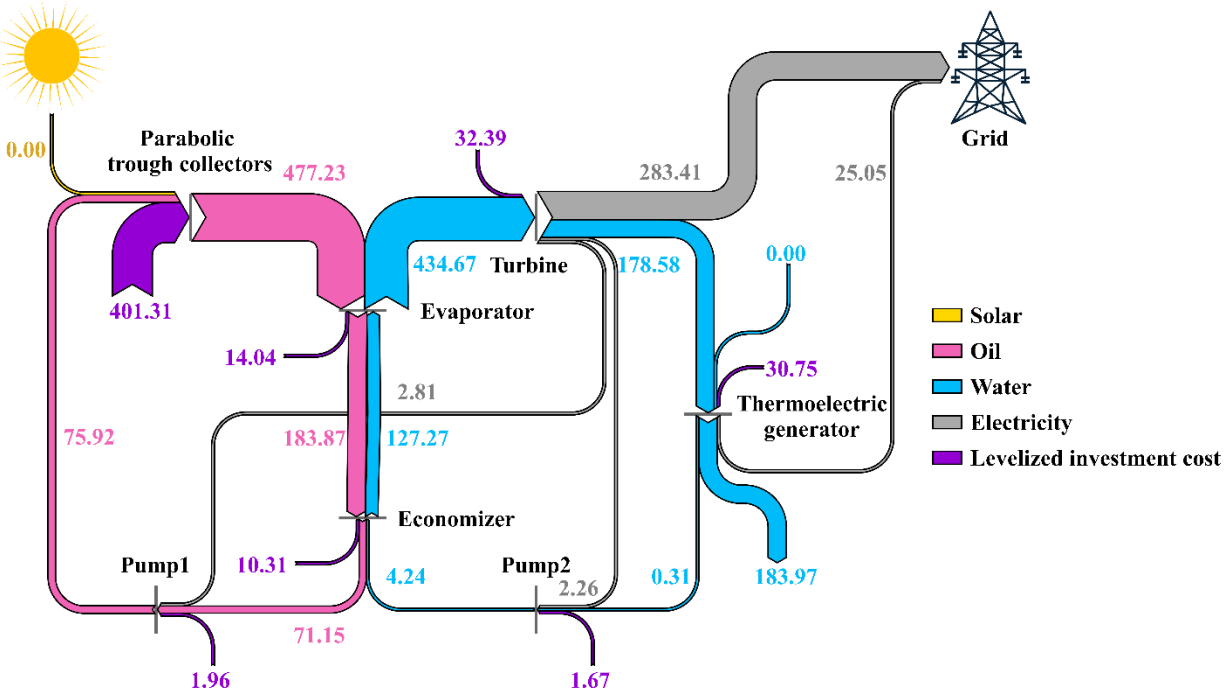

Figure 2.10: Exergoeconomic Sankey diagram for PTC and SRC-TEG subsystems under optimal conditions.

One of the influential parameters in energy systems is cost rate. The total cost rate distribution of different units of the reference system is presented in Figure 2.11. As mentioned earlier, the performance of the proposed system is divided into two parts, the baseload, and the peak load. The baseload unit is responsible for 61% of the total cost rate; 82% of which is related to PTC. The peak load generation unit includes PEME and PEMFC, which together cover 39% of the total system cost, most of which are associate with the fuel cell. The parameter affecting the cost rate of fuel cell and electrolyzer is the input cost rate of the electrolyzer. The more the input electricity cost rate, the higher the cost rate of electrolyzer and fuel cell, which will be discussed in detail in the next section.

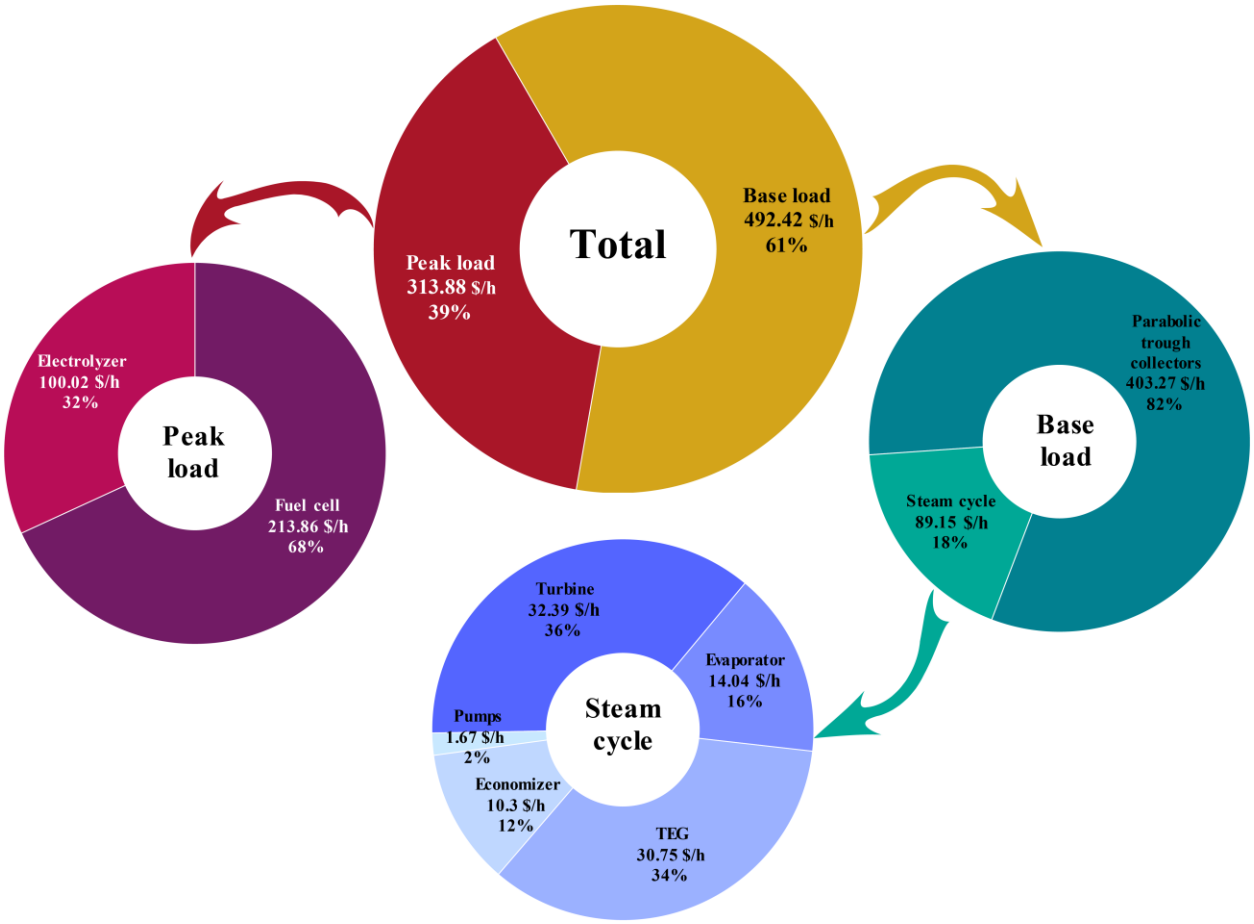

Figure 2.11: The cost rate of different subsystems and their percentage.

2.3.3 Sensitivity analysis

The performance of the hybrid systems can always change under the influence of various factors. Therefore, the evaluation of critical parameters is of great importance which is scrutinized in this section.

2.3.3.1 Direct normal irradiance

The amount of direct normal irradiance (DNI) is one of the most important parameters affecting the power generation of the solar field during the base load, which is a function of the time and position of the system. Hence, the effect of DNI on the performance of the reference system is

evaluated in Figure 2.12. It is obvious that more heat is received by thermal oil at higher DNIs. Therefore, the energy density of thermal oil is increased, resulting in an improvement in the amount of heat received by the evaporator and economizer. Consequently, increasing the heat input enhances the production capacity of the SRC-TEG subsystem. The exergy efficiency and the amount of power transmitted to the electrolyzer during the off-peak time will be improved at higher production capacities of the SRC-TEG unit. It means that the ratio of excess to the produced hydrogen (ETP) is decreased at higher DNIs. All the mentioned points and the free access to solar energy around the world cause a cost reduction of products at higher DNIs.

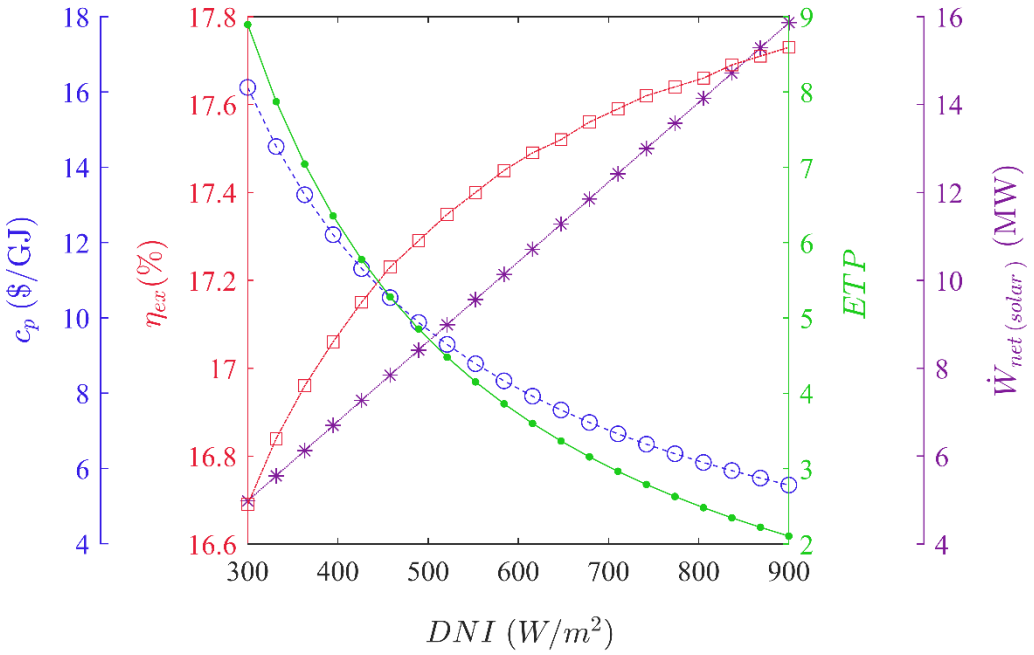

Figure 2.12: Impact of direct normal irradiance (DNI) on the ratio of excess hydrogen to the produced hydrogen (ETP), system power output, exergy efficiency, and product cost rates.

2.3.3.2 Charging and discharging time

In general, power distribution networks are divided into three periods based on consumption: off-, mid- and on-peak. During off-peak times, the extra power generated by the SRC-TEG subsystem is given to the PEME, where hydrogen is produced and stored in special tanks. Then, at mid-peak

times, all the electricity generated by the SRC-TEG subsystem is transmitted to the grid. Finally, at on-peak times, due to the need for excess electricity, stored hydrogen is transferred to the PEMFC subsystem for further power generation to help grid stability, peak shaving, and power scarcity. According to Figure 2.13, the most effective parameters at on-peak time are the discharge period and the amount of power required. As the peak time increases, the amount of the required hydrogen is linearly increased, resulting in an enhancement at ETP. To shed light on this issue in the proposed system, four different scenarios are considered for the share of power generation by the PEMFC, which are 20, 30, 40, and 50% of the power generated by the SRC-TEG subsystem. According to Figure 2.13, the amount of excess hydrogen required is increased with increasing discharge period ($T_{Discharge}$) and share of the power provided by the PEMFC. The differences between ETP values at various discharge periods are written in separate lines above columns to indicate their linear alteration.

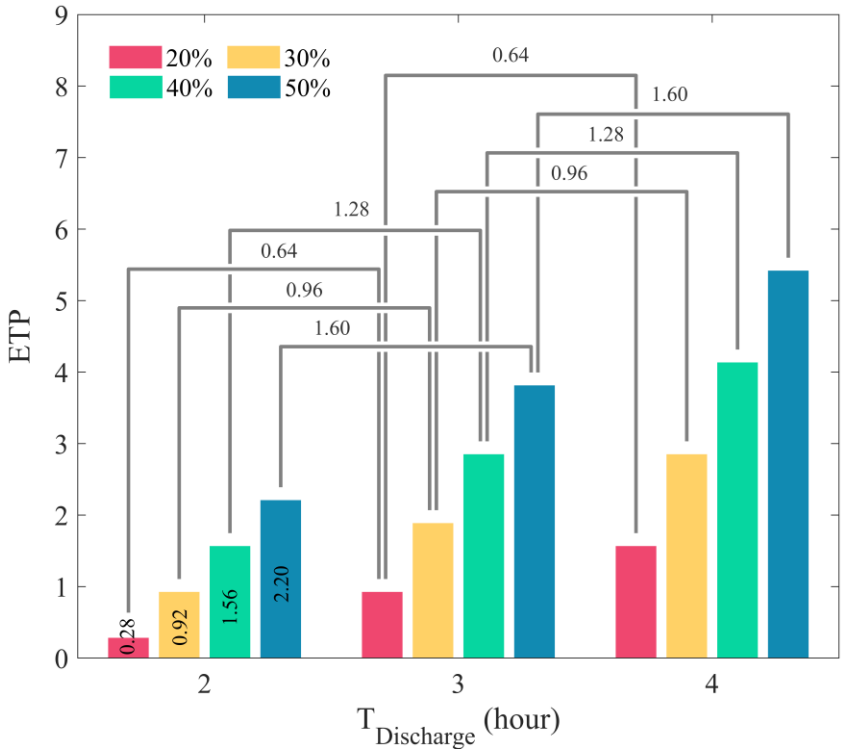

Figure 2.13: The effect of discharge time and PEMFC power generation on the required excess hydrogen ratio.

Charging time and the amount of power input to PEME are among the other important parameters affecting the PEME performance. As shown in Figure 2.14, when the charging time increases, the amount of hydrogen produced by the PEME is improved, while the amount of required excess hydrogen and ETP are decreased. However, against the discharging period, there is no linear relationship between the alterations of ETP at different charging periods.

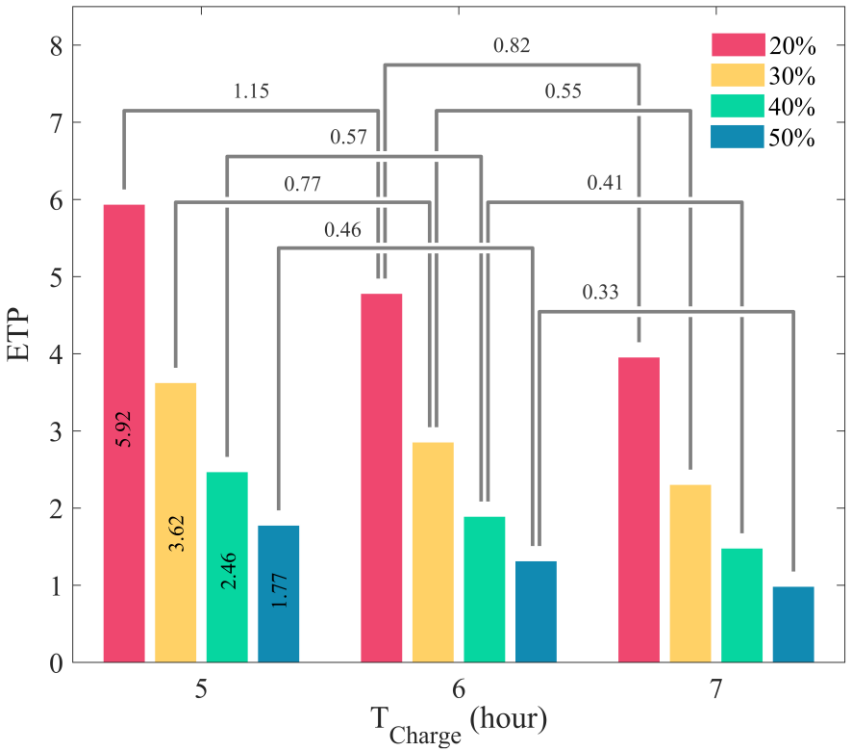

Figure 2.14: Effect of charge time and amount of power input to PEME on the ratio of excess hydrogen required.

2.3.3.3 Fuel cell temperature

Figure 2.15 and Figure 2.16 show the effect of temperature and current density on PEMFC performance. As shown in Figure 2.15, enhancing the temperature of the fuel cell improves its performance, because as the temperature increases, the exchange current density rises, and the losses in the PEMFC is decreased. Furthermore, as the fuel cell temperature rises, the polarization curve in the current density region decreases, indicating an improvement in the PEMFC

performance at higher temperatures. On the other hand, at low flow densities, if the fuel cell temperature is more than the humidification temperature (70 ℃) and kept constant at that temperature, the membrane material in the catalyst layer would not be entirely hydrated. Therefore, this can reduce the active level of the catalyst. But if the current density increases, the membrane material in the catalyst layer will become more hydrated; therefore, the active surface of the catalyst layers increases. This is because the amount of water produced by the PEMFC at high current densities increases and improves the performance of the fuel cell.

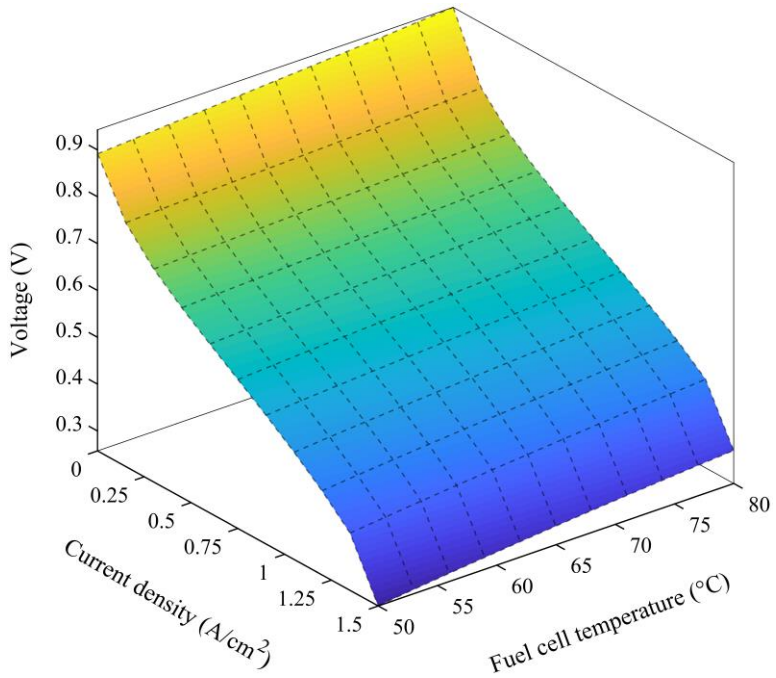

Figure 2.15: The effect of fuel cell temperature on current density and voltage under the PEMFC system.

As shown in Figure 2.15, the current density of PEMFC increases with increasing fuel cell temperature. Therefore, the amounts of penetration and mass transfer are increased at higher temperatures. Hence, because of the rise in conductivity of the PEMFC membrane at higher temperature and current density, the polarization curves will be towards higher voltages. The effect of temperature and current density on the power generation of the PEMFC is shown in Figure 2.16. As shown in Figure 2.15, higher current densities will reduce voltage levels and increase voltage

losses in PEMFCs. But, according to Figure 2.16, the power generated in the PEMFC is improved by increasing the current density. However, at current densities above 1.25 A/cm^2, the effect of voltage drop on PEMFC performance is dominated and output power decreases.

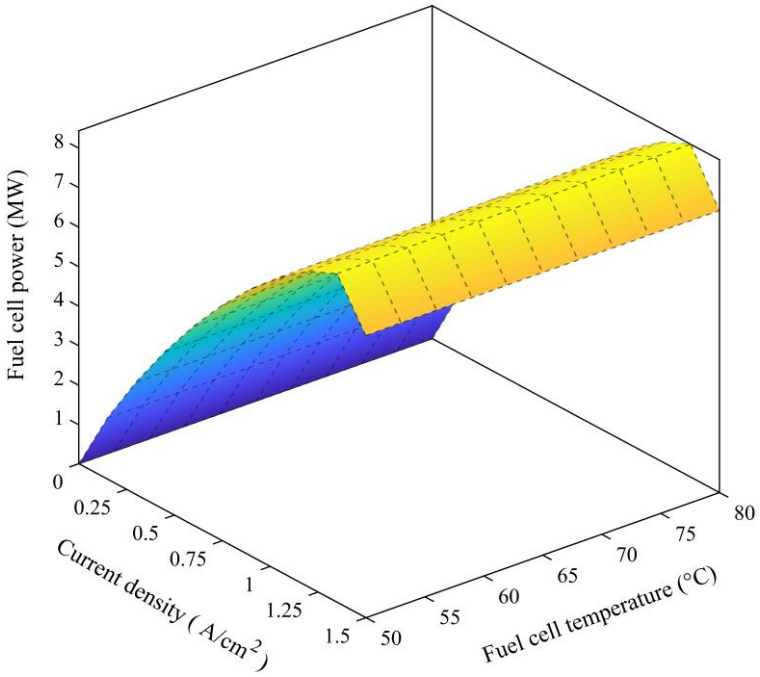

Figure 2.16: Influence of fuel cell temperature on flow density and output power under PEMFC system.

2.4 Summary of chapter

In this chapter, an innovative combination of PEME, PEMFC, and PTC solar power units was presented. The main purpose of this work was to supply extra power generation of the solar field during off-peak periods for peak shaving, without any greenhouse gas emissions. Another objective was to introduce a new concept for green hydrogen production. The developed model was first validated with the experimental data in literature and then the proposed system was thoroughly studied in terms of thermodynamics and exergoeconomic. Moreover, the system performance was optimized with the help of an artificial neural network and multi-objective optimization with a new grey wolf algorithm. The major findings of this study are as follows:

(1) The Dowtherm^{TM} A was found as the ideal choice for working fluid of the solar unit among five different alternatives with various properties by considering a trade-off between the minimum cost rate and the maximum exergy efficiency.

(2) The proposed system can produce 9, 14.9, and 20.1 MW of power during a cycle, at off-, mid-, and on-peak times to the distribution grid, respectively. This is accomplished by the ratio of the excess hydrogen to the produced hydrogen of 2.3.

(3) The exergy efficiency of the proposed system is 17.64%. A total exergy destruction of 68.29 MW happens in the whole PTC-SRC-TEG subsystem, most of which are associated with the PTC unit.

(4) The results of the exergoeconomic analysis show that the PTC subsystem accounts for nearly 82% of the total cost of the baseload part. In addition, the peak load components including the electrolyzer and fuel cell are responsible for around 39% of the total cost rate. The optimal cost rate of the system products and levelized cost of electricity are respectively 492.42 $/hr, and 62.6 $/MWh.

(5) The sensitivity analysis based on fuel cell temperature, DNI, charge, and discharge periods showed that the system performance highly depends on DNI. The better the system location (higher DNI), the higher the system performance and economic feasibility. The parametric analysis also indicated that lower additional hydrogen will be needed in cases of higher charging temperature or lower discharging temperature.

2.5 Uncertainty consideration

In this analysis, key economic parameters, including capital investment, operating and maintenance costs, and interest rates, were considered as per common practice in the literature. However, more detailed cost elements, such as those related to engineering, installation, insurance, and other ancillary expenses, have been excluded from the scope of this study. These exclusions introduce a degree of uncertainty to the presented calculations. Future analyses should aim to address these uncertainties by incorporating a comprehensive set of cost factors, supported by up-to-date and reliable cost functions as they become available. Such refinements would enhance the robustness and reliability of the economic analysis, aligning it more closely with real-world conditions.

Chapter 3: Design and Techno-Economic Analysis of a Novel Solar-Based Solid Oxide Electrolyzer and Fuel Cells System[1]

Green hydrogen production is facing challenges in balancing economic feasibility with sustainability. Employing efficient hydrogen production designs and benefiting from the potential of hydrogen storage provide two promising strategies to mitigate the economic constraints associated with green hydrogen production. This chapter proposes a novel hybrid design for green hydrogen production/utilization based on efficient high-temperature thermal units, including heliostat solar field, solid oxide electrolyzer cell (SOEC), and solid oxide fuel cell (SOFC). The proposed system is comprehensively investigated from thermodynamic and economic perspectives, along with conducting a case study based on hourly electricity prices and actual solar data. The system demonstrates a hydrogen production rate of 7.76 ton/day using the SOEC and a power generation of 54.3 MWh in the SOFC for peak demand shaving, yielding an overall round trip efficiency of 74.2%. The case study results indicate that the economic feasibility is significantly compromised if all the produced hydrogen is sold at prices below 2.75 $/kg; while, implementation of hydrogen storage for peak shaving can yield a promising payback period of less than 2 years. The hydrogen and hourly electricity prices, along with the duration of peak times, are the other critical factors that affect economic viability.

[1] This chapter is based on [3].

3.1 System description

The schematic diagram of the proposed novel design for green hydrogen production, storage, and utilization is shown in Figure 3.1.

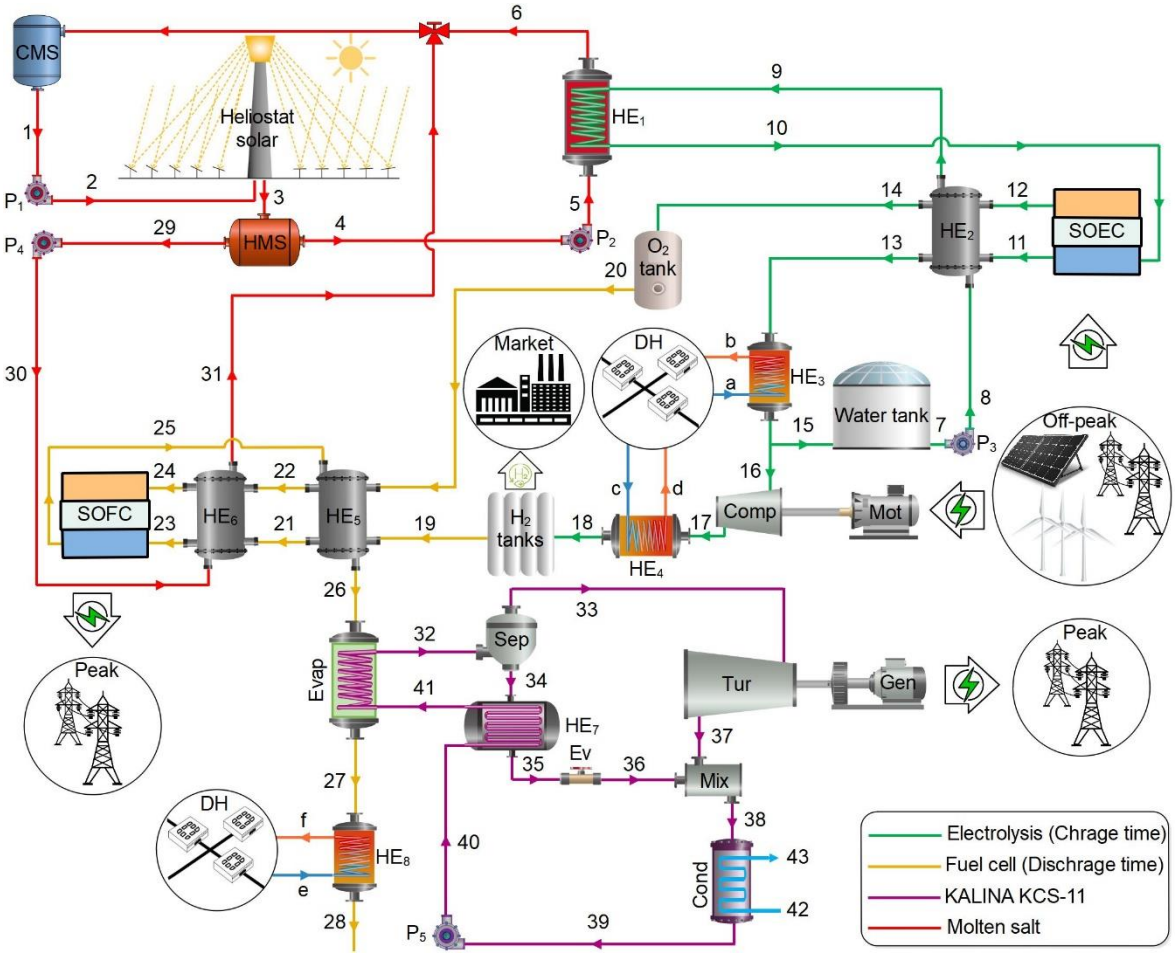

Figure 3.1: Schematic diagram of the proposed system based on heliostat solar, SOEC, SOFC, and Kalina cycle for green hydrogen storage.

The proposed system comprises four primary units, including heliostat solar field, SOEC, SOFC, and Kalina cycle, each of which serves a distinct function that will be elaborated in detail in the following paragraphs:

The cycle operation initiates with the absorption and storage of solar energy within the heliostat unit during periods of sunlight. The cold molten salt is pumped to the central receiver of the heliostat tower, where the solar energy is achieved through the precise reflection of the sunlight by the controlled mirrors within the field (point 2). The high-temperature thermal energy is transferred to the molten salt as it passes over the receiver, following which the produced hot molten salt is stored in an isolated tank for future utilization (point 3). The implementation of a molten salt storage tank as a sensible TES system mitigates the fluctuations inherent in solar energy dynamics, providing a more stable and consistent thermal output for the SOEC and SOFC units.

During the off-peak period, low-cost surplus power generated by renewable energy sources, in conjunction with a fraction of the supplied molten salt, are employed to run the SOEC and compressor. The water, with the ambient temperature, undergoes vaporization and superheating within two heat exchangers, utilizing the waste heat of the SOEC (points 8 to 9) and a fraction of the stored solar heat (points 9 to 10). The high-temperature vapor subsequently enters the SOEC (point 10), wherein electrochemical reactions take place, resulting in hydrogen (point 11) and oxygen (point 12) production. After heat recovery in heat exchanger 2, the produced oxygen is stored in the oxygen tank with the ambient pressure (point 14), while the green hydrogen is pressurized to 300 bar through passing a three-stage compressor (points 16 to 17). The required hydrogen for power generation during peak demand periods is stored in the hydrogen tank, while the surplus amount is sold in the hydrogen market. The lower the temperature of hydrogen in the compressor inlet (point 16), the lesser the compressor power consumption. In addition, hydrogen compression is accompanied by heat generation in the compressor outlet. Therefore, two heat exchangers (HE_3 and HE_4) have been designed to exploit this extra heat for district heating purposes.

During peak demand periods, the supplied oxygen and hydrogen are utilized to run the SOFC after undergoing heating in two heat exchangers. Initially, hydrogen and oxygen are preheated by the exhaust gases of the SOFC through passing the heat exchanger 5 (HE_5). Subsequently, the desired temperature in the SOFC inlet is achieved by using the supplied high-temperature molten salt in the heat exchanger 6 (HE_6). After power generation in the SOFC for peak demand shaving, the outlet high-temperature gasses are recovered to minimize heat loss to the environment as much as possible. Although a significant amount of the waste heat can be recovered in HE_5, there is still high energy density in point 26, which is recovered through two additional steps. Given the correlation between waste heat generation and peak demand periods, a Kalina cycle has been designed to generate more power for peak demand shaving. The Kalina cycle is selected because of its environmentally-friendly working fluid as a mixture of ammonia and water for extra power generation during peak times. Finally, the remaining low-quality waste heat is recovered as much as possible in the heat exchanger 8 (HE8) for district heating applications.

3.2 System modelling

In this section, the governing equations for thermodynamic analysis, including energy and exergy analyses, along with the economic analysis, are presented in detail. The design conditions and input values of different units are presented in Table 3.1:

Table 3.1: Design conditions of different units for the modeling of the proposed system.

Subsystem	Parameter	Value	Unit
Heliostat solar [191,219,220]	Concentration ratio	1000	-
	Direct normal irradiance	700	W/m^2
	Emissivity coefficient	0.8	-
	Inlet diameter of the receiver tube	3.75	cm
	Number of the heliostat	150	-
	Optical efficiency	75	%
	Outlet diameter of the receiver tube	4	cm
	Reflectivity coefficient of the receiver surface	0.04	-
	Stephan-Boltzmann constant	5.67×10^{-8}	$W/m^2.K^4$

	Solar time duration	8	hrs
	Speed of the wind	5	m/s
	Surface area of the mirrors	121	m^2
	Temperature of the cold molten salt	600	℃
	Temperature of the hot molten salt	1100	℃
	Temperature of the sun	5504.85	℃
	Thermal conductivity of the receiver tube	24.5	W/m.K
	Thermal conductivity of the tube-insulation	0.03	W/m.K
	Thickness of the tube-insulation	10	cm
	View factor	0.8	-
Solid oxide cells [206,221–224]	Air utilization factor	0.4	-
	Activation energy of cathode	142000	J/mol
	Activation energy of anode	140000	J/mol
	Anode thickness	500	µm
	Average length of grain contact	0.6	µm
	Average pore diameter of electrodes	3	µm
	Average grain size of electrodes	1.5	µm
	Cathode thickness	20	µm
	Current density	8000	A/m^2
	Cell active area	0.04	m^2
	Charge-transfer coefficient	0.5	-
	Compressibility factor of hydrogen	1.2	-
	Electrode porosity	48	%
	Electrolyte thickness	10	µm
	Tortuosity	5.4	-
	Faraday constant	96486	sA/mol
	Fuel utilization factor	0.8	-
	Interconnect thickness	3	mm
	Isentropic efficiency of the hydrogen compressor	88	%
	Low heating value of hydrogen	119.9	MJ/kg
	Number of cells	34000	-
	Operating temperature of SOEC	850	℃
	Operating temperature of SOFC	900	℃
	Pressure of the hydrogen storage tank	300	bar
	Pre-exponential factor for cathode	2.35×10^9	A/m^2
	Pre-exponential factor for anode	6.5×10^9	A/m^2
	Steam utilization factor	0.6	-
	Life time of solid oxide cells	40000	hrs
	Annual operating and maintenance costs	22	%
	Universal gas constant	8.314	J/mol.K
Kalina cycle [192,225]	Condenser efficiency	80	%
	Evaporator efficiency	80	%
	Evaporator concentration	0.8	-
	High pressure of Kalina cycle	40	bar
	Isentropic efficiency of the Kalina turbine	85	%
General [207,226–229]	Annual operating and maintenance costs	6	%
	Ambient pressure	1.01	bar
	Ambient temperature	20	℃
	Charging time period	19	hrs
	Discharging time period	5	hrs
	District heating cold temperature	20	℃
	District heating warm temperature	60	℃

Heat exchangers' efficiency	80	%
Interest rate	5	%
Isentropic efficiency of the pumps	80	%
Standard chemical exergy of H_2	236.09	kJ/mol
Standard chemical exergy of H_2O (g)	9.49	kJ/mol
Standard chemical exergy of H_2O (l)	0.9	kJ/mol
Standard chemical exergy of O_2	3.97	kJ/mol
Standard chemical exergy of NH_3	337.9	kJ/mol
Service time of the system	20	yrs

The flowchart depicting the system modelling process is presented in Figure 3.2. Initially, solar DNI data is acquired and serves as input to the solar unit. Next, the solar heliostat unit is designed and modelled based on the available DNI and desired amounts of products. Ultimately, the hot molten salt production rate and corresponding storage amount are determined. The available hot molten salt is exploited to drive either the SOEC or SOFC unit, depending on whether it is an off-peak or peak time. The rates of hydrogen and oxygen production are calculated based on the SOEC unit design, the utilized molten salt, and the duration of the off-peak period. Then, based on the remaining molten salt in the tank and the duration of peak times, power generation and hydrogen consumption rates in the SOFC can be computed. The rates at which district heating can be generated during both off-peak and peak times are calculated by considering waste heat temperatures and flow rates. Likewise, additional power is generated through the Kalina cycle by utilizing downstream waste heat parameters. Finally, a comprehensive investigation of the system performance is conducted by taking into account energy, exergy, and economic (3E) analyses. The rates of heat transfer, power generation, and consumption in different equipment are the most important findings of energy analysis. The sources of exergy destructions, inefficiencies, and irreversibilities are identified by the exergy analysis. Additionally, the economic analysis is performed to calculate the capital cost of units and components, as well as determining the system profitability and payback period.

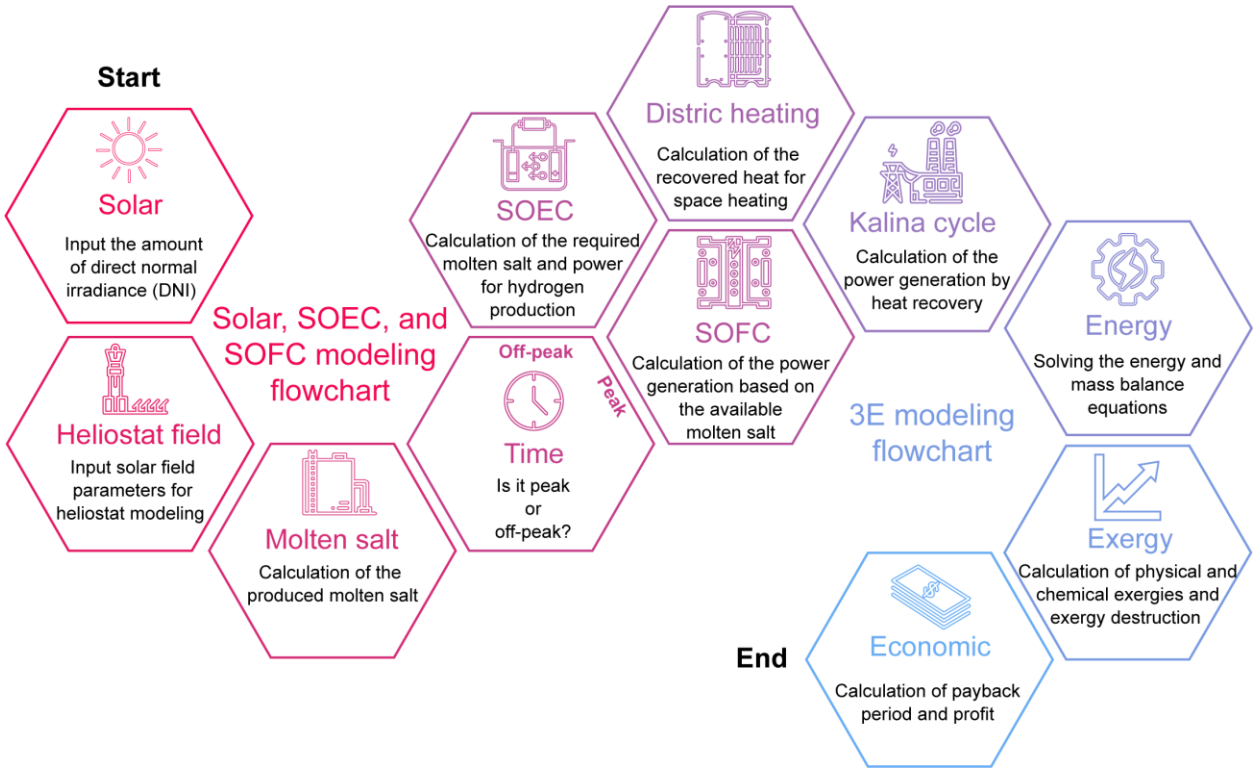

Figure 3.2: Flowchart of the system modeling process and the applied methodologies.

3.2.1 Energy analysis

The energy analysis is based on the first law of thermodynamics, which states that energy can neither be generated nor destroyed, but can only be transformed from one form to another form, or transferred from one system to another. The mass, concentration, and energy conversion equations for different components can be written as follows [230]:

$$\sum \dot{m}_{in} = \sum \dot{m}_{out} \tag{3.1}$$

$$\sum \dot{m}_{in} X_{in} = \sum \dot{m}_{out} X_{out} \tag{3.2}$$

$$\sum \dot{m}_{in} h_{in} + \dot{Q} = \sum \dot{m}_{out} h_{out} + \dot{W} \tag{3.3}$$

In the following subsections, the governing energy equations for different units and components are presented in detail. The optimum sizing of each system component in Figure 3.1 is calculated based on the design conditions specified in Table 3.1 and the governing equations listed below.

3.2.1.1 Heliostat solar unit

The heliostat unit comprises a heliostat field, heliostat tower, cavity receiver, and high-temperature thermal storage. The amount of energy emitted from the sun to the heliostat field can be calculated as follows [231]:

$$\dot{Q}_{Sun} = I_{Sun} \cdot A_{Hel} \cdot N_{Hel} \tag{3.4}$$

where N_{Hel}, A_{Hel}, I_{Sun} indicate the number of mirrors in the heliostat field, the area of each mirror, and the level of DNI. The rate at which solar energy is reflected the cavity receiver is a function of the heliostat optical efficiency, calculated as follows [232]:

$$\eta_{Hel} = \frac{\dot{Q}_{Rec}}{\dot{Q}_{Sun}} \tag{3.5}$$

where, η_{Hel} and $\dot{Q}_{Rec}$ are the heliostat optical efficiency and the reflected solar energy to the cavity receiver. A portion of the energy that enters the receiver is lost by conduction, convection, radiation, and reflection mechanisms, and the remaining is absorbed by the molten salt passing through the receiver. The energy balance in the receiver can be calculated by [233]:

$$\dot{Q}_{Rec} = \dot{Q}_{Abs} + \dot{Q}_{Loss,Rec} \tag{3.6}$$

$$\dot{Q}_{Loss,Rec} = \dot{Q}_{Cd} + \dot{Q}_{Cv} + \dot{Q}_{Rad} + \dot{Q}_{Ref} \tag{3.7}$$

where, $\dot{Q}_{Abs}$ and $\dot{Q}_{Loss,Rec}$ are the heat absorbed and lost in the receiver. In addition, the subscripts *Cd*, *Cv*, *Rad*, and *Ref* denote the conduction, convection, radiation, and reflection.

The energy balance in the receiver can also be found based on the average temperatures of the receiver surface $\left(T_{Rec,sur}\right)$ and the molten salt $\left(T_{MS}\right)$ within the receiver tube [220]. The convective heat transfer coefficient of molten salt can be calculated from the Dittus–Boelter equation [234].

$$\dot{q}_{Rec} = \frac{\dot{Q}_{Rec}}{A_{Rec,sur}} = \frac{\left(T_{Rec,sur} - T_{MS}\right)}{\left(\frac{d_O}{d_i \cdot hc_{MS}}\right) + \left(\frac{d_O}{d_i \cdot K_{Rec,tube}} \ln \frac{d_O}{d_i}\right)} \tag{3.8}$$

$$Nu_{MS} = \frac{hc_{MS} \cdot d_i}{K_{MS}} = 0.023 \cdot \mathrm{Re}_{MS}^{0.8} \cdot \mathrm{Pr}_{MS}^{0.4} \tag{3.9}$$

$$\mathrm{Re}_{MS} = \frac{4 \cdot \dot{m}_{MS}}{\pi . N_{Rec,tube} . d_i . \mu_{MS}} \tag{3.10}$$

$$\mathrm{Pr}_{MS} = \frac{\mu_{MS} \cdot C_{P_{MS}}}{K_{MS}} \tag{3.11}$$

$$T_{MS} = \frac{T_{HMS} + T_{CMS}}{2} \tag{3.12}$$

where, d_i and d_o are the inlet and outlet diameters of the receiver tube, K is thermal conductivity, *hc* is convective heat transfer coefficient, and μ is dynamic viscosity. In addition, *Nu*, *Re*, and *Pr* show Nusselt, Reynolds, and Prandtl numbers.

Concentration ratio (C) and view factor (Fr) are two key parameters for determining the required surface and aperture areas of the receiver, and the number of heliostats. To simplify the calculations, it is supposed that the width of the receiver aperture (W) is half its height (H) [220].

$$Fr = \frac{A_{Rec,ap}}{A_{Rec,sur}} \tag{3.13}$$

$$A_{Rec,ap} = H \cdot W = \frac{H^2}{2} \tag{3.14}$$

$$C = \frac{A_{Field}}{A_{Rec,ap}} = \frac{A_{Hel} \cdot N_{Hel}}{A_{Rec,ap}} \tag{3.15}$$

Another important parameter to be calculated is the radiative heat loss between the receiver surface and the surrounding [233]:

$$\dot{Q}_{Rad} = \left(\frac{\varepsilon_W \cdot \sigma \cdot A_{Rec,sur} \cdot \left(T_{Rec,sur}^4 - T_{Amb}^4 \right)}{\left(\frac{\varepsilon_W}{Fr} \right) + \left(1 - \varepsilon_W \right)} \right) \tag{3.16}$$

where σ is Stefan–Boltzmann's constant (5.67×10^{-8} W.m^{-2}.K^{-4}) and ε_W presents the receiver surface absorptivity coefficient. The reflection of aperture escape incident rays is another source of heat waste in the receiver, which is calculated by [235]:

$$\dot{Q}_{Ref} = \alpha \cdot \dot{Q}_{Rec} \cdot Fr \tag{3.17}$$

Convection heat loss in the receiver is based on both natural and forced convections, which are determined by [220]:

$$\dot{Q}_{Cv} = \dot{Q}_{N,Cv} + \dot{Q}_{F,Cv} \tag{3.18}$$

$$\dot{Q}_{N,Cv} = 0.81 \cdot A_{Rec,sur} \cdot \left(T_{Rec,sur} - T_{Amb}\right)^{1.426} \tag{3.19}$$

$$\dot{Q}_{F,Cv} = hc_{F,Cv} \cdot A_{Rec,ap} \cdot \left(T_{Rec,sur} - T_{Amb}\right) \tag{3.20}$$

$$Nu_{F,Cv} = \frac{hc_{F,Cv} \cdot H}{K_{Air}} = 0.0287 \cdot \mathrm{Re}_{F,Cv}^{0.8} \cdot \mathrm{Pr}_{Air}^{0.333} \tag{3.21}$$

$$\mathrm{Re}_{F,Cv} = \frac{\rho_{Air} \cdot V_{Wind} \cdot H}{\mu_{Air}} \tag{3.22}$$

$$\mathrm{Pr}_{Air} = \frac{\mu_{Air} \cdot C_{P_{Air}}}{K_{Air}} \tag{3.23}$$

where, V_{Wind} is the wind speed (m/s).

The smallest share of the heat losses in the receiver belongs to conductive heat transfer, which mostly happens in the insulation layers and the support material [236]. Considering the dominancy of heat waste in the insulation layers, conduction heat loss is defined by [220]:

$$\dot{Q}_{Cd} = \frac{K_{Ins} \cdot A_{Rec,sur}}{\delta_{Ins}} \cdot \left(T_{Rec,sur} - T_{Ins}\right) = hc_{Mix} \cdot A_{Rec,sur} \cdot \left(T_{Ins} - T_{Amb}\right) \tag{3.24}$$

$$hc_{Mix} = hc_{Air,fc} + hc_{Air,nc} \tag{3.25}$$

$$hc_{Air,nc} = 1.24 \cdot \left(T_{Ins} - T_{Amb}\right)^{0.333} \tag{3.26}$$

$$Nu_{Air,fc} = \frac{hc_{Air,fc} \cdot H}{K_{Air}} = 0.02657 \cdot \mathrm{Re}_{Air,fc}^{0.805} \cdot \mathrm{Pr}_{Air}^{0.45} \cdot \left(\frac{T_{Ins}}{T_{Amb}}\right)^{0.2} \tag{3.27}$$

It is noted that KCl-$MgCl_2$ molten salt with the molar fraction of 68% KCl, and 32% $MgCl_2$ was utilized as heat transfer fluid in the heliostat solar unit because of its better fit with the operating

temperature of SOEC and SOFC to avoid crystallization in the pipes [237]. The rate at which thermal energy is absorbed by the molten salt in the receiver can be calculated by [220]:

$$\frac{\dot{Q}_{Abs}}{1000} = \dot{m}_2 \cdot (h_3 - h_2) \tag{3.28}$$

3.2.1.2 Solid oxide electrolyzer

The cell voltage is the most critical factor in the SOEC, which is calculated based on Nernst voltage, Ohmic, activation, and concentration polarizations as follows [238]:

$$V_{SOEC} = E_{Nernst,SOEC} + V_{Ohm} + V_{Act,i} + V_{Con,i} \tag{3.29}$$

$$E_{Nernst,SOEC} = E^0 + \frac{RT_{SOEC}}{2F} \ln\left(\frac{P^0_{H_2} P^{0\,1/2}_{O_2}}{P^0_{H_2O}} \right) \tag{3.30}$$

$$E^0 = 1.253 - 2.4516 \times 10^{-4} T_{SOEC} \tag{3.31}$$

where, E^0 and P^0 are the standard cell potential and partial pressure of hydrogen, oxygen, and water.

Ohmic loss is a type of overpotential loss in the SOEC which is associated with the resistance of cell components (anode, cathode, and electrolyte) and calculated by [224]:

$$V_{Ohm} = (\rho_{An} L_{An} + \rho_{Ca} L_{Ca} + \rho_{Elc} L_{Elc} + \rho_{Int} L_{Int}) . j \tag{3.32}$$

$$\rho_{An} = \left[\left(\frac{9.5 \times 10^7}{T_{cell}} \right) . \exp\left(\frac{-1150}{T_{cell}} \right) \right]^{-1} \tag{3.33}$$

$$\rho_{Ca} = \left[\left(\frac{4.2 \times 10^7}{T_{cell}} \right) . \exp\left(\frac{-1200}{T_{cell}} \right) \right]^{-1} \tag{3.34}$$

$$\rho_{Elc} = \left[28400.\exp\left(\frac{-10300}{T_{cell}} \right) \right]^{-1} \tag{3.35}$$

$$\rho_{Elc} = \left[\left(\frac{9.3\times10^{6}}{T_{cell}} \right).\exp\left(\frac{-1100}{T_{cell}} \right) \right]^{-1} \tag{3.36}$$

where, ρ (Ω.cm) and L (cm) are the electrical resistivity and thickness of the cell components.

The activation loss is the voltage required to overcome the energy required to start the electrochemical reactions, which is calculated based on cell microstructure as follows [222]:

$$V_{Act} = \frac{RT}{F}\left(Sinh^{-1}\frac{j}{2j_{0,An}} + Sinh^{-1}\frac{j}{2j_{0,Ca}} \right) \tag{3.37}$$

where, j_0 is the exchange current density, presenting the ability of the electrodes (anode and cathode) to proceed with electrochemical reactions. Therefore, the greater the j_0, the quicker the electrochemical reactions. The values of J_0 for the cathode and anode are a function of different microstructure and operating factors, calculated as follows [222]:

$$j_{0,An} = k_{An}\frac{72\,X_{Ave}.\varepsilon.\left[r_{Pore} - \varepsilon\left(r_{Pore} + d_{Grain} \right) \right]}{r_{Pore}^{2}.d_{Grain}^{2}\left(1-\sqrt{1-X_{Ave}^{2}} \right)} \times \left(\frac{P_{H_2}^{0}}{P_0} \right) \times \left(\frac{P_{H_2O}^{0}}{P_0} \right) \times \exp\left(-\frac{E_{Act,An}}{RT_{cell}} \right) \tag{3.38}$$

$$j_{0,Ca} = k_{Ca}\frac{72\,X_{Ave}.\varepsilon.\left[r_{Pore} - \varepsilon\left(r_{Pore} + d_{Grain} \right) \right]}{r_{Pore}^{2}.d_{Grain}^{2}\left(1-\sqrt{1-\alpha^{2}} \right)} \times \left(\frac{P_{O_2}^{0}}{P_0} \right) \times \exp\left(-\frac{E_{Act,Ca}}{RT_{cell}} \right) \tag{3.39}$$

where k, X_{Ave}, α, and ε show the coefficient of the exchange current density, the average length of grain contact, symmetrical charge-transfer coefficient, and porosity of electrodes, respectively. In addition, E_{Act}, r_{Pore}, and d_{Grain} show the activation energy of the electrodes, average pore radius, and average grain size.

The resistance in transporting reactants and products to or from the reaction sites of the electrodes results in concentration losses. The purities of fuel and oxidant gases, as well as the microstructure parameters, are responsible for a substantial portion of the concentration overpotential, calculated as follows [222,239]:

$$V_{Con} = \frac{RT_{cell}}{2F}\ln\left(\frac{P_{H_2}^0.P_{H_2O}^{TPB}}{P_{H_2O}^0.P_{H_2}^{TPB}}\right) + \frac{RT_{cell}}{4F}\ln\left(\frac{P_{O_2}^0}{P_{O_2}^{TPB}}\right) \tag{3.40}$$

where, P_i^{TPB} is the triple-phase boundary pressure of the species, achieved by [239]:

$$\begin{cases} P_{H_2O}^{TPB} = P_{H_2O}^0 + \dfrac{j.L_{An}.R.T_{cell}}{2F.D_{H_2O}^{eff}} \\ P_{H_2}^{TPB} = P_{H_2}^0 - \dfrac{j.L_{An}.R.T_{cell}}{2F.D_{H_2}^{eff}} \\ P_{O_2}^{TPB} = P_{O_2}^0 - \dfrac{j.L_{Ca}.R.T_{cell}}{4F.D_{O_2}^{eff}} \end{cases} \tag{3.41}$$

where, D_i^{eff} represents the effective diffusion coefficient, outlined as follows [240]:

$$\begin{cases} D_{H_2O}^{eff} = \dfrac{\varepsilon}{\tau}\left(\dfrac{1}{D_{H_2O-H_2}} + \dfrac{1}{D_{H_2O}}\right)^{-1} \\ D_{H_2}^{eff} = \dfrac{\varepsilon}{\tau}\left(\dfrac{1}{D_{H_2-H_2O}} + \dfrac{1}{D_{H_2}}\right)^{-1} \\ D_{O_2}^{eff} = \dfrac{\varepsilon}{\tau}\left(\dfrac{1}{D_{O_2-N_2}} + \dfrac{1}{D_{O_2}}\right)^{-1} \end{cases} \tag{3.42}$$

where, D_i and $D_{i\text{-}j}$ are Knudsen and binary diffusions, which can be calculated by [222,239]:

$$D_{i-j} = \frac{0.00143 T_{cell}^{1.75}}{P_0 M_{i-j}^{0.5} \left[\left(\sum v \right)_i^{1/3} + \left(\sum v \right)_j^{1/3} \right]^2} \tag{3.43}$$

$$D_i = 97 r_{pore} \left(\frac{T_{cell}}{M_i} \right)^{0.5} \tag{3.44}$$

where, M_i is the molecular weight of species i and $\sum v$ is the diffusion volume (which is 16.3 for O_2, 13.1 for H_2O, 6.12 for H_2, and 18.5 for N_2). In addition, M_{i-j} can be found by the following equation [239]:

$$M_{i-j} = 2 \left(\frac{1}{M_i} + \frac{1}{M_j} \right)^{-1} \tag{3.45}$$

Another important parameter in the SOEC is the steam utilization factor, which is obtained as follows:

$$U_S = \frac{\gamma}{\dot{n}_{H_2O,in}} \tag{3.46}$$

$$\gamma = \frac{j_{SOEC} . A_{SOEC} . N_{SOEC}}{2F} \tag{3.47}$$

where, U_s and γ are the steam utilization factor and the consumed vapor in the SOEC.

Finally, calculating different types of overpotential losses and the cell voltage, the power consumption of the SOEC stack can be calculated by [241]:

$$\dot{W}_{SOEC} = N_{SOEC} . A_{SOEC} . V_{SOEC} . j_{SOEC} \tag{3.48}$$

where N and A are the number of cells and the active area of each cell.

The power consumption and isentropic efficiency of the hydrogen compressor are:

$$\dot{W}_{Com} = \dot{m}_{17} \cdot \left(h_{17} - h_{16} \right) \tag{3.49}$$

$$\eta_{Com} = \frac{h_{17,s} - h_{16}}{h_{17} - h_{16}} \tag{3.50}$$

3.2.1.3 Solid oxide fuel cell

The principal equations for calculating the overpotential losses of the SOFC is similar to those of the SOEC. The only difference is the calculation of the SOFC voltage, in which the overpotential losses are subtracted from the Nernst voltage [223]:

$$V_{SOFC} = E_{Nernst,SOFC} - V_{Ohm} - V_{Act,i} - V_{Con,i} \tag{3.51}$$

$$E = -\frac{\Delta g^0}{2F} + \frac{RT_{SOFC}}{2F} \ln \left\{ \frac{P_{H_2}^0 \cdot P_{O_2}^{0\ 0.5}}{P_{H_2O}^0} \right\} \tag{3.52}$$

$$\Delta g^0 = g_{H_2O}^0 - g_{H_2}^0 - 0.5 g_{O_2}^0 \tag{3.53}$$

$$g_i = h_i(T = T_{SOFC}) - T_{SOFC}\, s_i(T = T_{SOFC}, P = P_0) \tag{3.54}$$

where, *h*, *s*, *g*, and *R* are specific enthalpy, specific entropy, and specific free Gibbs energy, and universal gas constant, respectively.

The hydrogen consumed by the SOFC, *x* (mol/s), can be calculated by the cell characteristics as follows [120]:

$$x = \frac{j_{SOFC} A_{SOFC}}{2F} \tag{3.55}$$

In addition, fuel and air utilization factors for the SOFC are defined by [242,243]:

$$U_f = \frac{\text{Fuel}_{\text{consumed}}}{\text{Fuel}_{\text{supplied}}} = \frac{x}{\dot{n}_{H_2,in}} \tag{3.56}$$

$$U_a = \frac{\text{Air}_{\text{consumed}}}{\text{Air}_{\text{supplied}}} = \frac{\frac{x}{2}}{\dot{n}_{O_2,in}} \tag{3.57}$$

Finally, the power generation of the SOFC stack is calculated by:

$$\dot{W}_{SOFC} = N_{SOFC}.A_{SOFC}.V_{SOFC}.j_{SOFC} \tag{3.58}$$

3.2.1.4 Kalina cycle

The remaining heat is recovered in the evaporator, according to the following equations [244]:

$$\dot{Q}_{Evap} = \dot{m}_{32} \cdot \left(h_{32} - h_{41}\right) \tag{3.59}$$

$$\dot{m}_{27} \cdot \left(h_{26} - h_{27}\right) = \dot{m}_{32} \cdot \left(h_{32} - h_{41}\right) \tag{3.60}$$

Finally, the isentropic efficiency and power generated in the Kalina turbine are presented as follows [244]:

$$\eta_{Tur} = \frac{h_{33} - h_{37}}{h_{33} - h_{37,s}} \tag{3.61}$$

$$\dot{W}_{Tur} = \dot{m}_{33} \cdot \left(h_{33} - h_{37}\right) \tag{3.62}$$

3.2.1.5 District heating

The capacities of district heating in different heat exchangers can be calculated by:

$$\dot{Q}_{DH} = \dot{m}_{DH} \cdot \left(h_{DH,Hot} - h_{DH,Cold} \right) = \dot{m}_{WH} \cdot \left(h_{WH,Hot} - h_{WH,Cold} \right) \quad (3.63)$$

3.2.2 Exergy analysis

The exergy analysis, which is based on the second law of thermodynamics, is a method for evaluating the maximum beneficial work that can be attained from a system. It provides a more comprehensive assessment of the system operation by considering the quality and availability of energy, as well as irreversibilities and inefficiencies in the energy conversion processes. Therefore, exergy analysis provides a more accurate identification of potential zones and components to be improved and optimized for achieving greater efficiency with lower cost and environmental issues. The basic form of the exergy balance equation, which can be applied to all components, is presented below [245]:

$$\sum \dot{m}_{in} e_{in} + \dot{E}_Q = \sum \dot{m}_{out} e_{out} + \dot{E}_W + \dot{E}_D \quad (3.64)$$

here, subscripts *in* and *out* show the inlet and outlet streams of the control volume and $\dot{E}_D$, $\dot{E}_Q$, and $\dot{E}_W$ indicate the exergy destruction of the control volume, heat exergy, and work exergy. In addition, e shows the stream exergy, which is divided into physical (e^{Ph}) and chemical (e^{Ch}) exergies (neglecting kinetic and potential exergy changes) [246]:

$$\dot{E}_Q = \left(1 - \frac{T_0}{T_k} \right) \dot{Q}_k \quad (3.65)$$

$$\dot{E}_W = \dot{W}_k \quad (3.66)$$

$$e = e^{Ph} + e^{Ch} \quad (3.67)$$

$$e_i^{Ph} = \left(h_i - h_0\right) - T_0\left(s_i - s_0\right) \tag{3.68}$$

$$e_i^{Ch} = \sum_{i=1}^{n} x_i e_{0,i}^{ch} + RT_0 \sum_{i=1}^{n} x_i \, ln\left(x_i\right) \tag{3.69}$$

where subscript 0 and $e_{0,i}^{ch}$ relate to the reference condition and standard chemical exergy of substance *i*.

3.2.3 Performance criteria

Finally, the performance indicators of system operation are outlined in the present subsection. Given that the solar, charge, and discharge periods occur at different intervals and durations, conventional efficiency metrics are not able to evaluate the proposed system. Consequently, to address this issue, round-trip efficiency (RTE) and exergy round trip efficiency (ERTE) are defined as the performance criteria of the proposed system as follows:

$$RTE = \frac{m_{H_2,Sale}.LHV_{H_2} + \left(\dot{W}_{SOFC} + \dot{W}_{Tur}\right).t_{dch} + \left(\dot{Q}_{DH_1} + \dot{Q}_{DH_2}\right).t_{ch} + \dot{Q}_{DH_3}.t_{dch}}{\left(\dot{W}_{SOEC} + \dot{W}_{Com} + P_2 + P_3\right).t_{ch} + \left(\dot{Q}_{Solar} + P_1\right).t_{solar} + \left(P_4 + P_5\right).t_{dch}} \times 100 \tag{3.70}$$

$$ERTE = \frac{m_{H_2,Sale}.LHV_{H_2} + \left(\dot{W}_{SOFC} + \dot{W}_{Tur}\right).t_{dch} + \left[\dot{Q}_{DH_1}\left(1 - \frac{T_0}{T_b}\right) + \dot{Q}_{DH_2}\left(1 - \frac{T_0}{T_d}\right)\right].t_{ch} + \dot{Q}_{DH_3}\left(1 - \frac{T_0}{T_f}\right).t_{dch}}{\left(\dot{W}_{SOEC} + \dot{W}_{Com} + P_2 + P_3\right).t_{ch} + \left[\dot{Q}_{Solar}\left(1 - \frac{T_0}{T_{Sun}}\right) + P_1\right].t_{solar} + \left(P_4 + P_5\right).t_{dch}} \times 100 \tag{3.71}$$

3.2.4 Economic analysis

The net present value (NPV) method is a financial approach for analyzing the economic feasibility of a system, which evaluates the profitability and payback period of a project by calculating the current value of its projected cash flows (inflows and outflows) over time, converted to the present

using a specific rate of return. The NPV signifies the variance between the current value of the projected cash inflows and outflows. A positive NPV indicates that the project or investment is profitable and will generate value for the investor, while a negative NPV indicates that the project or investment is not financially viable. The net cash flow at the end of the year is discounted to its present value based on the interest rate according to the following equation [247]:

$$NPV = \sum_{N=0}^{20} Y_N (1+i)^{-1} \tag{3.72}$$

where, N and i show the year and interest rate, and Y_N specifies the net cash flow at the end of Nth year. As mentioned in Table 2, an interest rate of 5% and a service time of 20 years are considered for the proposed system. It is noted that the service time of SOFC, and SOEC units are 40,000 hours. In addition, it is presumed that the operating and maintenance (O&M) cost of each component is 6% of its capital cost (excluding solid oxide cells with an annual O&M cost of 22% of capital cost). The capital cost functions for different components are listed in Table 3.2.

Table 3.2: Capital cost functions of different units and components [191,225,248].

Component	Capital cost function ($)
Condenser	$Z_{Cond} = 8000 \cdot (\frac{A_{Cond}}{100})^{0.6}$ $A_{Cond} = \frac{Q_{Cond}}{U_{Cond}.LMTD_{Cond}}$
Evaporator	$Z_{Evap} = 16000 \cdot (\frac{A_{Evap}}{100})^{0.6}$ $A_{Evap} = \frac{Q_{Evap}}{U_{Evap}.LMTD_{Evap}}$
Expansion valve	$Z_{Ev} = 114.5 \cdot \dot{m}_{in}$
Heliostat field land	$Z_{Land} = 8.9 \cdot A_{HEL} \cdot N_{HEL}$
Heliostat field mirrors	$Z_{Hel} = 150 \cdot A_{HEL} \cdot N_{HEL}$
HE_1, HE_3, HE_4, HE_7, and HE_8	$Z_{HE} = 12000 \cdot (\frac{A_{HE}}{100})^{0.6}$ $A_{HE} = \frac{Q_{HE}}{U_{HE}.LMTD_{HE}}$
HE_2, HE_5, and HE_6	$Z_{HE} = 32800 \cdot (\frac{A_{HE}}{80})^{0.68}$ $A_{HE} = \frac{Q_{HE}}{U_{HE}.LMTD_{HE}}$
Hydrogen compressor	$Z_{Com} = 44.71 \dot{m}_{in} \left[1/\left(0.95 - \eta_{Com}\right)\right] \times P_{out} \times ln\left(P_{out}\right)$
Hydrogen tank	$Z_{H_2 tank} = 300 \times 3600 \times \dot{m}_{19}\, t_{dch}$

Kalina turbine	$Z_{Tur} = 6000 \cdot \dot{W}_{Tur}^{0.7}$
KCl-$MgCl_2$ salt	$Z_{MS} = (0.62 \cdot 485 + 0.38 \cdot 382) \cdot 3.6 \cdot t_{Solar} \cdot \dot{m}_{MS}$
Mixer	$Z_{Mix} = 114.5 \cdot \dot{m}_{Out}^{0.67}$
Molten salt pump	$Z_{P_7} = 2100 \cdot (\frac{\dot{W}_P}{10})^{0.26} \cdot (\frac{1-\eta_P}{\eta_P})^{0.5}$
Molten salt tanks	$Z_{MST} = 687.5 \cdot (V_{CST} + V_{HST})$
Oxygen tank	$Z_{O_2 tank} = 1.218 f_m \, exp\left[2.631 + 1.3673\left(lnV_{O_2 tank}\right) - 0.06309\left(lnV_{O_2 tank}\right)^2\right]$ $f_m = 1\left(\text{Carbon steel}\right)$
Pumps	$Z_P = 2100 \cdot (\frac{\dot{W}_P}{10})^{0.26} \cdot (\frac{1-\eta_P}{\eta_P})^{0.5}$
Receiver	$Z_{Rec} = A_{Rc,sur} \cdot \left(79 \cdot T_{Rc,sur} - 42000\right)$
Separator	$Z_{Sep} = 114.5 \cdot \dot{m}_{in}^{0.67}$
Solid oxide electrolyzer	$Z_{SOEC} = A_{SOEC} \cdot N_{SOEC} \cdot \left(2.96 T_{SOEC} - 1907\right)$
Solid oxide fuel cell	$Z_{SOFC} = A_{SOFC} \cdot N_{SOFC} \cdot \left(2.96 T_{SOFC} - 1907\right)$

3.3 Result and discussion

The simulation results of the proposed hybrid system are outlined in three subsections of model validation, steady-state modelling results, and parametric analysis.

3.3.1 Model validation

The proposed hybrid system to produce and utilize green hydrogen using solar, SOEC, and SOFC is a novel design, which has not been previously studied. Hence, the accuracy of the modelling of each unit is verified individually with related data in the literature. The simulation results of the SOEC and SOFC units are compared with the measured data of Ebbesen et al. [249] and Zhao and Virkar [250] in Figure 3.3, respectively. Additionally, the precision of the simulation results for the heliostat solar unit and the Kalina cycle are validated with the reported data of Tehrani and Taylor [220] and Li et al. [251] in Table 3.3. As shown in Figure 3.3 and Table 3.3, there are negligible differences between the results of the present simulation and the related data in the

literature. Therefore, the model accuracy is deemed to be reliable, and the resulting data can be considered dependable.

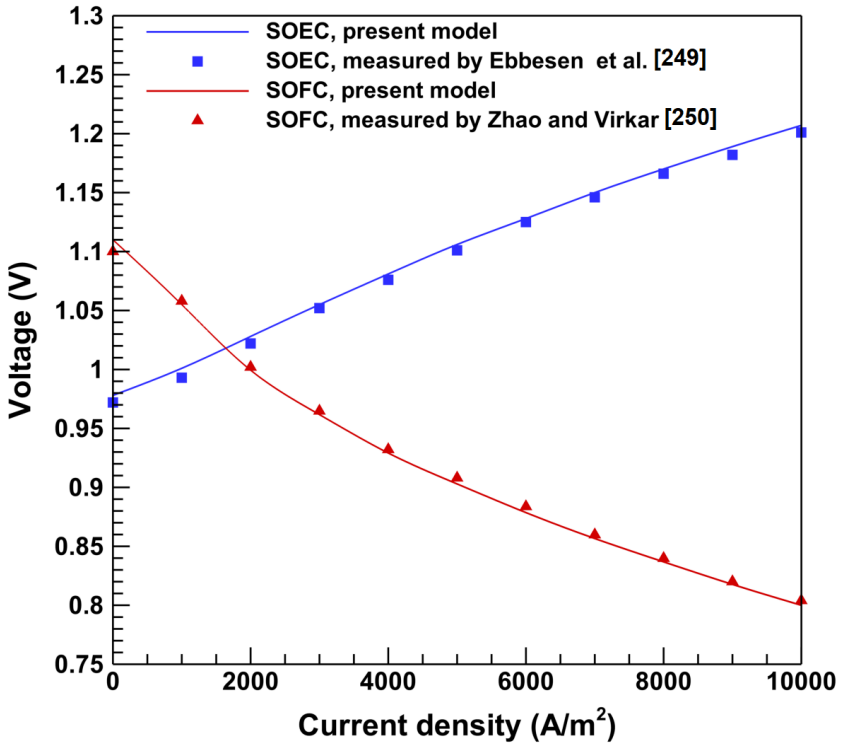

Figure 3.3: The validations of the SOEC and SOFC units with the measured data in the literature [249,250].

Table 3.3: Comparison of the present model with the respective articles [220,251].

Unit	Parameter	Present model	Literature	Error (%)
Heliostat solar [220]	Temperature of the receiver surface [K]	779.9	770.5	1.2
	Energy efficiency of the receiver [%]	90.6	89.0	1.8
	Exhaust heat of the receiver [MW]	143.9	142.0	1.4
	Heliostat field mass flow rate [kg/s]	349	343	1.7
Kalina cycle [251]	Energy efficiency [%]	7.7	7.8	1.3
	Heat input [kW]	161.1	164.1	1.8
	Net power generation [kW]	12.4	12.7	2.4
	Kalina turbine temperature [°C]	344.1	344.5	0.2

3.3.2 Steady-state modelling

In this section, the results of thermodynamic and economic analyses are presented based on the steady-state design conditions listed in Table 3.1. Initially, to more clarification of the system processes, the important thermodynamic properties of streams are outlined in Table 3.4.

Table 3.4: Thermodynamic properties of different streams of the proposed hybrid system.

State	Working fluid	*P* (bar)	*T* (K)	$\dot{m}$ (kg/s)	*h* (kJ/kg)	*s* (kJ/kg. K)
1	$KCl\text{-}MgCl_2$	1.01	873.2	7.78	201.3	0.257
2	$KCl\text{-}MgCl_2$	1.03	873.2	7.78	201.3	0.257
3	$KCl\text{-}MgCl_2$	1.01	1373	7.78	779.7	0.781
4	$KCl\text{-}MgCl_2$	1.01	1373	2.05	779.7	0.781
5	$KCl\text{-}MgCl_2$	1.03	1373	2.05	779.7	0.781
6	$KCl\text{-}MgCl_2$	1.01	873.2	2.05	201.3	0.257
7	H_2O	1.01	293.2	1.69	83.93	0.296
8	H_2O	1.03	293.1	1.69	83.93	0.296
9	H_2O	1.02	842.5	1.69	3638	9.015
10	H_2O	1.01	1123	1.69	4277	9.669
11	$H_2\text{-}H_2O$	1.01	1123	0.79	5970	19.66
12	O_2	1.01	1123	0.90	841.8	1.327
13	$H_2\text{-}H_2O$	1.01	373.2	0.79	3019	15.38
14	O_2	1.01	313.2	0.90	13.80	0.046
15	H_2O	1.01	303.2	0.68	125.8	0.436
16	H_2	1.01	303.2	0.11	4003	53.62
17	H_2	300	544.2	0.11	8113	55.19
18	H_2	300	318.2	0.11	4392	30.67
19	H_2	1.01	293.2	0.14	3860	53.14
20	O_2	1.01	293.2	2.25	-4.593	-0.015
21	H_2	1.01	757.1	0.14	10597	66.90
22	O_2	1.01	757.1	2.25	449.3	0.904
23	H_2	1.01	1173	0.14	16815	73.44
24	O_2	1.01	1173	2.25	896.9	1.375
25	H_2O	1.01	1173	2.39	2569	6.169
26	H_2O	1.01	473.2	2.39	1388	4.656
27	H_2O	1.01	350.0	2.39	218.8	1.430
28	H_2O	1.01	298.2	2.39	91.09	1.035
29	$KCl\text{-}MgCl_2$	1.01	1373	4.67	779.7	0.781
30	$KCl\text{-}MgCl_2$	1.01	1373	4.67	779.7	0.781
31	$KCl\text{-}MgCl_2$	1.01	873.2	4.67	201.3	0.257
32	$NH_3\text{-}H_2O$	40.0	448.2	1.61	1763	4.947
33	$NH_3\text{-}H_2O$	40.0	448.2	1.57	1793	5.018
34	$NH_3\text{-}H_2O$	40.0	448.2	0.04	607.7	2.148
35	$NH_3\text{-}H_2O$	40.0	313.9	0.04	-11.71	0.515
36	$NH_3\text{-}H_2O$	9.41	314.6	0.04	-11.71	0.526
37	$NH_3\text{-}H_2O$	9.41	387.5	1.57	1579	5.116
38	$NH_3\text{-}H_2O$	9.41	387.0	1.61	1539	5.005
39	$NH_3\text{-}H_2O$	9.41	303.2	1.61	0.023	0.401
40	$NH_3\text{-}H_2O$	40.0	303.9	1.61	5.523	0.405

41	NH_3-H_2O	40.0	307.2	1.61	20.88	0.455
42	NH_3-H_2O	1.01	293.2	14.8	83.93	0.296
43	NH_3-H_2O	1.01	333.2	14.8	251.2	0.831
a	H_2O	1.01	293.2	0.51	83.93	0.296
b	H_2O	1.01	333.2	0.51	251.2	0.831
c	H_2O	1.01	293.2	13.5	83.93	0.296
d	H_2O	1.01	333.2	13.5	251.2	0.831
e	H_2O	1.01	293.2	1.83	83.93	0.296
f	H_2O	1.01	333.2	1.83	251.2	0.831

In addition, applying the design conditions in Table 3.1 and the governing equations, a summary of important results of the proposed system is presented in Table 3.5. The SOEC unit is capable of producing 7.76 ton H_2/day while consuming 11.89 MW of power during 19 hrs of off-peak periods. The produced hydrogen is subsequently pressurized to 300 bar via a compressor utilizing 2.31 MW of power. About 2.55 ton of the produced hydrogen is exploited to generate 10.86 MW power during 5 hours for peak shaving, while the remaining 5.21 ton is sold to hydrogen markets. Recovering the produced waste heat for district heating productions of 2.35 and 0.31 during off-peak and peak periods and extra power generation of 0.34 MW in the Kalina cycle in peak hours, an RTE and ERTE of 74.21 and 64.15% are achieved.

Table 3.5: Summary of important thermodynamic results of the proposed system.

Parameter	Unit	Value
RTE	%	74.21
$ERTE$	%	64.15
$\dot{m}_{H_2,SOEC}$	ton/day	7.76
$\dot{m}_{H_2,Sale}$	ton/day	5.21
$\dot{m}_{H_2,SOFC}$	ton/day	2.55
$\dot{Q}_{Abs}$	MW	4.50
$\dot{Q}_{Cond}$	MW	2.47
$\dot{Q}_{Evap}$	MW	2.80
$\dot{Q}_{HE_1}$	MW	1.08
$\dot{Q}_{HE_2}$	MW	6.01
$\dot{Q}_{HE_3}$ & $\dot{Q}_{DH_1}$	MW	0.09
$\dot{Q}_{HE_4}$ & $\dot{Q}_{DH_2}$	MW	2.26
$\dot{Q}_{HE_5}$	MW	3.01

$\dot{Q}_{HE_6}$	MW	2.70
$\dot{Q}_{HE_7}$	MW	0.03
$\dot{Q}_{HE_8}$ & $\dot{Q}_{DH_3}$	MW	0.31
$\dot{Q}_{Sun}$	MW	12.71
V_{CMS} &V_{HMS}	m^3	130
$V_{H_2\,tank}$	m^3	410
$V_{O_2\,tank}$	m^3	30000
$\dot{W}_{Com}$	MW	2.31
$\dot{W}_{SOEC}$	MW	11.89
$\dot{W}_{SOFC}$	MW	10.86
$\dot{W}_{Tur}$	MW	0.34

In addition, a comprehensive exergy Sankey diagram of the novel system is presented in Figure 3.4 (units are in Megawatts hour, MWh). This diagram is really helpful for understanding the sources of exergy losses and waste within the system, which provides an inclusive picture of the system's inefficiencies. These information can be used to identify areas for improvement and optimization, resulting in higher efficiencies and lower waste and operating costs. As shown in Figure 3.4, the thickness of the arrows represents the quantity of exergy flows between different components. In addition, the black arrow shows the rate at which exergy is destructed at each component.

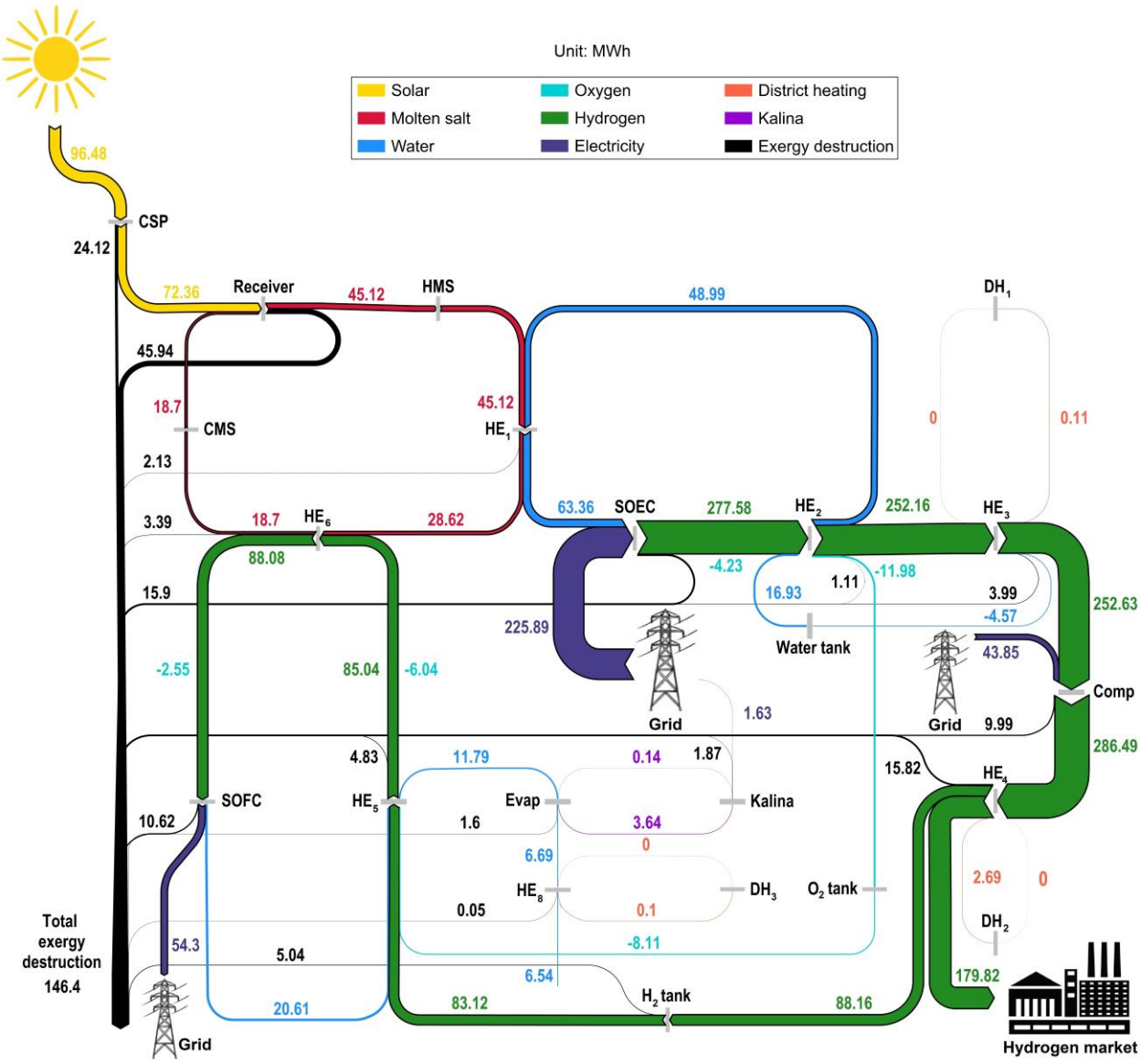

Figure 3.4: Sankey exergy diagram of the proposed hybrid system.

As shown in Figure 3.4, the SOEC, solar receiver, and SOFC are responsible for the highest rates of exergy destruction, respectively. The internal irreversibilities and their significant temperature difference with the ambient temperature are the most important reasons for high exergy destruction. It should be noted that the greater exergy destruction in the SOEC associates with the longer operation per cycle.

The capital cost of different units and their components is another important aspect of complex energy systems. Accurate estimation and representation of the costs can help decision-makers to evaluate and select the optimal design for their applications. In this regard, the capital costs of different units of the proposed system and their contribution to total capital cost is shown in Figure 3.5.

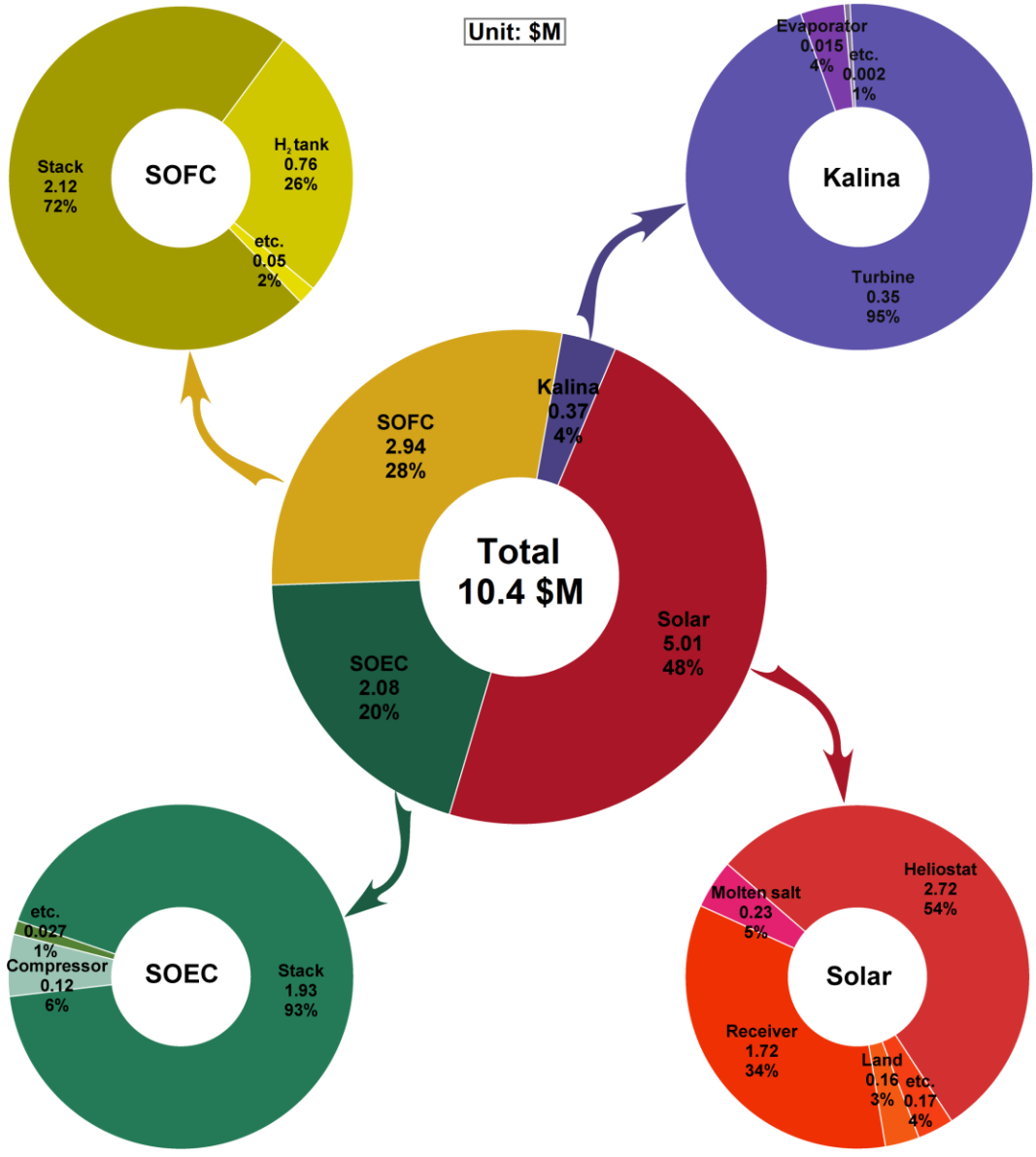

Figure 3.5: Capital costs of different units and components and their contribution to total capital cost.

As shown, the solar unit is the most expensive part, which costs about 48% of the total capital cost. Solar heliostat and receiver are responsible for 88% of the total cost of the solar unit. On the other hand, considering the identical capacity of the SOEC and SOFC stacks, they have almost the same price with a small difference because of their different operating temperature and resulting degradation rate. It is also noted that 26% percent of the SOEC unit associated with hydrogen storage tank because of its expensive material to avoid leakage and embrittlement in high pressure. Finally, the Kalina cycle, due to its small size for operation as a waste heat recovery unit, is the cheapest unit, with about 4% of the total capital cost of the system.

3.3.3 Parametric analysis

In this section, a detailed parametric analysis is carried out to assess the impact of key factors on the performance of the hybrid system. It is worth noting that all parameters, except the under-study parameter, are kept constant as per the specifications listed in Table 3.1.

The effect of DNI and solar exposure duration on critical parameters are shown in Figure 3.6. As shown in Figure 3.6 (a), greater DNI and longer solar exposure durations result in higher quantities of supplied molten salt within the tank. Consequently, leveraging the increased capacity of the molten salt can lead to higher capacities for the SOEC and SOFC. Assuming equivalent operational scales for the SOEC and SOFC, this improvement leads to corresponding enhancements in their consumption and production rates. The increased operational scales of the SOEC and SOFC yield more waste heat production and district heating, as represented in Figure 3.6 (b).

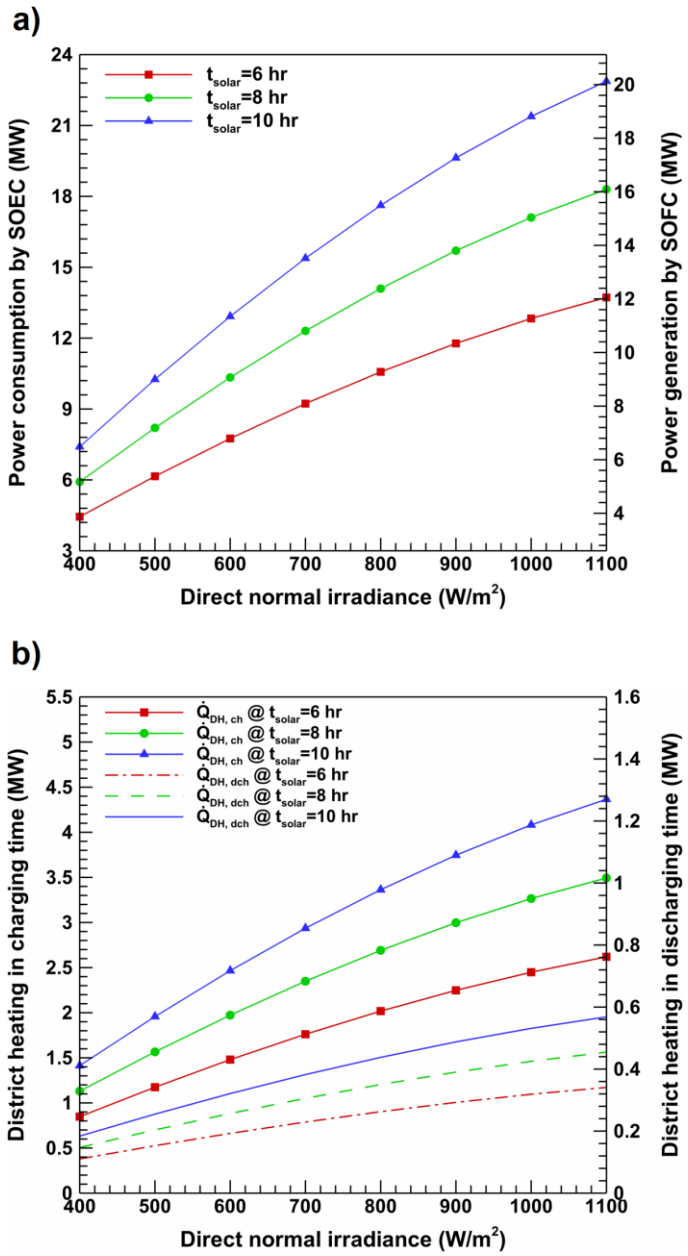

Figure 3.6: The effect of direct normal irradiance and solar time on a) power consumption and generation of SOEC and SOFC, b) charge and discharge district heating capacities.

Furthermore, Figure 3.7 (a) illustrates the impact of DNI and solar exposure duration on daily hydrogen sales and the capacity of the hydrogen compressor. As deducted from Figure 3.6 (a), the capacity of SOEC is increased at high DNIs and solar exposure durations, resulting in greater hydrogen production and sales to hydrogen markets. In addition, as per Eq. (3.49), the greater the hydrogen production in the SOEC, the higher the power consumption of the hydrogen compressor.

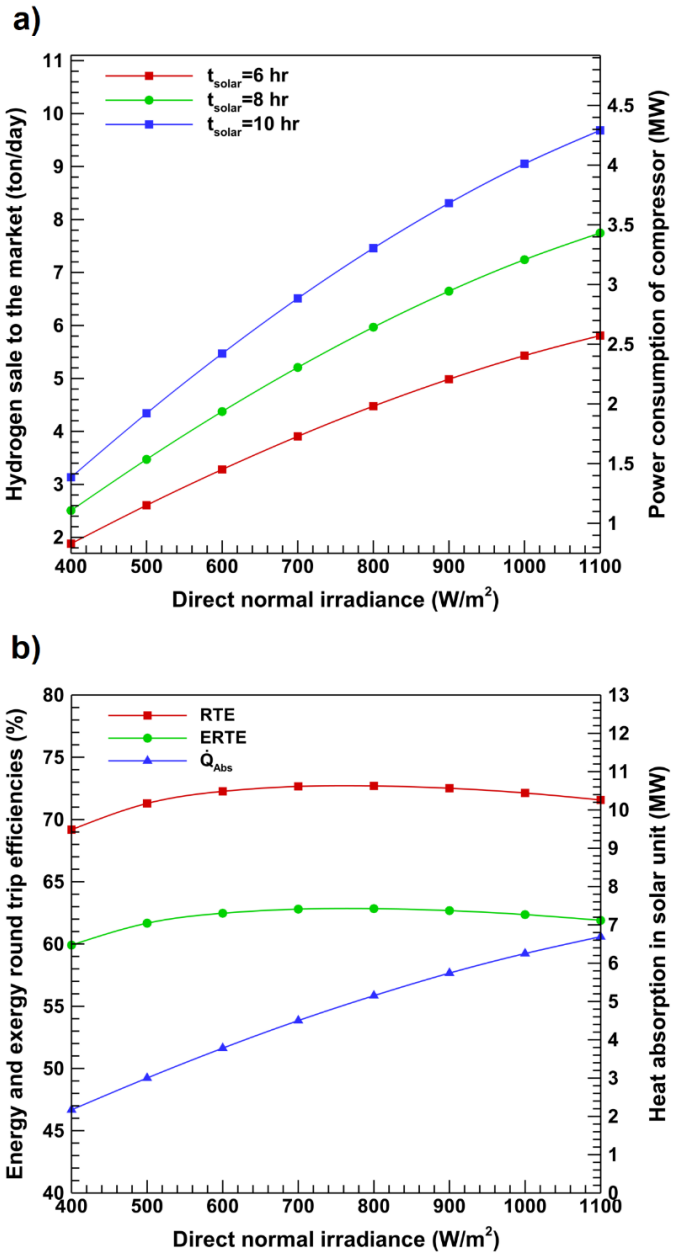

Figure 3.7: The effect of direct normal irradiance on a) hydrogen sale to the market and power consumption of hydrogen compressors at various solar times, b) RTE, ERTE, and heat absorption in the solar unit.

Finally, how solar DNI alters RTE, ERTE, and heat absorption in the solar unit is presented in Figure 3.7 (b). Heat absorption within is directly proportional to DNI and escalates at higher DNI levels. In addition, both RTE and ERTE exhibit a rising trend up to an optimal DNI threshold of approximately 800, beyond which a marginal decline can be observed.

Additional noteworthy parameters to assess are the current densities and temperatures of the SOEC and SOFC units, which are illustrated in Figure 3.8 and Figure 3.9.

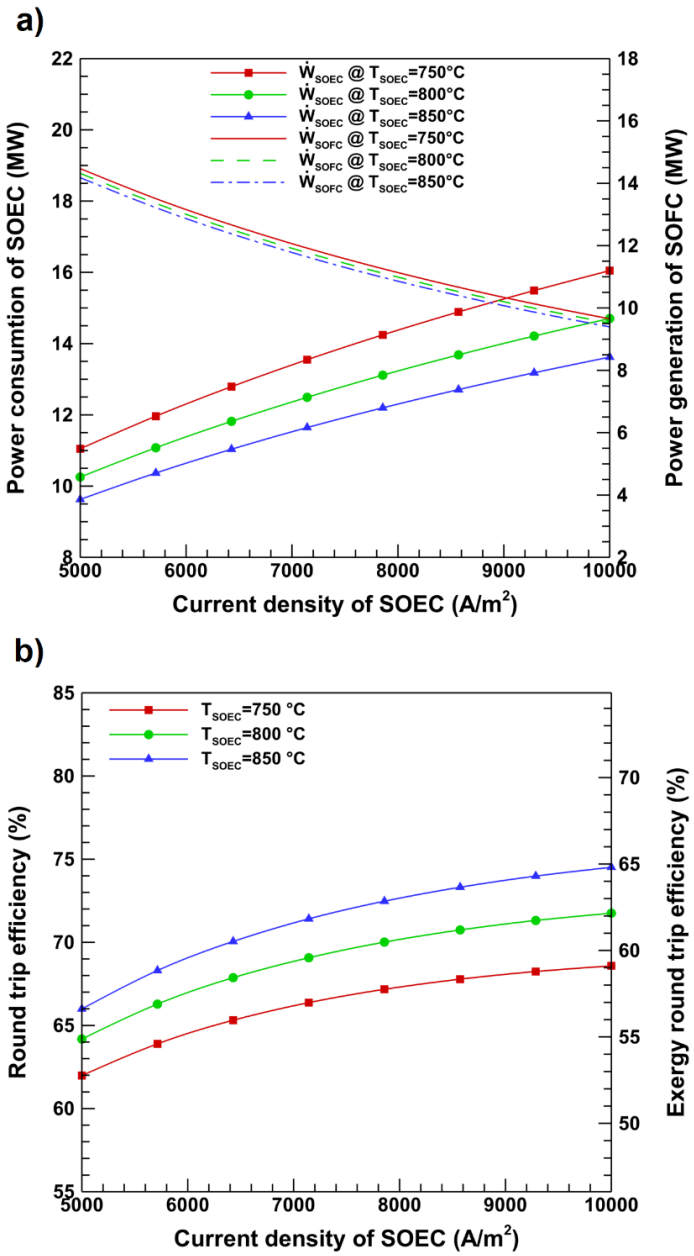

Figure 3.8: The effect of current density and operating temperature of SOEC on a) power consumption and generation of SOEC and SOFC, b) RTE, ERTE.

As presented in Figure 3.8 (a), a reverse trend is observable between the power consumption of the SOEC and the power generation of the SOFC at higher current densities of the SOEC. This

can be attributed to more steam requirements to drive the SOEC at higher current densities, which leads to an increase in both power consumption and hydrogen production. Therefore, the rate at which the supplied molten salt is exploited to provide the required steam in the SOEC rises, reducing the amount of molten salt available for the SOFC. Consequently, as shown in Figure 3.8 (a), the power generated in the SOFC is decreased in higher current densities of the SOEC. On the other hand, the higher the operating temperature of the SOEC, the less the SOEC power consumption due to the increased reaction rates. In addition, more molten salt is required to provide steam at higher temperatures, which leads to lower power generation in the SOFC because of the decreased available molten salt. These alterations in the current density and temperature of the SOEC can also affect RTE and ERTE, as shown in Figure 3.8 (b). Higher current density and temperature of the SOEC can enhance its performance and hydrogen production rate, thereby improving the RTE and ERTE according to Eqs. (3.70) and (3.71).

Figure 3.9 represents how the current density and temperature of the SOFC unit can affect the power generation and consumption in the SOFC and SOEC units, along with the overall performance of the system. As shown in Figure 3.9 (a), more power is generated in the SOFC unit at higher temperatures and current densities. This increase can be attributed to the higher SOFC efficiency, which is achieved by the increased input of hydrogen and oxygen. Increasing the input of gases leads to a higher utilization of the supplied molten salt for operating the SOFC, which in turn results in a lower allocation of molten salt to the SOEC. Consequently, the SOEC operates at a lower capacity, with decreased power consumption and hydrogen production rates. In contrast to the SOEC unit, the RTE, and ERTE have an inverse correlation with the increase in the current density of the SOFC (Figure 3.9 (b)). This can be attributed to the fact that the sale of hydrogen to the market is more efficient than its conversion to power from the thermodynamic point of view.

However, similar to the SOEC, the higher the operating temperature of the SOFC, the higher the conversion rate and its efficiency, which results in greater RTE and ERTE.

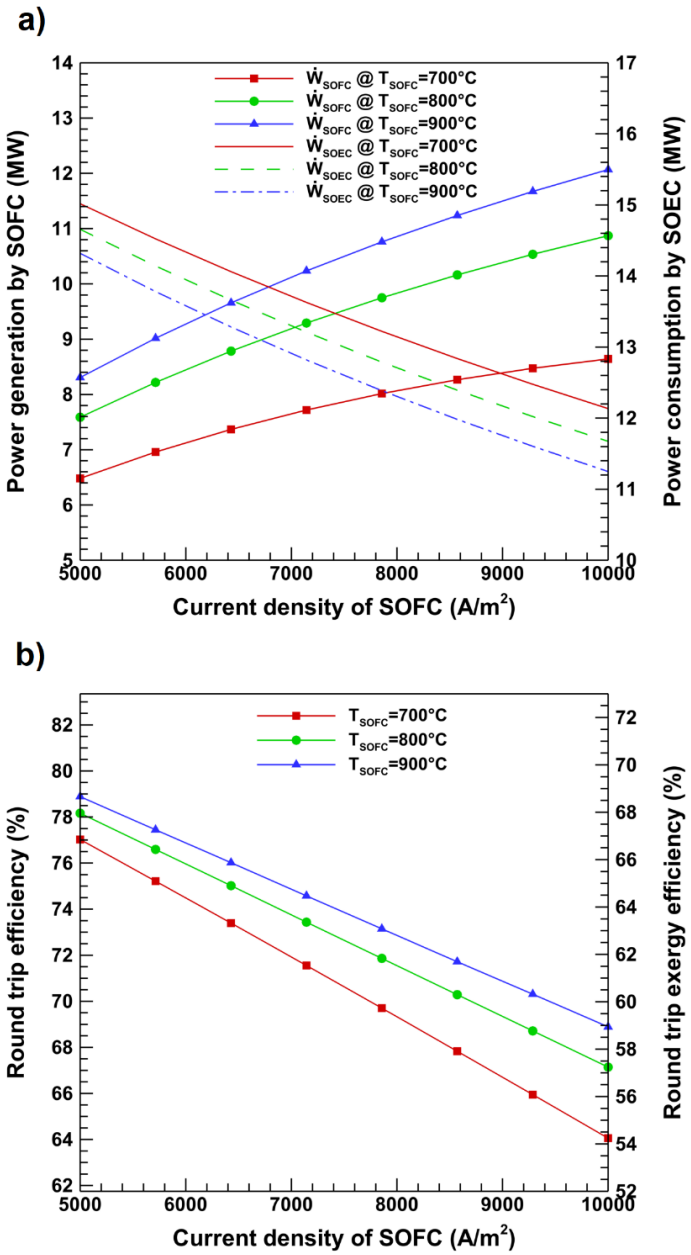

Figure 3.9: The effect of current density and operating temperature of SOFC on a) power consumption and generation of SOEC and SOFC, b) RTE, ERTE.

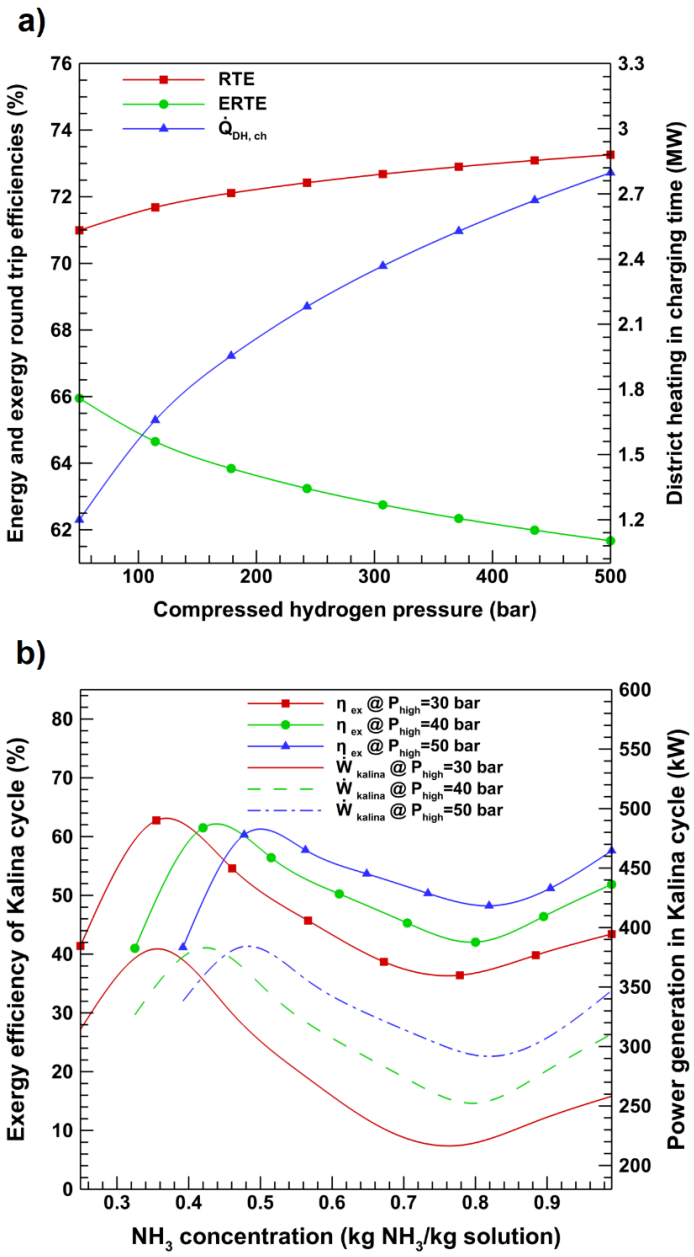

Figure 3.10: The effect of a) compressed hydrogen pressure on RTE, ERTE, and charging district heating capacity, b) ammoniac concentration of the Kalina cycle on its exergy efficiency and power generation.

Figure 3.10 (a) presents an overview of the impact of compressed hydrogen pressure on RTE, ERTE, and charging district heating. The compression process accompanies heat production. As a result, the more the hydrogen pressure, the higher the waste heat produced in the compressor. Hence, more heat can be produced for district heating applications at higher pressures. Considering that the produced heat has lower quality compared to the consumed power in the compressor, the

ERTE decreases in higher pressures according to the second law of thermodynamics and Eq. (3.71). However, there is marginal improvement in RTE at increased hydrogen pressures.

Figure 3.10 (b) represents the effect of the ammoniac concentration of the evaporator on the exergy efficiency and power generation of the Kalina cycle. As shown, there are optimum values for ammoniac concentration based on the high pressure of the Kalina cycle. For instance, an exergy efficiency of 60% and power generation of 370 kW can be attained by optimizing the ammoniac concentration to a value of 0.5 under a higher pressure condition of 50 bar.

3.4 Case study

Performing a case study analysis for hybrid energy systems is of great importance to determine the most efficient and cost-effective approaches for integrating renewable energies into the existing energy grid. It can also provide insights into technical and economic aspects of complex energy systems, which helps to improve and optimize the system performance under different operating conditions. In this section, a detailed case study based on the real solar DNI data and hourly electricity price is performed for Los Angeles, California. The available dynamic electricity price and desirable solar exposure conditions for high-temperature solar thermal units were the most important reasons for selecting this city as a case study. Figure 3.11 provides a depiction of hourly DNI in various months of the year for the case study of Los Angeles, based on the available data in Meteonorm software [252].

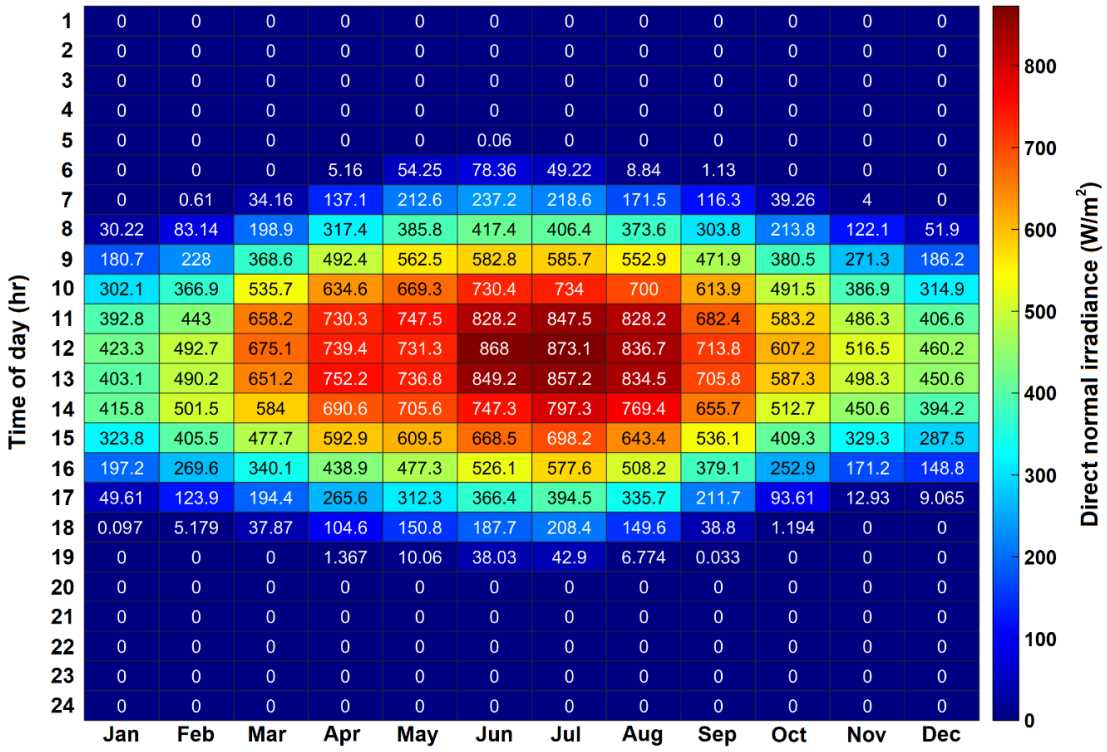

Figure 3.11: Hourly direct normal irradiance at different months for the case study of Los Angeles, California, data is taken from Meteonorm software [252].

Hydrogen storage has emerged as a highly promising option for both short- and long-term energy storage. This capacity is particularly significant in addressing the intermittency and variability challenges of renewable energy sources. Figure 3.12 (a) and (b) offer a comprehensive insight into DNI and hydrogen production capacity of the proposed system across different seasons and months in Los Angeles. As shown in Figure 3.12 (b), the proposed system has the potential to produce approximately 2156 tons of green hydrogen based on the solar exposure conditions in Los Angeles. It is assumed that the solar unit can operate optimally at DNI levels exceeding 300 W/m^2, resulting in operational periods of 6 hrs in winter, 9 hrs in Spring, 10 hrs in summer, and 7 hrs in fall. Consequently, there will be substantial variation in the rate of hydrogen production across different seasons and months, as shown in Figure 3.12 (b). For instance, over three times more green hydrogen can be produced in summer, compared to winter. Therefore, given the specific

requirements of the case study, various scenarios ranging from hourly to monthly and seasonal hydrogen storage options could be defined to facilitate for optimal and economical operation of the system.

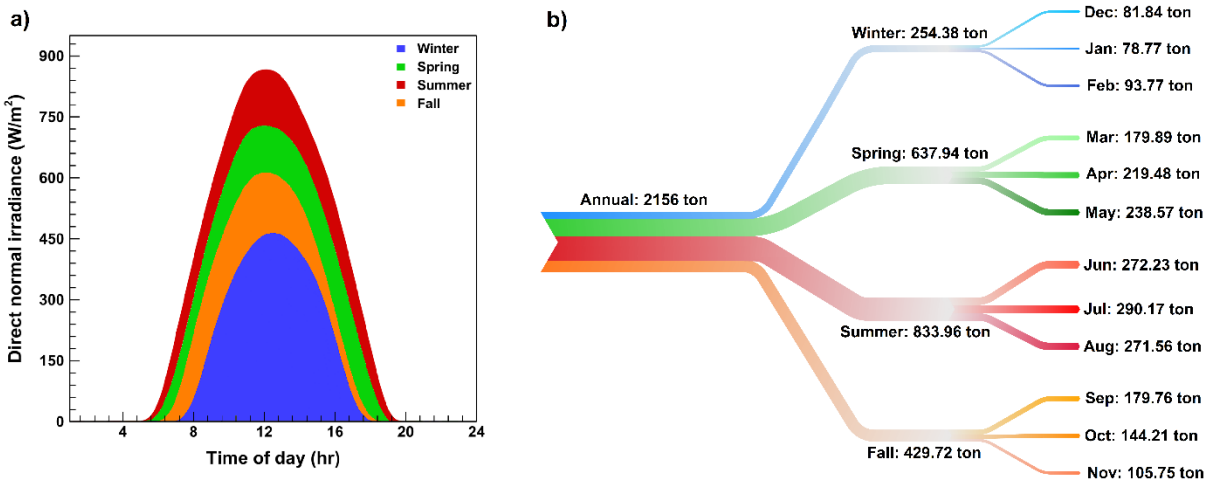

Figure 3.12: a) Hourly DNI in different seasons b) Annual, seasonal, and monthly hydrogen production rate for the case study of Los Angeles, California, data is taken from Meteonorm software [252].

Hourly electricity price for different seasons in Los Angeles is listed in Table 3.6. As it can be observed, the electricity price is prohibitively high during summer, which happens to coincide with the period when the proposed system is capable of generating maximum power. Conversely, the winter season is characterized by the lowest rate of hydrogen production that fits the minimum electricity demand. Consequently, hydrogen storage on a daily basis appears to be the most viable scenario for the city of Los Angeles. In accordance with the assumptions outlined in Table 3.1, the proposed system is designed to charge during off-peak periods spanning 19 hrs, while discharging for 5 hrs during periods when the cost of electricity is at its highest. As an example, in the summer season, the SOEC unit is activated for 19 hrs during the low-price periods characterized by an average electricity price of 0.133 $/kWh, whereas the SOFC unit generates power during 5 hrs of peak demand when the sale price of electricity reaches an average of 0.858 $/kWh.

Table 3.6: Hourly electricity prices ($/kWh) for different seasons in Los Angeles, California [253].

Time	Winter ($/kWh)	Spring ($/kWh)	Summer ($/kWh)	Fall ($/kWh)
1	0.0345	0.0298	0.0344	0.0266
2	0.0308	0.0250	0.0292	0.0232
3	0.0286	0.0207	0.0241	0.0200
4	0.0283	0.0189	0.0225	0.0180
5	0.0310	0.0217	0.0243	0.0199
6	0.0384	0.0268	0.0313	0.0250
7	0.0443	0.0300	0.0335	0.0272
8	0.0474	0.0343	0.0375	0.0311
9	0.0475	0.0378	0.0530	0.0357
10	0.0487	0.0424	0.0801	0.0409
11	0.0504	0.0563	0.1713	0.0447
12	0.0504	0.0641	0.2732	0.0467
13	0.0496	0.0862	0.3985	0.0485
14	0.0496	0.2142	0.6441	0.0508
15	0.0491	0.3451	0.8337	0.0559
16	0.0490	0.4485	1.0757	0.0608
17	0.0499	0.4559	0.9879	0.0595
18	0.0533	0.2877	0.7480	0.0515
19	0.0554	0.1594	0.3799	0.0489
20	0.0556	0.1087	0.2561	0.0461
21	0.0534	0.1086	0.4159	0.0484
22	0.0493	0.0565	0.1612	0.0449
23	0.0447	0.0420	0.0678	0.0410
24	0.0379	0.0360	0.0400	0.0330

Benefiting the potential of hydrogen storage can considerably enhance the economic feasibility of green hydrogen production units. In this regard, Figure 3.13 represents the profitability of the system over time and the payback period based on the varying ratios of hydrogen consumption in the SOFC to the total hydrogen production in the SOEC. Considering the high production cost of green hydrogen, it is yet to compete with alternative technologies like steam methane reforming, which can produce hydrogen at a lower cost of less than 2 $/kg. Consequently, selling all the produced hydrogen at an even higher price of 2.75 $/kg to the market results in a payback period of around 17.5 years, which is considerably high. Moreover, it is worth noting that even the capital cost cannot be recovered if the produced hydrogen is sold below 2.75 $/kg. However, as shown in Figure 3.13, employing hydrogen storage to generate power during peak demand periods can significantly reduce the payback period. For instance, utilizing 25, 50, and 75% of the hydrogen produced by the SOEC for power generation in the SOFC results in payback periods of 2.52, 1.86,

and 1.63 years, respectively. The lowest payback period of 1.51 years is achieved when all the produced hydrogen is consumed in the SOFC unit. Under this condition, the system has the potential to generate a profit of over $78 million during its economic book life, which is over 7.7 times of its capital cost ($10.1 million). It is important to note that the capacities of the SOFC and Kalina cycle increase with higher hydrogen consumption rates, leading to higher capital cost, as shown by the negative value at the beginning of the time series in Figure 3.13.

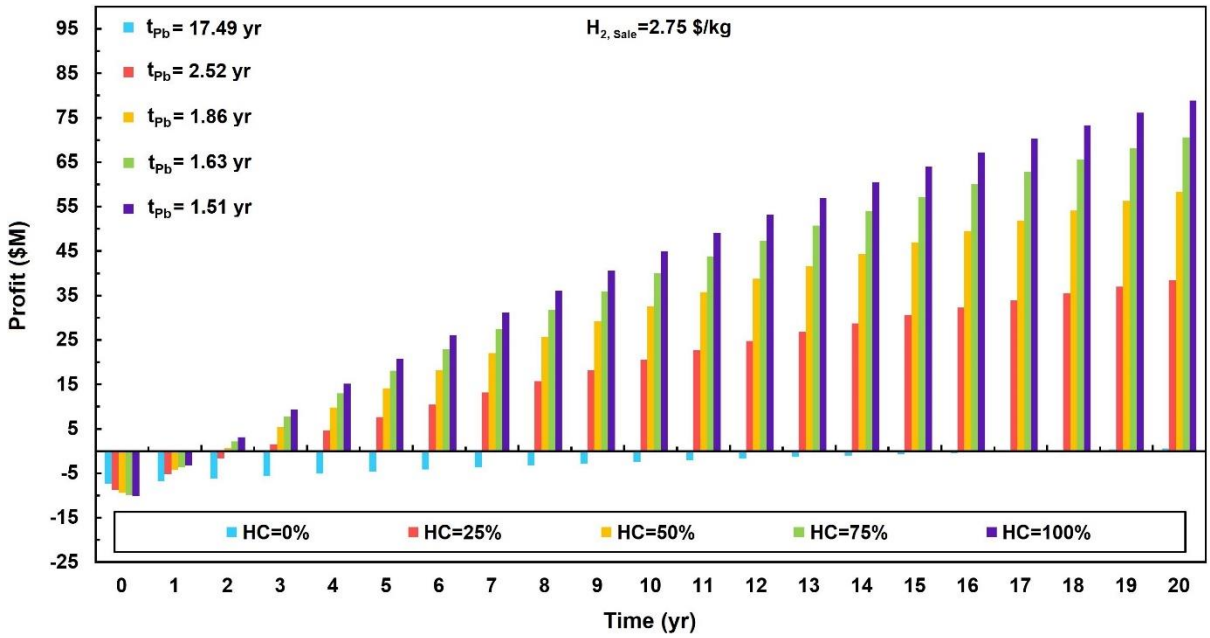

Figure 3.13: System profit over time and payback period based on the percentage of hydrogen consumption in the SOFC to the produced hydrogen in the SOEC, HC: hydrogen consumption in the SOFC.

To further elaborate on the significance of hydrogen storage, Figure 3.14 (a) and (b) depict the system profitability and payback period at different hydrogen sales prices based on 0 and 50% utilization of the produced hydrogen for peak shaving, respectively. As shown in Figure 3.14 (a), the capital cost of the system cannot be recovered if all the hydrogen is sold at $2/kg, rendering the system fully detrimental. However, if half of the produced hydrogen is stored for peak shaving, a payback period of 2.14 years can be achieved, as shown in Figure 3.14 (b). The same trend can be observed at a hydrogen sale price of 3 $/kg, whereby a 4-year reduction in the payback period

can be achieved by storing half of the produced hydrogen for peak shaving applications. Nevertheless, a hydrogen sale price of 4 $/kg is a threshold for choosing between hydrogen storage or direct sale. In other words, selling hydrogen at prices exceeding 4 $/kg is more economically viable than storing half of it for power generation during peak times.

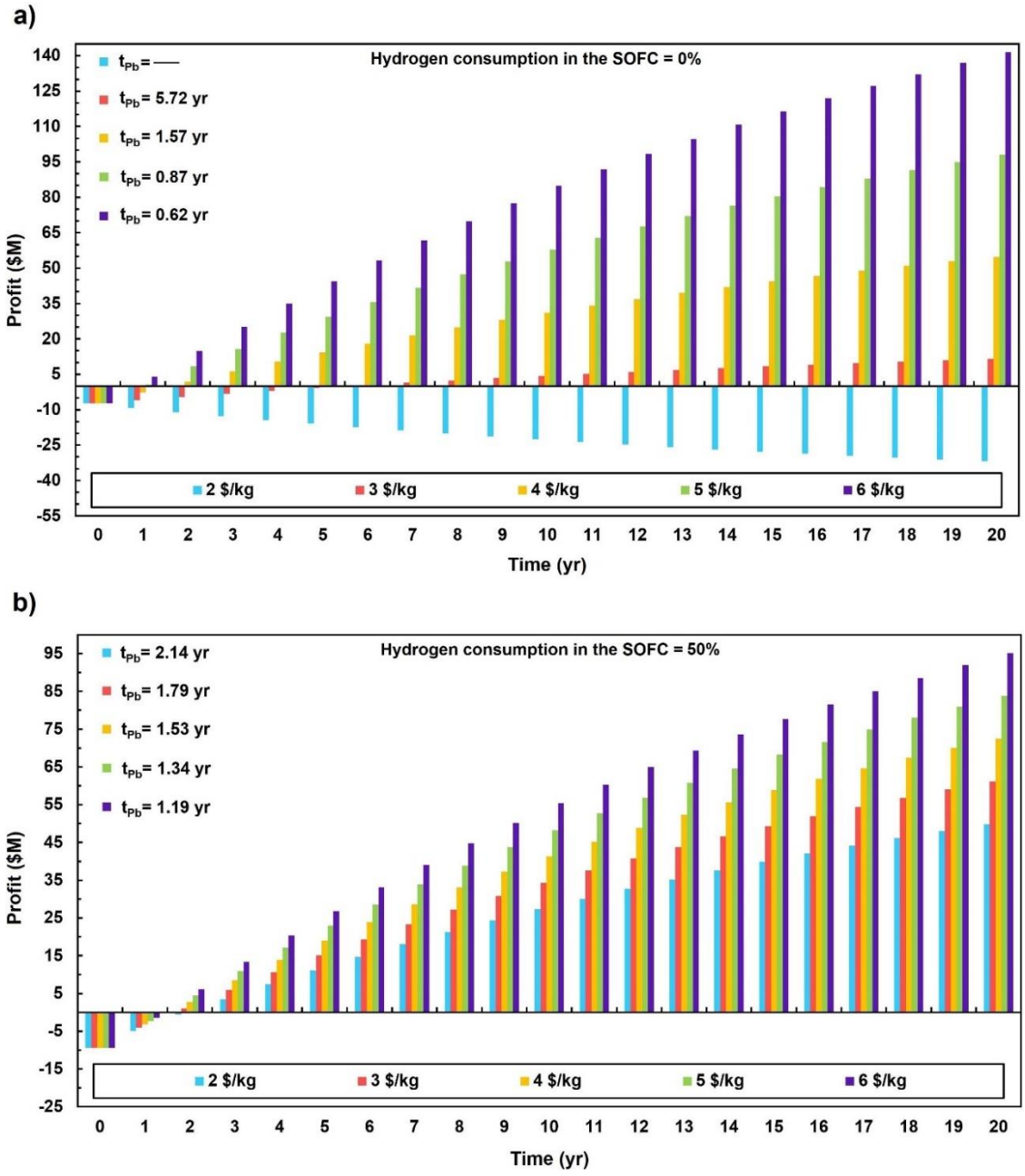

Figure 3.14: System profit over time and payback period in different hydrogen sale prices of 2-6 $/kg at a) no hydrogen consumption b) 50% consumption of the produced hydrogen for peak shaving in the SOFC.

From these results, it can be concluded that, for now, hydrogen storage can be a promising solution since the production cost of green hydrogen is not yet competitive with alternative technologies. However, the situation may change in the future by reducing renewable energy and, consequently hydrogen production costs. It is also essential to note that more profit can be attained either through hydrogen storage with lower hydrogen prices or hydrogen sales at hydrogen prices.

The durations of charging and discharging periods are the other significant parameters for economic analyses, as depicted in Figure 3.15. The lower the discharge time, the higher the capital and maintenance costs, because bigger components are needed to generate more power, while utilizing a constant value of the supplied hydrogen and molten salt heat. On the other hand, the average electricity sale price is higher for shorter durations, according to Table 3.6. Hence, it is important to find a balance between higher electricity sale prices and capital costs. As shown in Figure 3.15, increasing the discharge time from 2 to 5 hrs reduces the payback period from 3.35 to 2.14 years. However, considering a major reduction in average electricity sale price at longer discharge durations, the payback period goes to a higher value of 2.25 at a discharge duration of 6 hrs. Therefore, based on the case study of Los Angeles, the optimal values for charge and discharge periods are 19 and 5 hrs, respectively.

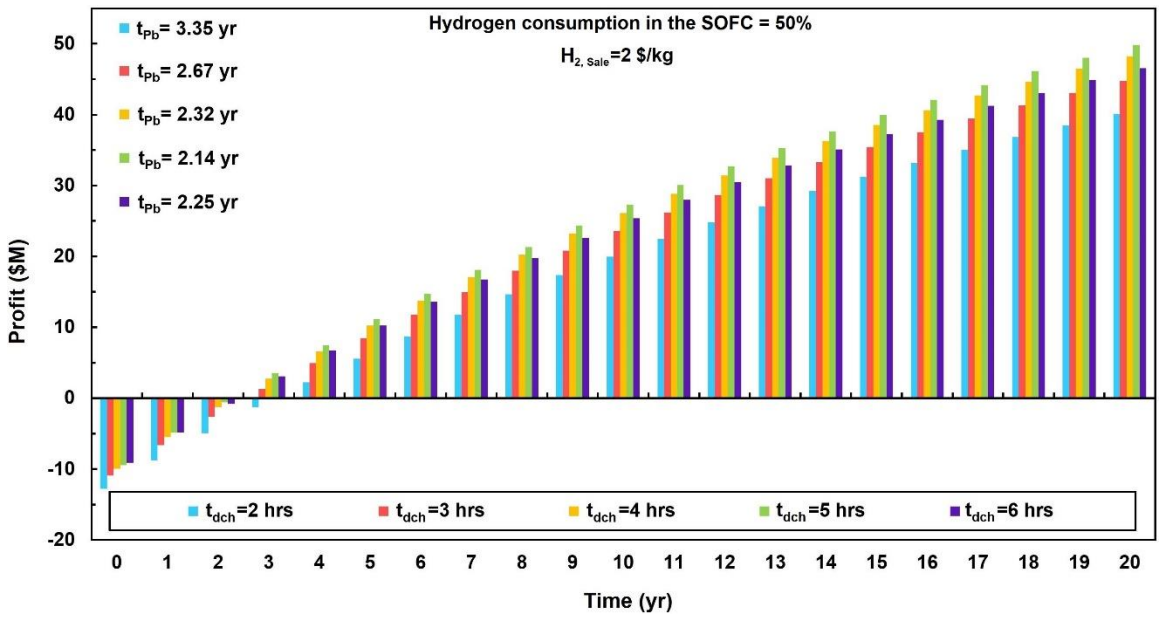

Figure 3.15: System profit over time and payback period in different discharge times based on 50% hydrogen consumption in the SOFC and hydrogen sale price of 2 $/kg.

3.5 Summary of chapter

In this chapter, a novel hybrid system was proposed to integrate reversible solid oxide cells (SOEC and SOFC) with a heliostat solar unit. The primary objective of this study was to improve the economic viability of green hydrogen production through the implementation of efficient high-temperature units and the utilization of hydrogen storage potential. In addition, the proposed system can be a promising solution for peak shaving and grid balancing with near-zero carbon intensity. The developed models for various units of the proposed system were separately validated using relevant experimental data in the literature. Thereafter, the system was analyzed comprehensively using energy, exergy, and economic methods. Finally, a case study was conducted using hourly electricity price and solar direct normal irradiance (DNI) to evaluate the hydrogen production rate, payback period, and system profitability. The major achievements of the present study are summarized as follows:

- The proposed system, which has a capital cost of $10.4 million, is capable of operating with a round-trip efficiency of 74.2% in its reversible solid oxide mode, where both the SOEC and SOFC operate at identical capacities. In this mode, 7.76 ton/day of hydrogen can be produced in the SOEC unit, of which 2.55 ton/day is utilized for 54.3 MWh power generation during peak demand periods, and the rest is sold to hydrogen markets.

- The economic analysis highlighted the significance of incorporating hydrogen storage to enhance the viability of green hydrogen production, particularly when it is not economically competitive with alternative hydrogen production technologies (e.g., steam methane reforming with a production cost of less than 1.5 $/kg H_2). However, the storage of produced hydrogen and its utilization for power generation yields an excellent payback period of less than 2 years in cities with a high electricity prices during peak demand periods like Los Angeles.

- The critical factors for designing an economical hydrogen storage plan include: i) the proportion of the utilized hydrogen for power generation in the SOFC to the total produced hydrogen in the SOEC, ii) solar DNI, iii) hydrogen cost, iv) hourly electricity price, and v) the duration of peak times.

- The results for the case study of Los Angeles revealed that over three times more hydrogen could be produced in summer (834 ton), when the electricity price is at its peak, compared to winter (254 ton). Consequently, there was no need for costly seasonal hydrogen storage in this case study.

- The results of the exergy analysis and Sankey diagram indicated that the high-temperature units, including the solar, SOEC, and SOFC are the sources of the highest

rates of irreversibility and exergy destruction in the hybrid system. Therefore, improvement and optimization of these units can result in higher overall efficiencies and lower waste heat production.

3.6 Uncertainty consideration

In this analysis, key economic parameters, including capital investment, operating and maintenance costs, and interest rates, were considered in line with common practices in the literature. However, more detailed cost elements, such as those related to engineering, installation, insurance, and other ancillary expenses, have been excluded from the scope of this study. These exclusions introduce a degree of uncertainty to the presented calculations, as they represent potential costs that could significantly influence the overall economic performance.

In addition, the current temperature range of commercialized heliostat fields utilizing molten salt is limited to approximately 700°C due to corrosion issues at higher temperatures. This limitation represents a technical constraint that affects both the capital and operational costs of such systems. As the objective of the present work is to highlight the golden opportunities for advancing the temperature capabilities of molten salt-based heliostat systems, the findings aim to motivate further research and development in development of higher temperature heliostat solar thermal fields. Future analyses should therefore seek to address these uncertainties by incorporating a more comprehensive set of cost factors, including those related to higher temperature materials and corrosion-resistant technologies, supported by up-to-date and reliable cost functions as they become available. Such refinements would enhance the robustness and reliability of the economic analysis, aligning it more closely with real-world conditions and paving the way for more cost-effective and technically advanced solutions in the future.

Chapter 4: Design and Techno-Economic Analysis of a Novel Solar-Based Methane Pyrolysis in Molten Salt System[1]

Methane pyrolysis has emerged as a promising low-carbon hydrogen production method, serving as a bridge from conventional fossil fuels to renewable energy sources. A recent technique for sustainable hydrogen production involves the process of methane pyrolysis in molten salt. To better understand the potential of sustainable turquoise hydrogen production, this chapter presents a techno-economic assessment of methane pyrolysis in molten salt combined with a high-temperature heliostat solar thermal field. In addition, a high-temperature thermal energy storage (HTES) unit is utilized to ensure uninterrupted hydrogen production during periods of solar unavailability, thereby contributing to the economic viability of the overall system. The proposed system can produce 9 tons of H_2/day and 27 tons of solid carbon/day with a round-trip efficiency of 49.8% and a levelized cost of hydrogen (LCOH) of 1.93 $/kg. To further decarbonize the process, the feasibility of utilizing renewable energies as the source of electricity for the HTES was analyzed, yielding a synergistic achievement of clean and economic hydrogen production. This configuration resulted in a LCOH of 1.28 $/kg, after including the United States (US) hydrogen incentives. The proposed system shows the potential to achieve the US Department of Energy target of 1 $/kg of hydrogen with a 20% reduction in the cost of renewable energy infrastructure.

[1] This chapter is based on [4].

4.1 System description

The graphical illustration of the proposed innovative concept for turquoise hydrogen production, incorporating molten salt bubble column reactor, heliostat solar field, and HTES, is shown in Figure 4.1.

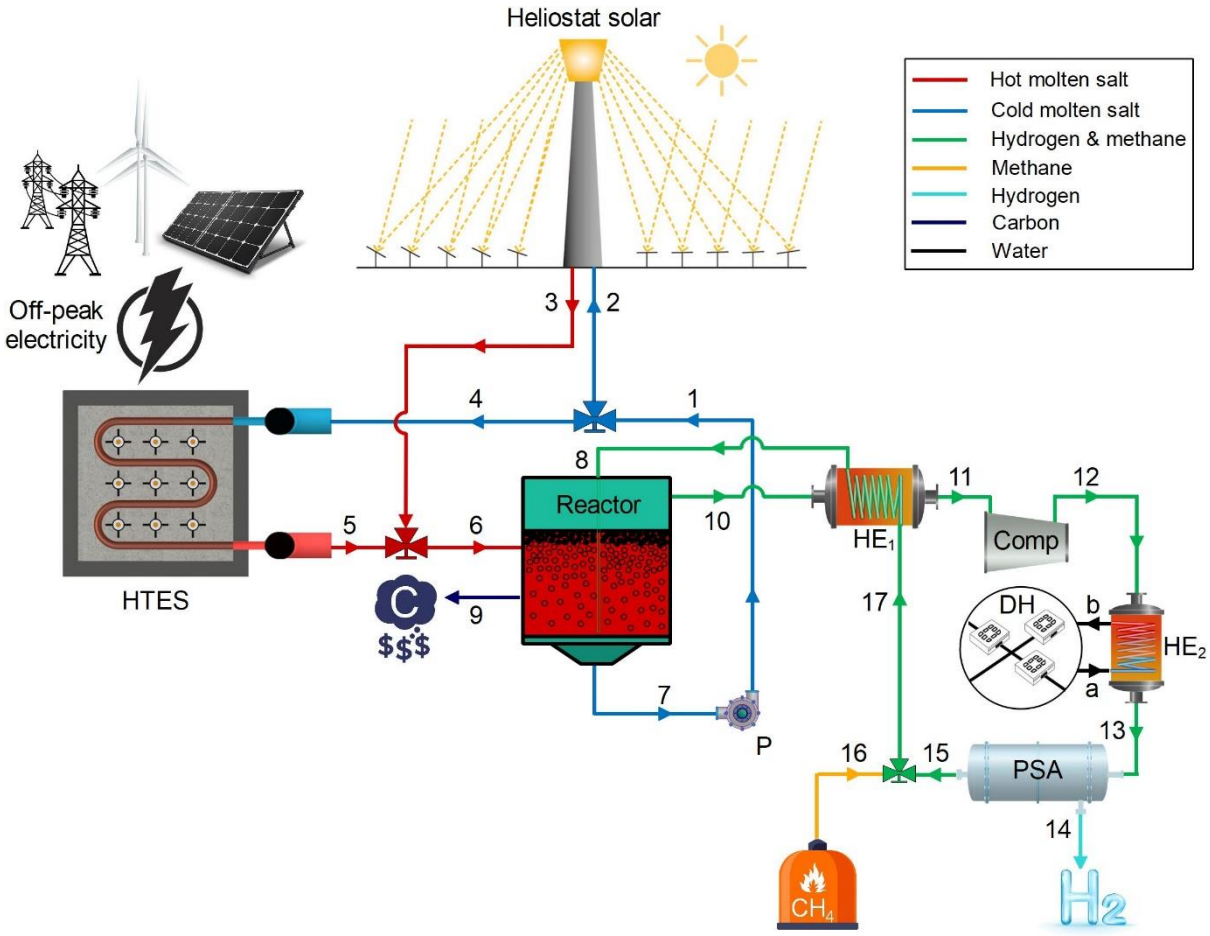

Figure 4.1: Graphical illustration of the proposed innovative concept for turquoise hydrogen production based on molten salt bubble column reactor, heliostat solar field, and HTES. HE: Heat exchange, Comp: Compressor, HTES: High-temperature thermal energy storage, P: Pump, PSA: Pressure swing adsorption.

During periods of sunlight exposure, solar energy harnessed by the heliostat tower's receiver is directed towards the incoming molten salt (stream 2). The resultant heated molten salt (stream 3) is conveyed to the bubble column reactor (stream 6), where it facilitates the decomposition of methane into hydrogen and solid carbon. Concurrently, the preheated methane, containing some

unseparated hydrogen, is introduced into the reactor after passing through the heat exchanger 1 (HE_1), including streams 17 to 8. Acting as a catalyst within the reactor, molten salt aids in the decomposition of methane into carbon and hydrogen (streams 9 and 10). The lower density of the generated carbon, compared to molten salt, enables straightforward separation from the salt surface. The produced hydrogen and unreacted methane (stream 10) pass through HE_1 to increase the inlet methane temperature for the reactor and decrease compressor power consumption at reduced inlet temperature. Recognizing that the compression process entails heat generation, a district heating (DH) unit is designed to capture waste heat, providing the desired flow temperature for the pressure swing adsorption (PSA) process. Utilizing a solid adsorbent like activated carbon or zeolite, PSA alternates between pressurization and depressurization cycles. During pressurization, the adsorbent selectively captures hydrogen molecules, enabling methane to pass through (stream 15). Subsequently, during depressurization, the captured hydrogen is released from the adsorbent (stream 14). The unreacted methane is blended with external methane (stream 16), heated in HE_1, and cycled back into the reactor to ensure a continuous process.

The HTES, constructed with refractory concrete and effectively insulated using ceramic materials to mitigate heat dissipation, has been specifically configured for charging during periods of excess low-cost grid electricity or RE availability, particularly during off-peak hours. Embedded within the molten salt channels, a series of nickel-chromium (NiCr) resistive wires with high thermal conductivity serves to transform electrical energy into thermal energy. When solar energy is not available, the molten salt undergoes heating as it passes through the HTES (streams 4 to 5) to provide the desired conditions for methane pyrolysis in the reactor. The subsequent phases of the cycle mirror those observed during solar availability.

4.2 Mathematical modelling

In this section, a comprehensive description of the governing equations pertaining the techno-economic analysis of the proposed system is provided. The input values and assumptions for modelling various components are listed in Table 4.1:

Table 4.1: Input values and assumptions for modeling of various components and cycles.

Subsystem	Parameter	Value	Unit
Heliostat solar [191,219,220,254]	Concentration ratio	1000	-
	Direct normal irradiance	600	W/m^2
	Emissivity coefficient	0.8	-
	Inlet diameter of the receiver tube	3.75	cm
	Number of the heliostat	150	-
	Outlet diameter of the receiver tube	4	cm
	Reflectivity coefficient of the receiver surface	0.04	-
	Solar time period per day	8	hrs
	Surface area of the mirrors	121	m^2
	Temperature of the cold molten salt	900	℃
	Temperature of the hot molten salt	1200	℃
	Temperature of the sun	5504.85	℃
	Thermal conductivity of the receiver tube	24.5	W/m.K
	Thermal conductivity of the tube-insulation	0.03	W/m.K
	Thickness of the tube-insulation	10	cm
	View factor	0.8	-
	Wind speed	5	m/s
HTES [207,255,256]	Electrical efficiency	90	%
	Minimum temperature of HTES	800	℃
	Maximum temperature of HTES	1300	℃
	Specific heat capacity of the HTES	0.88	kJ/kg.K
	Temperature of the cold molten salt	900	℃
	Temperature of the hot molten salt	1200	℃
Methane pyrolysis [136,139,141,257]	Compressor pressure ratio	7	-
	Density of methane	0.657	kg/m^3
	Density of molten salt ($MnCl_2$-KCl)	1880	kg/m^3
	Dynamic viscosity of molten salt ($MnCl_2$-KCl)	0.0006	kg/ms
	Feeder inner diameter	28×10^{-4}	m
	Hydrogen selectivity	90	%
	Immersed height of the column	2	m
	PSA efficiency	90	%
	Reactor temperature	1050	℃
	Surface tension of molten salt ($MnCl_2$-KCl)	0.063	N/m
General [136,139,141]	Acceleration due to gravity	9.8	m/s^2
	Annual operating and maintenance costs	6	% of CAPEX
	Ambient pressure	1.01	bar
	Ambient temperature	20	℃
	Average off-peak electricity price	3	¢/kWh

Average daily electricity price	15	¢/kWh
Carbon sale price	300	$/ton
District heating inlet temperature	20	°C
District heating outlet temperature	70	°C
Interest rate	6	%
Methane purchase price	6	$/GJ
Molten salt lifetime	1	year
Molten salt price	10	$/kg
Pinch point temperature difference	20	°C
Stephan-Boltzmann constant	5.67×10^{-8}	$W/m^2.K^4$
System lifespan	20	yrs
Universal gas constant	8.314	J/mol.K

4.2.1 System modelling

The initial phase of the techno-economic analysis involves the systematic modelling of individual units. Consequently, this process entails the formulation of governing equations to represent distinct sections within the proposed system, which are presented in the subsequent sections. The optimum sizing of each system component in Figure 4.1 is calculated based on the design conditions specified in Table 4.1 and the governing equations listed below.

4.2.1.1 Heliostat solar unit

The heliostat solar unit consists of the heliostat field, tower, and cavity receiver. The calculation of the solar energy ($\dot{Q}_{Sun}$) received by the heliostat field can be determined using the following equation [231]:

$$\dot{Q}_{Sun} = I_{Sun} \cdot A_{Hel} \cdot N_{Hel} \tag{4.1}$$

where N_{Hel}, A_{Hel}, I_{Sun} show the quantity of mirrors within the heliostat field, the surface area of every mirror, and the direct normal irradiance (DNI) level. The efficiency of the heliostat, determining the amount of which solar energy is redirected to the cavity receiver, is computed through the following calculation [232]:

$$\eta_{Hel} = \frac{\dot{Q}_{Rec}}{\dot{Q}_{Sun}} \tag{4.2}$$

here, η_{Hel} represents the heliostat optical efficiency. In addition, $\dot{Q}_{Rec}$ denotes the redirected solar energy into the receiver, a fraction of which is dissipated through conduction, convection, radiation, and reflection. The residual energy can be absorbed by molten salt flowing over the receiver. The energy equilibrium within the receiver is determined through the following equations [233,258]:

$$\dot{Q}_{Rec} = \dot{Q}_{Abs} + \dot{Q}_{Loss,Rec} \tag{4.3}$$

$$\dot{Q}_{Loss,Rec} = \dot{Q}_{Cd} + \dot{Q}_{Cv} + \dot{Q}_{Rad} + \dot{Q}_{Ref} \tag{4.4}$$

where, $\dot{Q}_{Abs}$ represents the heat absorbed in the receiver, and $\dot{Q}_{Loss,Rec}$ denotes the heat lost in the receiver. Furthermore, the subscripts *Cd*, *Cv*, *Rad*, and *Ref* respectively signify conduction, convection, radiation, and reflection.

The energy equilibrium within the receiver could be determined by considering the average temperatures of the receiver surface $\left(T_{Rec,sur}\right)$ and the molten salt $\left(T_{MS}\right)$ inside the receiver tube [220]. The convective heat transfer coefficient of molten salt is computed using the Dittus–Boelter equation [8,234].

$$\dot{q}_{Rec} = \frac{\dot{Q}_{Rec}}{A_{Rec,sur}} = \frac{\left(T_{Rec,sur} - T_{MS}\right)}{\left(\frac{d_O}{d_i \cdot h_{c_{MS}}}\right) + \left(\frac{d_O}{d_i \cdot K_{Rec,tube}} \ln \frac{d_O}{d_i}\right)} \tag{4.5}$$

$$Nu_{MS} = \frac{h_{c_{MS}} \cdot d_i}{K_{MS}} = 0.023 \cdot \mathrm{Re}_{MS}^{0.8} \cdot \mathrm{Pr}_{MS}^{0.4} \tag{4.6}$$

$$\mathrm{Re}_{MS} = \frac{4 \cdot \dot{m}_{MS}}{\pi . N_{Rec,tube} . d_i . \mu_{MS}} \tag{4.7}$$

$$\mathrm{Pr}_{MS} = \frac{\mu_{MS} \cdot C_{P_{MS}}}{K_{MS}} \tag{4.8}$$

$$T_{MS} = \frac{T_{HMS} + T_{CMS}}{2} \tag{4.9}$$

where, d_i and d_o represent the inlet and outlet diameters of the receiver tube, K denotes thermal conductivity, h_c signifies the convective heat transfer coefficient, and μ stands for dynamic viscosity. Additionally, *Nu*, *Re*, and *Pr* respectively denote the Nusselt, Reynolds, and Prandtl numbers. The subscripts *MS*, *HMS*, and *CMS* represent molten salt, hot molten salt, and cold molten salt, respectively.

The concentration ratio (C) and view factor (Fr) are used for calculating the necessary surface ($A_{Rec,sur}$) and aperture area ($A_{Rec,ap}$) of the receiver, as well as the quantity of heliostats required. It is assumed that the width of the receiver aperture (W) is half of its height (H) [220].

$$Fr = \frac{A_{Rec,ap}}{A_{Rec,sur}} \tag{4.10}$$

$$A_{Rec,ap} = H \cdot W = \frac{H^2}{2} \tag{4.11}$$

$$C = \frac{A_{Field}}{A_{Rec,ap}} = \frac{A_{Hel} \cdot N_{Hel}}{A_{Rec,ap}} \tag{4.12}$$

Another crucial factor to be computed involves the radiation heat loss occurring among the receiver surface and its surroundings [233]:

$$\dot{Q}_{Rad} = \left(\frac{\varepsilon_W \cdot \sigma \cdot A_{Rec,sur} \cdot \left(T_{Rec,sur}^4 - T_{Amb}^4 \right)}{\left(\frac{\varepsilon_W}{Fr} \right) + \left(1 - \varepsilon_W \right)} \right) \tag{4.13}$$

here σ denotes Stefan–Boltzmann constant and ε_W represents the absorptivity coefficient of the receiver surface. Additionally, the reflection of incident rays escaping from the aperture constitutes another factor contributing to heat dissipation in the receiver, and this can be quantified through the following calculation [235]:

$$\dot{Q}_{Ref} = \alpha \cdot \dot{Q}_{Rec} \cdot Fr \tag{4.14}$$

The convective heat loss within the receiver is influenced by both natural and forced convection, calculated by the following equations [220]:

$$\dot{Q}_{Cv} = \dot{Q}_{N,Cv} + \dot{Q}_{F,Cv} \tag{4.15}$$

$$\dot{Q}_{N,Cv} = 0.81 \cdot A_{Rec,sur} \cdot \left(T_{Rec,sur} - T_{Amb} \right)^{1.426} \tag{4.16}$$

$$\dot{Q}_{F,Cv} = hc_{F,Cv} \cdot A_{Rec,ap} \cdot \left(T_{Rec,sur} - T_{Amb} \right) \tag{4.17}$$

$$Nu_{F,Cv} = \frac{hc_{F,Cv} \cdot H}{K_{Air}} = 0.0287 \cdot \mathrm{Re}_{F,Cv}^{0.8} \cdot \mathrm{Pr}_{Air}^{0.333} \tag{4.18}$$

$$\mathrm{Re}_{F,Cv} = \frac{\rho_{Air} \cdot V_{Wind} \cdot H}{\mu_{Air}} \tag{4.19}$$

$$\mathrm{Pr}_{Air} = \frac{\mu_{Air} \cdot C_{P_{Air}}}{K_{Air}} \tag{4.20}$$

where, V_{Wind} denotes the wind speed.

The least significant portion of heat loss within the receiver is attributed to conduction heat transfer, predominantly occurring in the insulated area and backing materials. Given the predominant role of heat dissipation in the insulated area, conductive heat loss can be quantified by [220]:

$$\dot{Q}_{Cd} = \frac{K_{Ins} \cdot A_{Rec,sur}}{\delta_{Ins}} \cdot \left(T_{Rec,sur} - T_{Ins}\right) = hc_{Mix} \cdot A_{Rec,sur} \cdot \left(T_{Ins} - T_{Amb}\right) \tag{4.21}$$

$$hc_{Mix} = hc_{Air,fc} + hc_{Air,nc} \tag{4.22}$$

$$hc_{Air,nc} = 1.24 \cdot \left(T_{Ins} - T_{Amb}\right)^{0.333} \tag{4.23}$$

$$Nu_{Air,fc} = \frac{hc_{Air,fc} \cdot H}{K_{Air}} = 0.02657 \cdot \mathrm{Re}_{Air,fc}^{0.805} \cdot \mathrm{Pr}_{Air}^{0.45} \cdot \left(\frac{T_{Ins}}{T_{Amb}}\right)^{0.2} \tag{4.24}$$

It is worth mentioning that the operating fluid employed in the solar-based pyrolysis design is $MnCl_2$-KCl molten salt, with a molar ratio of 50% $MnCl_2$, and 50% KCl. This choice was based on its proven effectiveness in facilitating methane pyrolysis in molten salt, as documented in prior research by Kang et al. [136]. The calculation of the thermal energy which can be absorbed by $MnCl_2$-KCl molten salt in the solar receiver is outlined in accordance with the following equation [237]:

$$\frac{\dot{Q}_{Abs}}{1000} = \dot{m}_2 \cdot \left(h_3 - h_2\right) \tag{4.25}$$

4.2.1.2 High-temperature thermal energy storage

The HTES unit has been specifically designed to fulfil the thermal demands of methane pyrolysis in periods of solar unavailability. During off-peak times, the HTES thermal elements utilize surplus low-cost electricity to elevate the temperature of refractory concrete, facilitating the subsequent economic heat utilization. This process involves the conversion of electrical energy into heat, as described by the following equation [11]:

$$Q_{HTES} = \int \dot{W}_{HTES} . \eta_{HTES} \, dt \tag{4.26}$$

where, η_{HTES} denotes the conversion efficiency of electricity to heat within the HTES unit. The accumulated thermal energy can be employed to heat the molten salt for methane pyrolysis during times that solar is not available [259]:

$$Q_{HTES} = \dot{m}_4 (h_5 - h_4) . t_{HTES} \tag{4.27}$$

where, t_{HTES} represents the cumulative daily intervals of solar unavailability, during which the HTES heat is employed for methane pyrolysis.

In addition, the concrete mass of the HTES unit can be calculated as follows [255,256]:

$$M_{HTES} = \frac{Q_{HTES}}{C_{HTES} \left(T_{\max,HTES} - T_{min,HTES} \right)} \tag{4.28}$$

where, C_{HTES} represents the heat capacity of the HTES.

4.2.1.3 Methane pyrolysis in molten salt

Methane pyrolysis in molten salt involves the utilization of high-temperature molten salt as a

medium to facilitate the thermal decomposition of methane (CH_4) into its constituent components, and hydrogen (H_2) solid carbon (C), in the absence of oxygen [260]:

$$CH_4(g) \rightarrow C(s) + 2H_2(g) \qquad \Delta H_{298} = 74.85\ kJ/mol \tag{4.29}$$

The molten salt serves as both a heat exchange fluid and a reactive catalyst, contributing to the dissociation of methane into its components. The MCR in pyrolysis within a molten salt holds paramount importance in determining the efficiency and economic feasibility of the process. In the proposed chemical reaction, the duration that chemical components remain within the reaction medium, known as residence time, plays a crucial role in influencing the MCR. Consequently, it is imperative to calculate the residence time for a comprehensive analysis. When dealing with molten salt, an initial step involves determining the bubble diameter for subsequent calculation of its rising velocity. The bubble diameter is primarily contingent on the inner radius of the feeder and certain physical attributes of the liquid phase, and its estimation can be facilitated through the application of Tate's law [150]:

$$D_b = \left(\frac{6D_0.\sigma}{(\rho_l - \rho_g).g} \right)^{1/3} \tag{4.30}$$

where, D_0 is the feeder inner diameter, σ is the surface tension of the molten salt, g is the acceleration due to gravity, ρ_l is the density of the liquid molten salt, and ρ_g is the density of methane.

The determination of rise velocity of bubbles is another important parameter. An empirical equation is employed for the precise calculation of the rise velocity of bubbles within a gas-liquid system [140,257]:

$$v_b = 0.2969(100\,D_b)^{0.316} \tag{4.31}$$

Then, the residence time can be calculated based on the following equation [257,261]:

$$\tau = \frac{H_{im}}{v_b} \tag{4.32}$$

where, H_{im} is the immersed height of the molten salt column. Given that the reactor employed in this study features a singular nozzle generating sequential bubbles, the calculations of residence time intentionally excluded considerations for bubble coalescence.

As the bubbles rise within the molten salt column, two concurrent reactions take place. One involves uncatalyzed gas-phase pyrolysis within the bubble, while the other entails catalyzed reactions at the gas-liquid interface. For the sake of simplification, it is assumed that the pyrolysis in the molten salt column is predominantly first-order with respect to methane concentration [257]:

$$-r_{CH_4} = k_r C_{CH_4} \tag{4.33}$$

where, r_{CH_4}, k_r, C_{CH_4} are respectively the rate of reaction, reaction rate constant, and the immediate concentration of methane in the gas mixture.

The utilization of the performance equation for a first-order reaction in a plug flow reactor with variable densities is applicable in this context, given the gas-phase nature of the reaction and the consequential alteration in the number of moles due to stoichiometry. The implemented performance equation is as follows [257]:

$$k_r \tau = \left(1+\varepsilon_{CH_4}\right)\ln\frac{1}{1-0.01MCR} - \frac{\varepsilon_{CH_4} MCR}{100} \tag{4.34}$$

here, *MCR* is the methane conversion rate and ε_{CH_4} signifies the fractional alteration in gas volume ranging from zero to complete conversion of the reactant, arising from the production of two moles of hydrogen through the pyrolysis of one mole of methane. The following equation can be also implemented for better understanding of the reactions in the proposed system [141]:

$$MCR = 1 - \frac{\dot{n}_{10,CH_4}}{\dot{n}_{8,CH_4}} \times 100 \tag{4.35}$$

where, $\dot{n}$ denotes the molar flow rate.

To establish optimal conditions for the separation of hydrogen and methane in the PSA, the outlet gas flow undergoes compression in a compressor. The consumed electricity ($\dot{W}_{Com}$) and efficiency of this compressor (η_{Com}) are expressed as follows:

$$\dot{W}_{Com} = \dot{m}_{11} \cdot \left(h_{12} - h_{11} \right) \tag{4.36}$$

$$\eta_{Com} = \frac{h_{12,s} - h_{11}}{h_{12} - h_{11}} \tag{4.37}$$

Providing the desired temperature and pressure conditions, the PSA enables the effective separation of hydrogen and methane as follows [31]:

$$\eta_{PSA} = \frac{\dot{n}_{14,H_2}}{\dot{n}_{13,H_2}} \times 100 \tag{4.38}$$

where, η_{PSA} shows the efficiency of the PSA for the separation of hydrogen and methane.

4.2.2 Economic analysis

In the present research, the net present value (NPV) is employed as a financial methodology for conducting economic analysis. This method is instrumental in scrutinizing the economic feasibility of the proposed system, as it systematically evaluates the profitability of the system. This involves computation of the present value of the anticipated cash flows (both inputs and outputs) during the system lifespan, subsequently adjusted to their present worth through the application of a predetermined rate of return. The NPV is representative of the discrepancy among the present values of the anticipated cash inputs and outputs. Various parameters, such as the market prices for hydrogen, carbon, and hot water, as well as the acquisition costs of methane and electricity, exert a direct influence on the monetary inflow and outflow within the cash flow valuation. A positive NPV serves as an indicator of the project's or investment's profitability, indicating the potential generation of value for investors. Conversely, a negative NPV denotes the lack of financial viability in the project or investment. The net cash flow at the conclusion of each year is subjected to discounting to its present value, depending on the prevailing interest rate, exposed as follows [247]:

$$NPV = \sum_{N=0}^{20} Y_N (1+i)^{-1} \tag{4.39}$$

herein, the variables N and i represent the system's lifespan and interest rate, respectively, while Y_N denotes the net cash flow at the culmination of the N^{th} year.

According to Table 4.1, the analysis incorporates an interest rate of 6% and an economic lifespan of 20 years. Furthermore, it is assumed that the operational and maintenance expenses for the components amount to 6% of their corresponding capital costs. In the context of the current

investigation, with the base year set as 2022, the chemical engineering plant cost index (CEPCI) serves as the metric for adjusting the investment cost rate of each component from its original baseline year to the year 2022, as expressed by the following equation:

$$Z_k = Z_{k,ref} \times \frac{CEPCI_{2022}}{CEPCI_{ref}} \tag{4.40}$$

It is noted that the CEPCI for the year 2022 is recorded as 816 [262]. The capital cost equation for each component in its reference year is outlined in Table 4.2.

Table 4.2: Capital cost equation of each component in its reference year [31,210,255,256,263]. CEPCI: chemical engineering plant cost index.

Component	Capital investment cost (US$)	Reference year	CEPCI
Compressor	$Z_{Com} = 91562\left(\frac{\dot{W}_{Com}}{455}\right)^{0.67}$	2003	402
Heat exchangers	$Z_{HE} = 130 \cdot (\frac{A_{HE}}{0.093})^{0.78} \quad A_{HE} = \frac{Q_{HE}}{U_{HE}.LMTD_{HE}}$	2005	486.2
Heliostat land	$Z_{Land} = 8.9 \cdot A_{HEL} \cdot N_{HEL}$	2008	575.4
Heliostat mirrors	$Z_{Hel} = 150 \cdot A_{HEL} \cdot N_{HEL}$	2008	575.4
HTES	$Z_{HTES} = 2.2M_{HTES}$	2018	603.1
PSA	$Z_{PSA} = 30800000 \times \left(\frac{3600\dot{m}_{in}}{8474000}\right)^{0.7}$	2003	402
Pump	$Z_P = 2100 \cdot (\frac{\dot{W}_P}{10})^{0.26} \cdot (\frac{1-\eta_P}{\eta_P})^{0.5}$	2002	395.6
Reactor	$Z_{Reac} = 34400000 \times \left(\frac{3600\dot{m}_{in}}{52163}\right)^{0.7}$	2013	567.3
Receiver	$Z_{Rec} = A_{Rc,sur} \cdot \left(79 \cdot T_{Rc,sur} - 42000\right)$	2008	575.4

4.2.3 Performance and economic criteria

Ultimately, the performance metrics for system operation are presented in this section. Due to the diverse sources supplying the required heat for methane pyrolysis, encompassing both solar and

HTES during distinct periods, traditional efficiency metrics cannot be used for assessing the proposed system. In response to this challenge, the performance criteria for the solar-based methane pyrolysis are established in terms of round-trip efficiency (RTE) and exergy round-trip efficiency (ERTE), as delineated below:

$$RTE = \frac{Q_{DH} + m_{H_2} LHV_{H_2}}{m_{CH_4} LHV_{CH_4} + W_{Com} + Q_{Solar} + W_P + W_{HTES}} \times 100 \tag{4.41}$$

$$ERTE = \frac{Ex_{DH} + m_{H_2} LHV_{H_2}}{m_{CH_4} LHV_{CH_4} + W_{Com} + Ex_{Solar} + W_P + W_{HTES}} \times 100 \tag{4.42}$$

where, Q, W, m, LHV, and Ex stand for heat, power, mass, lower heating value, and exergy. In addition, the subscript *DH* represents district heating.

In addition, the primary economic metric in the present research is the LCOH, which is defined as the selling price of hydrogen necessary to equate the NPV in Eq. (4.39) to zero at the end of the economic lifespan of the proposed system.

4.3 Results and discussion

The modeling results of the novel design for methane pyrolysis in molten salt are presented and discussed in three sections, encompassing the model validation, modelling results, and parametric analysis.

4.3.1 Model validation

The proposed system represents a pioneering approach for methane pyrolysis in molten salt based on solar energy, a domain that has not been previously explored. Therefore, to ensure the robustness of the model, each unit within the system undergoes thorough validation using pertinent

data from existing literature. The design conditions and assumptions of the corresponding sources are employed for the validation of each unit. As outlined in Table 4.3, the models of the heliostat solar and the HTES units align with the findings reported by Kandezi et al. [254] and Nabat et al. [11]. In addition, Figure 4.2 shows the validation of the present model with the experimental data reported by Kang et al. [136]. The comparison presented in Table 4.3 and Figure 4.2 reveals minimal disparities between the results obtained from this model and the relevant literature data. This consistency highlights the validity of the models and the resultant data as dependable and reliable sources for further analysis and application in the field.

Table 4.3: Validation of the modelling results for different units with their corresponding papers in literature.

Unit	Parameter	This work	Literature	Error (%)
Heliostat solar [254]	Reflected solar energy into the receiver [kW]	40218	39208	2.57
	Absorbed heat by the receiver [kW]	21261	20559	3.41
	Receiver efficiency [%]	52.86	52.43	0.82
	Enthalpy of hot molten salt [kJ/kg]	687.6	687.6	0.00
	Molten salt flow rate [kg/s]	26.54	26.38	0.60
HTES [11]	Maximum temperature of the HTES [°C]	1327	1327	0.00
	Minimum temperature of the HTES [°C]	1027	1027	0.00
	Heat generation of the HTES [MWh]	39.3	39.1	0.51
	Power consumption of the HTES [MWh]	38.5	38.3	0.52

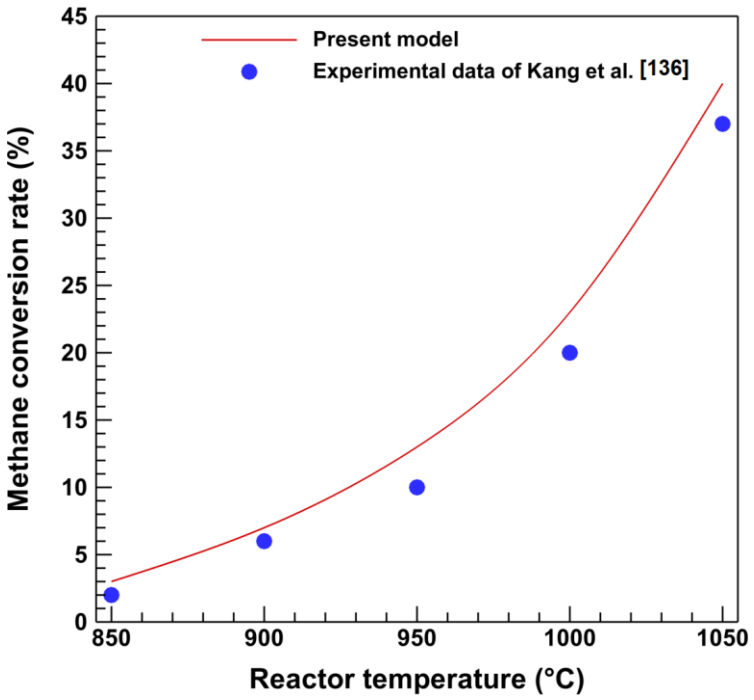

Figure 4.2: The validation of the present model for methane pyrolysis with the experimental data of Kang et al [136].

4.3.2 Modelling results

In this section, the modelling results from techno-economic analysis of the proposed novel design for methane pyrolysis are presented, utilizing the design values and assumptions mentioned in Table 4.1. To enhance clarity regarding the system operation, the fundamental thermodynamic properties and molar composition of streams are listed in Table 4.4.

Table 4.4: Thermodynamic properties and molar composition of each stream in Figure 4.1.

Stream	T (°C)	P (bar)	$\dot{m}$ (kg/s)	Molar fraction				
				$MnCl_2$-KCl	CH_4	H_2	C	H_2O
1	900	2	4.317	1				
2	900	2	4.317	1				
3	1200	1	4.317	1				
4	900	2	4.317	1				
5	1200	1	4.317	1				
6	1200	1	4.317	1				
7	900	1	4.317	1				
8	943	12.6	1.062		0.918	0.082		
9	1050	1	0.315				1	
10	1050	2.7	0.747		0.403	0.597		
11	63	2.3	0.747		0.403	0.597		
12	403	16.1	0.747		0.403	0.597		
13	57	14	0.747		0.403	0.597		

14	57	14	0.105		1		
15	57	14	0.642	0.871	0.129		
16	20	14	0.420	1			
17	42	14	1.062	0.918	0.082		
a	20	1	2.115			1	
b	70	1	2.115			1	

A summary of key calculated parameters for the proposed cycle (Figure 4.1) is presented in Table 4.5. The proposed novel design absorbs 11.97 MWh/day of solar energy for methane pyrolysis during solar energy availability. To enhance economic viability through continuous operation of pyrolysis during solar unavailability, a HTES unit is incorporated. The HTES unit utilizes 26.59 MWh/day of off-peak low-cost electricity for heat generation, maintaining the molten salt temperature required for methane pyrolysis during periods of solar unavailability. Consequently, the process yields 9.08 tons/day of hydrogen and 27.24 tons/day carbon, through the consumption of 36.32 tons/day of methane. Calculations reveal an RTE of 49.82% and ERTE of 48.72%, culminating in a competitive LCOH of 1.93 $/kg.

Table 4.5: Overview of key calculated parameters for the proposed cycle (Figure 4.1).

Parameter	Unit	Value
$ERTE$	%	48.72
D_b	mm	4.08
τ	s	8.49
$LCOH$	$/kg	1.93
$\dot{m}_C$	ton/day	27.24
$\dot{m}_{CH_4}$	ton/day	36.32
$\dot{m}_{H_2}$	ton/day	9.08
MCR	%	40.2
M_{HTES}	ton	326
RTE	%	49.82
$\dot{Q}_{Abs}$	MWh/day	11.97
$\dot{Q}_{Cd}$	kWh/day	70.87
$\dot{Q}_{Cv}$	MWh/day	4.39
$\dot{Q}_{DH}$	MWh/day	10.62
$\dot{Q}_{HE_1}$	MWh/day	100.17

$\dot{Q}_{Rad}$	MWh/day	46.82
$\dot{Q}_{Ref}$	MWh/day	2.09
$\dot{Q}_{Sun}$	MWh/day	87.12
v_b	m/s	0.221
$\dot{W}_{Com}$	MWh/day	10.13
$\dot{W}_{HTES}$	MWh/day	26.59
$\dot{W}_P$	kWh/day	5.52

A comprehensive energy Sankey diagram of the proposed system is presented in Figure 4.3 to provide a better understanding of system operation (units are in Megawatts hour, MWh). Figure 4.3 (a) shows the operation of the system during the day and solar availability. It is noteworthy that a substantial volume of methane and hydrogen mixture is circulated within the cycle, as denoted by the green arrows, correlating with a modest MCR of 40%. Consequently, a higher MCR would correspond to a reduction in the magnitude of green arrows. Figure 4.3 (b) presents the operation of the system during night-time periods when solar energy is unavailable, facilitated by the employment of the HTES unit. Given a daily solar availability of 8 hours (Table 4.1), the system is required to operate for 16 hours at full capacity in the absence of solar input, resulting in a doubling of inputs and hydrogen production during this timeframe.

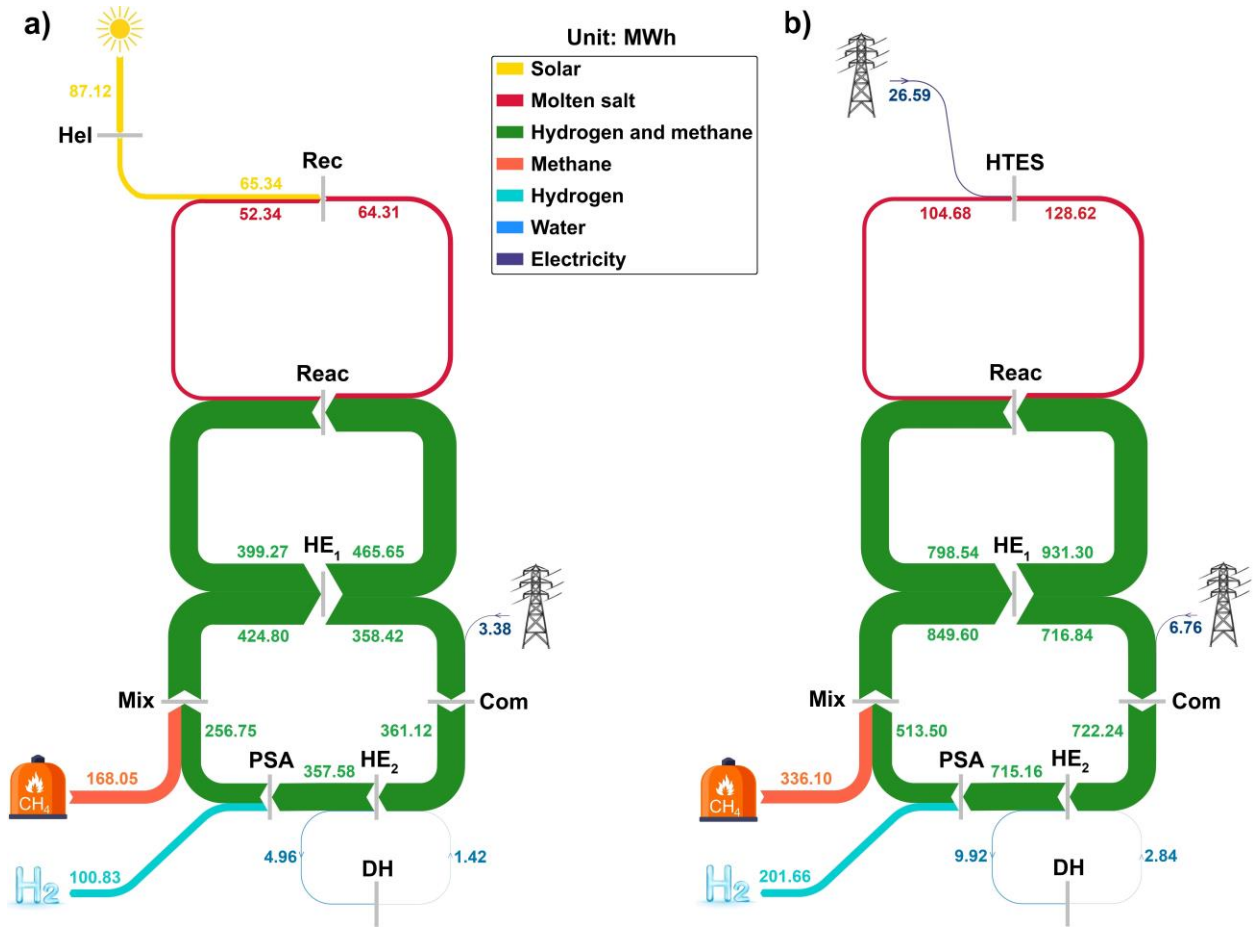

Figure 4.3:. Energy Sankey diagram of the proposed system during a) day and b) night. Com: Compressor, DH: District Heating, HE: Heat exchanger, Hel: Heliostat field, HTES: High-temperature thermal energy storage, Mix: Mixer, PSA: Pressure swing adsorption, Reac: Reactor, Rec: Receiver,

In complicated energy systems, the consideration of capital costs of various units and their respective components holds significant importance. Precise estimation and comprehensive representation of these costs play a pivotal role in enabling decision-makers to assess and choose the most suitable design for their specific application. To address this imperative, the capital expenditure (CAPEX) associated with diverse units within the proposed system, along with their proportional contributions to the overall capital expenditure, are graphically presented in Figure 4.4. This visual representation serves as a valuable tool for stakeholders in gaining insights into the financial implications of each unit, facilitating informed decision-making towards the optimal configuration.

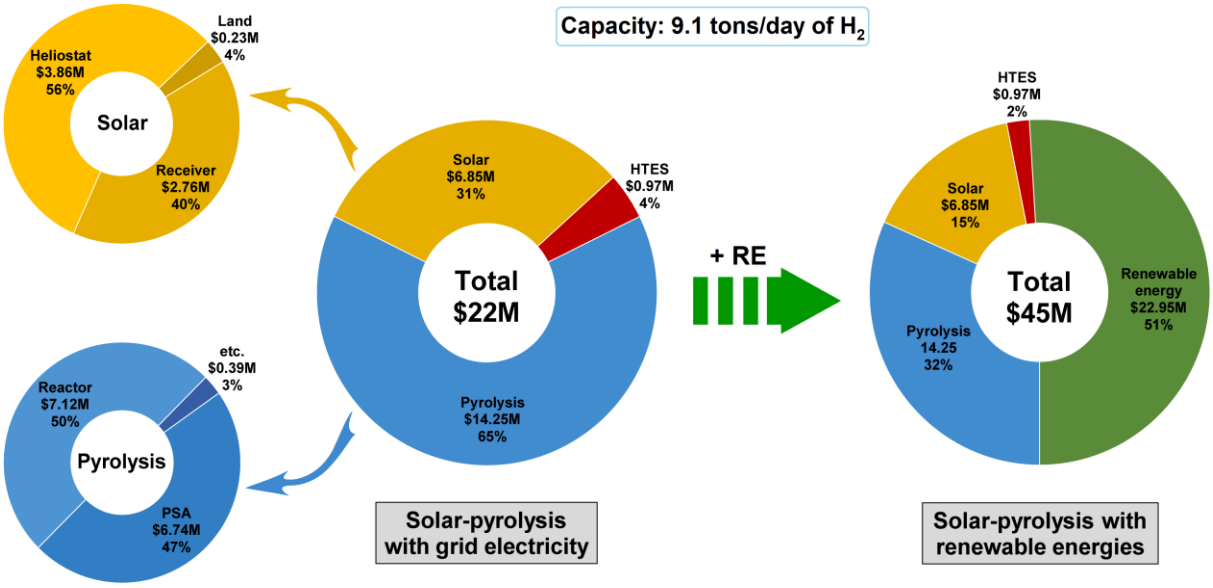

Figure 4.4: Capital costs of various elements and units and their impact on CAPEX with the grid electricity and renewable energy (RE) electricity sources.

4.3.3 Parametric analysis

A comprehensive parametric analysis is conducted in this section to evaluate the influence of critical factors on the performance of the novel solar-based design for turquoise hydrogen production. It is highlighted that all parameters, except for the parameter under investigation, are maintained at constant values in line with the specifications listed in Table 4.1.

The effect of solar DNI on the system's outputs and fuel is shown in Figure 4.5. With higher DNIs, there is an escalation in the heat absorbed by the solar unit, presenting the potential for increased pyrolysis capacity through augmented molten salt flow. Consequently, under constant operational parameters, a greater quantity of methane can be introduced into the reactor and the system via streams 8 and 16, respectively. It is noteworthy that the disparity between these quantities signifies the rate at which unreacted methane circulates in the system, owing to an MCR

value of 40%. Similarly, a higher DNI alongside an increased fuel flow rate corresponds to an increase in the production of hydrogen and solid carbon.

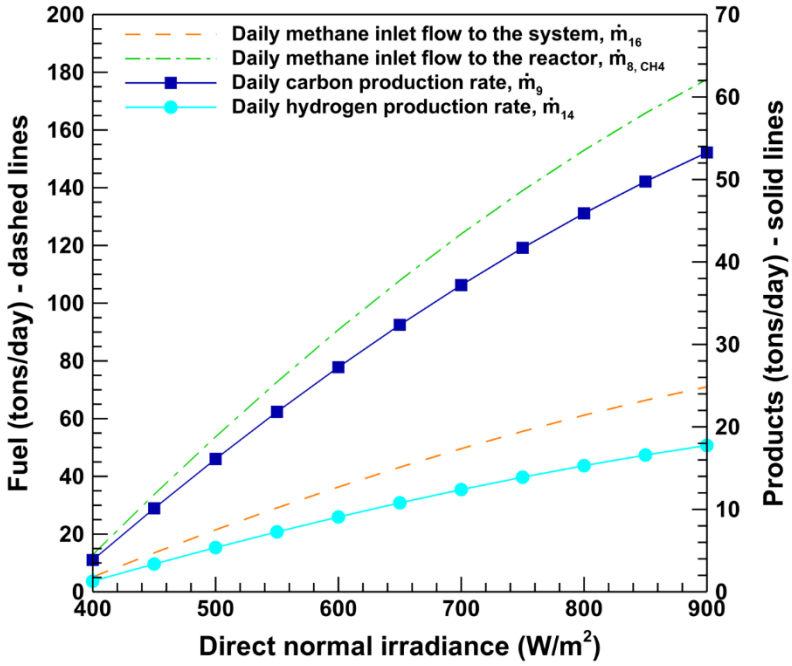

Figure 4.5: The effect of direct normal irradiance (DNI) on system products and fuel flow rates.

The effect of MCR on system products and fuel flow rates is shown in Figure 4.6. Under constant operating conditions, an elevated MCR correlates with an increased number of molar reactions taking place within the reactor. Consequently, an increase in MCR contributes to a reduction in the unreacted methane flow rates, resulting in identical values for both reactor and system methane flow rates. This implies the absence of unreacted methane in an MCR of 100%, resulting in significant energy savings that would otherwise have been allocated to the reheating process for unreacted methane circulating within the system. Moreover, heightened MCR values are associated with an increased production of products, namely hydrogen and carbon.

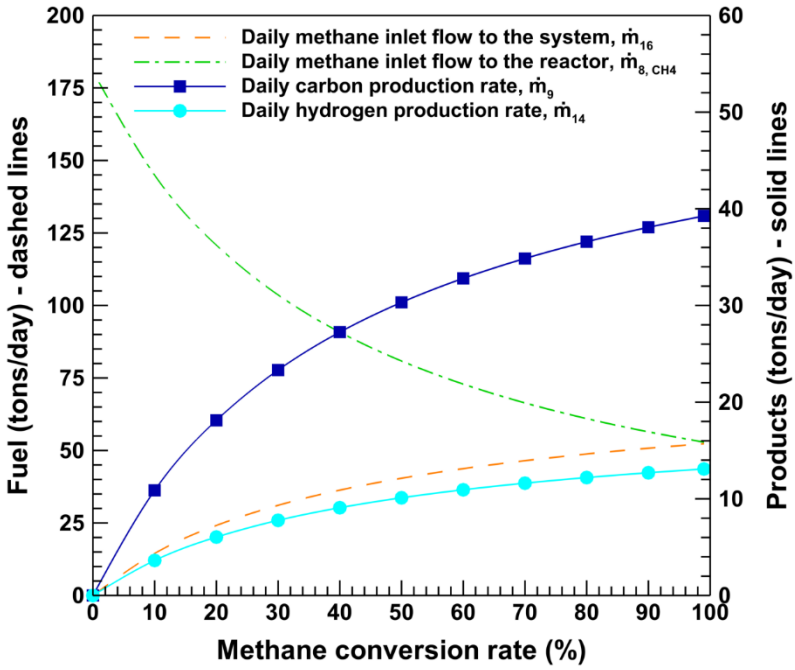

Figure 4.6: The effect of methane conversion rate on system products and fuel flow rates.

The average reactor temperature stands as a crucial parameter in the context of methane pyrolysis, as shown in Figure 4.7. The MCR is significantly influenced by the reactor temperature, and an increase in the reactor temperature leads to a corresponding rise in the MCR. A higher reactor temperature, coupled with an elevated MCR, translates to a diminished flow of unreacted and circulated methane to the reactor. However, the inlet methane to the system experiences an increase in higher reactor temperatures. The results indicate an optimum reactor temperature of approximately 1000 ℃, at which the highest rates of hydrogen and carbon are achieved. This optimal value is scrutinized in Figure 4.8, demonstrating that the heat absorption by the solar unit declines with heightened molten salt and solar receiver temperatures, attributable to increased radiation heat loss in the receiver. This reduction in absorbed heat in the solar unit overcomes the increased MCR and productions observed at reactor temperatures exceeding 1000 ℃. Consequently, an average reactor temperature of approximately 1000 ℃ emerges as the optimum

value for maximizing hydrogen and carbon production in the proposed solar-based methane pyrolysis. This optimal temperature choice is further reflected in the RTE and ERTE, both reaching their peak values at a reactor temperature of 1000 ℃. According to Eqs. (4.41) and (4.42), variations in the absorbed heat by the solar unit and district heating exert distinct effects on the RTE and ERTE, leading to minor differences in their outcomes at varying reactor temperatures.

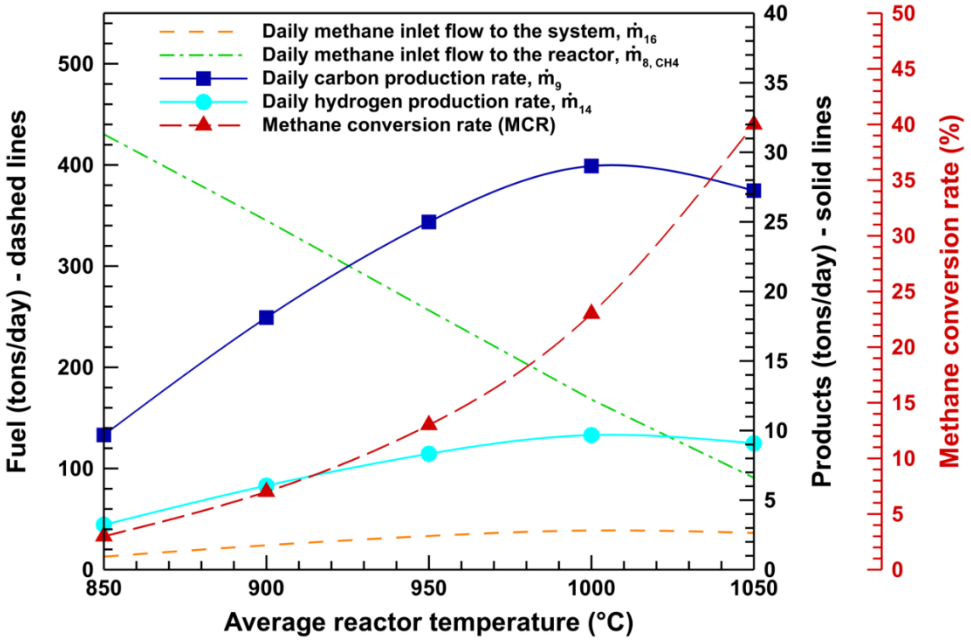

Figure 4.7: The effect of average reactor temperature on methane conversion rate (MCR), system products, and fuel flow rates.

While the average reactor temperature plays a significant role in determining the MCR, it is essential to acknowledge that it is not the only influencing parameter. Various parameters, such as the volume ratio and composition of molten salt, the incorporation of catalysts, etc. employ their own influence on the MCR. Hence, it is imperative to conduct a separate investigation into the effects of the MCR variations at constant temperatures on system performance.

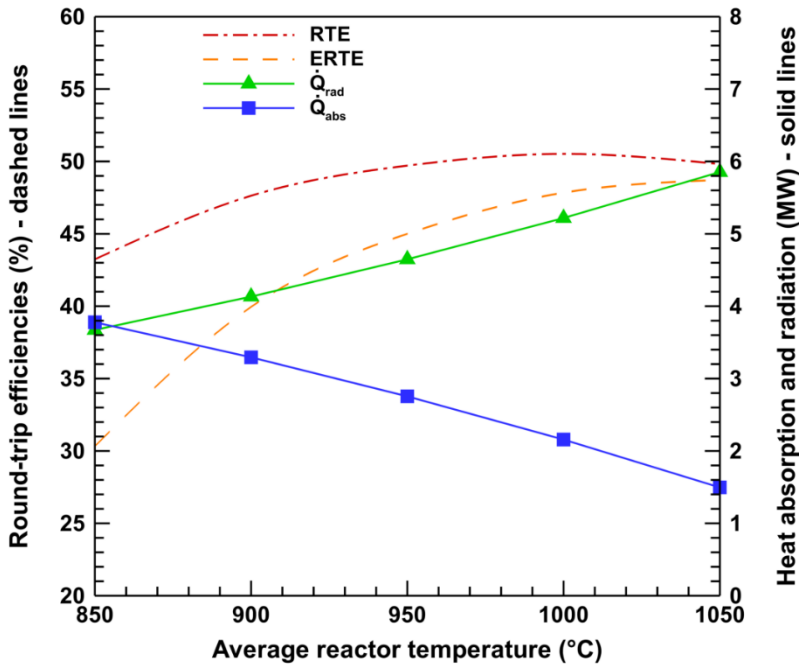

Figure 4.8: The effect of average reactor temperature on round-trip efficiency (RTE), exergy round-trip efficiency (ERTE), heat absorption and radiation losses in solar unit.

The effect of the MCR change (at a constant temperature) on the LCOH and CAPEX is shown in Figure 4.9. As highlighted earlier, the substantial reduction in unreacted methane at elevated MCRs translates to a significant decrease in the circulation rate of unreacted methane and, consequently, the flow rates of streams 10 to 17 (as depicted in Figure 4.1). This reduction manifests in lowered capacities for various components such as HEs, PSA, and the compressor, thereby contributing to a decrease in CAPEX. The diminished CAPEX, coupled with the reduced energy requirements for heating and compressing circulated methane, results in a corresponding reduction in LCOH. Furthermore, an increase in system capacity at higher DNI levels leads to an elevated CAPEX. However, it is noteworthy that an improved solar DNI correlates with increased hydrogen and carbon production, consequently fostering economically viable solar-based turquoise hydrogen production.

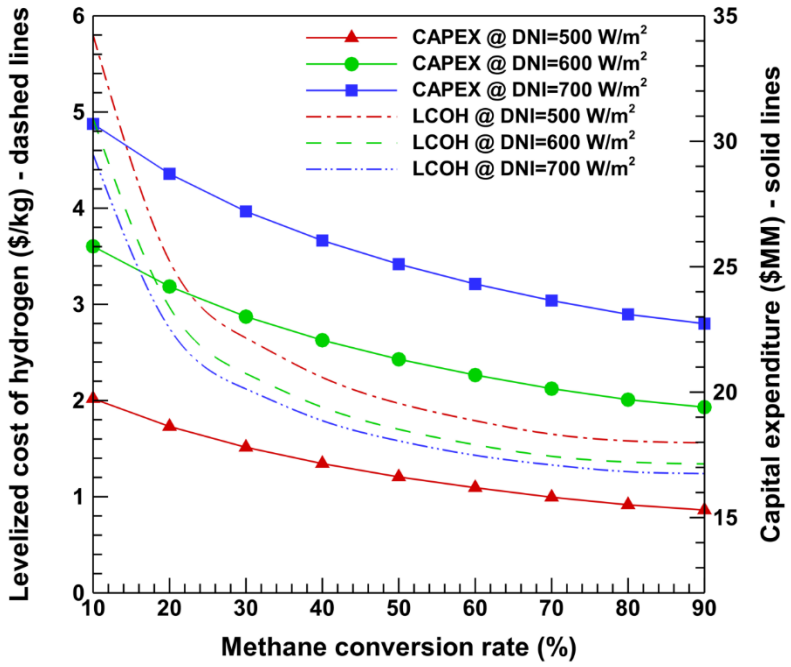

Figure 4.9: The effect of methane conversion rate on levelized cost of hydrogen (LCOH) and capital expenditure (CAPEX) at different direct normal irradiances (DNIs).

Figure 4.10 highlights the effect of average reactor temperature on the LCOH and CAPEX, taking into account various carbon sale prices. As mentioned in Figure 4.7, the MCR is intricately tied to the average reactor temperature, thereby directly influencing component sizes and, consequently, the system CAPEX. Therefore, a higher reactor temperature corresponds to an elevated MCR and a concomitant reduction in CAPEX. Furthermore, the LCOH experiences a decline with increased hydrogen and carbon production at higher reactor temperatures. It is noteworthy that this reduction in LCOH is further accentuated by a noteworthy finding: a 30 ¢/kg decrease in LCOH is observed with every 100 $/ton increase in the carbon sale price. This interaction between reactor temperature, MCR, carbon sale price, and associated economic metrics contributes valuable insights into the intricate relationships that underpin the economic viability of solar-based methane pyrolysis.

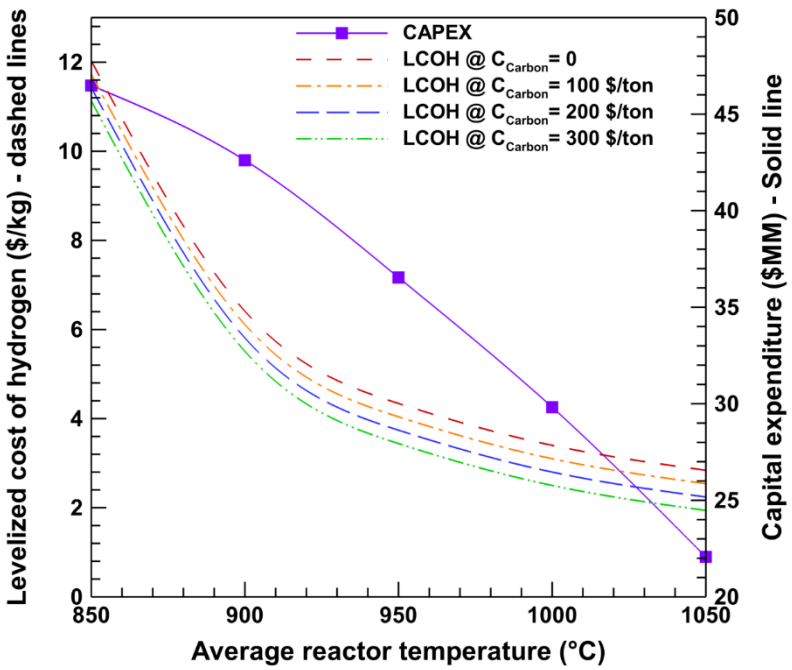

Figure 4.10: The effect of average reactor temperature on levelized cost of hydrogen (LCOH) and capital expenditure (CAPEX) at different carbon sale prices.

4.4. Techno-economic analysis results

The LCOH is the most important finding of the techno-economic analysis, which depends on various variables such as the carbon sale price, off-peak electricity price as HTES input, methane purchase price, and the system's lifespan. The effect of these variables, including the clean hydrogen production tax incentives of the US and Canada will be presented in the following. As listed in Table 4.6, the clean hydrogen production tax incentive in the US, known as the §45V tax credit, is subject to meeting specific reductions in both the final hydrogen production cost and a percentage of the CAPEX, both of which are linked to the carbon intensity of the process [264,265]. Table 4.7 outlines the Canadian government's clean hydrogen production tax incentive, determined by a specific percentage reduction from the CAPEX, correlating with the process carbon intensity. It is worth noting that the data for Canadian hydrogen tax incentives are initially introduced, and discussions on theses incentives are still active at the time of this publication. Since

this topic is not finalized in Canada, there might be future changes in the percentage of the tax incentives for hydrogen production pathways. The present study also assumes that methane pyrolysis as an emerging hydrogen production technique will be included in the hydrogen production tax incentives of both countries.

Table 4.6: Clean hydrogen production tax incentives of §45V for the United States [264,265].

Life cycle carbon intensity ($kgCO_2/kgH_2$)	Tax incentive ($/kgH$_2$)	Tax incentive (% of CAPEX)
<0.45	3.00	6
0.45-1.5	1.00	2
1.5-2.5	0.75	1.5
2.5-4	0.60	1.2

Table 4.7: Clean hydrogen production tax incentives for Canada [266,267].

Life cycle carbon intensity ($kgCO_2/kgH_2$)	Tax incentive (% of CAPEX)
<0.75	40
0.75-2	25
2-4	15

The carbon intensity of solar-based methane pyrolysis with grid electricity is primarily influenced by grid carbon intensity, methane production, and transportation. Calculations reveal a carbon intensity of less than 4 $kgCO_2/kgH_2$, leading to 60 ¢/kgH_2 and 1.2% of the CAPEX based on the tax incentives of the US and 15% of the CAPEX by Canada tax incentives [264–267]. On the other hand, when REs are employed as the source of electricity for the HTES, the primary contributor to carbon intensity stems from the inlet methane. Therefore, excluding the carbon intensity of the grid and the produced solid carbon, a carbon intensity of less than 2 $kgCO_2/kgH_2$ can be achieved for solar-based methane pyrolysis utilizing RE sources [30]. So, this configuration has the potential to receive 75 ¢/kgH_2 and 1.5% of the CAPEX based on the tax incentives established for the US, and 25% of the CAPEX for Canada [264–267].

The carbon sale price is one of the crucial factors in the computation of the hydrogen production cost. A 100 $/ton increase in the carbon sale price leads to a noteworthy reduction of

30 ¢/kg in the LCOH. Therefore, high-quality carbon production for methane pyrolysis in molten salt can contribute to economically viable hydrogen production. The effect of carbon sale price on the LCOH for solar-based pyrolysis with (a) grid electricity and (b) RE sources are shown in Figure 4.11.

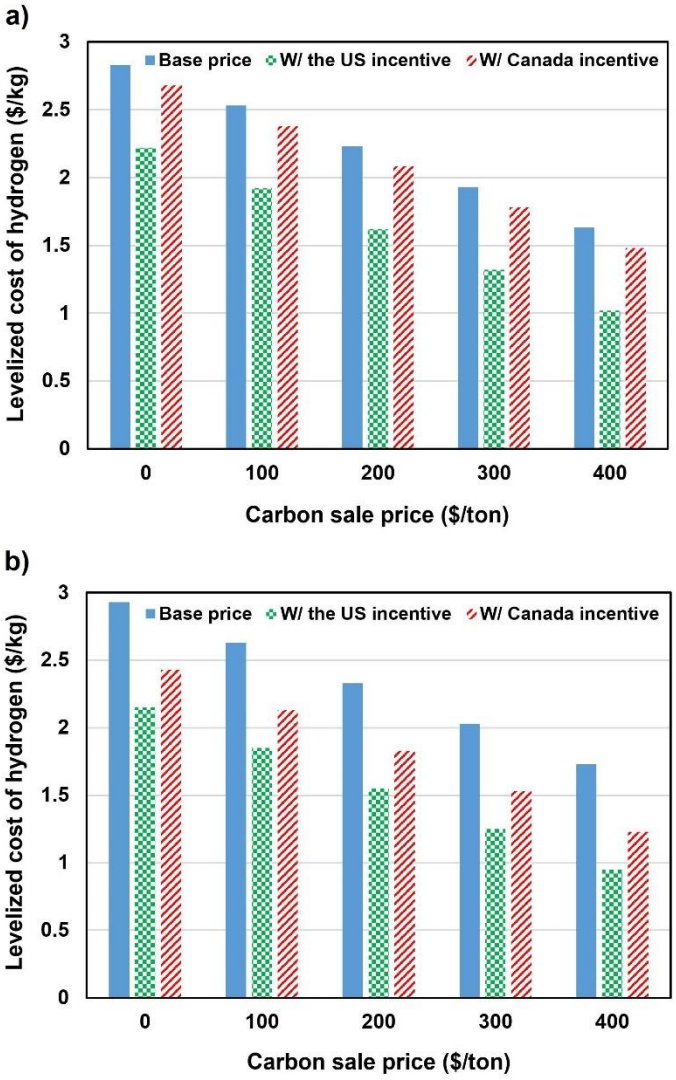

Figure 4.11: The effect of carbon sale price on the LCOH for solar-based methane pyrolysis with (a) grid electricity and (b) renewable energies. "W/" stands for "with".

The effect of the US hydrogen tax incentives on the LCOH is more noticeable, consistently yielding lower values across all scenarios. The base LCOH, excluding the carbon value, is determined 2.83 and 2.93 $/kg for solar-based methane pyrolysis with grid electricity and the RE,

respectively. Under an optimistic condition (carbon sale price of 400 $/ton), the LCOH can reach 0.95 $/kg and 1.23 $/kg for grid-based pyrolysis, including the tax incentives provided through the US and Canada, respectively.

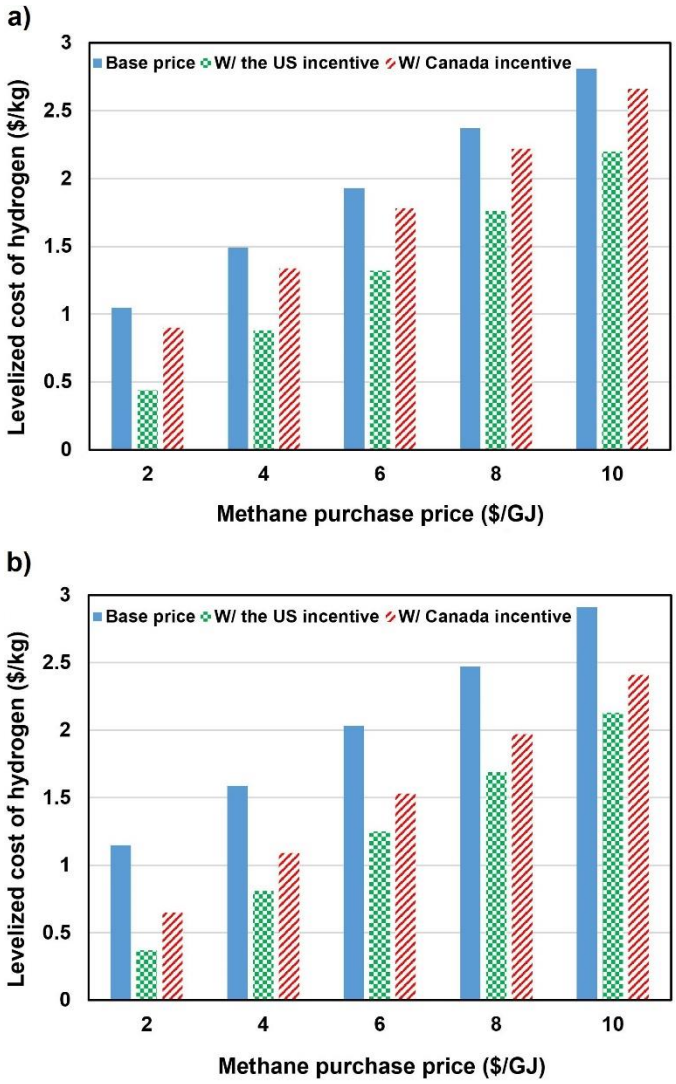

Figure 4.12: The effect of methane purchase price on the LCOH for solar-based methane pyrolysis with (a) grid electricity and (b) renewable energies. "W/" stands for "with".

The effect of methane purchase price on the LCOH for the solar-based pyrolysis with (a) grid electricity and (b) REs is shown in Figure 4.12 (a) and (b). This analysis accounts for the substantial variations in the LCOH corresponding to different methane purchase prices. It can provide valuable insights into the cost-effectiveness or expenditures associated with turquoise

hydrogen production across countries distinguished by different methane prices determined by their geographical locations. For instance, as shown in Figure 4.12 (a) the base LCOH can be increased from 1.05 to 2.81 $/kg by increasing the methane purchase price from 2 to 10 $/GJ. Hence, it is imperative to take into account geographical locations for methane pyrolysis, given that a higher methane price directly correlates with an increase in the LCOH.

The effect of off-peak electricity price on the LCOH of solar-based methane pyrolysis in molten salt relying on grid and RE sources are shown in Figure 4.13 (a) and (b). The LCOH of RE-based pyrolysis is independent from electricity price, maintaining a base LCOH of 2.03 $/kg, which further decreases to 1.25 $/kg and 1.53 $/kg when factoring the clean hydrogen tax incentives offered by the US and Canada. In contrast, grid-based solar pyrolysis may yield LCOH values either lower or higher than those of RE-based systems, depending on the off-peak electricity prices in the region. Therefore, it is imperative to account for the availability of off-peak electricity prices when assessing the economic viability of integrating solar-based methane pyrolysis with RE sources.

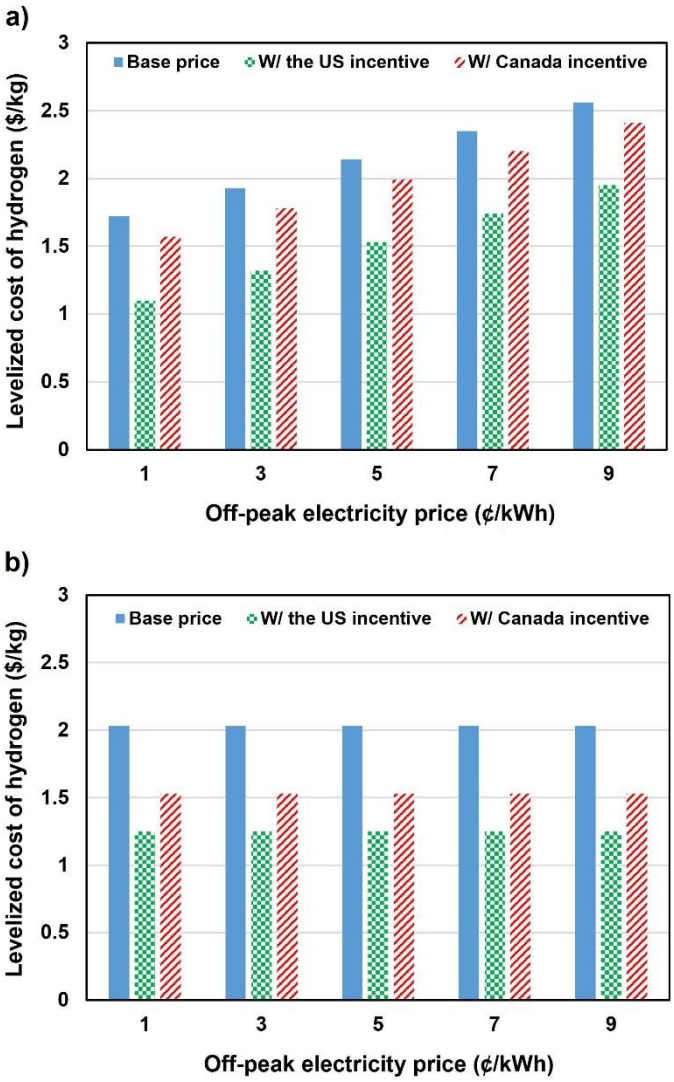

Figure 4.13: The effect of off-peak electricity price on the LCOH for solar-based methane pyrolysis with (a) grid electricity and (b) renewable energies. "W/" stands for "with".

The system's operational lifespan constitutes a pivotal factor influencing the LCOH. Developing the pyrolysis technology and REs to extend their operational duration can significantly contribute to the improvement of LCOH metrics. Figure 4.14 (a) and (b) show the effect of system lifespan on the LCOH for solar-based methane pyrolysis with the grid and RE sources. Calculations reveal reductions of 20 ¢/kg and 0.41 ¢/kg in LCOH when the system lifespan is extended from 15 to 30 years, for the grid-based and RE-based scenarios.

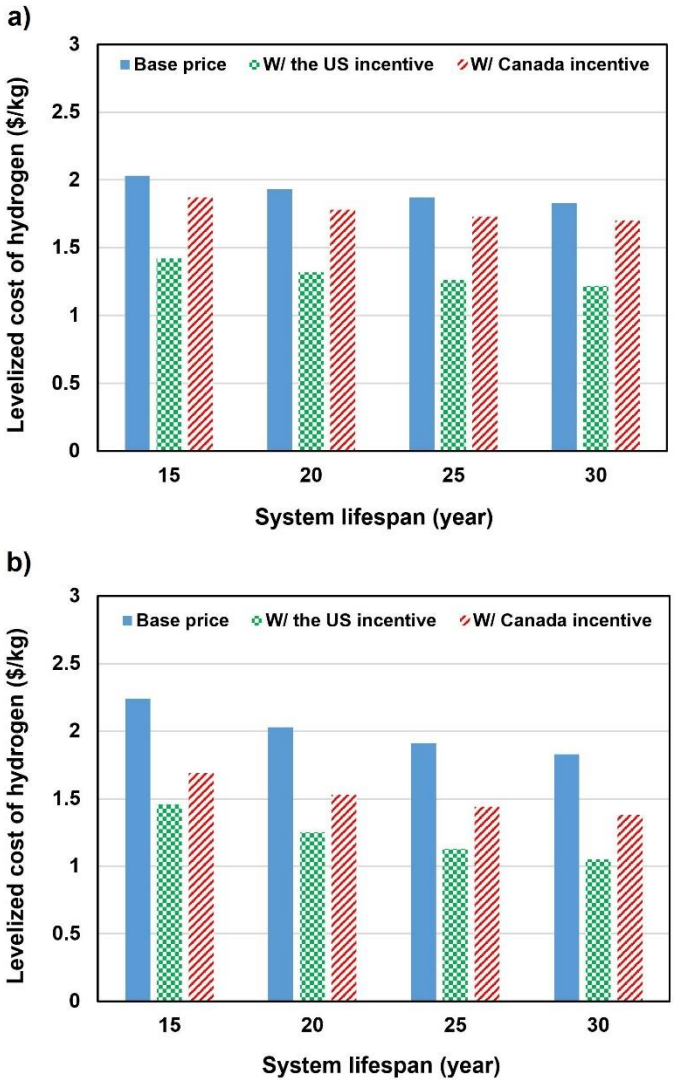

Figure 4.14: The effect of system lifespan on the LCOH for solar-based methane pyrolysis with (a) grid electricity and (b) renewable energies. "W/" stands for "with".

The projections indicate a significant decline in the cost of RE infrastructure in the coming years [268]. This development holds substantial implications for the LCOH of the proposed system, aiming to reach a value of 1 $/kg, as set by the US DOE Hydrogen Shot [25]. Figure 4.15 is presented to provide insight into how the reduction in RE infrastructure costs influences the LCOH. In Figure 4.15 (a), the LCOH of solar-based methane pyrolysis with grid electricity reveals that the cost reduction is selectively applied to the heliostat unit components. However, in Figure 4.15 (b), the LCOH of solar-based methane pyrolysis with the RE electricity shows a more

substantial reduction in CAPEX, incorporating the RE price, which includes 51% of the CAPEX (refer to Figure 4.4). Consequently, a notably pronounced reduction is observed for solar-based methane pyrolysis coupled with REs.

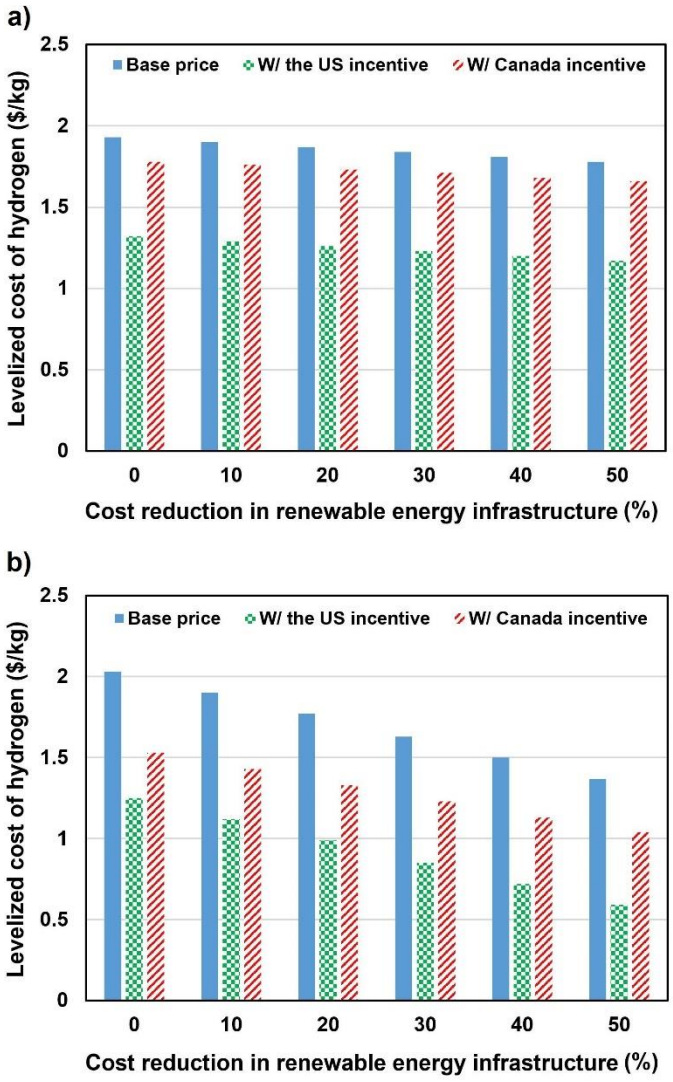

Figure 4.15: The effect of cost reduction in renewable energy infrastructure on the LCOH for solar-based methane pyrolysis with (a) grid electricity and (b) renewable energies. "W/" stands for "with".

The findings indicate a promising prospect: a mere 20% reduction in the price of RE infrastructure can lead to achieving the US DOE goal of 1 $/kg, including the US hydrogen tax incentive. However, greater than a 50% reduction in the RE infrastructure costs is required to achieve the same goal based on the clean hydrogen tax incentive offered by Canada.

4.4 Summary of chapter

This chapter introduced an innovative approach for turquoise hydrogen production, employing solar-based methane pyrolysis in molten salt to decrease the carbon footprint of the process. The proposed system was integrated with a high-temperature thermal energy storage (HTES) unit to ensure uninterrupted hydrogen production during periods of solar unavailability, thereby contributing to the economic viability of the overall system. Furthermore, a thorough investigation and comparison were conducted regarding the feasibility of employing grid or renewable energy electricity as the input for the HTES. A comprehensive techno-economic analysis was conducted to determine the levelized cost of hydrogen under various conditions. The key findings of this study are summarized as follows:

- Critical factors in the production of turquoise hydrogen through methane pyrolysis in molten salt include: I) methane conversion rate, II) reactor temperature, III) carbon quality and sale price, IV) methane purchase price, V) electricity price, VI) system lifespan, and VII) cost of renewable energy infrastructure.

- The proposed solar-based methane pyrolysis in molten salt, characterized by a capital expenditure (CAPEX) of $22 million, demonstrates a round-trip efficiency of 49.8% for turquoise hydrogen production. The system yields a daily production capacity exceeding 9 tons of hydrogen and 27 tons of carbon at a temperature of 1050 ℃, maintaining an experimentally validated methane conversion rate of 40%. Taking into account a market price of 300 $/ton for carbon, the levelized cost of hydrogen (LCOH) stands at a rate of 1.93 $/kg, excluding any clean hydrogen tax incentive.

- To further decarbonize the process, an additional investment of $23 million is required to produce the required electricity of the HTES from renewable energy sources. With the increased CAPEX to $45 million, the LCOH for solar-based methane pyrolysis in molten salt, integrated with renewable energies, experiences an increase to 2.03 $/kg.

- Higher methane prices directly lead to increased LCOH, illustrated by the base LCOH rising from 1 to 2.8 $/kg with methane prices going up from 2 to 10 $/GJ. Therefore, it is essential to carefully consider geographical locations, taking into account the cost-effective availability of methane, when planning the installation of a methane pyrolysis plant for hydrogen production.

- The effect of the US clean hydrogen tax incentives (the §45V tax credit) outweighs the corresponding tax incentives provided by Canada. Calculations project the feasibility of reaching a target LCOH of 1 $/kg set by the United States Department of Energy (DOE) through the proposed system. This achievement is contingent upon a 20% reduction in the cost of renewable energy infrastructure and the inclusion of the US hydrogen tax incentives.

4.5 Uncertainty consideration

In this analysis, key economic parameters, including capital investment, operating and maintenance costs, and interest rates, were considered in accordance with the existing cost functions in the literature. However, certain detailed cost elements, such as those related to engineering, installation, insurance, and other ancillary expenses, were excluded from the scope of this study. These omissions introduce inherent uncertainties in the economic outcomes, as they represent significant cost factors that could affect the overall financial viability of the system.

Additionally, the current temperature range of commercialized heliostat fields using molten salt is limited to approximately 700°C, primarily due to corrosion issues at higher temperatures. This constraint not only impacts system performance but also introduces cost uncertainties associated with material degradation and maintenance requirements. The objective of the present work is to highlight the significant potential for increasing the operating temperature of molten salt systems, thereby motivating further research and development to overcome these technical challenges. The high-temperature thermal energy storage (HTES) unit, a relatively new technology, is currently limited to steam and air applications. The use of molten salt in this context, along with its associated corrosion effects and potential cost increases, represents an additional uncertainty that should be addressed through the ongoing development of HTES technology. Furthermore, the carbon intensity of the methane feedstock for the methane pyrolysis system is based on current data from the National Inventory Report of Canada. This value may vary across countries or could decrease over time with advancements in sustainable natural gas extraction and transportation technologies.

To enhance the accuracy and reliability of the economic analysis, future studies should incorporate a more comprehensive set of cost factors, including those related to higher temperature materials, corrosion mitigation technologies, and region-specific carbon intensity values. Additionally, these analyses should be supported by up-to-date, reliable cost functions and data, as they become available. Such refinements would improve the robustness of the economic outcomes, better reflecting real-world conditions and enabling more informed decision-making in the design and implementation of these advanced energy systems.

PART 3: Comprehensive Comparison of Different Technologies and Case Studies

Chapter 5: Techno-Economic Comparison of Solar-Based Solid Oxide Electrolyzer with Solar-Based Methane Pyrolysis[1]

The transition towards clean and economically viable hydrogen production is crucial for ensuring energy sustainability and mitigating climate change. This transition can be effectively facilitated by using renewable energy sources and advanced hydrogen production methods. Methane pyrolysis and water electrolysis emerge as crucial techniques for achieving hydrogen production with minimal carbon intensity. Recognizing the unique opportunity presented by solar energy for both processes, this study presents a comparative techno-economic analysis between solar-based molten salt methane pyrolysis (SMSMP) and solar-based solid oxide electrolyzer cell (SSOEC). This study offers a guideline for selecting SMSMP vs SSOEC for cities across the world. In particular, a comprehensive case study including five cities worldwide—San Antonio, Edmonton, Auckland, Seville, and Lyon—is conducted, utilizing their dynamic solar data and localized prices of methane and electricity to provide a realistic comparison. The results indicate the superior economic feasibility of SMSMP across all case studies. Among different case studies, San Antonio and Auckland have the lowest hydrogen costs for SMSMP (2.31 \$/kgH_2) and SSOEC (5.19 \$/kgH_2), respectively. It was also concluded that SMSMP is preferred over SSOEC in average to ideal solar conditions, given its full dependency on solar thermal energy. However, the SSOEC has the potential to achieve better economic feasibility by incorporating clean hydrogen tax incentives and reducing the costs associated with renewable energy infrastructure in the future.

[1] This chapter is based on [5].

5.1 System description

In this section, the innovative designs for SMSMP and SSOEC, adapted from the previous two chapters, are presented, accompanied by explanations of their operational details. It is noted that the capacity of the solar unit remains consistent across both systems.

The schematic representation of the heliostat SMSMP system is shown in Figure 5.1. When solar energy is available, molten salt is transferred from the cold molten salt tank (CMST) to the heliostat tower (Streams 1 and 2) to absorb solar thermal energy as it passes through the solar receiver. Subsequently, the heated molten salt is supplied in the hot molten salt tank (HMST), Stream 3. From HMST, a portion of the molten salt is transferred at a reduced mass flow rate to cover the heat demand for a full cycle to the bubble column reactor (Streams 4 and 5) to facilitate methane cracking into hydrogen and solid carbon. Simultaneously, methane that has been preheated and contains some unseparated hydrogen is fed into the reactor after getting some heat in the heat exchanger 1 (HE_1), Streams 16 to 7. Functioning as a catalyst within the reactor, molten salt aids in methane cracking into solid carbon and hydrogen (Streams 8 and 9). The lower density of the resultant solid carbon, in comparison to molten salt, smooths its easy separation from the salt surface. The hydrogen produced along with unreacted methane (Stream 9) is directed through HE_1 to raise the methane inlet temperature to the reactor, thereby lowering compressor power usage at reduced inlet temperatures (Stream 10). In addition, the discharged low-temperature molten salt is stored in CMST for subsequent reheating during periods of solar availability (Stream 6). Considering that the compressor generates heat (Stream 11), a district heating (DH) unit has been incorporated to recycle this waste heat in HE_2 (Streams a and b), supplying the necessary inlet temperature for the pressure swing adsorption (PSA) unit (Stream 12). Exploiting a solid adsorbent, PSA employs cycles of pressurization and depressurization. While pressurized, the

adsorbent selectively traps hydrogen molecules, allowing methane to flow through (Stream 14). In the subsequent depressurization phase, the captured hydrogen is departed from the adsorbent (Stream 13). The unreacted methane is combined with extra methane (Stream 15), preheated in HE_1, and returned to the reactor to guarantee uninterrupted operation of the process.

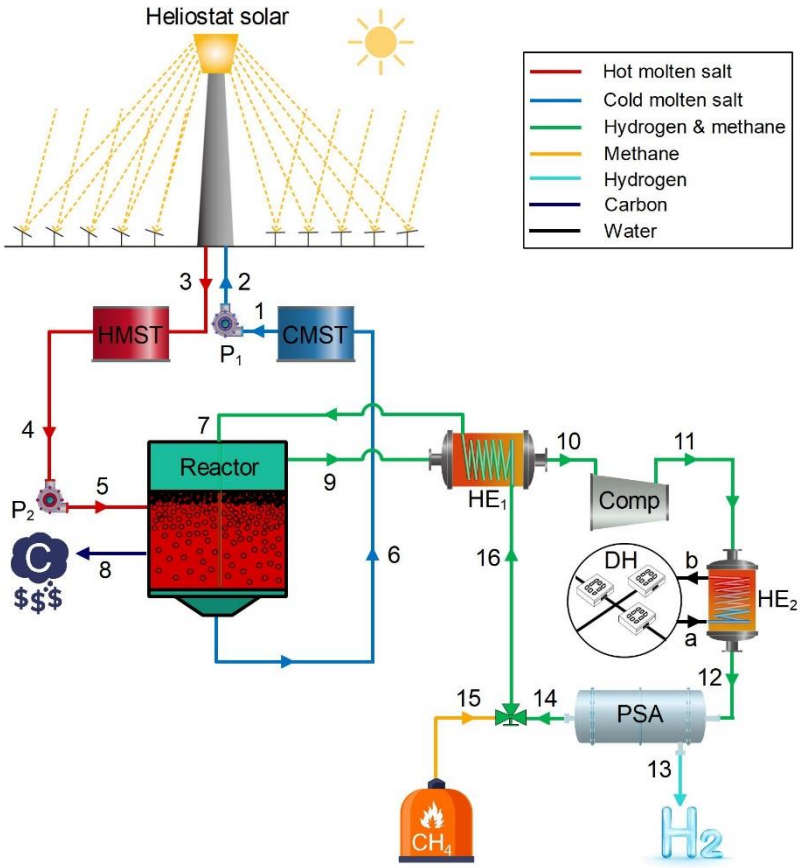

Figure 5.1:. Schematic diagram of the proposed novel design for turquoise hydrogen production based on heliostat solar field and molten salt-based methane pyrolysis. CMST: Cold molten salt tank, Comp: Compressor, DH: District heating, HE: Heat exchanger, HMST: Hot molten salt tank, P: Pump, PSA: Pressure swing adsorption.

The schematic representation of the SSOEC is shown in Figure 5.2. The solar unit (Streams 1-6) operates exactly like that of the methane pyrolysis system (Figure 5.1), albeit with the utilization of HE_1 instead of the methane pyrolysis reactor. Incoming water to the SOEC undergoes heating in two stages: firstly, through the waste heat recovery from the generated hydrogen and oxygen in HE_2 (Streams 8 to 9), and secondly, by utilizing the supplied hot molten salt in HE_1 (Streams 9 to

10). Unlike SMSMP, the SOEC requires electricity as an additional input, which can be sourced from either grid electricity or renewable energies. The implementation of a HMST as a sensible TES system mitigates the fluctuations inherent in solar energy dynamics, providing a more stable and consistent thermal output for both the methane pyrolysis and SOEC systems.

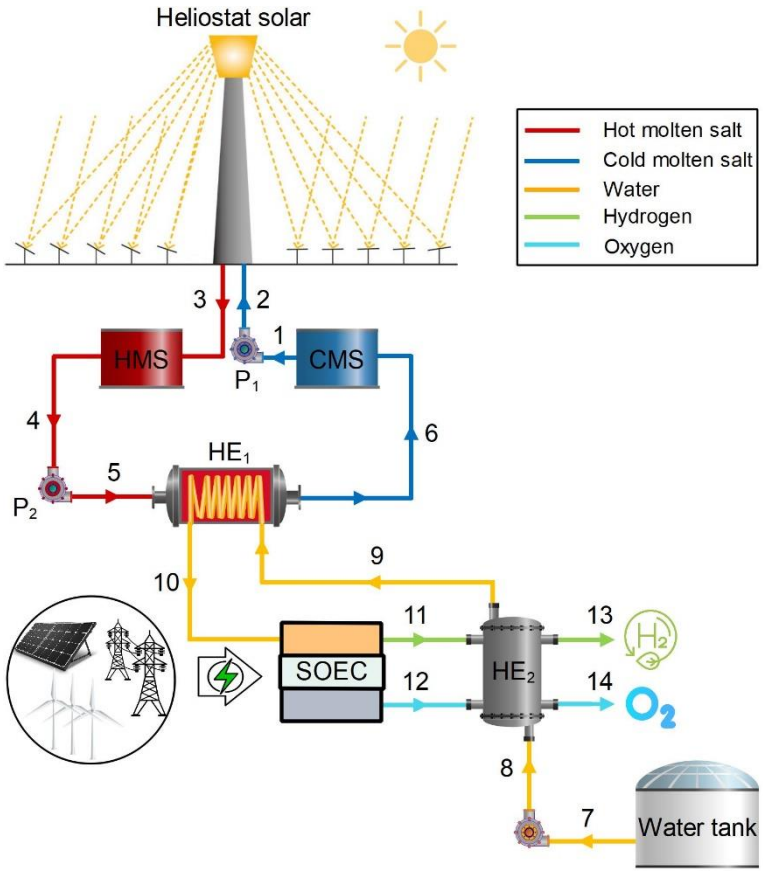

Figure 5.2: Schematic diagram of the proposed design for green hydrogen production based on heliostat solar field and solid oxide water electrolysis. CMST: Cold molten salt tank, HE: Heat exchanger, HMST: Hot molten salt tank, P: Pump, SOEC: Solid oxide electrolyzer cell.

Table 5.1 contains the design parameters and assumptions employed to model different subsystems and equipment. A detailed mathematical modelling of the solar, methane pyrolysis, and electrolysis units and techno-economic equations are included in Chapters 2 and 3 to allow for the briefly of the main body of this chapter.

Table 5.1: Design parameters and assumptions of different equipment and systems.

Subsystem	Parameter	Value	Unit
Heliostat solar [191,219,220,254]	Concentration ratio	1000	-
	Direct normal irradiance	600	W/m^2
	Emissivity coefficient	0.8	-
	Inner diameter of the receiver tube	3.75	cm
	Number of the heliostat	200	-
	Outer diameter of the receiver tube	4	cm
	Reflectivity coefficient of the receiver surface	0.04	-
	Solar availability per day	9	hour
	Surface area of the heliostats	11×11	m^2
	Temperature of the sun	5505	℃
	Thermal conductivity of the receiver tube	24.5	W/m.K
	Thermal conductivity of the tube-insulation	0.03	W/m.K
	Thickness of the tube-insulation	10	cm
	View factor	0.8	-
	Wind speed	6	m/s
Methane pyrolysis [4,136,139,141,257]	Density of methane	0.657	kg/m^3
	Density of molten salt	1880	kg/m^3
	Dynamic viscosity of molten salt	0.0006	kg/ms
	Feeder inner diameter	28×10^{-4}	m
	Hydrogen selectivity	90	%
	Immersed height of the column	2	m
	Methane purchase price	6	$/GJ
	Molten salt lifetime	1	year
	Molten salt price	10	$/kg
	PSA efficiency	90	%
	Reactor temperature	1050	℃
	Surface tension of molten salt	0.063	N/m
Solid oxide electrolysis [206,221–224,269]	Activation energy of anode	140000	J/mol
	Activation energy of cathode	142000	J/mol
	Anode thickness	500	µm
	Average length of grain contact	0.6	µm
	Average pore diameter of electrodes	3	µm
	Average grain size of electrodes	1.5	µm
	Cathode thickness	20	µm
	Current density	8000	A/m^2
	Cell active area	0.04	m^2
	Charge-transfer coefficient	0.5	-
	Electrode porosity	48	%
	Electrode thickness	10	µm
	Tortuosity	5.4	-
	Interconnect thicknesses	3	mm
	Number of cells	47650	-
	Operating temperature of SOEC	800	℃
	Pre-exponential factor for anode	6.5×10^9	A/m^2
	Pre-exponential factor for cathode	2.35×10^9	A/m^2
	Steam utilization factor	0.6	-
	Service time of SOEC	40000	hrs
	Annual operating and maintenance costs	22	% of CAPEX
General [136,139,141]	Acceleration due to gravity	9.8	m/s^2
	Annual operating and maintenance costs	6	% of CAPEX

Ambient pressure	1.01	bar
Ambient temperature	20	℃
Electricity price	10	¢/kWh
Faraday constant	96486	sA/mol
Interest rate	6	%
Lower heating value of hydrogen	33.31	kWh/kg
Lower heating value of methane	13.88	kWh/kg
Stephan-Boltzmann constant	5.67×10^{-8}	$W/m^2.K^4$
System lifespan	20	year
Universal gas constant	8.314	J/mol.K

5.2 Results and discussion

The findings from the proposed systems designed for methane pyrolysis and water electrolysis are presented within four distinct sections, including the validation of models, modelling results, parametric analysis, and case studies.

5.2.1 Validation of models

The SMSMP and SSOEC systems proposed in this research have been designed based on three primary units, each rigorously validated against relevant literature data to ensure accuracy and reliability. Given the novelty of this study and the systems under investigation, no single comprehensive study exists for direct validation. Therefore, each unit of the system has been individually validated by comparing the simulation results to data from established studies. Using design parameters and assumptions derived from corresponding sources, each unit underwent a thorough validation process to ensure its accuracy. Table 5.2 presents the validation of the heliostat solar unit, where four key results from the proposed model are compared with those reported by Kandezi et al. [254].

Table 5.2: Validation of the model for heliostat solar field [254].

Factor	This model	Kandezi et al. [254]	Error (%)
Reflected rate of solar energy into the receiver [MW]	40.22	39.21	2.6
Heat absorption rate by the solar receiver [MW]	21.26	20.56	3.4
Enthalpy of hot molten salt [kJ/kg]	687.6	687.6	0.0
Molten salt flow rate [kg/s]	26.54	26.38	0.6

Furthermore, the validation of the current models for methane pyrolysis and the SOEC is demonstrated in Figure 5.3, utilizing experimental data reported by Kang et al. [136] and Ebbesen et al. [249], respectively.

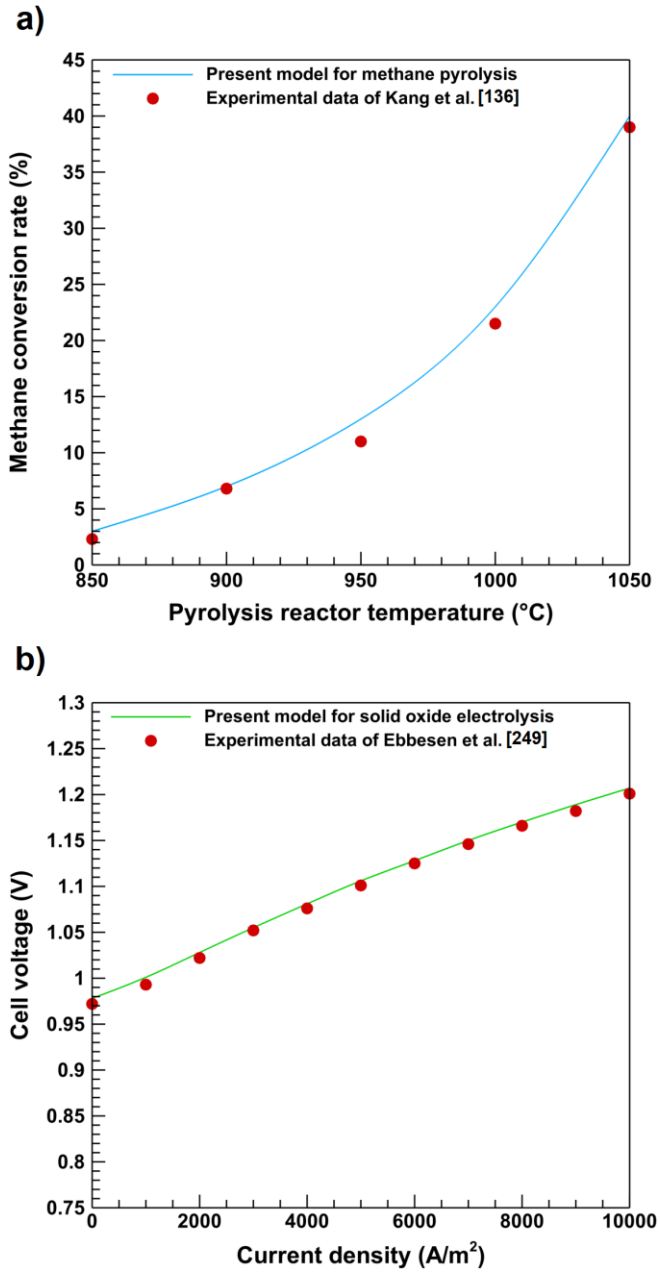

Figure 5.3: The validation of the proposed models for methane pyrolysis (Kang et al. [136]) and the SOEC (Ebbesen et al. [249]).

It is evident from the plots that negligible differences are observed between the proposed models and those detailed in related studies within the literature. This consistent alignment confirms the

robustness of the models and allows using the resulting data from these models for investigation and analysis in this domain.

5.2.2 Modelling results

This section presents the modelling results from the techno-economic assessment of the proposed SMSMP and SSOEC systems, based on the design values and assumptions outlined in Table 5.1. To provide a better understanding of the operation of these systems, the fundamental thermodynamic properties of SMSMP and SSOEC are detailed in Table 5.3 and Table 5.4, respectively.

Table 5.3: Properties and molar fraction of different streams of the SMSMP (Figure 5.1).

Stream	T (°C)	P (bar)	$\dot{m}$ (kg/s)	Molar fraction				
				$MnCl_2$-KCl	CH_4	H_2	C	H_2O
1	900	1	5.76	1				
2	900	2.5	5.76	1				
3	1200	2	5.76	1				
4	1200	1	2.16	1				
5	1200	2.5	2.16	1				
6	900	2.2	2.16	1				
7	945	2.7	0.52		0.915	0.085		
8	1050	1	0.16				1	
9	1050	2.2	0.36		0.383	0.617		
10	62	2	0.36		0.383	0.617		
11	406	16	0.36		0.383	0.617		
12	57	14.4	0.36		0.383	0.617		
13	57	3	0.05			1		
14	57	3	0.30		0.861	0.139		
15	20	3	0.22		1			
16	42	3	0.52		0.915	0.085		
a	20	1	0.99					1
b	70	1	0.99					1

Table 5.4: Properties of different streams of the SSOEC (Figure 5.2).

Stream	Working fluid	T (°C)	P (bar)	$\dot{m}$ (kg/s)
1	$MnCl_2$-KCl	600	1	8.71
2	$MnCl_2$-KCl	600	2.5	8.71
3	$MnCl_2$-KCl	1100	2	8.71
4	$MnCl_2$-KCl	1100	1	3.27

5	$MnCl_2$-KCl	1100	2.5	3.27
6	$MnCl_2$-KCl	1100	2.2	3.27
7	H_2O	20	1	2.37
8	H_2O	20	2.5	2.37
9	H_2O	480	2	2.37
10	H_2O	800	1.5	2.37
11	H_2	750	1	0.16
11'	H_2O	750	1	0.95
12	O_2	750	1	1.26
13	H_2	80	1	0.16
13'	H_2O	80	1	0.95
14	O_2	80	1	1.26

A summary of the significant findings for the proposed systems (Figure 5.1 and Figure 5.2) is provided in Table 5.5. The SMSMP system can produce 4.65 tons per day of hydrogen, along with 13.95 tons per day of solid carbon as a by-product, with an MCR of 42% and an RTE of 40.6%. This process requires 17.97 MWh/day of solar thermal energy and 18.62 tons per day of methane. Additionally, the system consumes approximately 4.76 MWh/day of electricity for compression and generates 4.97 MWh/day of district heating. Unlike the SMSMP, SSOEC requires both thermal and electrical energies. Specifically, the SOEC unit consumes 479.1 MWh/day of electricity and 45.35 MWh/day of thermal energy, along with 123.1 tons/day of water. This process produces 13.76 tons of hydrogen and 109.2 tons of oxygen as a by-product, achieving an RTE of 75.2% and an LCOH of 5.34 $/kg.

Table 5.5: A summary of significant findings for the SMSMP and SSOEC units.

System	Parameter	Value	Unit
SMSMP	$LCOH @ C_C = 300\$/\text{ton}$	1.93	$/kg
	$LCOH @ C_C = 0$	2.83	$/kg
	$\dot{m}_C$	13.95	tons/day
	$\dot{m}_{CH_4}$	18.62	tons/day
	$\dot{m}_{H_2}$	4.65	tons/day
	MCR	42	%
	RTE	40.61	%
	$\dot{Q}_{Abs}$	17.97	MWh/day
	$\dot{Q}_{Cd}$	0.11	kWh/day

	$\dot{Q}_{Cv}$	6.57	MWh/day
	$\dot{Q}_{DH}$	4.97	MWh/day
	$\dot{Q}_{Rad}$	70.23	MWh/day
	$\dot{Q}_{Rec}$	98.01	MWh/day
	$\dot{Q}_{Ref}$	3.13	MWh/day
	$\dot{Q}_{Sun}$	130.68	MWh/day
	$\dot{W}_{Com}$	4.76	MWh/day
SSOEC	$LCOH$	5.34	$/kg
	$\dot{m}_{H_2}$	13.76	tons/day
	$\dot{m}_{H_2O}$	123.1	tons/day
	$\dot{m}_{O_2}$	109.2	tons/day
	RTE	75.18	%
	$\dot{Q}_{Abs}$	45.35	MWh/day
	$\dot{Q}_{Cd}$	0.09	kWh/day
	$\dot{Q}_{Cv}$	5.37	MWh/day
	$\dot{Q}_{Rad}$	44.06	MWh/day
	$\dot{Q}_{Rec}$	98.01	MWh/day
	$\dot{Q}_{Ref}$	3.14	MWh/day
	$\dot{Q}_{Sun}$	130.68	MWh/day
	$\dot{W}_{SOEC}$	479.1	MWh/day

For a more comprehensive comparison of the SMSMP and SSOEC units, their Sankey diagrams are presented in Figure 5.4 (a) and (b), respectively, with values in Megawatt hours (MWh). As illustrated, a considerable amount of the methane and hydrogen blend circulates within Figure 5.4 (a), indicated by the green arrows, due to the low MCR of 42%. Additionally, SMSMS operates at a higher temperature compared to SSOEC, necessitating the use of higher-temperature molten salt. This requirement results in lower thermal absorption in the solar receiver of the SMSMP system (17.97 MWh) compared to that of SSOEC (45.35 MWh), primarily due to more significant radiation heat loss at higher temperatures in the solar receiver. Consequently, SSOEC produces

more hydrogen (519.75 MWh) compared to SMSMP (173.87 MWh), attributed to the utilization of electricity in the electrolysis process.

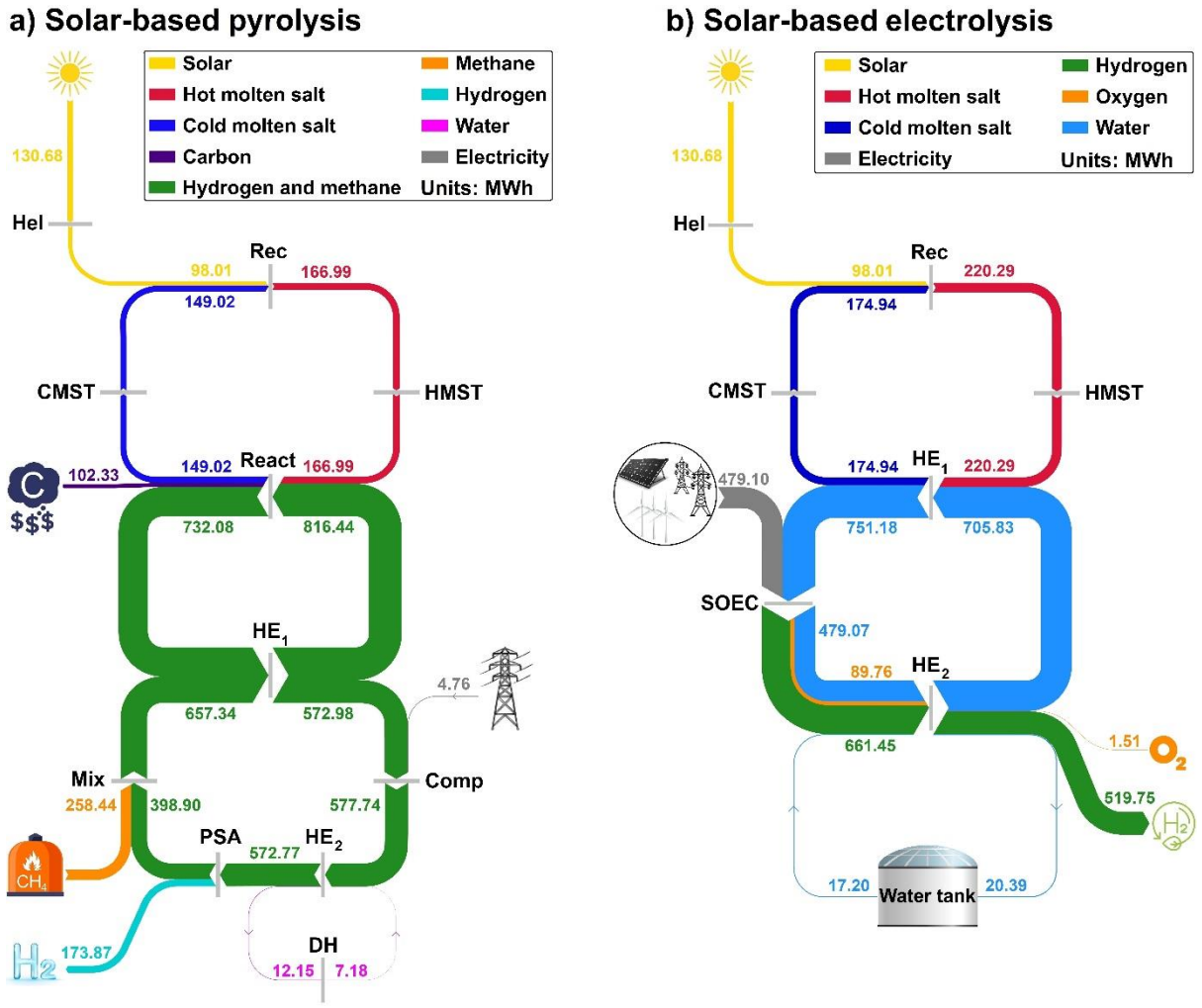

Figure 5.4: Sankey diagrams for a) solar-based molten salt methane pyrolysis (SMSMP) and b) solar-based solid oxide electrolyzer cell (SSOEC). CMST: Cold molten salt tank, Comp: Compressor, DH: District Heating, HE: Heat exchanger, Hel: Heliostat field, HMST: Hot molten salt tank, Mix: Mixer, PSA: Pressure swing adsorption, React: Reactor, Rec: Receiver, SOEC: Solid oxide electrolyzer cell.

In complex energy systems, accurately estimating and thoroughly representing the capital costs of different systems and their equipment is crucial. These accurate estimations are vital for investors to evaluate and select the most appropriate proposal for their certain applications. To meet this

need, the capital expenditure (CAPEX) of the different systems in the proposed systems, in conjunction with their relative shares to the total CAPEX, are illustrated in Figure 5.5.

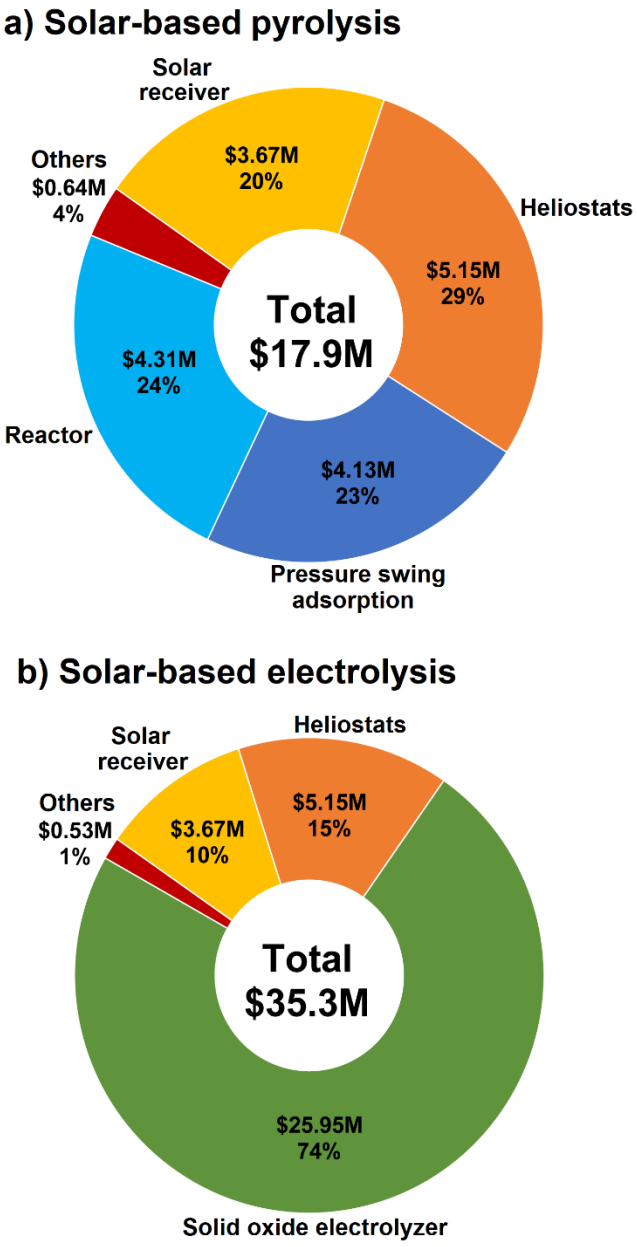

Figure 5.5: Capital expenditure of a) solar-based molten salt methane pyrolysis (SMSMP), b) solar-based solid oxide electrolyzer cell (SSOEC).

This visual representation provides stakeholders with valuable perceptions about the economic implications of different units, aiding in policymaking for the optimum system configurations. As

depicted in Figure 5.5 (a), the total CAPEX for the SMSMP system is approximately $17.9 million, whereas the SSOEC unit has a CAPEX of $35.3 million (Figure 5.5 (b)). The heliostat solar components, including the heliostat field (29%) and the solar receiver (20%), constitute a significant portion of the CAPEX for the SMSMP. In addition, the pyrolysis components, including the reactor (24%) and the PSA (23%), are responsible for 47% of the total costs. In contrast, as shown in Figure 5.5 (b), the SOEC unit itself accounts for 74% of the CAPEX for SSOEC, while only 25% of the CAPEX relates to solar components, including the solar receiver (10%) and the heliostat field (15%). The remaining components account for approximately 4% and 1% of the CAPEX for the SMSMP and the SSOEC systems, respectively.

5.2.3 Parametric analysis

In this section, a thorough parametric analysis is performed to evaluate and contrast the effect of key variables on the efficiency of the SMSMP and the SSOEC units. It is noted that all parameters, excluding the one being analyzed, are kept unchanged according to the specifications provided in Table 5.1.

The heliostat solar unit serves as the mutual element between the proposed systems for SMSMP and SSOEC, with variations in its parameters impacting the performance of both units differently. The most crucial parameters for the solar unit are the solar DNI and available time, whose impacts on RTE, LCOH, and hydrogen production rate are shown in Figure 5.6 and Figure 5.7. The SMSMP relies entirely on the thermal energy provided by the solar unit for hydrogen production, whereas the SSOEC unit uses both thermal and electrical energies for hydrogen production. Consequently, the SMSMP unit is more significantly impacted by solar parameters compared to the SSOEC unit. As shown in Figure 5.6, higher DNI results in more economic and

efficient hydrogen production by both of the proposed systems. The RTE of the SSOEC unit is higher than that of the SMSMP; however, the SMSMP unit can produce more economically viable hydrogen under most solar conditions, except under very poor solar DNIs (e.g., DNI<440 W/m^2). This is because SMSMP is fully dependent on solar thermal energy for the hydrogen production process, leading to a sharp increase in LCOH at low DNIs.

The available solar time is another critical parameter influencing system performance. For the SMSMP and the SSOEC units, increasing solar availability from 4 to 12 hours per day can raise the hydrogen production rate from approximately 2.1 to 6.2 tons/day and 6.1 to 18.4 tons/day, respectively. Correspondingly, the LCOH for the SMSMP can decrease from 4.1 to 2.5 \$/kgH_2, and for the SSOEC, from 5.7 to 5.3 \$/kgH_2. It is also highlighted that the LCOH of the SMSMP can be further reduced by 30 ¢/kgH_2 by selling the solid carbon by-product at a price of 10 ¢/kgC.

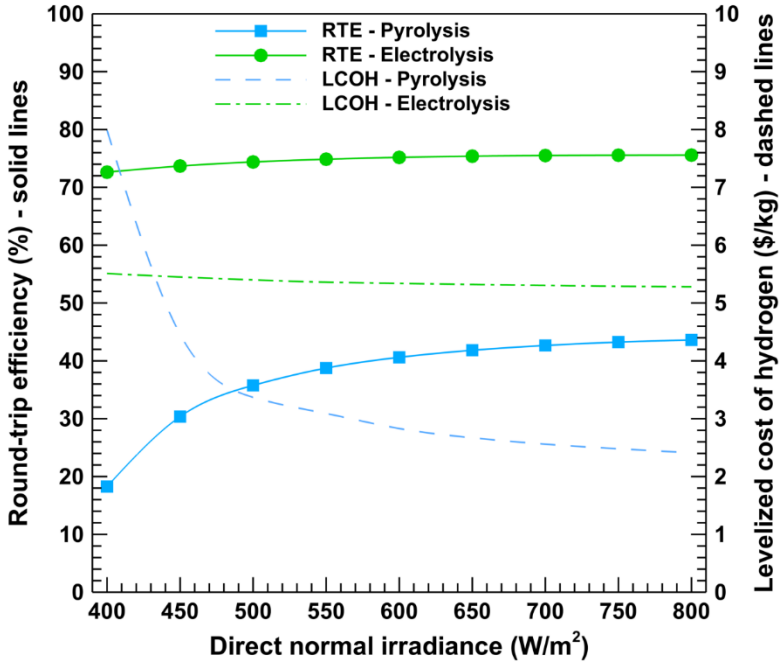

Figure 5.6: The effect of direct normal irradiance (DNI) on round trip efficiency (RTE) and levelized cost of hydrogen (LCOH) by solar-based molten salt methane pyrolysis and solid oxide electrolysis.

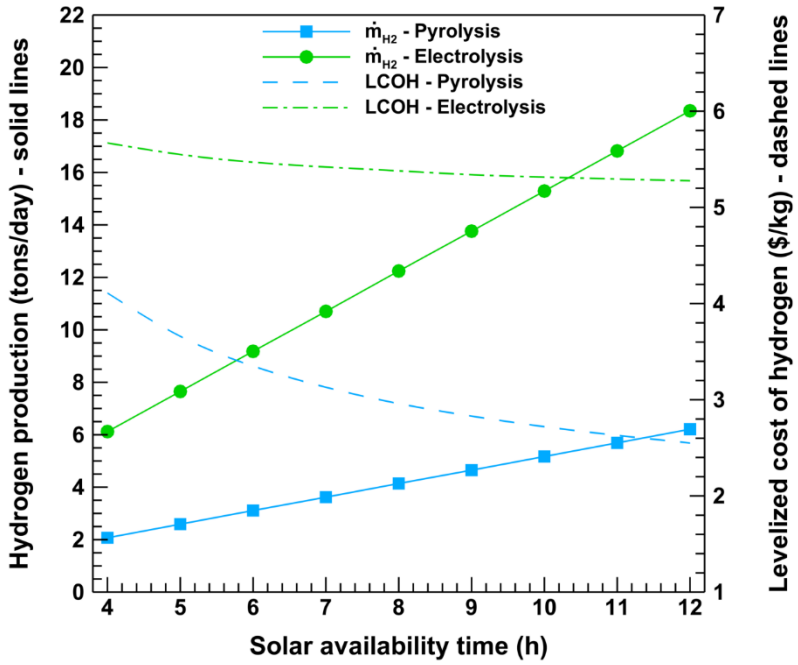

Figure 5.7: The effect of solar available time on the rate of hydrogen production and levelized cost of hydrogen (LCOH) by solar-based molten salt methane pyrolysis and solid oxide electrolysis.

The effect of the number of heliostat mirrors on the capacity of hydrogen production, methane consumption, and water consumption by the SMSMP and SSOEC systems is presented in Figure 5.8. Increasing the number of heliostat mirrors linearly affects the systems' inputs and consequently outputs. As depicted, the SSOEC system produces approximately three times more hydrogen than the SMSMP system, owing to its dual input of electrical and thermal energy. In addition, approximately 4 kg of methane and 9 kg of water are required for the production of 1 kg of hydrogen by the SMSMP and SSOEC units, respectively. Therefore, in addition to solar availability, it is crucial to consider locations with abundant water resources for electrolysis and economical access to methane for pyrolysis.

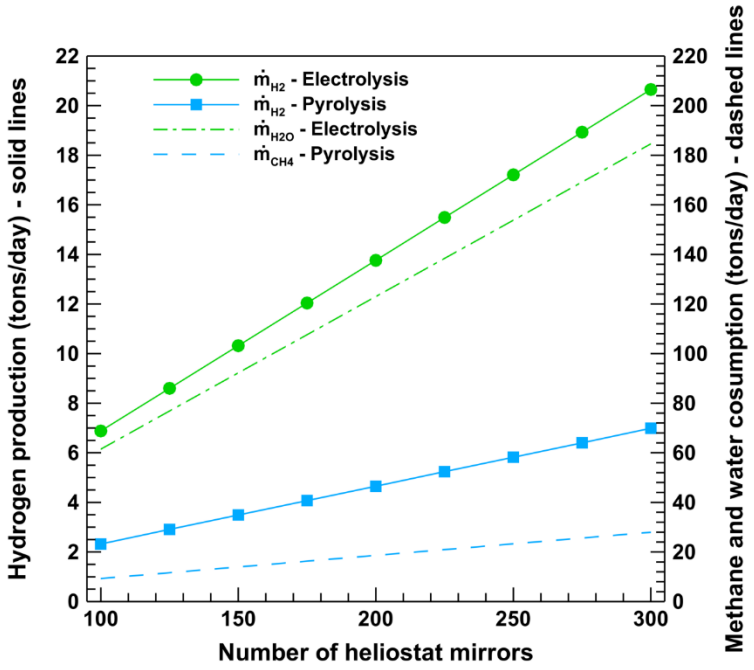

Figure 5.8: The effect of the number of heliostat mirrors on the rate of hydrogen production and methane and water consumption by solar-based molten salt methane pyrolysis and solid oxide electrolysis.

The effect of methane and electricity prices, as the most important economic parameters affecting the LCOH, are shown in Figure 5.9 and Figure 5.10. A higher methane price increases the LCOH of hydrogen production via the SMSMP. In contrast, the LCOH of the SSOEC remains independent of methane price at a constant value of 5.34 $/kg$H_2$. As shown in Figure 5.9, the LCOH of the SMSMP is also influenced by the MCR. A higher MCR results in increased hydrogen production with a consistent heat input, leading to improved performance and a lower LCOH. It is noteworthy that for methane prices below approximately 15 $/GJ (at an MCR of 30%), the SMSMP is more cost-effective than the SSOEC. At the optimal MCR of 90% for methane pyrolysis, the hydrogen production cost via the SSOEC becomes more economical than SMSMP for methane prices of greater than 19 $/GJ. Changes in electricity prices have a negligible impact on the LCOH of the SMSMP, as only the compressor consumes a small amount of electricity in this system. In contrast, electricity prices can significantly affect the LCOH of the SSOEC.

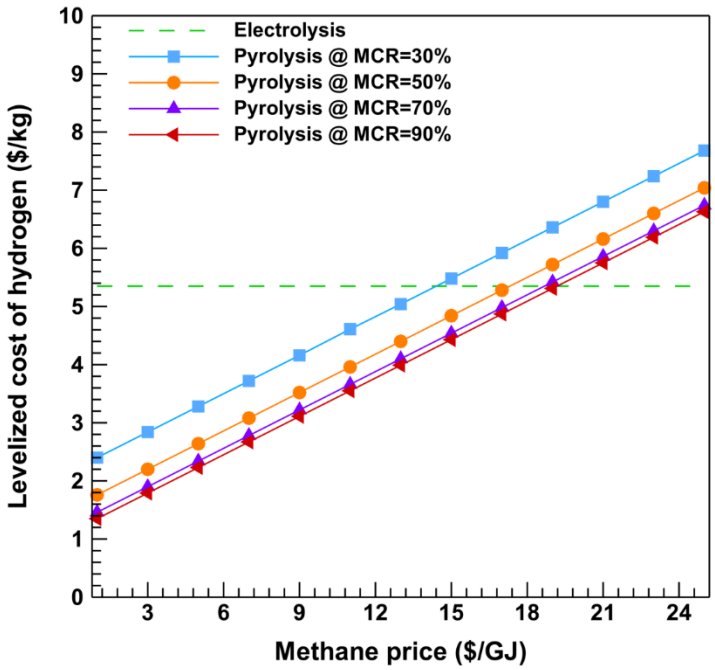

Figure 5.9: The effect of methane price on levelized cost of hydrogen (LCOH) of solar-based molten salt methane pyrolysis and solid oxide electrolysis.

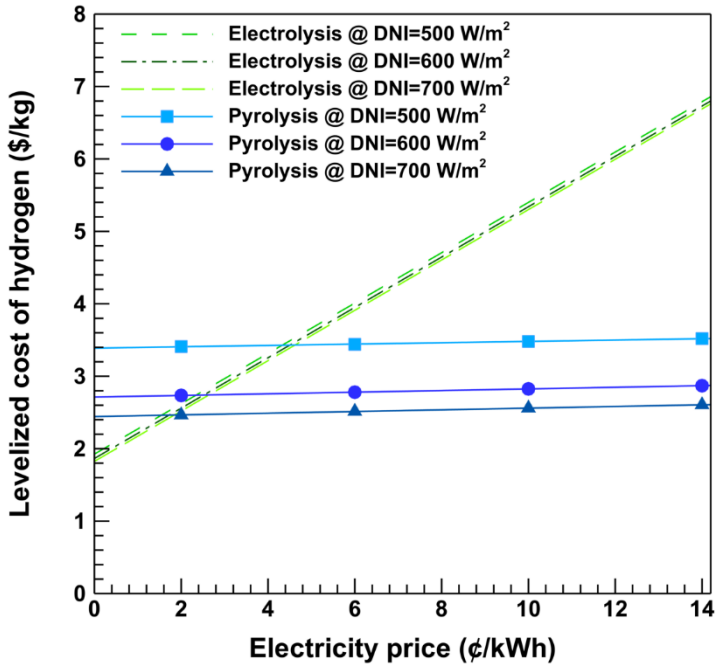

Figure 5.10: The effect of electricity price on levelized cost of hydrogen (LCOH) of solar-based molten salt methane pyrolysis and solid oxide electrolysis.

Moreover, the solar DNI has a negligible effect on the LCOH of the SSOEC but a significant impact on the SMSMP. As shown in Figure 5.10, the SSOEC becomes the preferred option over

the SMSMP at electricity prices lower than approximately 2 and 5 ¢/kWh for the ideal (700 W/m^2) and low (500 W/m^2) solar DNIs, respectively.

The impact of cost reduction in renewable energy infrastructure on the LCOH of the SMSMP and the SSOEC is presented in Figure 5.11. As shown, the LCOH of the SSOEC is significantly influenced by electricity prices or the cost of renewable energy infrastructure. In contrast, there is a minor change in the LCOH of the SMSMP as the only electricity-consuming component in this system is the compressor. The results indicate that a cost reduction of over 90% in renewable energy infrastructure is necessary for the SSOEC to achieve a competitive LCOH compared to the SMSMP (excluding potential revenue from carbon sales). This finding underscores that substantial investments in clean hydrogen tax incentives are essential to make the SSOEC economically competitive with the SMSMP.

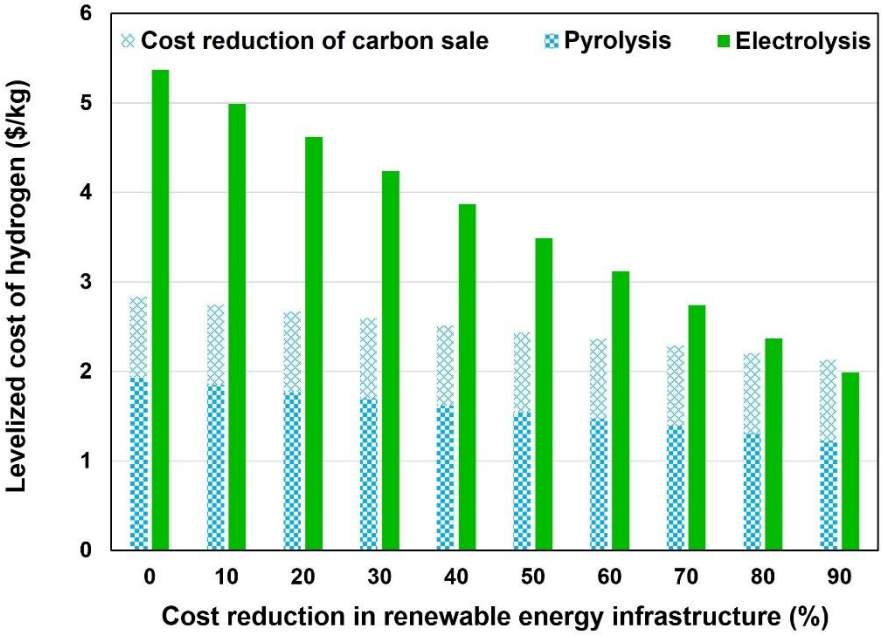

Figure 5.11: The effect of cost reduction in renewable energy infrastructure on levelized cost of hydrogen (LCOH) for solar-based molten salt methane pyrolysis and solid oxide electrolysis.

5.2.4 Case studies

To evaluate and compare the SMSMP and SSOEC technologies, five case studies are conducted in this section by using real hourly solar data, methane prices, and electricity prices.

5.2.4.1 Case study selection

To begin, a pool of fifty randomly selected cities with varying solar conditions and methane prices was compiled, as illustrated in Figure 5.12. These cities are represented based on two key ratios: the ratio of their actual solar DNI to the average DNI ($DNI_{Ave} = 500\,W/m^2$) and the ratio of the methane price in the case studies to the average methane price price ($C_{CH_4,\,Ave} = 5\,\$/GJ$).

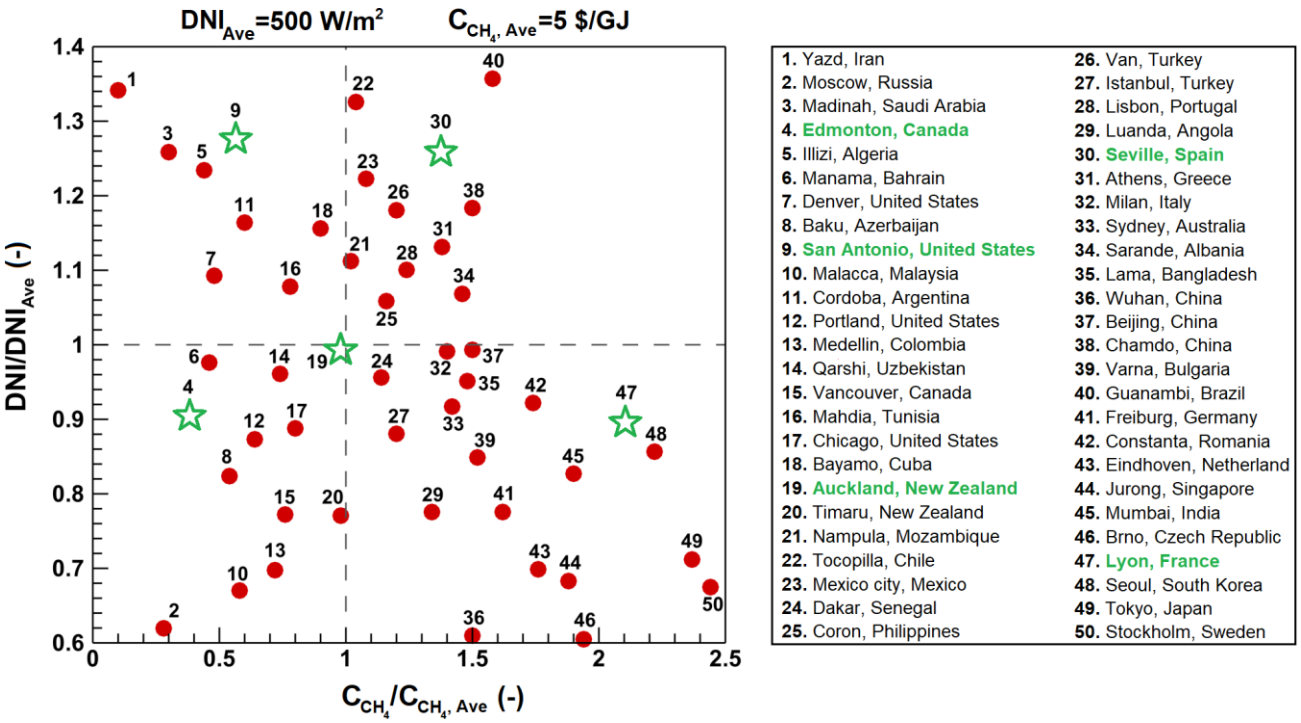

Figure 5.12: Selection of five case studies from fifty candidates all over the world with different solar direct normal irradiances (DNIs) and industrial methane prices (C_{CH_4}) [270][271–280].

From this pool of 50 candidates, five cities—Edmonton, San Antonio, Auckland, Seville, and Lyon—were selected for detailed analysis due to their diverse solar conditions and methane prices.

According to Figure 5.12, Edmonton exhibits low solar DNI and a low methane price, placing it in the lower-left quadrant of the pool. San Antonio, with high solar DNI and relatively affordable methane prices, is positioned in the upper-left quadrant. Auckland represents a city with average solar DNI and methane prices, situating itself at the center of the pool. Seville is characterized by high solar DNI and high methane prices, appearing in the upper-right quadrant, while Lyon, with low solar DNI and high methane prices, is placed in the lower-right quadrant. This selection ensures representation of a wide range of scenarios across diverse global regions, allowing evaluation of how different combinations of solar availability and resource costs affect the feasibility and performance of SMSMP and SSOEC technologies

To provide a more comprehensive comparison of the selected cities, a spider map based on five critical parameters—solar DNI, solar time, grid carbon intensity, electricity price, methane price, and methane carbon intensity—is presented in Figure 5.13. The map illustrates that San Antonio and Seville have more favorable solar conditions in terms of DNI and time, while Edmonton and Lyon exhibit weaker solar conditions. Conversely, industrial methane price and methane carbon intensity are significantly lower in Edmonton and San Antonio compared to Seville and Lyon. Auckland displays moderate solar conditions and a moderate methane price, aligning with the average values depicted in Figure 5.12. The grid electricity price and carbon intensity are the other crucial factors that significantly influence the economic and environmental aspects of the SSOEC system. Due to the substantial reliance on fossil fuels for power generation in Edmonton and San Antonio, these cities have higher grid carbon intensity than the other case studies. In contrast, Auckland, Seville, and Lyon benefit from lower carbon intensity, owing to a higher proportion of renewable energy sources in their power generation mix. Among the selected case studies, Edmonton also has the highest electricity price.

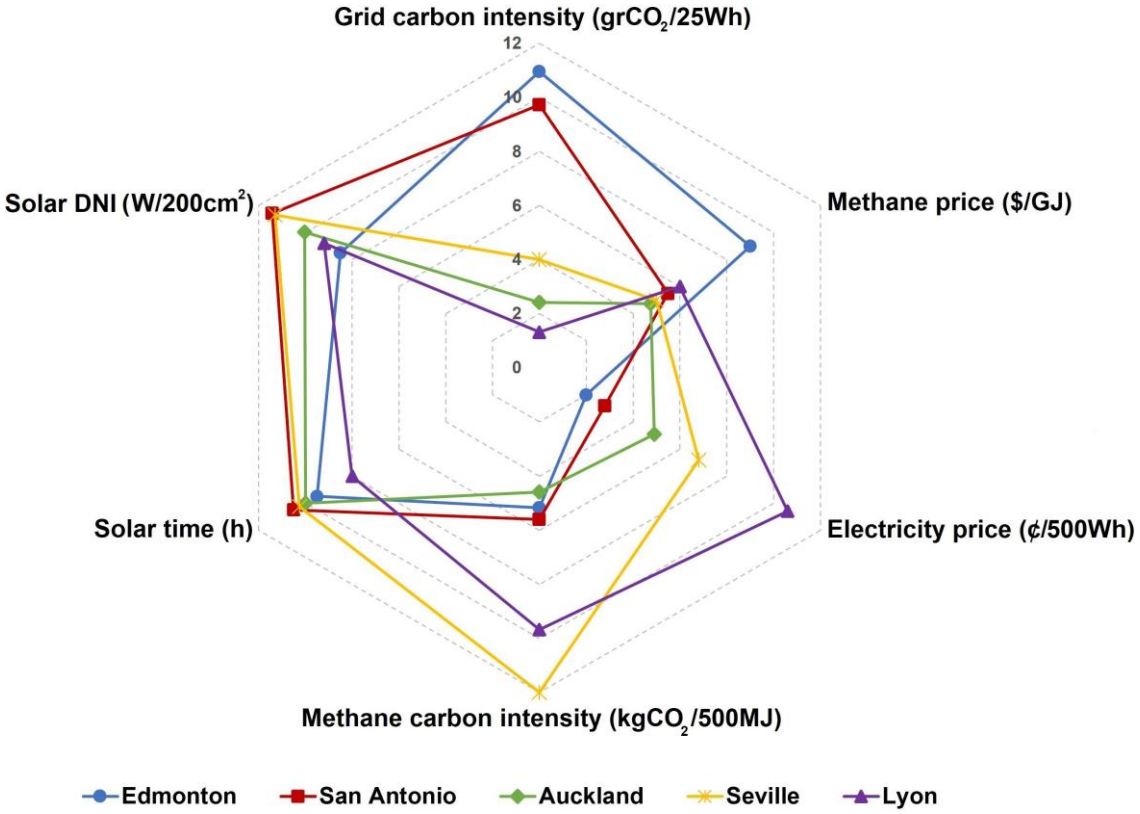

Figure 5.13: The spider chart presentation of the values of the major critical parameters for the five selected case studies [273–285].

5.2.4.2 Hydrogen production by case studies

The annual hourly DNI and the corresponding hydrogen production rates for the SMSMP and SSOEC systems in the selected case studies are illustrated in Figure 5.14 to Figure 5.18. The dynamic DNI values, spanning the entire year from the first hour of January to the last hour of December (8760 hours), are sourced from the latest solar data published (2022) by the National Renewable Energy Laboratory (NREL). As Figure 5.14 (b), approximately 484 tons of hydrogen can be produced annually by the SMSMP in the Edmonton case study. While, with the same solar field capacity, about 3,368 tons of hydrogen—seven times the amount from pyrolysis—can be produced by the SSOEC. This significant difference is due to the dual input of the SSOEC (thermal and electrical), which makes it less dependent on solar conditions. The cold winters and limited

solar availability (Figure 5.14 (b)) in Edmonton result in a low hydrogen production rate during winter, posing a significant barrier to solar-based hydrogen production in this region. Conversely, due to the high intensity and duration of sunlight, approximately 62% of the total annual hydrogen production occurs during summer.

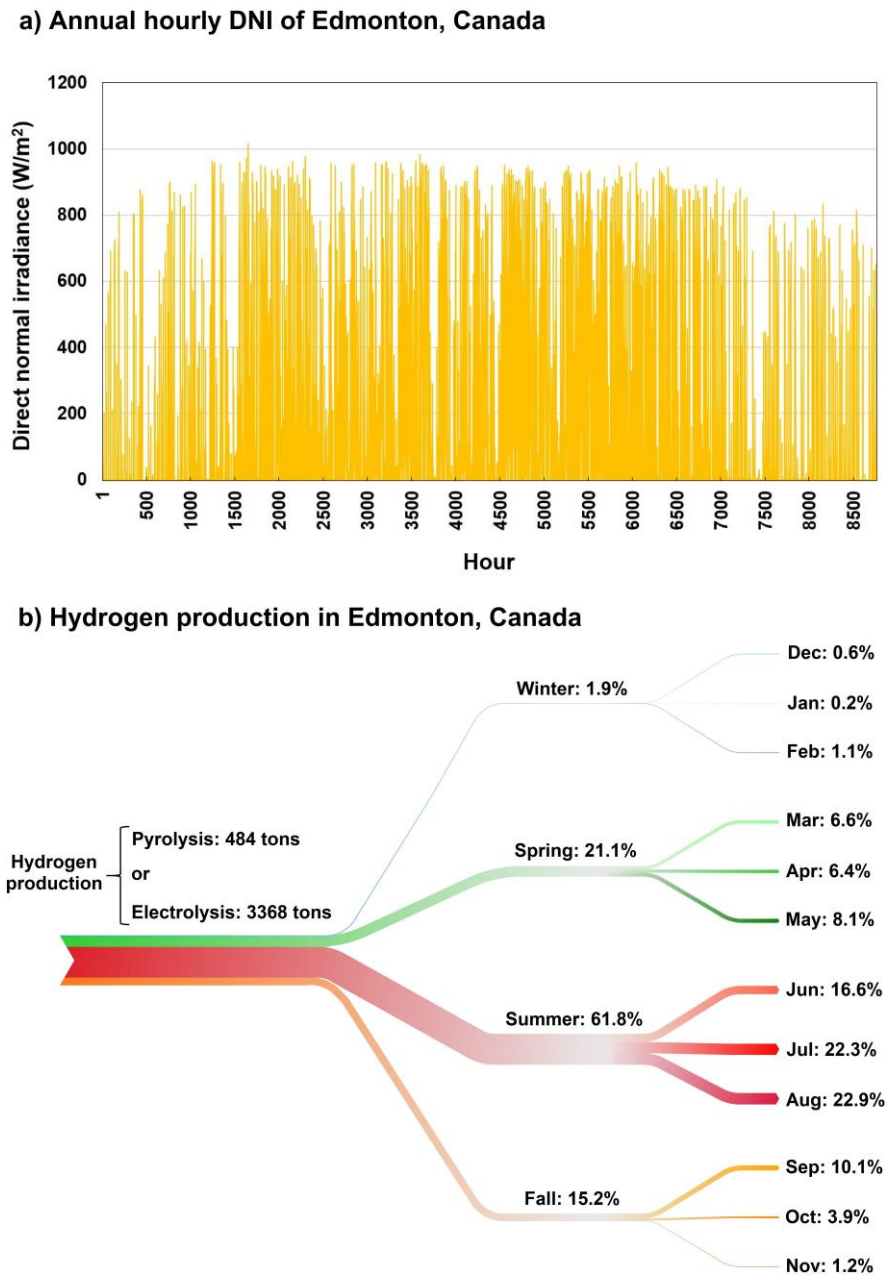

Figure 5.14. (a) Annual hourly direct normal irradiance (DNI) and b) annual, seasonal, and monthly hydrogen production by solar-based molten salt methane pyrolysis (SMSMP) and solar-based solid oxide electrolyzer cell (SSOEC) for the case study of Edmonton, Canada.

In contrast to the solar condition of Edmonton, a comparable seasonal trend in DNI (Figure 5.15 (a)) and hydrogen production (Figure 5.15 (b)) can be observed in San Antonio, making it an attractive location for solar-based hydrogen production.

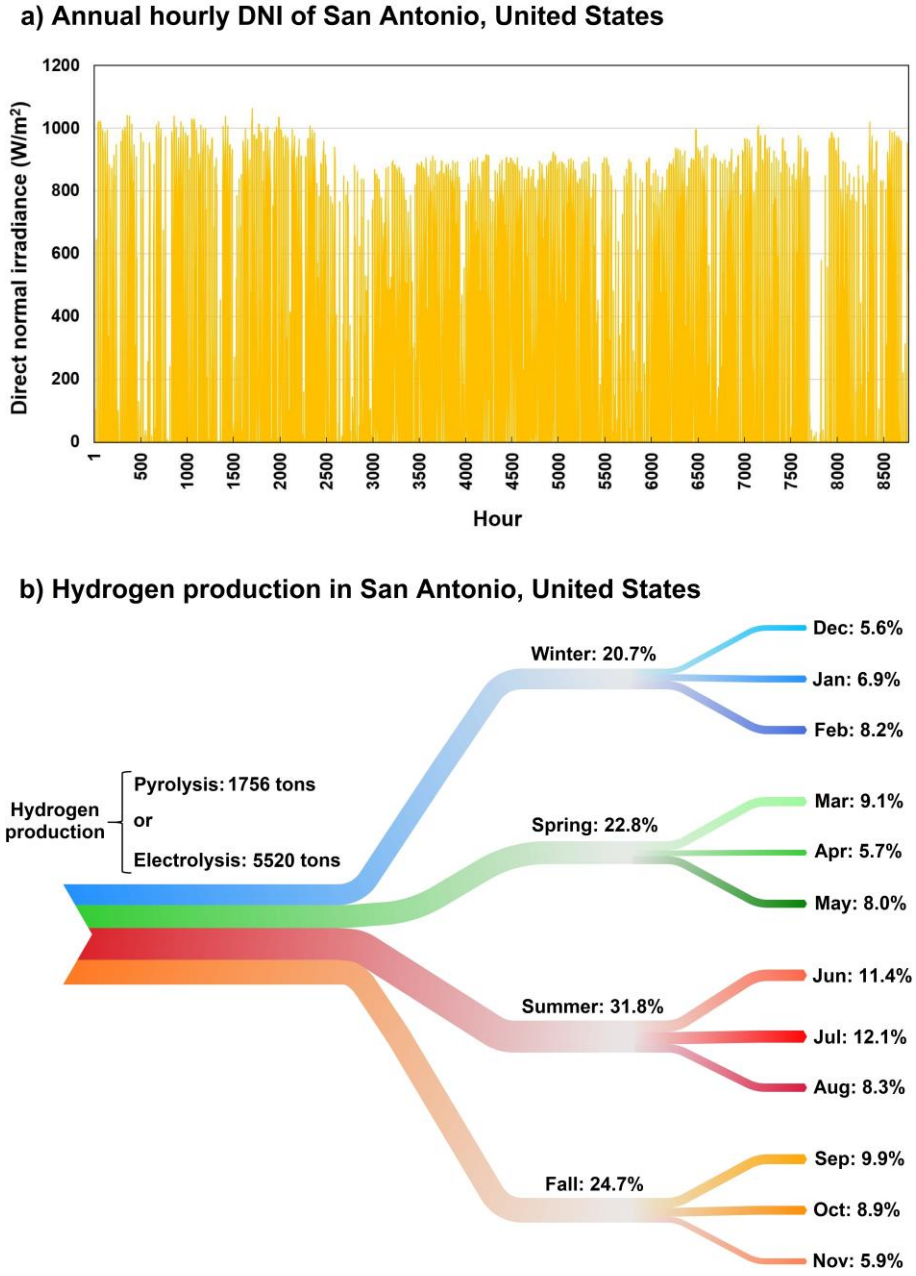

Figure 5.15. (a) Annual hourly direct normal irradiance (DNI) and b) annual, seasonal, and monthly hydrogen production by solar-based molten salt methane pyrolysis (SMSMP) and solar-based solid oxide electrolyzer cell (SSOEC) for the case study of of San Antonio, United States.

The better availability of solar energy in San Antonio yields approximately 1,756 tons of hydrogen by the SMSMP and 5,520 tons of hydrogen by the SSOEC, which means about 3.1 times more hydrogen production via the SMSMP, as shown in Figure 5.15.

In addition, the solar DNI and hydrogen production rates by the SMSMP and the SSOEC in Auckland are illustrated in Figure 5.16. As shown in Figure 5.16 (a), due to Auckland's location in the Southern Hemisphere, its hot seasons are opposite to those in the Northern Hemisphere. Consequently, according to Figure 5.16 (b), over 48% of the total annual hydrogen is produced from December to February, when solar radiation is at its peak. Given its moderate solar conditions, the hydrogen production by the SSOEC (4,460 tons) is 3.9 times that of the SMSMP (1,135 tons).

Figure 5.17 illustrates the annual solar DNI and hydrogen production rates achieved through SMSMP and SSOEC technologies in Seville. The results highlight that over 46% of the total annual hydrogen is produced during the summer months, while production in the other seasons remains relatively consistent, with variations of less than 5%. This seasonal distribution is attributed to Seville's exceptional solar conditions, as shown in Figure 5.17 (a), which make it highly suitable for solar-driven hydrogen production. The comparative performance of the two technologies reveals that approximately 5,322 tons of hydrogen can be generated annually using the SSOEC system—approximately 3.2 times the production capacity of the SMSMP system, which produces 1,669 tons annually. This substantial production capability underscores Seville's potential as a strategic hub for the deployment of solar-based hydrogen production systems

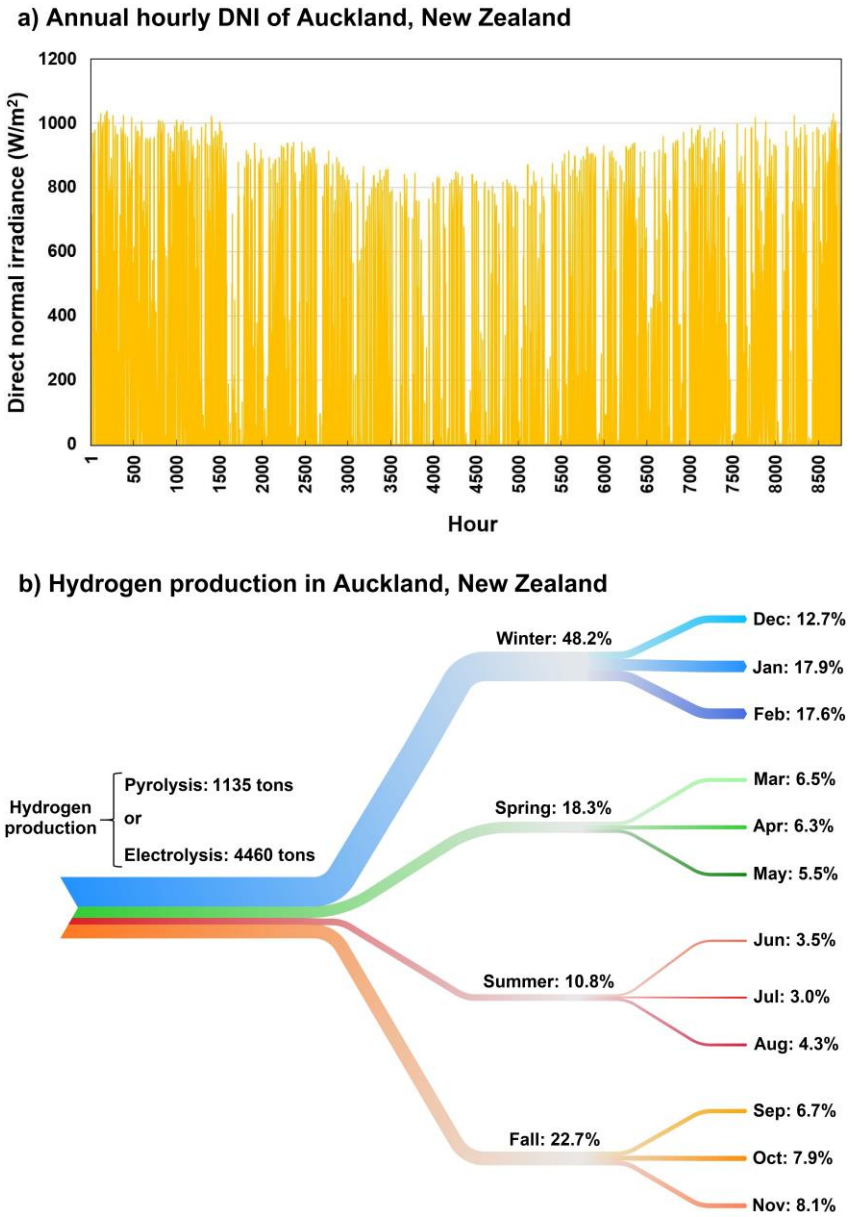

Figure 5.16. (a) Annual hourly direct normal irradiance (DNI) and b) annual, seasonal, and monthly hydrogen production by solar-based molten salt methane pyrolysis (SMSMP) and solar-based solid oxide electrolyzer cell (SSOEC) for the case study of Auckland, New Zealand.

Finally, the annual hourly solar DNI, along with the annual, seasonal, and monthly hydrogen production levels in Lyon are presented in Figure 5.18. Unlike Seville, less than 3% of the total annual hydrogen is produced during the winter and fall seasons. However, the summer season significantly compensates for this disparity, contributing over 74% of the total annual hydrogen output. Remarkably, Lyon's summer hydrogen production surpasses the entire annual production of Edmonton, as shown in Figure 5.18. The comparison between the two technologies indicates

that the SMSMP system produces approximately 3,194 tons of hydrogen annually, which is nearly 4.9 times the production capacity of the SSOEC system, at 654 tons. This stark difference highlights the critical role of technology selection and local solar conditions in optimizing hydrogen production potential.

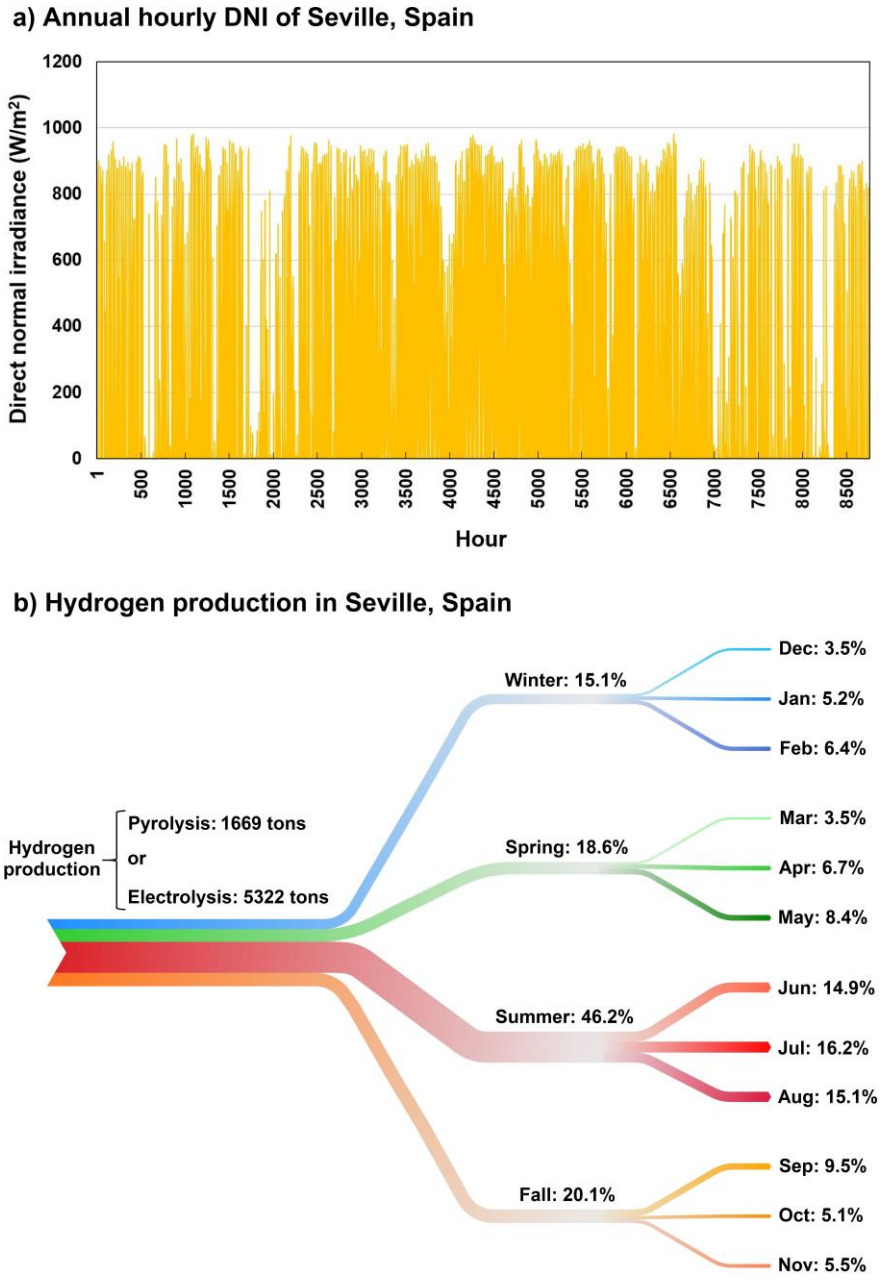

Figure 5.17. Annual, seasonal, and monthly hydrogen production by solar-based molten salt methane pyrolysis (SMSMP) and solar-based solid oxide electrolyzer cell (SSOEC) for the case study of Seville, Spain.

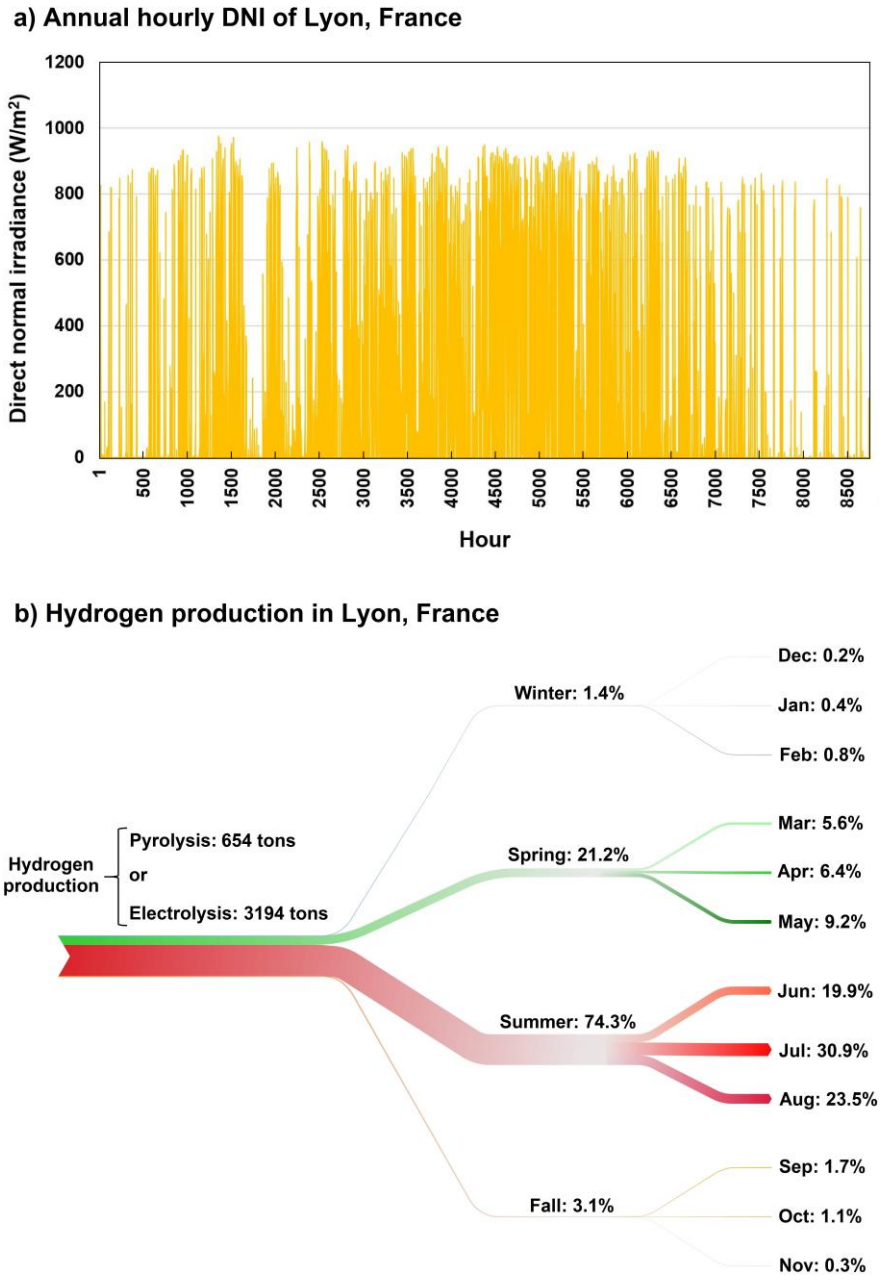

Figure 5.18. (a) Annual hourly direct normal irradiance (DNI) and b) annual, seasonal, and monthly hydrogen production by solar-based molten salt methane pyrolysis (SMSMP) and solar-based solid oxide electrolyzer cell (SSOEC) for the case study of Lyon, France.

4.4.3. Summary of case study results

A comprehensive summary of the results of the five case studies is presented in Table 5.6. The analysis indicates that, across all case studies, hydrogen production via the SMSMP method is

more cost-effective than the SSOEC method. Despite Edmonton benefiting from the lowest methane price among the studied cities, it ranks second in terms of the most expensive LCOH production by the SMSMP (4.49 $/kg$H_2$), primarily due to its poor solar conditions. Furthermore, Edmonton has the highest LCOH (8.23 $/kg$H_2$) and carbon intensity (15.24 kgCO_2/kgH_2) for hydrogen production using the SSOEC, attributed to its expensive and carbon-intensive grid electricity. These results indicate that, although Edmonton is one of the Canadian cities with high solar potential, solar-based hydrogen production, particularly through electrolysis, is not an economically viable option. In contrast, San Antonio, with its excellent solar conditions, has the lowest LCOH for SMSMP (2.31 $/kg$H_2$), potentially dropping to 1.41 $/kg$H_2$ with the future opportunities for solid carbon sale with a cost of 300 $/ton. It also has an average LCOH for SSOEC (5.66 $/kg$H_2$), albeit with a high carbon intensity (13.54 kgCO_2/kgH_2). Auckland's lower solar potential, methane, and electricity prices compared to Seville result in similar LCOH values for both SMSMP and SSOEC. This underscores the critical need for meticulous consideration of all influencing factors, including solar conditions and the prices of electricity and methane, due to their intricate interdependencies. Notably, Auckland achieves the lowest carbon intensity for hydrogen production via SMSMP and ranks second lowest for SSOEC, attributable to its clean national methane extraction processes and grid electricity. Finally, like Edmonton, Lyon suffers from inadequate solar conditions for both SMSMP and SSOEC, with LCOH values of 5.56 $/kg$H_2$ and 6.17 $/kg$H_2$, respectively. However, Lyon's SSOEC method boasts the lowest carbon intensity for hydrogen production among all the cities analyzed. Therefore, providing a balance between economic feasibility and environmental impact is of paramount importance in the pursuit of sustainable hydrogen production. It is also worthy to mention that the results presented in Table 5.6 are highly depend on the current solar conditions, methane and grid carbon intensities, and

methane and grid electricity prices in these five cities, indicated in Figure 5.19. Therefore, any change in these data will affect the conclusions of this study.

Table 5.6: Summary of the techno-economic results for the five case studies.

Parameter (Units)	Case studies				
	Edmonton	San Antonio	Auckland	Seville	Lyon
Annual methane consumption by the SMSMP (ton)	1936	7024	4540	6676	2616
Annual hydrogen production by the SMSMP (ton)	484	1756	1135	1669	654
$LCOH_{SMSMP}$ @ no solid carbon sale ($/kg$H_2$)	4.49	2.31	3.26	3.23	5.56
$LCOH_{SMSMP}$ @ solid carbon sale of 300 $/ton ($/kgH_2)	3.59	1.41	2.36	2.33	4.66
Carbon intensity of hydrogen production by the SMSMP (kgCO_2/kgH_2)	2.34	2.51	2.01	5.27	4.19
Annual electricity consumption by the SSOEC (GWh)	117	192	155	185	111
Annual hydrogen production by the SSOEC (ton)	3368	5520	4460	5322	3194
$LCOH_{SSOEC}$ ($/kg$H_2$)	8.23	5.66	5.19	5.32	6.17
Carbon intensity of hydrogen production by the SSOEC (kgCO_2/kgH_2)	15.24	13.54	3.37	5.57	1.84

As a conclusion, three conclusive maps illustrating the selection criteria for the SMSMP and SSOEC, based on the electricity and methane prices under varying solar conditions, are presented in Figure 5.19 (a-c). As depicted in Figure 5.19 (a), due to the full dependency of the SMSMP on solar conditions, the SSOEC is preferable across a broader range of methane and electricity prices over the SMSMP within the ideal solar conditions. Furthermore, the potential positive impact of selling solid carbon at prices up to 300 $/ton is highlighted for a more comprehensive comparison. Under average solar conditions, as shown in Figure 5.19 (b), the solid carbon sale significantly enhances the competitiveness of the SMSMP over the SSOEC. Lastly, under ideal solar conditions, depicted in Figure 5.19 (c), the SMSMP emerges as the dominant technology over the SSOEC. The substantial change observed from low to average solar conditions, compared to the change from average to ideal conditions, can be attributed to the sharp decrease in the LCOH for the SMSMP process, as illustrated in Figure 5.6.

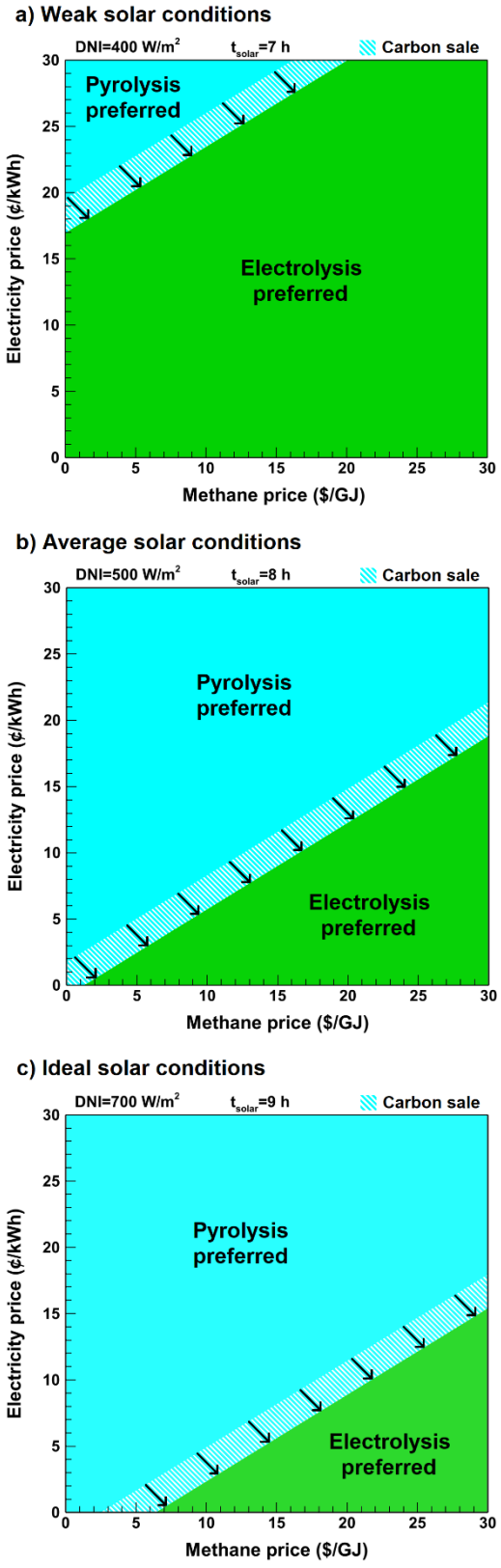

Figure 5.19: A comparison of solar-based pyrolysis vs electrolysis preference based on methane and electricity prices for a) weak, b) average, and c) ideal solar conditions.

5.3 Summary of chapter

Clean hydrogen production is essential for decarbonizing transportation, industry, and power generation, serving as a vital energy carrier and storage solution. Solar-based hydrogen production offers a sustainable and emission-free solution, which can advance renewable technologies and promote a circular economy, making it a critical element in achieving a sustainable energy future. This chapter provides a comparative techno-economic analysis of two innovative methods: solar-based molten salt methane pyrolysis (SMSMP) and solar-based solid oxide electrolyzer cell (SSOEC) for low-carbon and economic hydrogen production. To ensure a realistic comparison, a comprehensive case study involving five cities—Edmonton, San Antonio, Auckland, Seville, and Lyon—is presented. A summary of the main conclusions of this study is presented as follows:

- The investigation of the SMSMP and SSOEC systems revealed that the SSOEC unit, with its dual inputs of electrical and thermal energies, can produce significantly more hydrogen with the same solar capacity. Under the design conditions, the round-trip efficiency of the SMSMP was found to be 40.6%, compared to 75.2% for the SSOEC. However, the levelized cost of hydrogen (LCOH) produced by the SMSMP is lower, at 2.83 \$/kgH_2, compared to 5.34 \$/kgH_2 for the SSOEC. Additionally, the capital investment cost for the SMSMP, with a daily hydrogen production capacity of 4.65 tons is \$17.9 million. In comparison, the SSOEC, which produces 13.76 tons per day of hydrogen, requires an investment cost of \$35.3 million.

- A comparison of the SMSMP and SSOEC based on solar availability, methane, and electricity prices indicates that due to the SMSMP's full dependency on solar conditions, it is preferable across a broader range of methane and electricity prices under average to

ideal solar conditions. However, the SSOEC may present a more favourable option in instances of poor solar conditions, depending on grid carbon intensity and electricity prices.

- The case studies revealed how various parameters, such as solar conditions, methane and electricity prices, and carbon intensity, can intricately affect the economic and environmental aspects of hydrogen production by the SMSMP and SSOEC methods. For example, despite Edmonton benefiting from the lowest methane price among the studied cities, it ranks second in terms of the most expensive LCOH production by the SMSMP (4.49 $\$/kgH_2$), primarily due to its poor solar conditions. The most economical (2.31 $\$/kgH_2$) and cleanest (2.01 $kgCO_2/kgH_2$) hydrogen produced by the SMSMP can be found in San Antonio and Auckland, respectively. However, the cheapest hydrogen by the SSOEC can be produced in Auckland (5.19 $\$/kgH_2$) and Seville (5.32 $\$/kgH_2$), whereas the cleanest hydrogen can be generated in Lyon (1.84 $kgCO_2/kgH_2$).
- The investigations, considering potential future cost reductions of up to 90% in renewable infrastructure, indicated that the LCOH of the SSOEC would neither reach the LCOH achieved by the SMSMP, nor the target of 1 $\$/kgH_2$. Hence, it is imperative for governments to implement incentivizing policies such as clean hydrogen tax incentives to enhance the economic viability of the SSOEC if aiming for clean hydrogen production.

5.4 Uncertainty consideration

This analysis considers key economic parameters, including capital investment, operating and maintenance costs, and interest rates, in accordance with established practices in the literature. However, certain detailed cost elements, such as engineering, installation, insurance, and other ancillary expenses, have been excluded from the scope of this study. These exclusions introduce a degree of uncertainty, as they represent significant cost factors that could materially influence the overall economic performance of the system.

Moreover, the current temperature limit of approximately 700°C for commercialized heliostat fields utilizing molten salt is primarily dictated by corrosion issues at higher temperatures. This constraint not only impacts the system's technical performance but also affects both capital and operational costs. The primary objective of this work is to identify the substantial potential for improving the temperature capabilities of molten salt-based heliostat systems, thereby fostering further research and development efforts in the advancement of high-temperature solar thermal fields.

Future analyses should address these uncertainties by incorporating a more comprehensive set of cost factors, including those associated with higher temperature materials, corrosion-resistant technologies, and related system costs. Additionally, these analyses should integrate up-to-date, reliable cost functions and data as they become available. Such enhancements would significantly strengthen the robustness and reliability of the economic analysis, aligning it more closely with real-world conditions and creating a foundation for the development of more cost-effective and technically advanced solutions in the field.

Chapter 6: Hydrogen-Based Combined Heat and Power Systems[1]

This chapter presents a case study centered on the energy management of the University of Alberta (UofA) by comparing solid oxide fuel cell (SOFC)- and hydrogen internal combustion engine (HICE)-based CHPs. The HICE-based combined heat and power (CHP), with direct nitrogen oxide (NOx) emissions exceeding 4 tons, has lower capital ($140 million) and annual maintenance costs ($24.25 million) but higher environmental impacts. In contrast, the SOFC-based CHP, though more expensive ($280 million capital and $66.32 million annual maintenance costs), is expected to become economically competitive with technological advancements in the future. Currently, the HICE-based CHP is the more feasible option from the economic perspective, but the SOFC-based system holds greater promise as a sustainable, long-term solution for campus energy management. In addition, a techno-economic and environmental analysis of SOFC-based CHP systems was presented for the residential and commercial sectors in Alberta and Canada, examining their market potential, economic viability, job creation prospects, and environmental benefits. The findings indicate that SOFC-based CHP systems are positioned to drive significant market growth, create thousands of jobs, and contribute to substantial greenhouse gas (GHG) emissions reductions. By 2050, these systems are projected to generate $2.5 billion in Alberta and $15 billion across Canada, with the commercial sector capturing 80% of the total revenue. Job creation estimates suggest approximately 2,300 positions in Alberta and 13,800 across Canada by mid-century. Environmentally, SOFC-based CHPs could reduce GHG emissions by 1.6 million tons in Alberta's commercial sector and 7.8 million tons nationwide.

[1] This chapter is partially based on [6,7].

6.1 System description

In his section, the designed hydrogen-based CHP systems for UofA, Alberta, and Canada are described in details.

6.1.1 Hydrogen-based CHPs for the University of Alberta

UofA is one of Canada's leading post-secondary institutions, known for its extensive campus infrastructure and diverse academic community. The university operates across five campuses, including the main North Campus, which collectively host a population of over 60,000 students, staff, and faculty members. Spanning approximately 4 km^2, the campuses include 50 city blocks and over 150 buildings. The main campus includes a wide variety of buildings, such as advanced research laboratories, classrooms, student residences, libraries, and recreational facilities, a hospital, etc., each with unique energy requirements [286]. Meeting these diverse energy demands requires an advanced energy management system that ensures the reliable provision of electricity, heating, cooling, and ventilation while minimizing energy waste and greenhouse gas (GHG) emissions [287].

Located in Edmonton, Alberta, the UofA faces unique energy challenges due to the region's cold climate, characterized by extreme temperature variations ranging from below -30°C in winter to over 30°C in summer [288]. These fluctuations necessitate highly efficient energy systems capable of adapting to seasonal demands, with a significant focus on heating during the long winters and cooling during shorter but intense summers. The university addresses these challenges through a centralized district energy system, including CHP plants, which optimize the simultaneous production of electricity and heat. Currently a significant portion of the required electricity of the UofA is generated on-site through natural gas-fueled steam turbine generators,

supported by standby diesel generators for backup. The UofA Heating Plant houses two primary steam turbines: TG-1, a 13.3 MW back-pressure turbine installed in 1994, and TG-2, a 26.4 MW condensing turbine added in 2000. Together, these two turbines provide a peak output of approximately 45 MW, which covers about half of the university's annual electricity demand of 340 GWh, with a peak load of 67 MW. Additionally, three 1.5 MW diesel generators provide resilience during outages or periods of high demand, while 500 kW of PV capacity adds renewable energy to the mix [287].

A key focus of the UofA's energy management strategy is currently the advancement of low-carbon energy solutions [289]. This includes the integration of renewable energy infrastructure and the adoption of clean fuel technologies to promote sustainability and reduce carbon emissions [290]. As the province of Alberta positions itself as a global hydrogen hub [291], UofA's research and innovation in clean hydrogen energy systems play a critical role in shaping this transition. Aligned with Alberta's ambition as a global hydrogen hub, UofA can be the forefront of research and innovation in clean hydrogen energy systems, contributing to this transition [292].

A preliminary evaluation conducted on the feasibility of installing photovoltaic (PV) solar panels on university buildings revealed that such installations would fall short of meeting the campus's total electricity demand. In addition to their limited power generation capacity, rooftop PV systems face significant economic challenges, primarily due to the substantial capital expenditure associated with procuring and installing separate inverters and ancillary components for each building [290]. Therefore, an alternative solution, such as developing an off-site solar or wind farm around Edmonton, could offer a more cost-effective and scalable way to meet the campus's electricity demand, depending on university policies and external factors. On the other hand, hydrogen procurement emerges as a more practical option for the UofA, particularly in light

of Edmonton’s ambitious plans as the first hydrogen hub in Canada [291]. Direct hydrogen purchase, instead of developing costly on-site or off-site hydrogen production facilities, offers an efficient pathway to address both electricity and heat requirements for the campus. This approach supports a streamlined and sustainable energy strategy, enhancing the university’s overall energy resilience and reducing its carbon footprint. This study focuses on the assessment for the utilization of hydrogen for managing the university's heat and electricity demands. This study investigates the integration of hydrogen into the existing campus infrastructure, evaluating its potential to provide an efficient, and sustainable energy solution.

Figure 6.1 (a) presents a schematic representation of the UofA's main campus, highlighting the various buildings, the current thermal energy storage’s and power plant's locations, and the designated site for the proposed future CHP systems. To advance the sustainable development of heat and power management at the university, as shown in Figure 6.1, two innovative hydrogen-based systems are considered: SOFC-based CHP and HICE-based CHP. These technologies have been selected for their potential to significantly reduce carbon emissions while enhancing energy efficiency and grid stability, aligning with the university's long-term sustainability goals. The SOFC-based CHP system operates by converting hydrogen into electricity and heat through a high-temperature electrochemical process, characterized by high efficiency and minimal GHG emissions. The data for the SOFC-based CHP system, as shown in Figure 6.1 (b), is sourced from FuelCell Energy, a major provider of solid oxide fuel cells technologies [293]. Their proven solutions provide reliable and efficient power generation, offering a proper benchmark for this study. In parallel, the HICE-based CHP system, as shown in Figure 6.1 (c), utilizes hydrogen as the fuel for internal combustion engines to generate both electrical power and thermal energy. This approach is particularly notable for its adaptability to existing internal combustion engine technologies, allowing for a smoother transition towards decarbonization. The performance data

for the HICE-based CHP system is provided by 2G Energy, a well-recognized company specializing in hydrogen-based CHP systems [93].

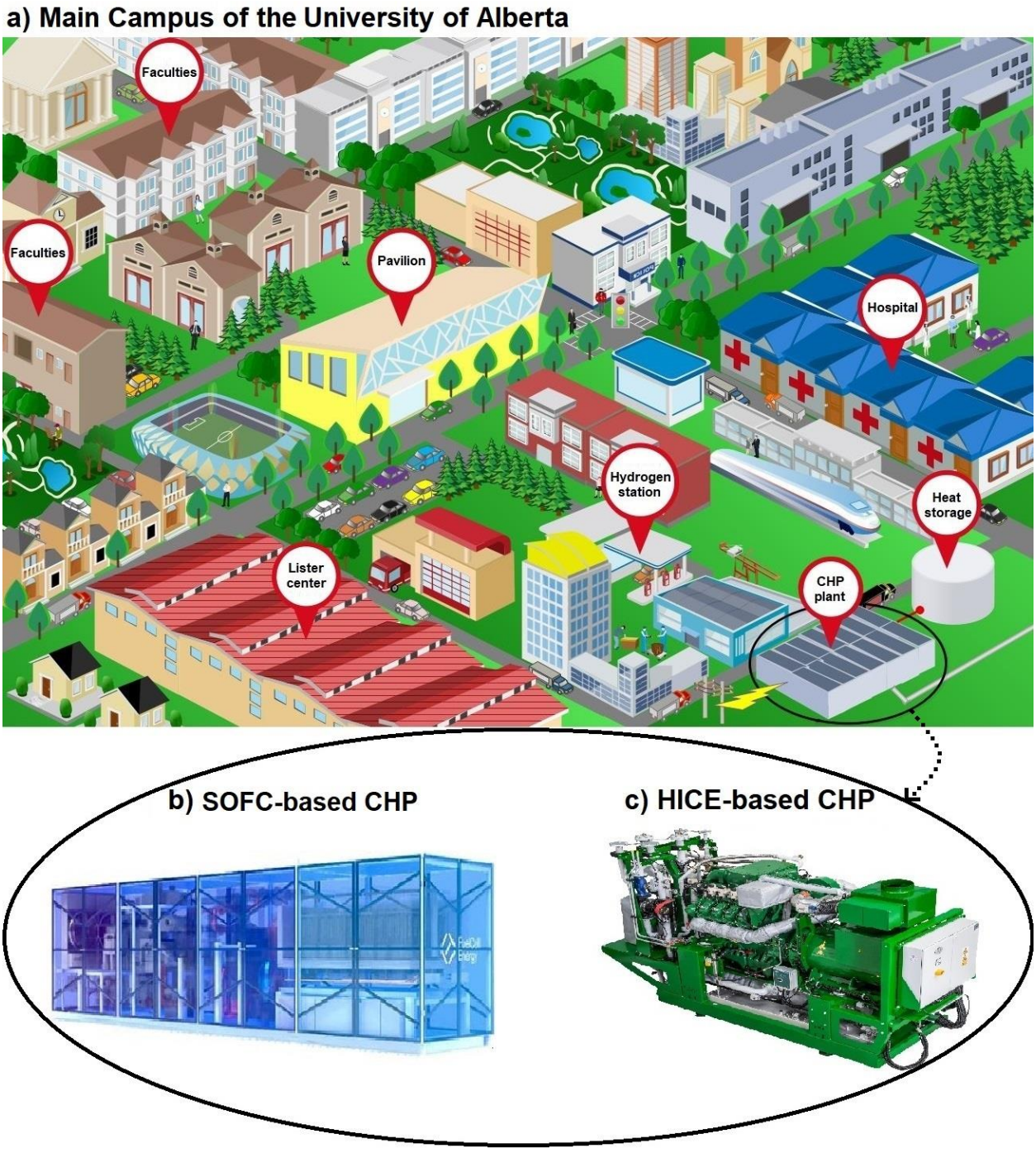

Figure 6.1. a) Schematic diagram of the main campus of the University of Alberta and the planned location for installing either b) solid oxide fuel cell (SOFC)-based combined heat and power (CHP) (FuelCell Energy [293]), or c) hydrogen fuelled internal combustion engine (HICE)-based CHP (2G Energy [93]) at the University of Alberta.

To address the additional heating demand at the UofA during the extreme winter conditions, modern air-source heat pumps [294] are considered as a viable solution from a sustainability perspective. The heat content of air at -18°C is about 85% of the heat contained at 21°C, thus heat can be provided by using heat pumps even at very low temperatures by transferring thermal energy from cold air to the buildings [295]. Today's advanced air-source heat pumps can capture the outdoor heat and use it for heating applications. For example, in extremely cold climates, where temperatures can plummet to -30°C or lower, the modern air-source heat pumps of the Mitsubishi model have proven to operate effectively with a coefficient of performance (COP) as high as 2 [296]. An experimental study conducted by Oak Ridge National Laboratory in Alaska demonstrated the capabilities of modern heat pump technologies in such harsh conditions, showing that these heat pumps can maintain a COP of 1.8 even at temperatures as low as -35°C [297]. This performance underscores the potential of modern heat pumps to provide efficient and sustainable heating solutions for institutions like UofA, particularly in regions with prolonged and severe winters.

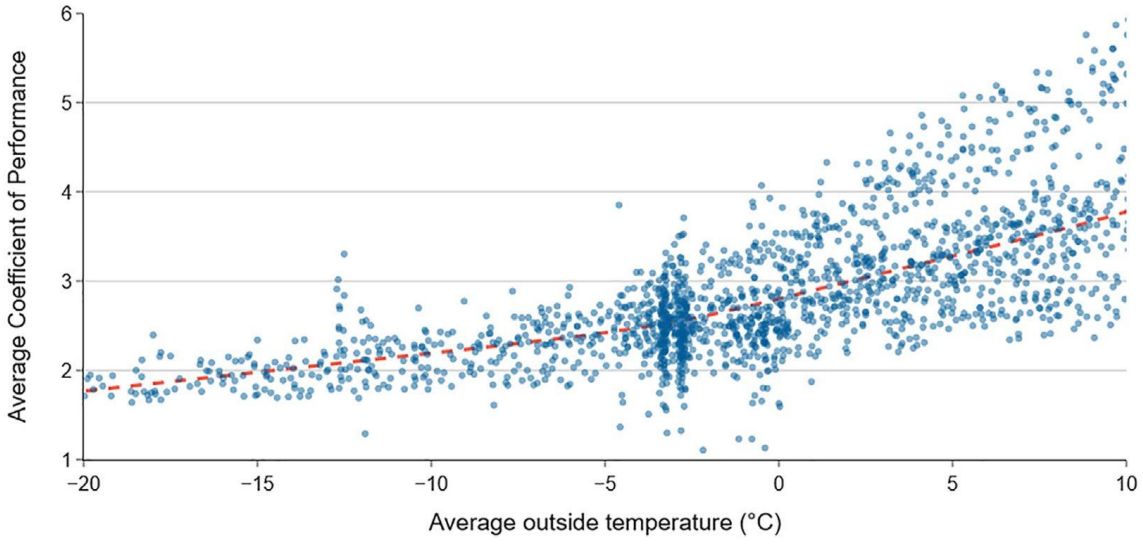

Figure 6.2. The average COP measurements for the advanced air-source heat pumps as a function of the ambient temperature [298].

Figure 6.2 presents the average COP measurements as a function of the ambient temperature, based on the data collected from seven field studies conducted across five countries, including Canada [298]. These measurements will be utilized to calculate the average monthly COP for the use of air-source heat pumps at UofA.

6.1.1.1 Methodology

In this section, the methodology, governing equations, and assumptions employed for the design and techno-economic assessment of SOFC- and HICE-based CHP systems for the energy management of the UofA are explained. The methodology of this study, as illustrated in Figure 6.3, focuses on evaluating the energy management of the University of Alberta under two different strategies.

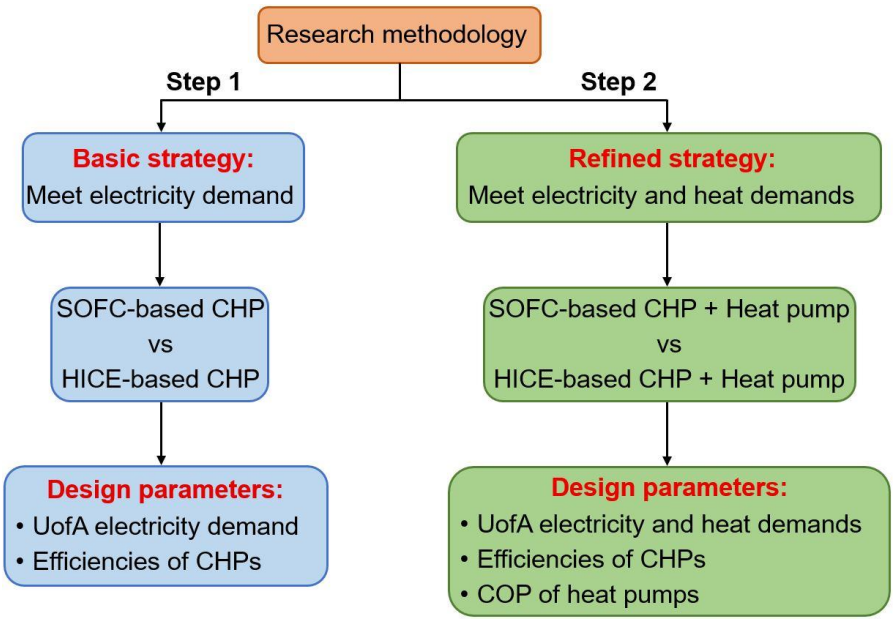

Figure 6.3. Research methodology and strategies considered in the present study. CHP: combined heat and power, COP: coefficient of performance, SOFC: solid oxide fuel cell, UofA: University of Alberta.

In the basic strategy (step 1), the investigation is centered on meeting only the university's electricity demands through the implementation of proposed CHP systems (SOFC-based and

HICE-based CHPs). In the refined strategy (step 2), the scope is expanded to address both the electricity and heat demands of the university. To enhance system flexibility and efficiency, particularly for heating requirements, the refined strategy incorporates the integration of modern air-source heat pumps to the proposed CHPs.

The analysis incorporates real-world operational data on electricity and heat consumption at the university to determine the required CHP capacity. Considering the design parameters, it assesses whether the same designed capacity could be sufficient for both strategies, requiring only adjustments to operational load factors, or if an increase in CHP capacity would be needed to accommodate the broader demands of the refined strategy. For both strategies, the operational load factors (defined as the ratio of operating capacity to total capacity) of the CHP systems are optimized to align with seasonal variations and overall energy requirements. By comparing the performance, economic feasibility, and environmental impacts of the proposed hydrogen-fuelled CHPs, the study aims to identify an optimal energy management solution that minimizes greenhouse gas emissions, reduces reliance on conventional natural gas-based heating, and supports the university's long-term sustainability and decarbonization goals.

Table 6.1. Critical parameters of the SOFC- and HICE-based CHPs and advanced air-source heat pumps.

Technology	Factor	Value
SOFC-based CHP [293]	Capital cost for large capacities (>1 MW)	4,000 $/kW
	System lifetime	40,000 hr
	Operating and maintenance cost	22% of CAPEX
	Electrical efficiency	62%
	Total CHP efficiency	90%
HICE-based CHP [93]	Capital cost for large capacities (>750 kW)	2,000 $/kW
	System lifetime	60,000 hr
	Operating and maintenance cost	14.5% of CAPEX
	Electrical efficiency	39.7%
	Total CHP efficiency	80.4%
	No_x emission	9.4 g/MWh
Advanced air-source heat pumps [299]	Capital cost for extreme cold-weather conditions	500 $/kW
	COP at the ambient temperature of 20℃	4.5
	System lifetime	20 years
	Operating and maintenance cost	6% of CAPEX

To ensure a realistic evaluation, the analysis incorporates established technologies and specifications provided by FuelCell Energy for the SOFC-based system and 2G Energy for the HICE-based system. Key parameters for both CHP systems have been determined based on quotations obtained from these companies and the current Canadian market conditions for modern air-source heat pumps. A summary of the key parameters is presented in Table 6.1.

According to FuelCell Energy, the efficiency of the SOFC-based CHP system is 90%, comprising 62% electrical efficiency and 28% thermal efficiency [293]. In addition, the SOFC-based CHP system has a lifespan of 40,000 hours and a total capital cost of 4,000 $/kW [293]. In comparison, 2G Energy reports that the HICE-based CHP system offers a lower capital cost of 2,000 $/kW and a longer lifespan of 60,000 hours relative to the SOFC system [93]. The HICE-based CHP system operates with electrical and thermal efficiencies of 39.7% and 40.7%, respectively [93]. However, this system emits 9.4 g/MWh of NO_x during operation [93]. Finally, as summarized in Table 6.1, modern air-source heat pumps have a capital cost of 500 $/kW under extreme cold conditions and a lifespan of 20 years. The COP for these heat pumps varies with ambient temperature (Figure 6.2), reaching a maximum value of 4.5 at an ambient temperature of 20°C [299].

In addition, the monthly average ambient temperature of Edmonton and the corresponding COP values for the air-source heat pumps (to be applied in the refined strategy) are summarized in Table 6.2.

Table 6.2. The monthly average ambient temperature and COP of the heat pump for operation in the city of Edmonton.

Month	**Ambient average temperature (°C)** [300]	**Average COP** [298]
January	-10.5	2.1
February	-7.5	2.3
March	-2.5	2.7
April	5.5	3.2
May	11.5	3.7
June	15.5	3.9
July	17.5	4.1
August	17	4
September	11.5	3.7
October	5	3.5
November	-4	2.5
December	-8.5	2.2

Based on the availability of hydrogen as the input fuel, the power and heat outputs generated by the SOFC-based CHP or the HICE-based CHP systems can be calculated using the following equations [301]:

$$\dot{W}(t) = \dot{m}_{H_2}(t) \times \eta_{Electrical} \times LHV_{H_2} \tag{6.1}$$

$$\dot{Q}(t) = \dot{m}_{H_2}(t) \times \eta_{Thermal} \times LHV_{H_2} \tag{6.2}$$

here, $\dot{W}$, $\dot{Q}$, LHV_{H_2}, and $\dot{m}_{H_2}$ present the power generated by the CHPs, waste heat as by-product, low heating value of hydrogen (33.3 kWh/kg [302]), and the demanded hydrogen fuel flow rate, respectively. Furthermore, $\eta_{Electrical}$ and $\eta_{Thermal}$ specify the electrical and thermal efficiencies of the SOFC-based or HICE-based CHPs.

6.1.2 Residential and commercial CHPs for Alberta and Canada

The proposed CHP systems for residential and commercial sectors are described in this section. The designs encompass two primary capacities: a 100 kW unit for commercial applications and a 5 kW unit designed for residential use. Initial market projections indicate a significant uptake in larger municipal commercial units, with widespread adoption anticipated to commence by 2030.

As the technology advances and becomes more cost-effective, it is expected to penetrate the residential market by 2035. The key characteristics and specifications of both the residential and commercial units are detailed in Table 6.3 and Table 6.4.

Table 6.3. Properties of the proposed residential CHP based on the SOFC with a base capacity of 5 kW in 2035.

Factor	Value
CHP capacity (kW)	5
Capital cost of a residential 5 kW CHP ($) [303,304]	18,000
Daily energy production (kWh)	120
Annual energy production (kWh)	43800
Daily hydrogen consumption (kg)	3

Table 6.4. Properties of the proposed commercial CHP based on the SOFC with a base capacity of 100 kW in 2030.

Factor	Value
CHP capacity (kW)	100
Capital cost of a commercial 100 kW CHP ($) [303,304]	400,000
Daily energy production (MWh)	2.4
Annual energy production (MWh)	876
Area energy coverage per unit (m^2) [305]	2440
Daily hydrogen consumption (kg)	60

Table 6.3 indicates that the installation of a 5 kW residential SOFC-based CHP system will require a capital investment of $18,000 in the initial development year of 2035 [303,304]. This system is capable of producing 120 kWh of energy per day, consuming 3 kg of hydrogen. For commercial applications, Table 6.4 outlines a base system capacity of 100 kW, with an initial investment cost of $400,000. This system provides the flexibility for expansion to several megawatts by connecting multiple base units. A base commercial unit with a capacity of 100 kW needs an initial investment cost of $400,000 [303,304]. These modular units can be scaled to several megawatts by interconnecting multiple base units. According to Natural Resources Canada, a single 100 kW commercial CHP unit can meet the energy demands of a commercial building with an area of approximately 2,440 m^2 [305].

6.2 Results and discussion

In this section, first the results of techno-economic analysis for installing SOFC-based and HICE-based CHPs for UofA will be elaborated. Then, the details of the technical, economic, and environmental analysis for commercial and residential CHPs in Alberta and Canada, along with the related sources and assumptions are presented.

6.2.1 University of Alberta

In this section, the results of the techno-economic analysis for installing SOFC-based and HICE-based CHPs for UofA will be elaborated. A summary of the heat and electricity consumption of UofA is shown in Figure 6.4, using real data based on measurements.

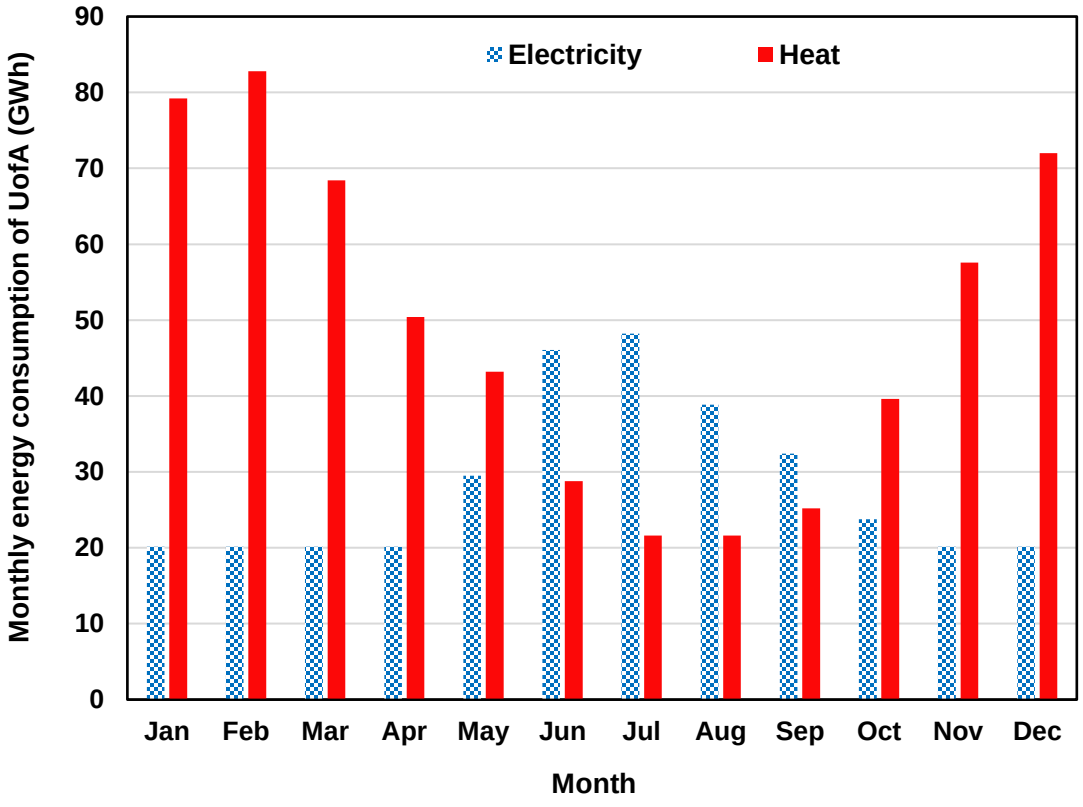

Figure 6.4. Monthly energy consumption of the University of Alberta (UofA). The data is based on year 2019.

As illustrated, there is a notable fluctuation in the university's heat consumption across the year, with a substantial increase during colder months and a marked reduction during the summer. In contrast, electricity consumption exhibits less variation, with its peak occurring in the summer due to the demand for air conditioning. These seasonal variations are critical factors in the design of new hydrogen-based energy systems and must be carefully accounted for to ensure system efficiency and reliability. The heat-to-power ratio across different months, as presented in Figure 6.5, further highlights these seasonal dynamics and their relevance to the optimum sizing of a CHP system. As shown, the minimum and the maximum ratio of heat-to-power ratio happen in July (0.45) and February (4.1), respectively.

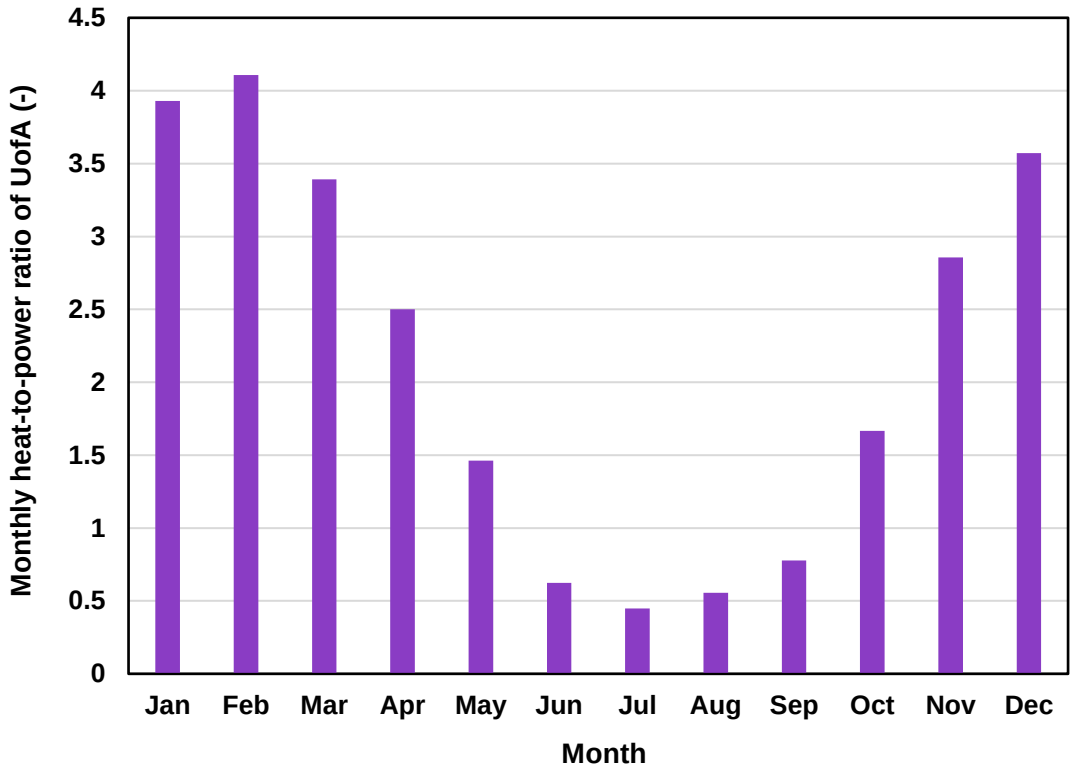

Figure 6.5. Monthly heat-to-power ratio of the University of Alberta (UofA). The data is based on year 2019.

6.2.1.1 Basic strategy

First, as the basic strategy, the usage of SOFC-based and HICE-based CHPs is assessed as the two potential hydrogen-based technologies for heat and power management of UofA. Considering the peak electricity demand of 67 MW, a CHP capacity of 70 MW is considered sufficient to cover the electricity needs of the university, ensuring a 3 MW safety margin for unexpected fluctuations.

a) Operational load factor of the CHPs

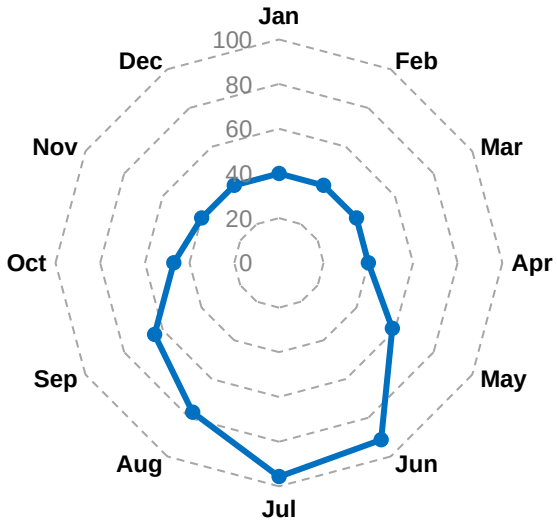

b) Heat coverage percentage of UofA by these CHPs

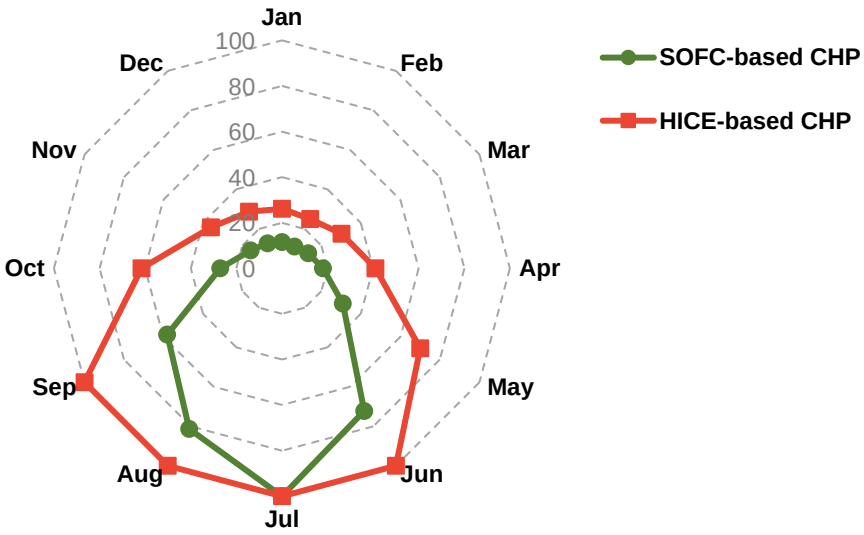

Figure 6.6. a) Percentage of the operational load factor of the CHPs to meet the electricity demand of UofA **b)** Heat coverage percentage of UofA by the designed CHPs.

As shown in Figure 6.6 (a), the operational load factor (the operating capacity to total capacity) of the CHP units is adjusted to meet the university electricity demand (Figure 6.4). This analysis highlights the capability of the CHP systems to maintain a stable power supply under the real operational conditions. However, a critical challenge arises during the winter months, as depicted in Figure 6.6 (b), to address the required heat loads. Although the CHP units produce valuable waste heat as a by-product, the quantity of recoverable thermal energy is inadequate to fully satisfy the university's significant heating demand during colder periods. This shortfall necessitates a strategic adjustment to ensure both thermal and electrical energy needs are met efficiently.

Figure 6.7 illustrates the hydrogen consumption required for each CHP system to fully meet the UofA's electricity demand, with partial heat coverage as shown in Figure 6.6 (b). The data in Figure 6.7 highlights that the HICE-based CHP requires more hydrogen compared to the SOFC-based CHP due to its lower electrical efficiency. However, despite the higher hydrogen consumption, the HICE-based system produces significantly more byproduct heat than that of the SOFC-based CHP. This is due to the nature of combustion process and HICE structure that leads to additional thermal energy via hot exhaust gases. These results in HICE's lower electrical conversion efficiency (e.g., 39.7% in this study). In contrast, the SOFC's advanced electrochemical conversion results in greater electrical efficiency (e.g., 62% in this study) and lower heat output.

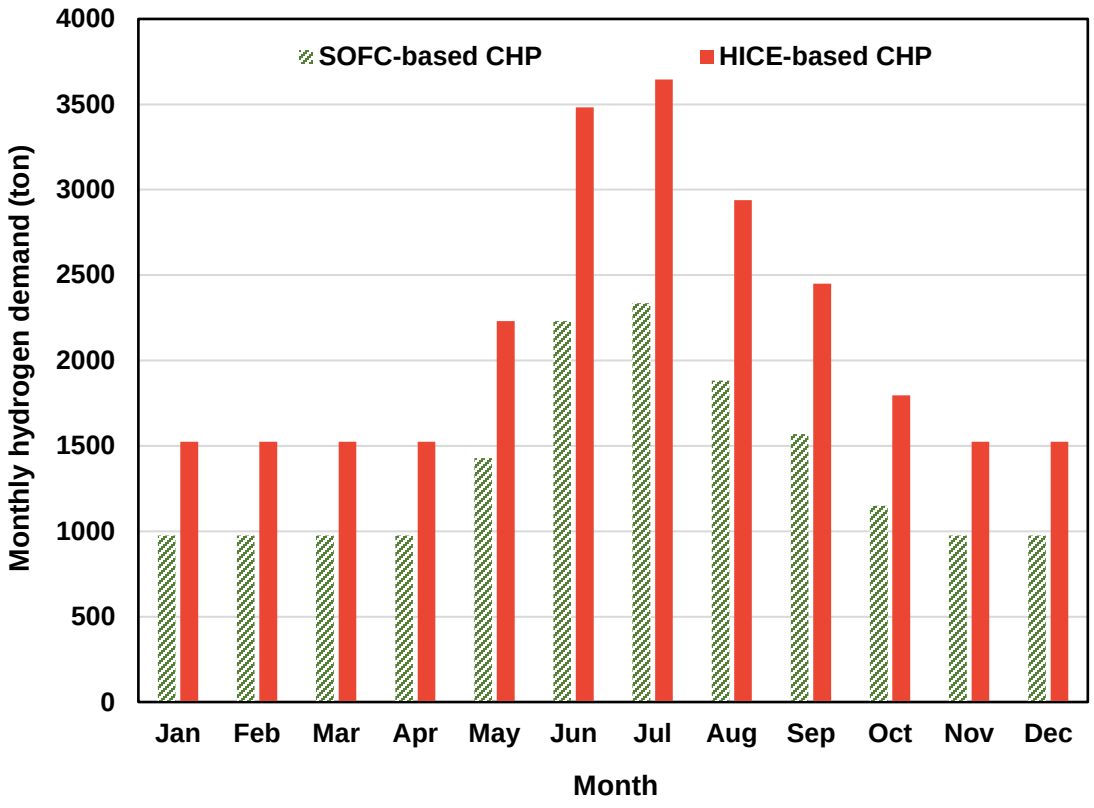

Figure 6.7. Monthly hydrogen demand of the SOFC-based and HICE-based CHPs to cover all the electricity demand of University of Alberta.

6.2.1.2 Refined strategy

In addition, a refined strategy is considered in this study to reduce the UofA's reliance on conventional natural gas-based heating systems. The analysis indicates that meeting both heating and electricity demands can be achieved only by adjusting the operational load factors of the CHP units, without the need to alter their designed capacity of 70 MW. This strategy integrates modern air-source heat pumps, which operate based on the temperature-dependent COPs outlined in Table 6.2. Therefore, the need for supplemental fossil fuels for heating is eliminated, supporting the university's decarbonization objectives. The operational load factors for each CHP configuration based on this refined strategy to cover both the electricity and heat demands are presented in Figure 6.8. It is important to note that these load factor profiles differ due to the varying electrical and

heat efficiencies (subsequent variable heat-to-power ratios) of the two technologies, as outlined in Table 6.1.

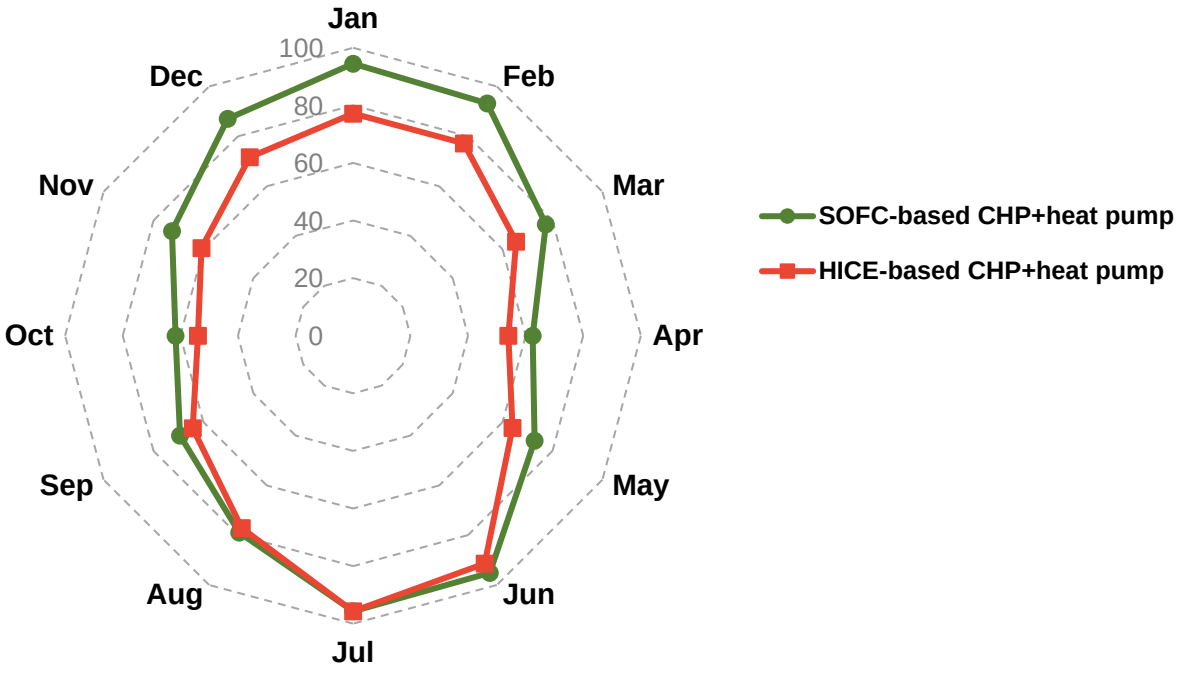

Figure 6.8. The operational load factor percentage to fully cover the heat and electricity demands of UofA by the designed SOFC-based and HICE-based CHPs.

To meet the peak electricity demand, which occurs in July and reaches approximately 67 MW, the CHP systems must operate at the maximum load factor of 95.8%, as shown in Figure 6.8. This ensures sufficient electricity generation capacity to handle the highest electricity consumption periods. During other months of spring and summer (March. April, May, June, August) and the month of September, when the focus remains on meeting the university's electricity needs, the HICE-based CHP system naturally produces a surplus of heat due to its higher thermal energy output. This excess heat is sufficient to cover the heating requirements of the university during the mentioned months without additional adjustments. In contrast, the SOFC-based CHP system, which has a lower heat by-product, must operate at higher load factors (shown in Figure 6.8) than what would be necessary for electricity alone (e.g., load factor of HICE-based CHP) to compensate

for its limited heat output and adequately meet the university's thermal needs. Consequently, it requires increased operational intensity during summer to maintain comprehensive energy coverage.

During the colder months, the energy strategy shifts. Both CHP systems need to operate at elevated load factors, exceeding the electricity-only requirements, to generate additional electricity necessary for powering heat pumps designed to meet the university's higher heating demands. However, the operational adjustment for the HICE-based CHP system is relatively modest compared to the SOFC-based system due to its lower heat-to-power ratio. The higher thermal by-product of the HICE-based system reduces the need for supplemental electricity production, resulting in a lower additional load increase for heating purposes. This analysis highlights the importance of tailoring CHP operational strategies to the specific characteristics of each technology. By adjusting load factors to accommodate seasonal fluctuations and capitalizing on the strengths of each CHP, overall efficiency was enhanced, and GHG emissions were reduced through the elimination of natural gas use.

Figure 6.9 illustrates the monthly hydrogen consumption required to meet the full energy demands—both electricity and heating—of the UofA. This profile aligns with the hydrogen consumption trend observed for electricity demand alone, as shown in Figure 6.7, with the peak energy and corresponding hydrogen requirement occurring in July. However, the hydrogen consumption rate varies across different months of the year, influenced by the fluctuating electricity and heat demands specific to each month. The analysis reveals that the annual hydrogen demand increases slightly when accounting for both electricity and heating requirements. For the SOFC-based CHP system, this adjustment results in an additional 7,170 tons of hydrogen per year,

raising the total consumption from 16,450 to 23,620 tons. Similarly, the HICE-based CHP requires an increase of 6,788 tons annually, with total hydrogen consumption rising from 25,687 to 32,475 tons.

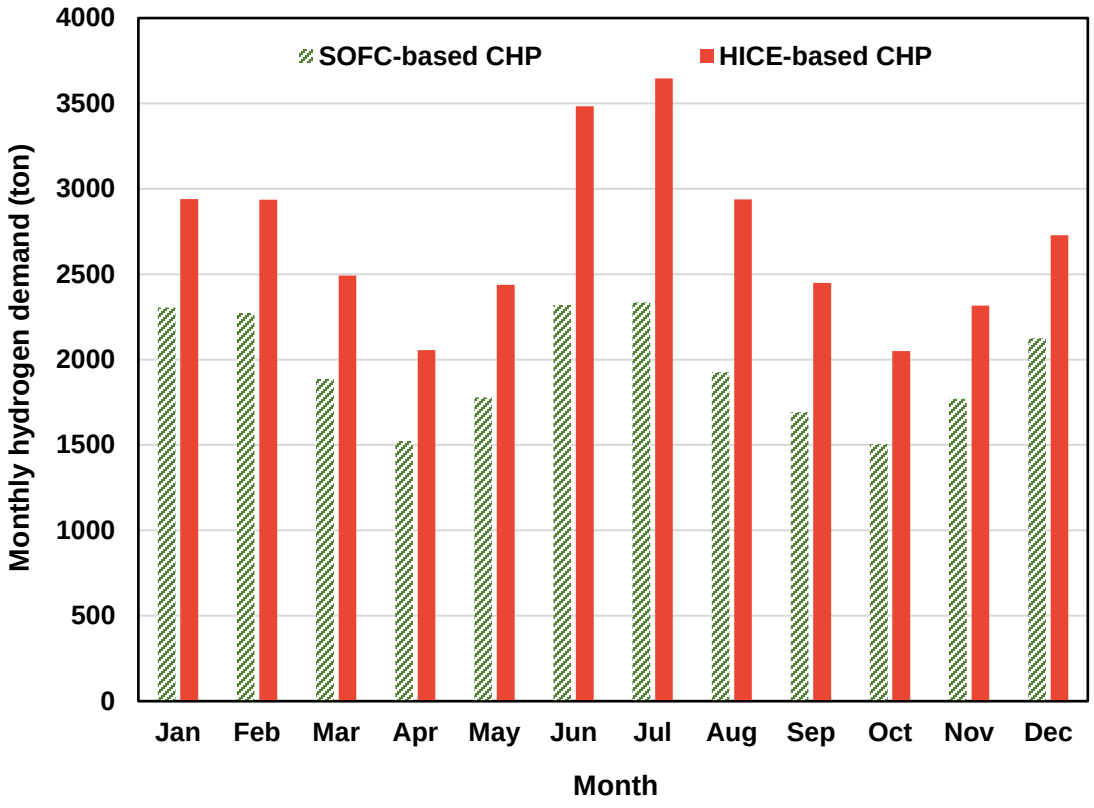

Figure 6.9. Monthly hydrogen demand of the SOFC-based and HICE-based CHPs to cover all the energy demand (electricity and heat) of University of Alberta.

A comprehensive summary of the key results for the designed CHP systems, alongside current energy parameters at UofA, is presented in Table 6.5. Currently, approximately half of the university's energy demand is met by a local power plant, while the remaining energy is sourced from the electrical grid. This arrangement results in an annual expenditure of about $32 million for electricity, $7 million for heating, plus the maintenance fees, with a corresponding CO_2 footprint of over 302,000 tons.

Table 6.5. Key metrics of the designed CHPs along with the university requirements. All the economic values are in USD.

Factor	SOFC-based CHP	HICE-based CHP	Current
Required CHP capacity	70 MW	70 MW	70 MW
Capital cost for CHP	$280 M	$140 M	-
Required heat pump capacity	200 MW	150 MW	-
Capital cost for heat pump	$100 M	$75 M	-
Annual hydrogen demand	23,620 ton	32,475 ton	-
Hydrogen cost (@ LCOH=2 $/kg)	$47.24 M	$64.95 M	-
Annual total operating and maintenance costs	$66.32 M	$24.25 M	-
Total annual costs for electricity and heat coverage	$113.56 M	$89.2 M	$39 M + maintenance fees
GHG Emissions	*	4 tons NO_x + *	+302,000 tons CO_2

* Depends on the hydrogen production carbon intensity and life cycle carbon intensity of the CHP systems.

The introduction of the proposed CHP systems has the potential to significantly reduce GHG emissions, albeit with a short-term increase in annual operational costs and a substantial initial capital investment. As mentioned, a CHP system with an electrical capacity of 70 MW would suffice to meet the university's total energy requirements, both for electricity and heating. For a 70 MW SOFC-based CHP system, the CAPEX is estimated to be approximately $280 million, while a HICE-based CHP system of equivalent capacity would require about half that amount, $140 million. However, this cost difference reflects the distinct performance characteristics of the two studied CHP technologies. The HICE-based CHP, with its comparatively lower electrical and overall efficiencies, demands a significantly higher annual hydrogen supply of 32,475 tons, whereas the SOFC-based system requires 23,620 tons. Assuming a hydrogen cost of $2 per kilogram, the annual hydrogen expenses would amount to $64.8 million for the HICE-based system and $47.2 million for the SOFC-based system.

In terms of operating and maintenance (O&M) costs, the current SOFC-based systems are limited by a lifespan of 40,000 hours, leading to an estimated annual O&M cost of $66.32 million. In contrast, considering a higher lifetime of the HICE-based CHP (60,000 hr), it has a lower O&M cost of $24.25 million annually. When all expenses are considered, including hydrogen and O&M, the total annual operational costs amount to approximately $113.6 million for the SOFC-based CHP and $89.2 million for the HICE-based system. Although the SOFC-based system has higher

operational costs compared to the HICE-based counterpart, it offers a more environmentally sustainable solution. Its lower hydrogen demand not only decreases the hydrogen purchase cost but also eliminates indirect GHG emissions of hydrogen production, making it a favourable choice from an environmental perspective. In contrast, the HICE-based CHP, despite its economic advantages, has a higher carbon intensity due to increased hydrogen consumption, along with the added burden of approximately 4 tons of NO_x emissions annually.

To sum up, the SOFC-based CHP stands out as the preferable option from the environmental standpoint due to its reduced carbon footprint and zero direct emissions. However, the HICE-based CHP remains a more economical choice, particularly in scenarios where budget constraints and upfront capital costs are significant factors. This analysis underscores the trade-offs between sustainability and cost-effectiveness, highlighting the need to carefully balance financial considerations with long-term environmental benefits when making strategic energy investments for the UofA.

Combustion engine technology, including the HICE-based system, is a well-established and mature field [306]. Due to its long history of development and widespread industrial applications, the projected CAPEX and lifespan for combustion engines exhibit only minor variations over time. These systems are characterized by predictable cost structures and durability, making them a stable investment with well-understood economic and operational parameters. In contrast, SOFC technology is currently in a relatively early stage of development. However, substantial advancements are expected in the coming years, particularly in areas such as efficiency enhancement, extended operational lifespans, and reductions in CAPEX [130]. For instance, the United States Department of Energy (US DOE) has recently established ambitious targets for SOFC systems, aiming to achieve an electrical efficiency of 65%, an operational lifespan of 80,000

hours, and a CAPEX of $1000/kW [307]. These projections are underpinned by ongoing research and development initiatives focused on optimizing material performance, improving system durability, and streamlining manufacturing processes to enable cost-effective large-scale production.

However, due to the inherent uncertainty in the technological advancement timeline, accurately predicting the pace and scale of these changes remains challenging. To provide an overview of the potential future landscape, Figure 6.10 illustrates a range of scenarios for the evolution of SOFC systems. This includes projected variations in both the expected lifetime and CAPEX, reflecting the potential outcomes as the technology matures. Figure 6.10 illustrates the potential for significant cost reductions in the annual energy management expenses for UofA through advancements in SOFC technology. A reduction in the CAPEX to 1,000 $/kW could lower total annual costs to $67.5 million. Alternatively, maintaining the current CAPEX of $4,000 per kW while extending the system's operational lifespan to 100,000 hours would reduce annual costs to $77 million. Both of these scenarios would make the SOFC-based CHP a more attractive choice compared to the HICE-based CHP, which currently has an annual operating cost of $89.2 million. The most impactful scenario involves simultaneous advancements in both CAPEX and system lifespan. A reduction in CAPEX coupled with an extension of the operational life would drive annual costs down to as low as $58 million, further solidifying the economic advantages of SOFC-based systems.

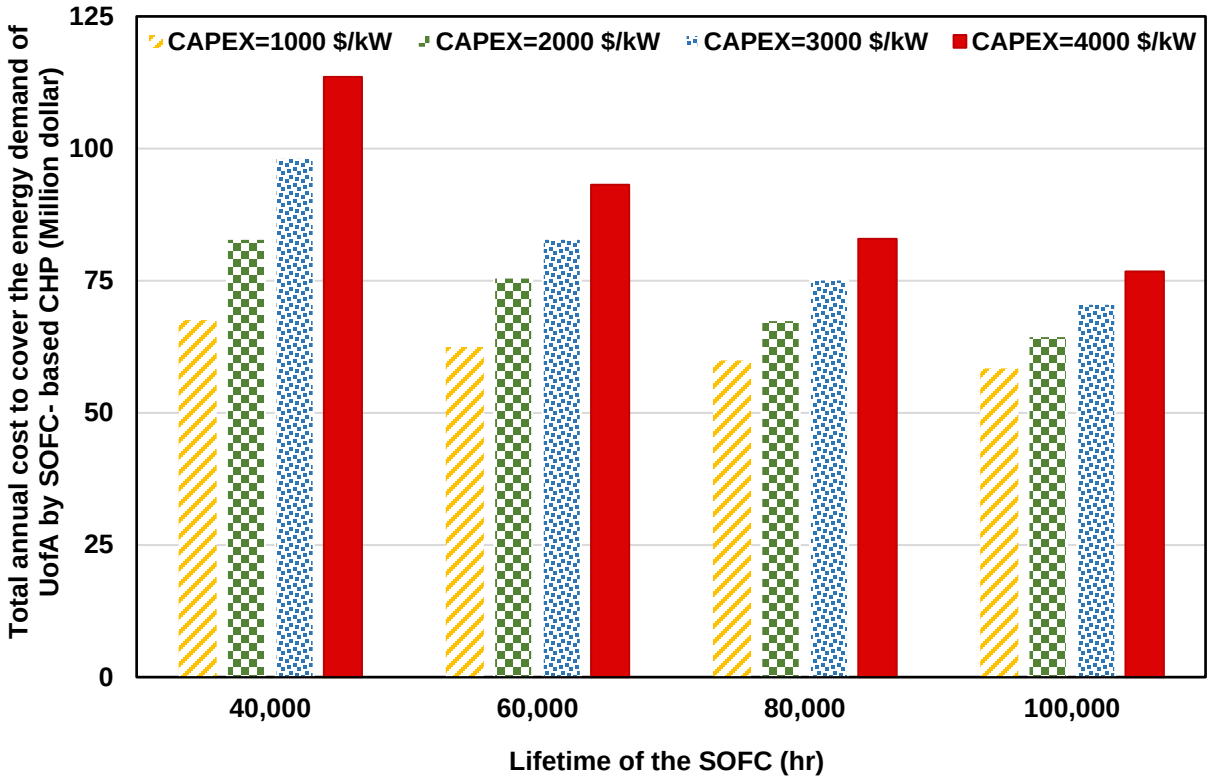

Figure 6.10. The effect of the SOFC lifetime and CAPEX on the total annual costs of the SOFC-based CHP to cover the energy (electricity and heat) demand of UofA.

These projections emphasize that anticipated improvements in SOFC technology have the potential to overcome initial drawbacks related to CAPEX and durability. As the technology matures, SOFC systems are poised to become increasingly competitive with conventional combustion engine-based alternatives. For institutions like UofA, which prioritize long-term sustainability and reduced carbon emissions, investing in SOFC technology represents a strategic, forward-looking decision. Although uncertainties remain regarding the exact timeline and magnitude of these technological advancements, the ongoing evolution in SOFC performance metrics offers a compelling case for considering it as a viable and sustainable energy solution.

In conclusion, Figure 6.11 presents a visual comparative analysis for selecting the most suitable CHP system for UofA. This diagram evaluates the potential variations in CAPEX and lifespan for

the SOFC-based CHP, while maintaining constant parameters for the HICE-based CHP. This visual comparison aims to highlight the impact of anticipated technological advancements in SOFC systems, providing a clear basis for decision-making regarding the optimal energy solution for UofA.

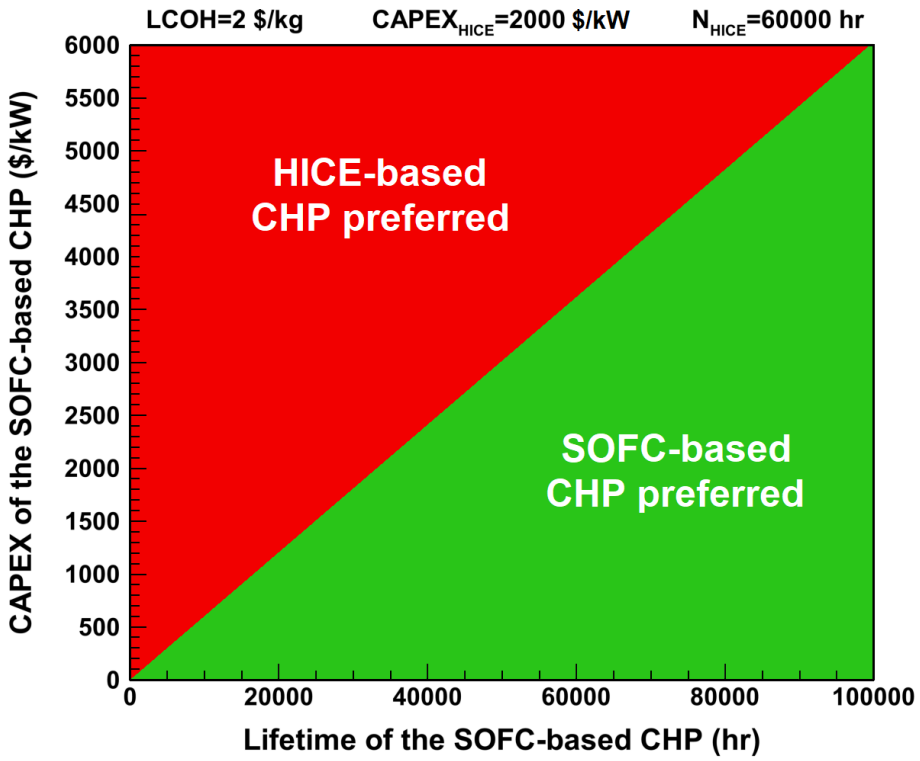

Figure 6.11. A comparative diagram for the selection of the SOFC-based CHP or the HICE-based CHP for University of Alberta based on the future variations in the lifetime and CAPEX of the SOFC-based CHP.

6.2.2 Alberta

Given Alberta's higher carbon intensity relative to other provinces, the implementation of SOFC-based CHP systems offers significant potential to contribute to the province's decarbonization efforts. Alberta's electricity grid is still heavily reliant on fossil fuels, which leads to elevated GHG emissions. By integrating SOFC-based CHP systems, which are highly efficient and capable of simultaneously generating electricity and utilizing waste heat, there is an opportunity to not only reduce energy consumption but also substantially lower GHG emissions at the point of use. This

technology aligns with Alberta's long-term goals of transitioning to cleaner energy sources while maintaining grid reliability and supporting economic growth. Furthermore, SOFC-based CHP systems can provide enhanced energy security and resilience for residential and commercial sectors, offering a decentralized energy solution that reduces reliance on the traditional grid. Their ability to operate efficiently using natural gas, which is abundant in Alberta, makes them particularly well-suited to the province's energy landscape while facilitating a gradual shift towards lower-carbon energy solutions.

6.2.2.1 Case studies for heat-to-power ratio of SOFC

One of the key advantages of SOFC-based CHP systems is their ability to simultaneously generate both heat and electricity, making them highly efficient for residential energy applications. However, optimizing the ratio of heat to power output is a critical factor in maximizing the performance of these systems. This is particularly important for residential homes in regions like Alberta, where energy demand can vary significantly across different seasons. In colder months, homes typically require much higher levels of heating, while electrical demand remains more consistent throughout the year. To address this, SOFC-based CHP systems must be capable of dynamically adjusting the proportion of heat and power produced to match the specific needs of the household at any given time.

The inherent flexibility of SOFC technology makes it well-suited for such demand-based adjustments. By leveraging the high electrical efficiency of SOFCs, excess thermal energy can be redirected towards heating during periods of lower electricity consumption. Conversely, during months with lower heating requirements, the system can prioritize electricity generation to meet the household's needs. This adaptable heat-to-power ratio not only enhances the overall energy

efficiency of the system but also contributes to a more sustainable energy model by minimizing waste and reducing reliance on external energy sources.

In addition to the energy efficiency benefits, SOFC-based CHP systems can help reduce operational costs for homeowners by optimizing fuel use and minimizing energy losses. They also provide a more resilient and decentralized energy solution, which can alleviate pressure on the electrical grid, particularly during peak demand periods. By fine-tuning the balance between heat and power output based on seasonal variations, these systems offer a highly tailored solution that supports both energy security and environmental sustainability, while maintaining comfort for residents throughout the year.

In this context, the electricity and natural gas consumption patterns of three residential houses located in distinct areas of Edmonton—specifically the South, West, and Central regions—are analyzed to assess the effectiveness of the proposed SOFC-based CHP system in meeting their energy needs throughout the different months from July 2023 to June 2024. By examining the variations in energy demand across these diverse geographical locations, this study aims to provide insights into the adaptability and performance of the SOFC-based CHP system under seasonal changes. This analysis will help determine the system's potential to deliver optimal energy solutions tailored to the specific requirements of each household, thereby enhancing its viability as a sustainable energy alternative.

House in South Edmonton

The monthly natural gas and electricity consumption for a residential property with an area of 2150 sqf located in South Edmonton, covering the period from July 2023 to June 2024, is illustrated in Figure 6.12. The data reveals that electricity consumption, which includes the operation of air

conditioning, remains relatively stable throughout the year with minimal seasonal fluctuation. In contrast, heat demand experiences a substantial surge during the colder months, with natural gas consumption averaging over four times higher in cold months compared to warmer months.

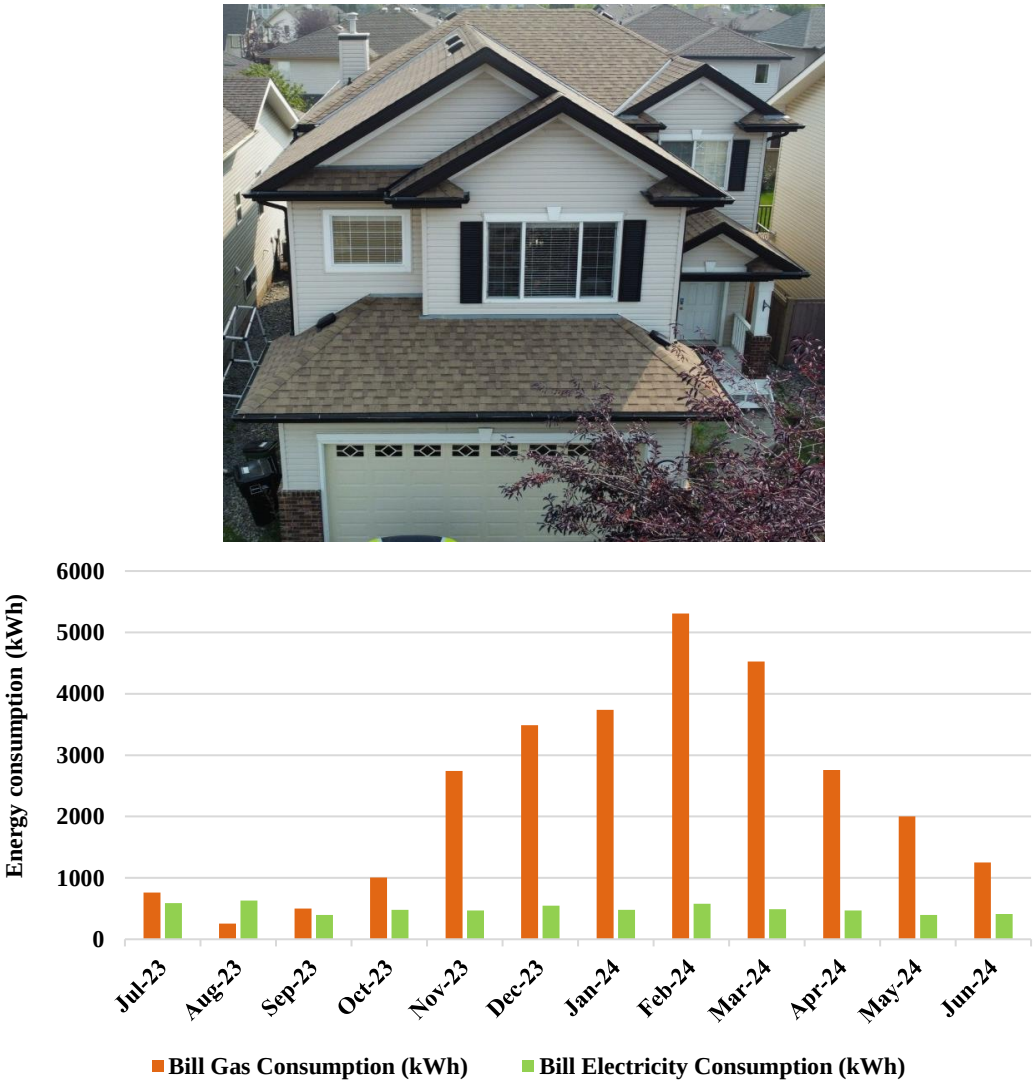

Figure 6.12: Monthly gas and electricity consumption of a house in South Edmonton from July 2023 to June 2024.

This seasonal fluctuation in natural gas usage reflects the varying heat-to-power ratio required to meet the home's energy needs. During periods of minimal heating demand, such as in August, the heat-to-power ratio is as low as 0.4. In contrast, during peak heating months like February, this

ratio rises dramatically to 9.2. These variations are clearly depicted in Figure 6.13, highlighting the critical role of seasonal factors in determining the home's energy consumption profile.

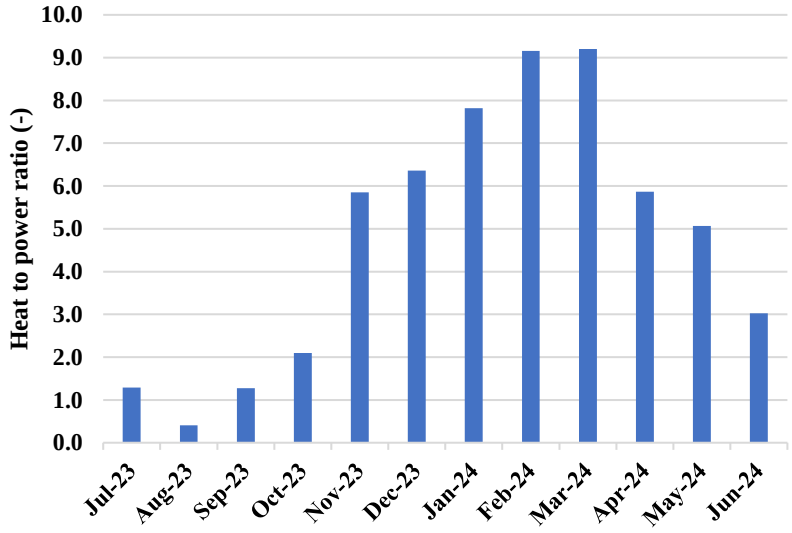

Figure 6.13: Monthly heat to power ratio of the CHP for a house in South Edmonton from July 2023 to June 2024.

House in West Edmonton

Another illustrative example is provided by the energy consumption profile, encompassing both electricity and heat, for a residence in West Edmonton with an area of 2400 sqf over the period from July 2023 to June 2024, as shown in Figure 6.14. Similar to the previous case, the electricity consumption in this household remains fairly consistent throughout the year, with negligible fluctuations across different months. However, the natural gas consumption experiences a substantial increase during the colder months, reflecting the higher demand for space heating during winter. This sharp contrast between stable electricity use and variable gas consumption has a notable impact on the heat-to-power ratio of the residence. As depicted in Figure 6.15, the heat-to-power ratio reaches its lowest point at 1.1 in August, a month with minimal heating requirements, and peaks at 13.4 in January, when the need for heating is at its highest. These figures emphasize the significant influence of seasonal heating demands on the overall energy

profile of the home, further illustrating the strong dependence of natural gas consumption on external temperature variations.

Figure 6.14: Monthly gas and electricity consumption of a house in West Edmonton from July 2023 to June 2024.

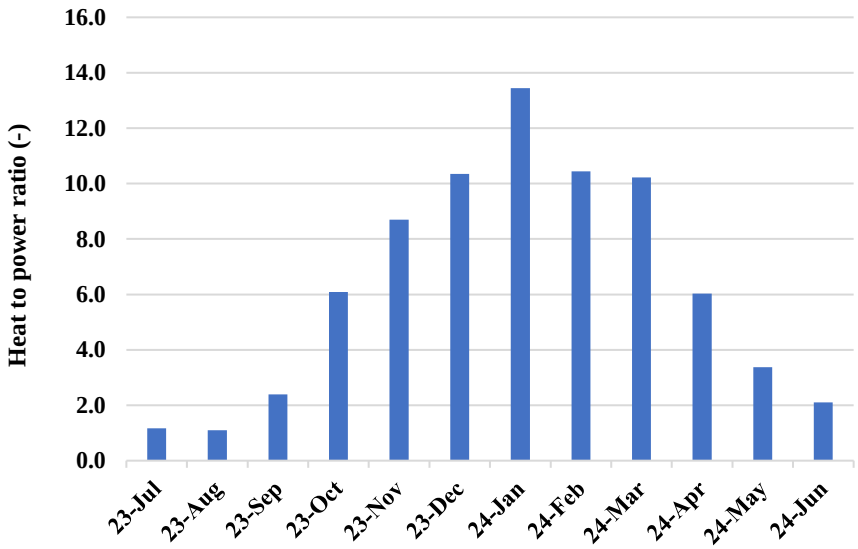

Figure 6.15: Monthly heat to power ratio of the CHP for a house in West Edmonton from July 2023 to June 2024.

House in Central Edmonton

Lastly, the gas and electricity consumption patterns for a 1,600 square foot residence located in Central Edmonton are illustrated in Figure 6.16. Consistent with the previous examples from South and West Edmonton, the household's electricity consumption remains relatively stable throughout the year, with no significant month-to-month variations. This stability is primarily due to consistent use of electrical appliances. However, the natural gas consumption exhibits a dramatic increase during the colder months, driven by the substantial heating requirements typical of Edmonton's harsh winter climate. This seasonal spike in gas usage directly affects the heat-to-power ratio of the home, as shown in Figure 6.17. In the warmer months, particularly in August, when heating needs are minimal, the heat-to-power ratio drops to its lowest point at 0.6. In contrast, during the coldest month of January, this ratio climbs sharply to 7.4, reflecting the heightened reliance on natural gas for heating purposes. These figures underscore the profound impact of seasonal temperature fluctuations on energy consumption, highlighting how the demand for heat dominates

during winter, while electricity usage remains more constant throughout the year. The significant variation in the heat-to-power ratio further emphasizes the importance of considering both gas and electricity consumption patterns when analyzing residential energy usage in cold-climate regions like Edmonton.

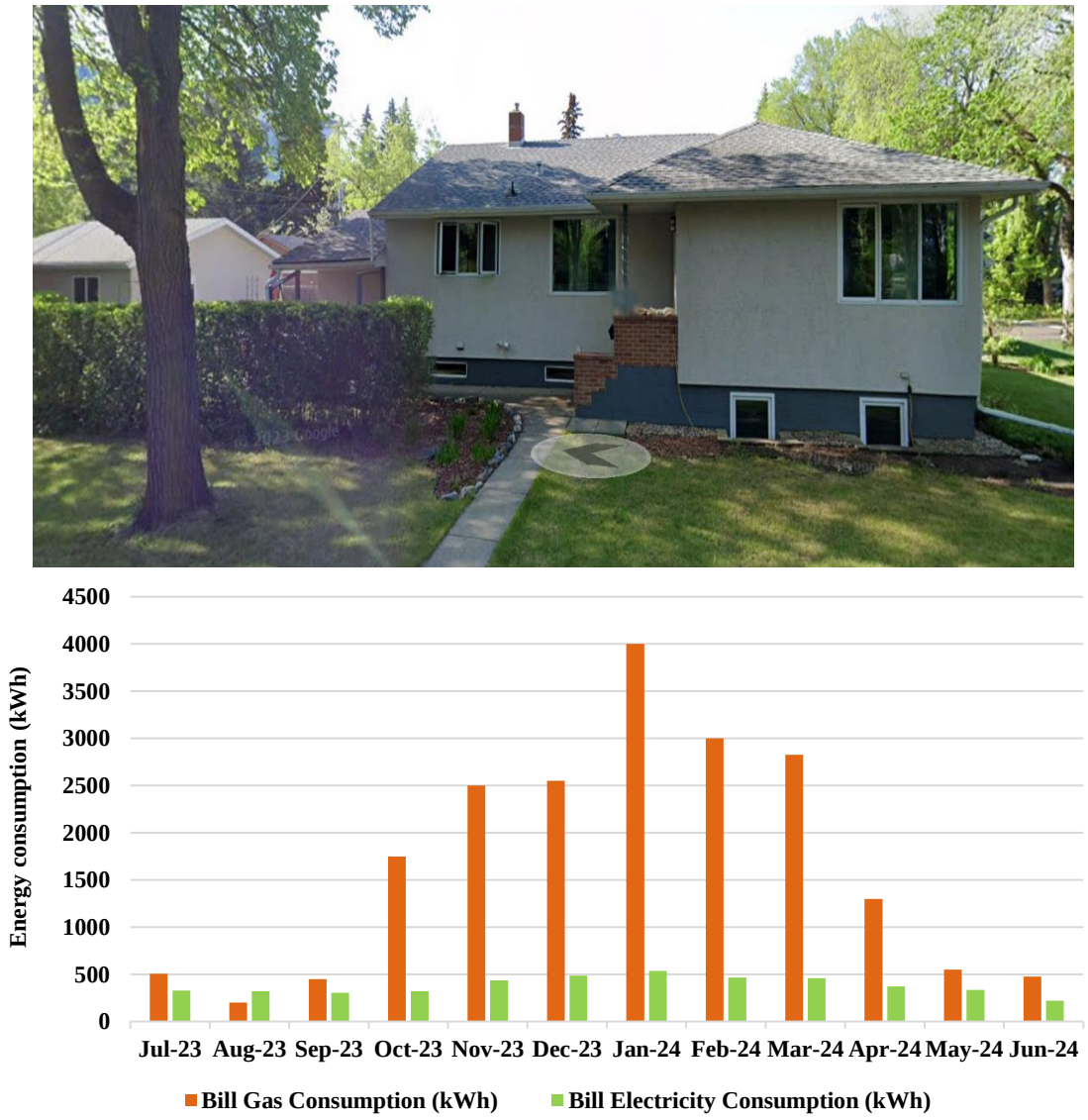

Figure 6.16: Monthly gas and electricity consumption of a house in Central Edmonton from July 2023 to June 2024.

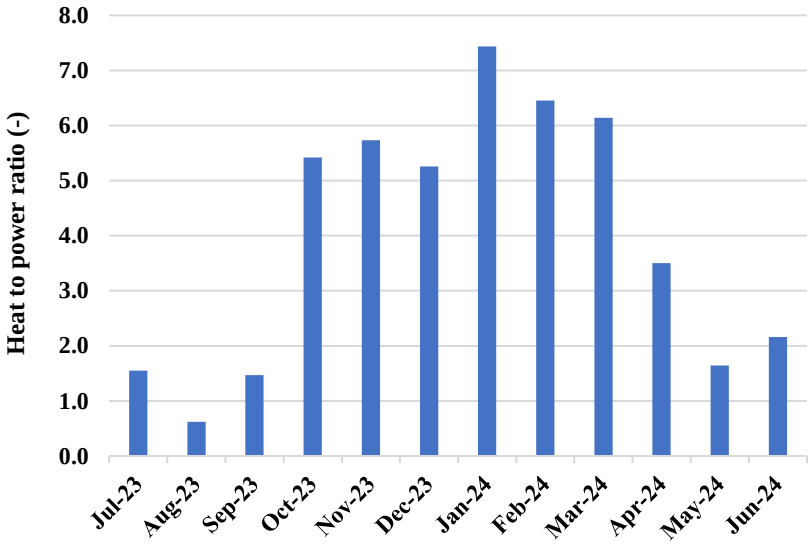

Figure 6.17: Monthly heat to power ratio of the CHP for a house in West Edmonton from July 2023 to June 2024.

Table 6.6 provides a summary of heat and electricity consumption, along with the corresponding heat to power ratios, for the three houses. The houses with air conditioning systems have higher electricity consumption during summer, which results is lower heat to power ratio in that period.

Table 6.6. A summary of heat and electricity consumption with corresponding heat to power ratio for the houses.

Parameter	**South Edmonton* (2,150 ft^2)**	**West Edmonton (2,400 ft^2)**	**Central Edmonton* (1,600 ft^2)**
Monthly heat consumption (kWh/sqf)	0.12-2.47	0.21-3.02	0.13-2.50
Monthly electricity consumption (kWh/sqf)	0.18-0.29	0.17-0.22	0.14-0.34
Heat to power ratio (-)	0.4-9.2	1.1-13.4	0.6-7.4

* These houses have air conditioning system.

SOFC-based CHP systems offer a unique capability to provide a highly flexible heat to power ratio, enabling them to adapt efficiently to fluctuating energy demands [308]. This operational adaptability can be achieved through precise control of key system parameters, including the fuel utilization factor, the management of electrochemical reactions within the fuel cell stack, and the configuration of heat recovery systems. For example, by adjusting the fuel utilization factor, the system can influence the proportion of fuel converted into electricity versus heat, thereby modulating its energy output balance [269]. Lowering the fuel utilization factor allows more fuel

to undergo afterburning in the system's exhaust stream, increasing the heat output. Conversely, raising the fuel utilization factor prioritizes electricity generation by maximizing the electrochemical conversion of fuel in the stack. Additionally, the amount of heat recovery can be dynamically regulated, enabling the system to adjust its thermal output in response to seasonal or real-time energy requirements. Through these mechanisms, SOFC-based CHP systems can operate across a wide range of heat-to-power ratios, from prioritizing electrical output to delivering nearly 100% of the available energy as heat. The operating heat to power ratio of the SOFC-based CHP is presented in Table 6.7, based on the properties of FuelCell Energy [293].

Table 6.7. Operating range of the SOFC-based CHP.

Heat (%)	Electricity (%)	Heat-to-power ratio	Note
31	69	0.4	When electricity is needed most
50	50	1	When heat and electricity are equally needed
100	0	Infinite	When only heat is needed

The SOFC-based CHP can operate with a minimum heat-to-power ratio of 0.4 when electricity demand is at its peak. This flexible operational capability allows the system to prioritize electricity generation during periods of high electrical demand. The system’s versatility extends further, as it can be adjusted to produce varying proportions of heat and electricity based on real-time requirements. For instance, the system can be configured to generate equal amounts of heat and electricity, or it can be set to produce up to 100% heat output when heating demand is high. The system's ability to operate with a heat to power ratio as low as 0.4 makes it particularly well-suited for addressing the energy requirements observed in the case studies of Edmonton. In all three residential houses, the heat to power ratios exceeded this minimum threshold, particularly during the colder months when heating demands surged. The SOFC-based CHP’s adaptability ensures that it can seamlessly adjust to provide the necessary heat and electricity, offering a highly efficient solution that can cater to the variable seasonal energy needs typical of residential homes in colder climates like Edmonton.

6.2.2.2 Residential CHPs in Alberta

This section presents the results of implementing the proposed SOFC-based CHP system in Alberta. As previously highlighted, Alberta has the highest grid carbon intensity in Canada, leading to substantial GHG emissions, particularly from residential heating and electricity consumption. A residential unit in Alberta produces approximately 4 metric tons of CO_2 annually from heating, predominantly through the use of natural gas, and an additional 3.6 metric tons of CO_2 per year from electricity consumption [285]. These records underscore the significant environmental challenge posed by the province's reliance on carbon-intensive energy sources.

Given this context, the introduction of SOFC-based CHP systems offers a highly promising solution for Alberta's decarbonization efforts. By generating both heat and electricity from a single fuel source with higher efficiency, these systems can significantly decrease the carbon footprint of residential units. This dual capability makes SOFC-based CHP systems particularly well-suited for Alberta's energy landscape, where the need to address high emissions from both heating and electricity is critical. The deployment of this technology presents a transformative opportunity to support Alberta's climate goals and contribute meaningfully to Canada's overall decarbonization strategy. Table 6.8 provides a comprehensive overview of the assumptions used in the development of residential CHP systems in Alberta over time. In addition, Table 6.9 presents the most recent emissions data available from Natural Resources Canada for various residential building types in Alberta. It is projected that the capital cost of residential SOFC-based CHP systems will decrease significantly, from $20,000 in 2030 to approximately $10,000 by 2050. This reduction is attributed to advancements in materials, improvements in system efficiency, and enhanced durability of solid oxide cells. The operational lifetime of these cells is anticipated to increase from 80,000 hours in 2030 to 120,000 hours by 2050.

Table 6.8: Assumptions used to calculate the technical, economic, and environmental impacts of residential CHP installations with 5 kW capacity in Alberta.

Year	2030	2035	2040	2045	2050
Installed units	0	1,000	5,000	15,000	50,000
Investment cost of a 5 kW residential CHP ($) [(1)]	20,000	18,000	15,000	13,000	10,000
Hydrogen cost ($/kg) [(2)]	1.5	1.4	1.3	1.2	1
System lifetime (hr) [(3)]	80,000	90,000	10,0000	110,000	120,000

(1) Estimated future capital costs based on the available prices and resources [303,304].

(2) Estimated future hydrogen costs based on the available costs and resources [25,29,309].

(3) Estimated future lifetime of the solid oxide fuel cells based on their degradation rate data [310,311].

Table 6.9: Space Heating Secondary Energy Use and GHG Emissions by Building Type in Alberta[1]

Factor	2017	2018	2019	2020
Total Space Heating Energy Use (PJ)	137.8	147.7	147.6	141.8
Energy Use by Building Type (PJ)				
Single Detached	106.5	114.3	114	109.3
Single Attached	9.6	10.5	10.7	10.4
Apartments	14.6	15.8	16	15.5
Mobile Homes	7	7.2	6.9	6.6
Shares (%)				
Single Detached	77.3	77.4	77.3	77.1
Single Attached	7	7.1	7.3	7.4
Apartments	10.6	10.7	10.8	10.9
Mobile Homes	5.1	4.9	4.7	4.7
Total Floor Space (million m^2)	230.3	234.3	238.4	242.4
Energy Intensity (GJ/m^2)	0.6	0.63	0.62	0.59
Total Space Heating GHG Emissions Excluding Electricity (Mt of CO_2e)	6.3	6.8	6.7	6.4
GHG Emissions by Building Type (Mt of CO_2e)				
Single Detached	4.9	5.2	5.2	4.9
Single Attached	0.4	0.5	0.5	0.5
Apartments	0.7	0.7	0.7	0.7
Mobile Homes	0.3	0.3	0.3	0.3
GHG Intensity (tone/TJ)	45.8	45.7	45.5	45.3
Heating Degree-Day Index	0.89	1	1.03	0.95

[(1)] Data on GHG emissions are presented excluding GHG emissions related to electricity production only [305].

As previously discussed, the deployment of residential CHP systems is expected to commence in 2035, following a five-year lag behind the adoption of commercial CHP systems. Additionally, the cost of hydrogen is assumed to decline from $1.5/kg in 2030 to $1/kg in 2050, considering technological advancements and increased production efficiency.

The key results for the residential CHP deployment in Alberta are summarized in Table 6.10. The analysis estimates a market value of $18 million by 2035 for residential SOFC-based CHP systems in Alberta, with potential growth to $500 million by 2050. With advancements in SOFC technology, the annual operating and maintenance costs for a 5 kW unit are projected to decrease from $2,200 in 2030 to approximately $730 by 2050. Hydrogen demand for these CHPs is expected to reach 1,100 tons annually by 2035, scaling up to 55,000 tons per year by 2050. Accounting for variables such as hydrogen prices, capital investment, and maintenance costs, the monthly expense for a household operating a 5 kW CHP unit is estimated at $321 in 2035, dropping to $152 in 2050 (in present-value terms, excluding interest). In addition to economic benefits, the widespread adoption of SOFC-based CHPs in Alberta's residential sector could lead to significant environmental and social impacts, including a reduction of approximately 380,000 tons of CO_2 emissions annually and the creation of over 450 jobs by 2050.

Table 6.10: A summary of important results for residential CHP installations with 5 kW capacity in Alberta.

Year	2030	2035	2040	2045	2050
Total investment cost of the installed CHPs for all households (Market) (Million dollars)	0	18	75	195	500
Annual repair and maintenance cost per a 5 kW unit ($)	2,200	1,755	1,317	1,034.8	730
Annual energy production of all the residential CHPs (TWh)	0	0.044	0.219	0.657	2.19
Annual hydrogen consumption of all the residential CHPs (thousand tons)	0	1.1	5.5	16.5	55
Annual hydrogen cost of a household ($)	1,650	1,540	1,430	1,320	1,100
Annual hydrogen cost of the households (Million dollars)	0	1.54	7.15	19.8	55
Monthly hydrogen and maintenance per household ($)	321	275	229	196	152
Annual total emission reduction of all households with CHPs (thousands of tons of CO_2) [(1)]	0	7.6	38	114	380
Number of direct jobs [(2)]	0	9	33	78	183
Number of indirect jobs[(3)]	0	8	36	99	275

(1) Each Alberta household (annually): 4 tons CO_2 (heating) + 3.6 tons (electricity) [285].
(2) Direct jobs are calculated based on the repair and maintenance cost of the installed units (every $200,000 creates 1 job [312]).
(3) Indirect jobs are calculated based on the total required hydrogen price for the installed units (every $200,000 creates 1 job [312]).

The visualization of the important findings for residential sector of Alberta is shown in Figure 6.18. As depicted in Figure 6.18 (a), the market for the proposed SOFC-based CHP system is projected to surpass $500 million by 2050, underscoring its substantial market potential and the anticipated growth in adoption across residential properties in Alberta. One of the most compelling advantages of this system lies in its ability to significantly reduce GHG emissions.

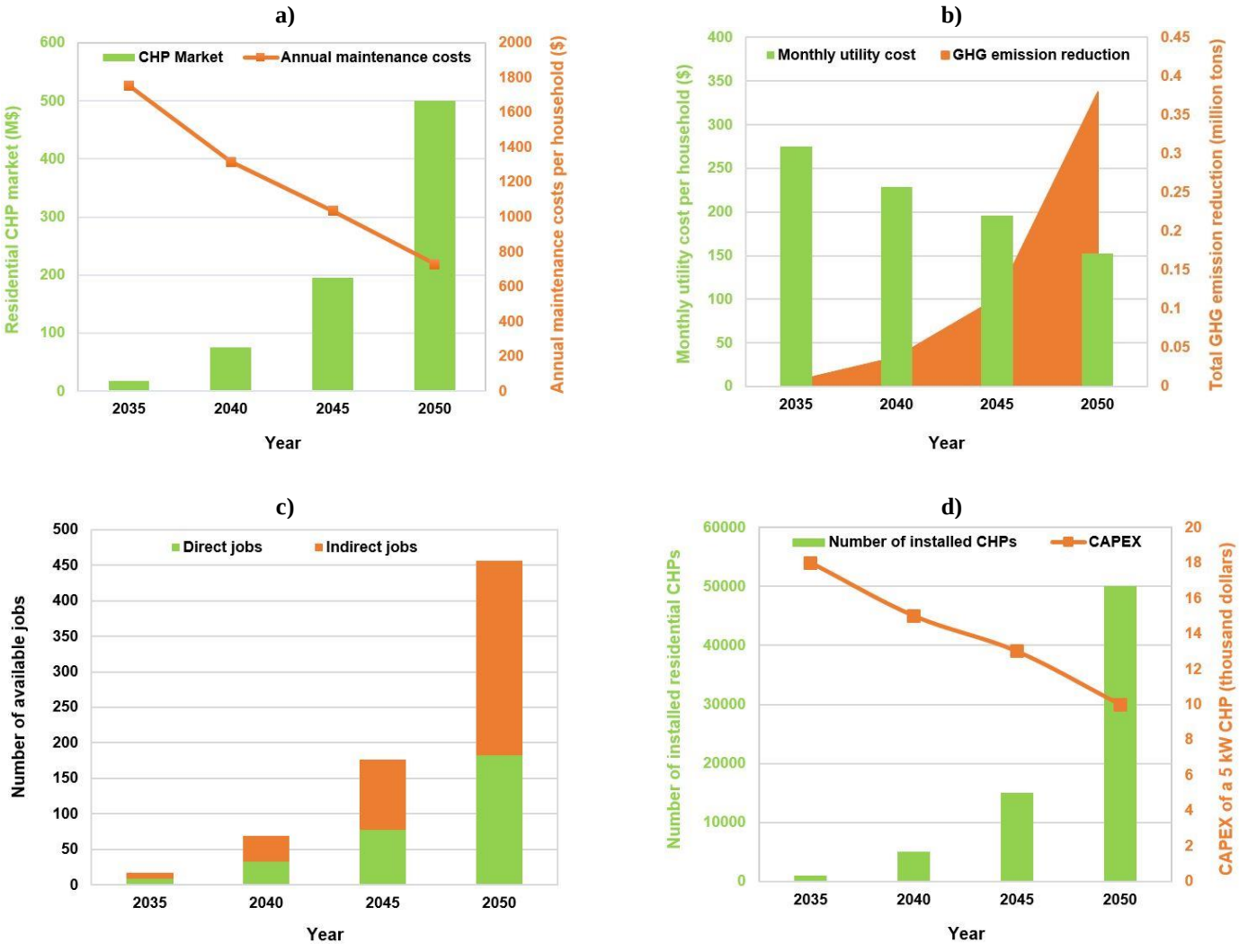

Figure 6.18: (a) CHP market and annual maintenance costs per unit, (b) Total GHG emission reduction and monthly utility cost per unit, (c) Number of the available direct and indirect jobs, and (d) total number and CAPEX per unit, following implementation of the SOFC based CHPs with 5 kW capacity per household in residential sectors of Alberta during 2035-2050.

The implementation of SOFC-based CHP systems in Alberta, a province responsible for a considerable portion of Canada's national GHG emissions, presents a powerful solution to address these environmental challenges. As illustrated in Figure 6.18 (b), deploying the proposed system—at an average monthly utility cost of $150 for a 5 kW unit—across approximately 50,000 residential properties in Alberta could prevent around 0.38 million tons of GHG emissions annually by 2050. This represents a critical contribution toward achieving Alberta's environmental goals and reducing the carbon footprint of residential energy consumption. Beyond the environmental impact, the widespread adoption of SOFC-based CHP systems is poised to create significant economic opportunities. The installation of these systems is projected to generate over 450 direct and indirect jobs across Canada by 2050, encompassing sectors such as manufacturing, installation, maintenance, and supply chain operations. This job creation not only highlights the system's role in advancing cleaner energy but also emphasizes its contribution to the broader socio-economic development associated with the transition to more sustainable energy solutions for residential households.

From a financial standpoint, the CAPEX per 5 kW system is expected to decrease substantially over time. Current estimates suggest that CAPEX will decline from approximately $18,000 per unit in 2035 to around $10,000 by 2050, as shown in Figure 6.18 (c). This reduction can be attributed to both technological advancements and economies of scale, making the system more economically feasible for widespread residential adoption in the coming decades. These cost savings, combined with the system's high efficiency and substantial environmental benefits, position SOFC-based CHP technology as a game-changing solution for sustainable energy in Canada's residential sector.

6.2.2.3 Commercial CHPs in Alberta

A summary of the assumptions for the deployment of the proposed SOFC-based CHP system in Alberta's commercial sector over the 2030 to 2050 timeframe is listed in Table 6.11. Similar to the assumption of the residential sector, these assumptions encompass a wide range of critical factors, the estimated installed units, fuel costs, capital and operational expenditures, as well as anticipated lifetime over the time. These elements provide a solid foundation for forecasting the financial viability, energy savings, and environmental benefits that can be realized by integrating this advanced technology into Alberta's commercial energy landscape. The primary distinction in the assumptions between the commercial and residential sectors is the anticipated earlier deployment of CHP systems in the commercial sector, which is projected to commence in 2030, five years ahead of the residential sector. Moreover, Table 6.12 provides in-depth data on current energy consumption patterns and GHG emissions within Alberta's commercial sector, which are essential inputs for the system performance and emissions reduction calculations.

Table 6.11: Project assumptions used to calculate the technical, economic, and environmental impacts of commercial CHP installations with 100 kW capacity in Alberta.

Year	2030	2035	2040	2045	2050
Installed units	50	250	750	2,500	10,000
Investment cost of a 100 kW commercial CHP (thousand dollars) [(1)]	400	360	300	260	200
Hydrogen cost ($/kg) [(2)]	1.5	1.4	1.3	1.2	1
System lifetime (hr) [(3)]	80,000	90,000	100,000	110,000	120,000

(1) Estimated future capital costs based on the available prices and resources [303,304].
(2) Estimated future hydrogen costs based on the available costs and resources [25,29,309].
(3) Estimated future lifetime of the solid oxide fuel cells based on their degradation rate data [310,311].

Table 6.12: Secondary energy use and GHG emissions of commercial sectors by energy source in Alberta[1]

Factor	2018	2019	2020	2021
Total Energy Use (PJ)	223.6	232.6	225.2	218.0
Energy Use by Energy Source (PJ)				
Electricity	63.4	68.4	69.4	68.9
Natural gas	150.6	153.9	146.4	140.6
Light Fuel Oil and Kerosene	0.1	0.1	0.0	0.1
Heavy Fuel Oil	0.1	0.1	0.0	0.0
Steam	0.0	0.0	0.0	0.0
Other	9.4	10.1	9.5	8.4
Shares (%)				
Electricity	28.4	29.4	30.8	31.6
Natural gas	67.3	66.2	65.0	64.5
Light Fuel Oil and Kerosene	0.0	0.0	0.0	0.0
Heavy Fuel Oil	0.0	0.0	0.0	0.0
Steam	0.0	0.0	0.0	0.0
Other	4.2	4.3	4.2	3.9
Activity				
Total Floor Space (million m^2)	111.0	110.3	109.8	109.8
Energy Intensity (GJ/m^2)	2.01	2.10	2.04	1.98
Total GHG Emissions Excluding Electricity (Mt of CO2e)	8.2	8.4	7.9	7.6
GHG Emissions by Energy Source (Mt of CO2e)				
Electricity	–	–	–	–
Natural gas	7.6	7.7	7.4	7.0
Light Fuel Oil and Kerosene	0.0	0.0	0.0	0.0
Heavy Fuel Oil	0.0	0.0	0.0	0.0
Steam	0.0	0.0	0.0	0.0
Other	0.6	0.6	0.6	0.5
GHG Intensity (tonne/TJ)	36.5	35.9	35.2	34.7
Heating Degree-Day Index	1.00	1.03	0.95	0.93
Cooling Degree-Day Index	1.22	0.40	0.98	2.28

(1) Data on GHG emissions are presented excluding GHG emissions related to electricity production [305]

The key findings for commercial CHP deployment in Alberta are presented in Table 6.13. The analysis projects a market value of $20 million for commercial SOFC-based CHP systems by 2030, with potential growth to $2 billion by 2050. Advancements in SOFC technology are expected to significantly reduce the annual operating and maintenance costs for a 100 kW commercial unit, decreasing from $44,000 in 2030 to approximately $14,600 by 2050. Hydrogen demand for these systems is forecasted to reach 1,100 tons per year by 2030, increasing substantially to 220,000 tons annually by 2050. Considering variables such as hydrogen prices, capital costs, and maintenance

expenses, the monthly operational cost for a 100 kW commercial CHP unit is estimated at $6,417 in 2030, declining to $3,050 in 2050 (in present-value terms, excluding interest). Beyond economic advantages, the widespread adoption of SOFC-based CHPs in Alberta's commercial sector could deliver significant environmental and social benefits, including an annual reduction of approximately 1.6 million tons of CO_2 emissions and the creation of over 1,800 jobs by 2050.

Table 6.13: A summary of important results for commercial CHP installations with 100 kW capacity in Alberta.

Year	2030	2035	2040	2045	2050
Total investment cost of the installed CHPs for all commercial units (Market) (Million dollars)	20	90	225	650	2000
Annual repair and maintenance cost per a 100 kW commercial CHP ($)	44,000	35,100	26,340	20,696	14,600
Annual energy production of all the commercial CHPs (TWh)	0.044	0.219	0.657	2.19	8.76
Annual hydrogen consumption of all the commercial CHPs (thousand tons)	1.1	5.5	16.5	55	220
Annual hydrogen consumption cost of a 100 kW commercial CHP ($)	33,000	30,800	28,600	26,400	22,000
Annual hydrogen consumption cost of all the commercial CHPs (Million dollars)	1.65	7.7	21.45	66	220
Monthly hydrogen and maintenance costs per a 100 kW CHP ($)	6,417	5,492	4,578	3,925	3,050
Annual total emission reduction of all commercial units with CHPs (thousands of tons of CO_2) [(1)]	8	40	120	400	1600
Number of direct jobs [(2)]	11	44	99	259	730
Number of indirect jobs [(3)]	9	39	108	330	1100

(1) Each commercial unit (annually): 1.6 tons CO_2/kW (heating + electricity) [313].
(2) Direct jobs are calculated based on the repair and maintenance cost of the installed units (every $200,000 creates 1 job [312]).
(3) Indirect jobs are calculated based on the total required hydrogen price for the installed units (every $200,000 creates 1 job [312]).

A summary of the results for installing the proposed SOFC-based CHP for the commercial sector of Alberta is shown in Figure 6.19. Notably, over 25% of the total GHG emissions reductions within Canada's commercial sector resulting from the deployment of these systems are expected to occur in Alberta. This highlights the province's pivotal role in contributing to national decarbonization efforts and underscores the substantial environmental impact that widespread adoption of CHP systems could have on Canada's overall carbon footprint. Alberta's high carbon

intensity grid and its reliance on fossil fuels further amplify the potential for significant GHG reductions, making it a strategic location for such clean energy solutions.

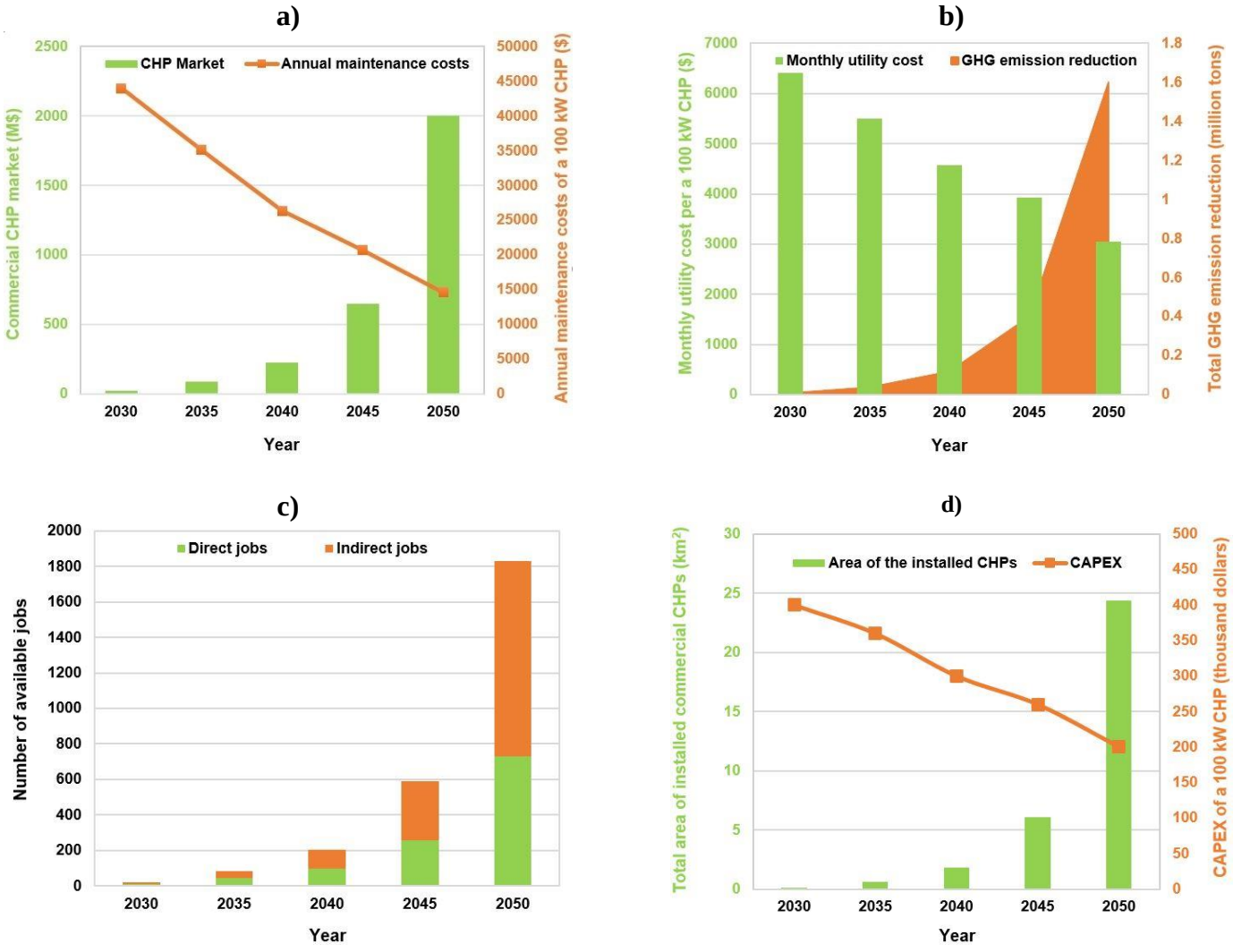

Figure 6.19: (a) CHP market and annual maintenance costs per unit, (b) Total GHG emission reduction and monthly utility cost per unit, (c) Number of the available direct and indirect jobs, and (d) total area and CAPEX per unit, following implementation of the SOFC based CHPs with 100 kW capacity per unit in commercial sectors of Alberta during 2030-2050.

The economic and environmental benefits of deploying SOFC-based CHP systems in Alberta are equally promising. By 2050, the commercial sector in Alberta is projected to encompass a market valued at approximately $2 billion, covering a commercial area of over 24 km². Within this

context, the installation of CHP systems could lead to a reduction of over 1.6 million tons of GHG emissions annually, directly contributing to Alberta's climate action targets. Furthermore, this initiative is expected to generate over 1,800 jobs, both direct and indirect, providing a substantial economic boost to the province. These jobs would span multiple sectors, including system manufacturing, installation, maintenance, and associated supply chains, reinforcing the economic viability of this initiative.

In addition to environmental and economic advantages, the deployment of these systems would result in lower monthly utility costs for Alberta's commercial sector compared to the national average, primarily due to the lower cost of hydrogen in the province. Alberta's abundant natural gas resources, coupled with its growing hydrogen production capabilities, create a favorable market for affordable hydrogen, further enhancing the attractiveness of SOFC-based CHP systems. This combination of lower energy costs, job creation, and significant emissions reductions makes the implementation of SOFC-based CHP technology a compelling strategy for Alberta, positioning the province as a leader in the transition towards a low-carbon, energy-efficient future.

6.2.3 Canada

Here, the results of techno-economic and environmental calculations for development of the SOFC-based CHPs across the residential and commercial sectors of Canada are presented.

6.2.3.1 Residential CHPs in Canada

This section provides a comprehensive overview of the results derived from the techno-economic analysis conducted for the deployment of SOFC-based CHP systems in the Canadian residential sector. The analysis aims to evaluate both the technical and economic viability of implementing this system to enhance energy efficiency and reduce carbon emissions. To begin with, Table 6.14

outlines the list of assumptions used in the development of the proposed system tailored specifically for the Canadian residential market. These assumptions are critical for accurately assessing the system's performance, costs, and potential market adoption. It is important to highlight that the only distinction in the assumptions between the residential sectors in Canada (Table 6.14) and Alberta (Table 6.8) pertains to the variation in hydrogen prices over time.

Table 6.14: Assumptions used to calculate the technical, economic, and environmental impacts of residential CHP installations with 5 kW capacity in Canada.

Year	2030	2035	2040	2045	2050
Installed units	0	6,000	30,000	90,000	300,000
Investment cost of a 5 kW residential CHP ($)[(1)]	20,000	18,000	15,000	13,000	10,000
Hydrogen cost ($/kg) [(2)]	1.7	1.6	1.4	1.2	1
System lifetime (hr) [(3)]	80,000	90,000	10,0000	110,000	120,000

(1) Estimated future capital costs based on the available prices and resources [303,304].
(2) Estimated future hydrogen costs based on the available costs and resources [25,29,309].
(3) Estimated future lifetime of the solid oxide fuel cells based on their degradation rate data [310,311].

The key findings for residential CHP deployment across Canada are presented in Table 6.15. The analysis projects a market valuation of $110 million for residential SOFC-based CHP systems by 2035, with potential growth exceeding $3 billion by 2050. The hydrogen demand required to support these systems is anticipated to reach 6,600 tons annually by 2035, expanding significantly to 330,000 tons per year by 2050. Considering factors such as hydrogen pricing, capital expenditures, and maintenance costs, the estimated monthly operational cost for a household utilizing a 5 kW CHP unit is $339 in 2035, decreasing to $152 in 2050 (in present-value terms, excluding interest). In addition to the economic advantages, the widespread implementation of SOFC-based CHPs in Canada's residential sector could yield substantial environmental and societal benefits. These include an annual reduction of approximately 696,000 tons of CO_2 emissions and the creation of over 2,700 jobs by 2050.

Table 6.15: A summary of important results for residential CHP installations with 5 kW capacity in Canada.

Year	2030	2035	2040	2045	2050
Total investment cost of the installed CHPs for all households (Market) (Billion dollars)	0	0.11	0.45	1.17	3.01
Annual repair and maintenance cost per a 5 kW unit ($)	2,200	1,755	1,317	1,034.8	730
Annual energy production of all the residential CHPs (TWh)	0	0.263	1.314	3.942	13.14
Annual hydrogen consumption of all the residential CHPs (thousand tons)	0	6.6	33	99	330
Annual hydrogen cost of a household ($)	1,870	1,760	1,540	1,320	1,100
Annual hydrogen cost of the households (Million dollars)	0	10.56	46.2	118.8	330
Monthly hydrogen and maintenance per household ($)	339	293	238	196	152
Annual total emission reduction of all households with CHPs (thousands of tons of CO_2) [(1)]	0	13.9	69.6	208.8	696.0
Number of direct jobs [(1)]	0	53	198	466	1095
Number of indirect jobs [(3)]	0	53	231	594	1650

(1) Each Canadian household (annually): 1.52 tons CO_2 (heating) + 0.8 tons (electricity) [285].
(2) Direct jobs are calculated based on the repair and maintenance cost of the installed units (every $200,000 creates 1 job [312]).
(3) Indirect jobs are calculated based on the total required hydrogen price for the installed units (every $200,000 creates 1 job [312]).

The visualization of important results is presented in Figure 6.20. As previously mentioned, it is assumed that the growth of CHP installations in the residential sector will commence with a five-year delay following the expansion in the commercial sector. As illustrated in Figure 6.20 (a), the market for the proposed system is projected to exceed $2.8 billion by 2050, reflecting its significant market potential and the anticipated increase in adoption across residential properties in Canada. One of the most compelling benefits of this system is its substantial potential to reduce GHG emissions. Currently, statistical data shows that each residential unit in Canada contributes approximately 1.52 metric tons of CO_2 annually from heating, with an additional 0.8 metric tons of CO2 produced from electricity consumption [285]. The adoption of SOFC-based CHPs can dramatically curtail these emissions. As shown in Figure 6.20 (b), by installing the proposed system, with an average monthly utility cost of $150 per 5 kW system, across a portion of the Canadian residential sector (covering approximately 300,000 units), it is estimated that about 0.7 million tons of GHG emissions could be avoided annually by 2050. This represents a significant

step toward achieving Canada's environmental targets, particularly in reducing the carbon footprint of residential energy use.

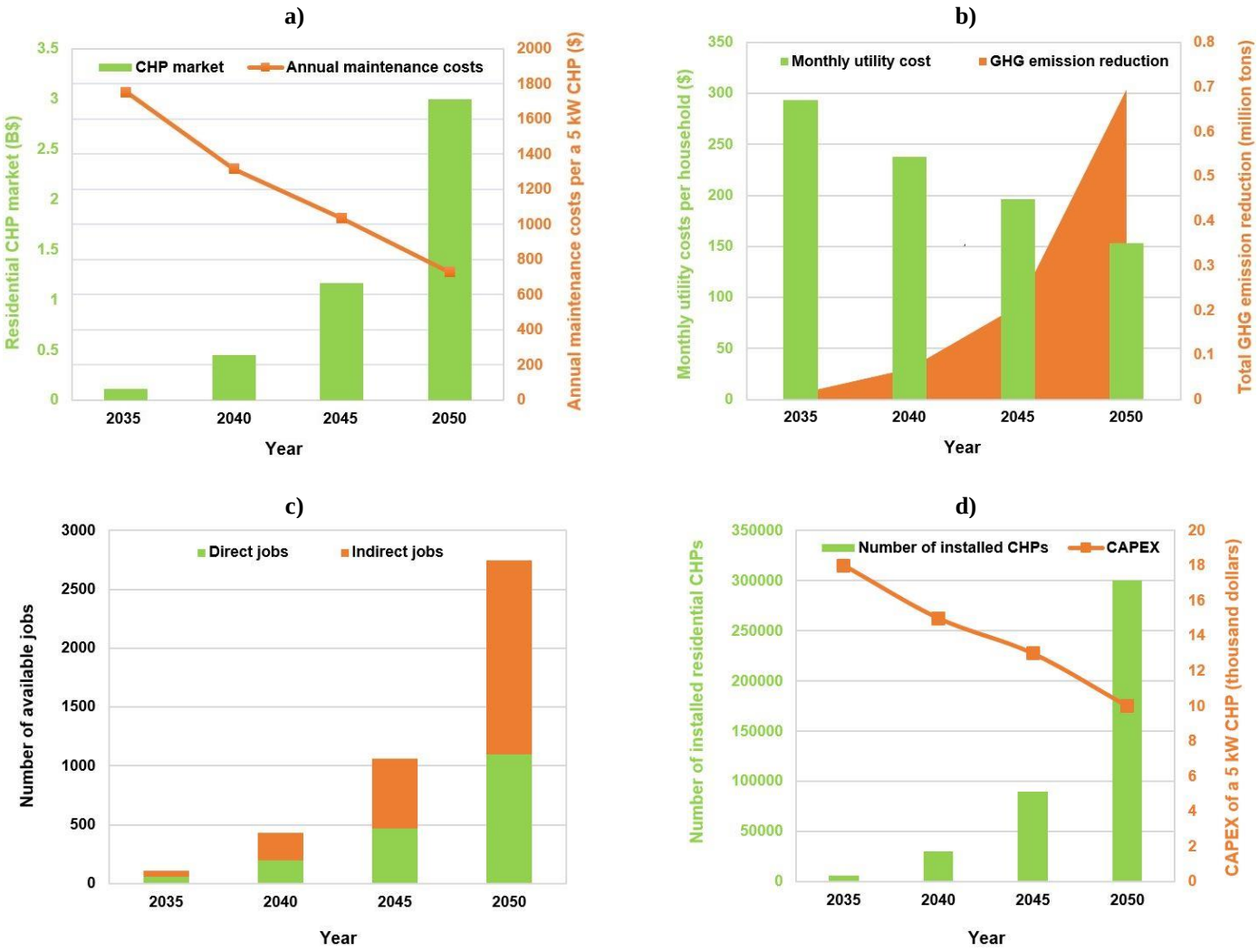

Figure 6.20: (a) CHP market and annual maintenance costs per unit, (b) Total GHG emission reduction and monthly utility cost per unit, (c) Number of the available direct and indirect jobs, and (d) total number and CAPEX per unit, following implementation of the SOFC based CHPs with 5 kW capacity per household in residential sectors of Canada during 2035-2050.

In addition to environmental benefits, the widespread implementation of SOFC-based CHPs will create significant economic opportunities. The installation of these systems is expected to generate over 2,700 direct and indirect jobs nationwide by 2050, spanning various sectors including manufacturing, installation, maintenance, and supply chain services. These job creation figures

underscore the broader socio-economic advantages of transitioning to cleaner, more efficient energy solutions for residential homes.

From a financial perspective, the CAPEX per 5 kW system is also expected to decrease considerably over time. Current projections indicate that CAPEX will decline from approximately $18,000 per unit in 2035 to about $10,000 by 2050, as shown in Figure 6.20 (d). This reduction reflects both technological advancements and economic improvements, making the proposed system more financially accessible for widespread residential adoption in the coming decades. These cost reductions, coupled with the system's efficiency and environmental benefits, position the SOFC-based CHP technology as a transformative solution for sustainable energy in Canada's residential sector.

6.2.3.2 Commercial CHPs in Canada

A summary of the assumption for the implementation of the SOFC-based CHP in Canada's commercial sector from 2030 to 2050 is presented in Table 6.16. Additionally, Table 6.17 provides detailed data on energy consumption and GHG emissions within the Canadian commercial sector, which were utilized for the calculations.

Table 6.16: Assumptions used to calculate the technical, economic, and environmental impacts of commercial CHP installations with 100 kW capacity in Canada.

Year	2030	2035	2040	2045	2050
Installed units	300	1500	4500	15,000	60,000
Investment cost of a 100 kW commercial CHP (thousand dollars) [(1)]	400	360	300	260	200
Hydrogen cost ($/kg) [(2)]	1.7	1.6	1.4	1.2	1
System lifetime (hr) [(3)]	80,000	90,000	100,000	110,000	120,000

(1) Estimated future capital costs based on the available prices and resources [303,304].
(2) Estimated future hydrogen costs based on the available costs and resources [25,29,309].
(3) Estimated future lifetime of the solid oxide fuel cells based on their degradation rate data [310,311].

Table 6.17: Secondary energy use and GHG emissions of commercial sectors by energy source in Canada[1]

Factor	2018	2019	2020	2021
Total Energy Use (PJ)	1,215.2	1,258.3	1,214.5	1,200.8
Energy Use by Activity Type (PJ)				
Wholesale Trade	63.6	66.2	62.1	61.4
Retail Trade	187.6	193.8	179.0	175.9
Transportation and Warehousing	44.0	46.2	44.6	44.3
Information and Cultural Industries	24.7	25.5	23.9	23.6
Offices	424.7	440.8	402.8	398.5
Educational Services	159.5	166.0	154.1	152.7
Health Care and Social Assistance	164.6	168.8	211.2	209.1
Arts, Entertainment and Recreation	29.2	29.8	26.7	26.0
Accommodation and Food Services	92.6	96.2	86.4	85.9
Other Services	17.9	18.5	17.4	17.1
Shares (%)				
Wholesale Trade	5.3	5.3	5.1	5.1
Retail Trade	15.5	15.5	14.8	14.7
Transportation and Warehousing	3.6	3.7	3.7	3.7
Information and Cultural Industries	2.0	2.0	2.0	2.0
Offices	35.1	35.2	33.3	33.4
Educational Services	13.2	13.3	12.8	12.8
Health Care and Social Assistance	13.6	13.5	17.5	17.5
Arts, Entertainment and Recreation	2.4	2.4	2.2	2.2
Accommodation and Food Services	7.7	7.7	7.1	7.2
Other Services	1.5	1.5	1.4	1.4
Activity				
Total Floor Space (million m^2)	756.4	758.4	760.6	765.5
Energy Intensity (GJ/m^2)	1.60	1.65	1.59	1.56
Total GHG Emissions Excluding Electricity (Mt of CO2e)	52.1	53.9	50.4	49.5
GHG Emissions by Energy Source (Mt of CO2e)				
Wholesale Trade	2.75	2.86	2.60	2.56
Retail Trade	8.08	8.32	7.40	7.23
Transportation and Warehousing	1.95	2.05	1.92	1.90
Information and Cultural Industries	1.07	1.10	1.00	0.98
Offices	17.87	18.55	16.36	16.05
Educational Services	6.90	7.16	6.45	6.36
Health Care and Social Assistance	7.20	7.36	8.93	8.80
Arts, Entertainment and Recreation	1.26	1.28	1.11	1.07
Accommodation and Food Services	4.06	4.22	3.67	3.63
Other Services	0.77	0.80	0.73	0.71

(1) Data on GHG emissions are presented including GHG emissions related to electricity production [305].

Table 6.18 outlines the key insights into the deployment of commercial CHP systems in Canada. The market value for commercial SOFC-based CHP systems is projected to reach $120 million by 2030, with the potential to grow to $12 billion by 2050. Technological advancements in SOFC

systems are expected to lead to a substantial reduction in annual operating and maintenance costs for a 100 kW unit, decreasing from $44,000 in 2030 to approximately $14,600 by 2050. The hydrogen demand associated with these systems is anticipated to reach 6600 tons annually by 2030 and is projected to scale up significantly to 1.32 million tons per year by 2050. Factoring in variables such as hydrogen prices, capital investment, and maintenance expenses, the monthly operational cost for a 100 kW commercial CHP unit is estimated at $6,784 in 2030, decreasing to $3,050 by 2050 (in present-value terms, excluding interest). In addition to the economic benefits, the extensive adoption of SOFC-based CHP systems in Canada's commercial sector could result in considerable environmental and social gains, including an annual reduction of approximately 7.8 million tons of CO_2 emissions and the creation of approximately 11,000 jobs by 2050.

Table 6.18: A summary of important results for commercial CHP installations with 100 kW capacity in Canada.

Year	2030	2035	2040	2045	2050
Total investment cost of the installed CHPs for all commercial units (Market) (billion dollars)	0.12	0.54	1.35	3.9	12
Annual repair and maintenance cost per a 100 kW commercial CHP ($)	44,000	35,100	26,340	20,696	14,600
Annual energy production of all the commercial CHPs (TWh)	0.263	1.314	3.942	13.14	52.56
Annual hydrogen consumption of all the commercial CHPs (thousand tons)	6.6	33	99	330	1,320
Annual hydrogen consumption cost of a 100 kW commercial CHP ($)	37,400	35,200	30,800	26,400	22,000
Annual hydrogen consumption cost of all the commercial CHPs (million dollars)	11.2	52.8	139	396	1320
Monthly hydrogen and maintenance costs per a 100 kW CHP ($)	6,784	5,859	4,762	3,925	3,050
Annual total emission reduction of all commercial units with CHPs (million tons of CO_2) [(1)]	0.039	0.195	0.585	1.95	7.8
Number of direct jobs [(2)]	66	264	593	1553	4380
Number of indirect jobs [(3)]	57	264	693	1980	6600

(1) Each commercial unit (annually): 1.3 tons CO_2/kW (heating + electricity) [305].

(2) Direct jobs are calculated based on the repair and maintenance cost of the installed units (every $200,000 creates 1 job [312]).

(3) Indirect jobs are calculated based on the total required hydrogen price for the installed units (every $200,000 creates 1 job [312]).

A summary of important results for the installation of the proposed SOFC-based CHP in commercial sector of Canada is shown in Figure 6.21.

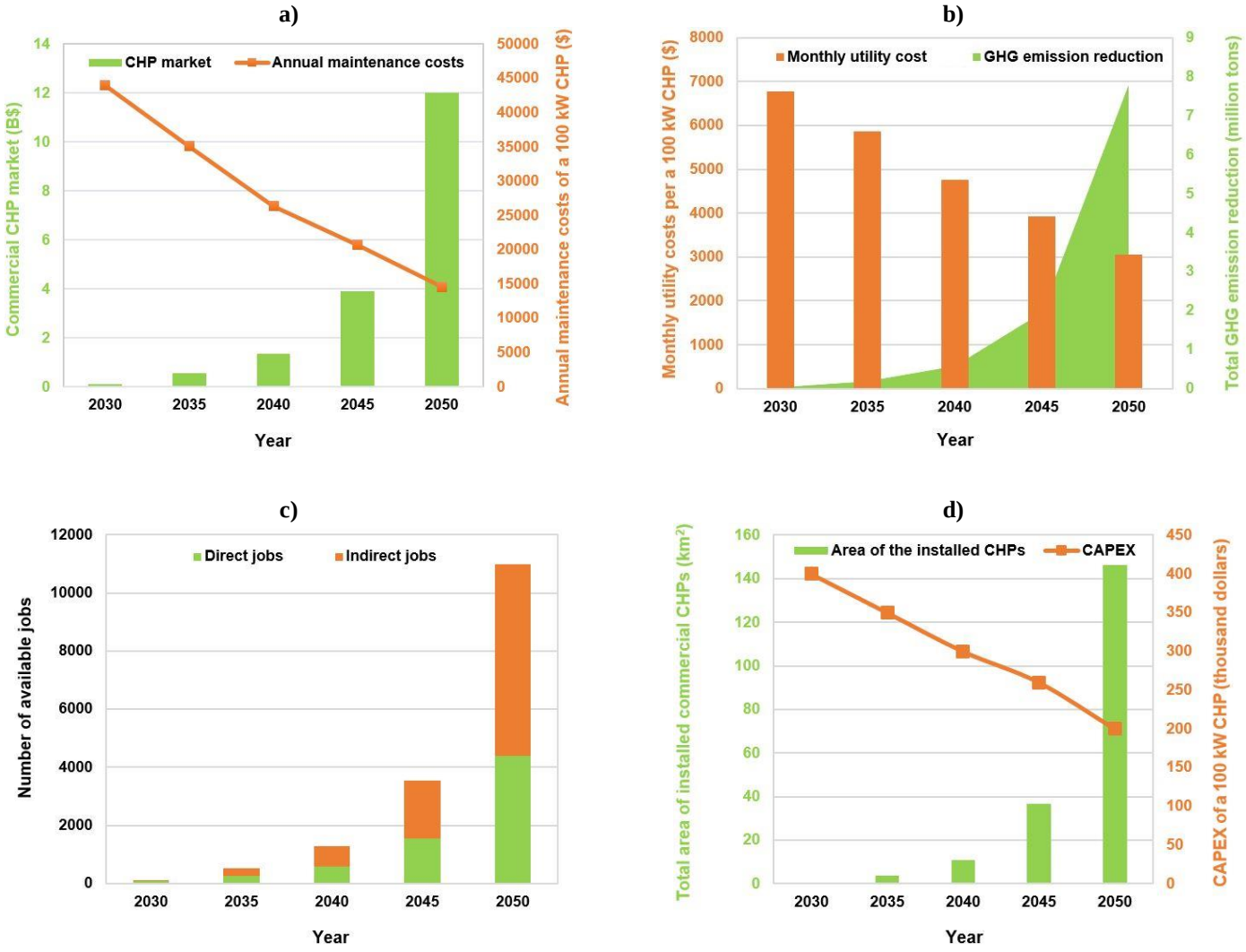

Figure 6.21: (a) CHP market and annual maintenance costs per unit, (b) Total GHG emission reduction and monthly utility cost per unit, (c) Number of the available direct and indirect jobs, and (d) total area and CAPEX per unit, following implementation of the SOFC based CHPs with 100 kW capacity per unit in commercial sectors of Canada during 2030-2050.

As shown in Figure 6.21 (a), the maintenance costs associated with SOFC-based CHP systems are projected to significantly decline over time, driven by the increased number of installed units across the commercial sector of Canada. This cost reduction trend highlights the growing efficiency and economies of scale anticipated as the technology matures. Each commercial unit

generates annual GHG emissions of 1.6 tons of CO_2 per kW in Canada [305,313]. It is estimated that the deployment of the proposed system could prevent approximately 8 million tons of GHG emissions annually by targeting even a small portion of Canada's commercial sector. This substantial environmental impact underscores the system's potential to contribute meaningfully to Canada's decarbonization goals. In addition to environmental benefits, this expansion will generate considerable economic advantages, notably reducing monthly utility costs for a 100 kW system from $6,784 in 2030 to an estimated $3,050 by 2050. This reduction in operational expenses would not only enhance the financial viability of commercial enterprises but also promote broader adoption of sustainable energy solutions. The deployment of SOFC-based CHPs is also expected to stimulate job creation, both directly and indirectly, with projections indicating the creation of approximately 11,000 jobs by 2050, contributing to economic growth and workforce development.

Further details, including estimates of the total installation area required for commercial CHP systems and the projected capital expenditure (CAPEX) per 100 kW system from 2030 to 2050, are presented in Figure 6.21 (d). These estimates aim to consider the scalability and cost trajectory of the proposed system over the next two decades, emphasizing its potential as a long-term sustainable energy solution.

6.3 Summary of chapter

In this chapter, a detailed case study was carried out for the University of Alberta, comparing SOFC- and HICE-based CHP systems to assess their suitability for sustainable campus energy management. Furthermore, a techno-economic and environmental assessment was performed to evaluate the viability and potential impacts of SOFC-based CHP systems for the residential and

commercial sectors in Alberta and Canada. This evaluation highlighted the economic and environmental advantages of SOFC-based CHP, particularly for larger-scale applications, and projected its potential for market growth, job creation, and emissions reduction. Key findings from this chapter include:

- **Case Study on the University of Alberta**:
    - Currently, the University of Alberta incurs an annual cost of $39 million for energy (electricity and heat) and generates over 300,000 tons of GHG emissions. Analysis indicates that a CHP capacity of 70 MW would be sufficient to meet the university's full energy demand.
    - HICE-based CHP has a lower initial capital cost of $140 million and total annual costs of $24.25 million, though it generates NOx emissions exceeding 4 tons.
    - SOFC-based CHP, though currently more expensive at $280 million capital cost and $66.32 million annual costs, holds long-term economic promise due to ongoing technological advancements.
    - Based on economic considerations alone, HICE-based CHP is preferable; however, in the long term, SOFC-based CHP is expected to offer superior environmental and economic benefits, positioning it as the optimal solution for sustainable energy management at the University of Alberta.
- **Case Study for Alberta and Canada**:
    - By 2050, SOFC-based CHP systems are projected to generate approximately $2.5 billion in Alberta and $15 billion across Canada.

- Revenue distribution is expected to favor commercial sectors, which will contribute around 80% of the total, while residential sectors will account for the remaining 20%.
- Deployment of SOFC-based CHP systems is projected to reduce GHG emissions by approximately 1.6 million tons in Alberta's commercial sector and 7.8 million tons in Canada's commercial sector by 2050.
- In the residential sector, GHG emissions reductions are estimated to reach 700,000 tons in Canada and 380,000 tons in Alberta.
- SOFC-based CHP systems are anticipated to create approximately 2,300 jobs in Alberta and 13,800 jobs across Canada by 2050.

These results underscore the strategic importance of advancing SOFC-based CHP technology to maximize economic returns, reduce environmental impacts, and enable sustainable energy solutions across multiple sectors.

6.4 Uncertainty consideration

In this analysis, key economic parameters, including capital investment, operating and maintenance costs, and interest rates, were considered as per common practice in the literature. However, more detailed cost elements, such as those related to engineering, installation, insurance, and other ancillary expenses, have been excluded from the scope of this study. These exclusions introduce a degree of uncertainty to the presented calculations. Future analyses should aim to address these uncertainties by incorporating a comprehensive set of cost factors, supported by up-to-date and reliable cost functions as they become available. Such refinements would enhance the robustness and reliability of the economic analysis, aligning it more closely with real-world conditions.

PART 4: Conclusions

Chapter 7: Conclusions

Achieving an optimal balance between the economic feasibility and sustainability in hydrogen production remains a critical challenge within the hydrogen sector. Given the superior efficiency of concentrated solar power compared to other renewable energy sources, coupled with the significant and largely unexplored opportunities in the literature concerning high-temperature solar thermal-driven hydrogen production, this thesis was dedicated to exploring solar-powered water electrolysis and methane pyrolysis techniques. A detailed comparative analysis of these methods was also presented for the novel proposed designs, highlighting their respective potentials and limitations in advancing sustainable hydrogen generation. Furthermore, the potential of hydrogen storage and hydrogen-based combined heat and power (CHP) systems was examined from multiple perspectives, focusing on the University of Alberta, Alberta, and Canada.

7.1 Solar-based water electrolysis and methane pyrolysis methods

Part II of this thesis (Chapters 2, 3, and 4) was dedicated to the design and techno-economic analysis of innovative cycles that integrate concentrated solar power (CSP) with proton exchange membrane (PEM) electrolyzer/fuel cell systems (Chapter 2), solid oxide electrolyzer/fuel cell systems (Chapter 3), and methane pyrolysis (Chapter 4) processes. The objective was to evaluate the technical feasibility and economic performance of these novel hybrid configurations in advancing solar-based hydrogen production technologies.

Key analyses of Chapter 2 involved designing a novel CSP-integrated PEM electrolyzer/fuel cell system, conducting sensitivity assessments to identify the most influential parameters affecting system performance, selecting the optimal working fluid to maximize the operational efficiency of the solar unit, and performing comprehensive techno-economic optimization. Despite

these efforts, the exergy round-trip efficiency (ERTE) of the CSP-PEM configuration remained limited to approximately 18%, with a cost rate of 492 $/hr. While this configuration demonstrated improved performance over photovoltaic (PV)-based systems, it lagged behind high-temperature technologies such as solid oxide electrolyzer cell (SOEC) and methane pyrolysis, which exhibited superior thermodynamic efficiencies and economic potentials.

In Chapter 3, a novel hydrogen production, storage, and utilization system was developed through the integration of a heliostat solar field with reversible solid oxide cells, and thoroughly examined from a techno-economic perspective. This investigation included a comprehensive analysis, supported by a real-world case study, to assess the system's viability and performance under practical conditions. The results demonstrated a hydrogen production rate of 7.76 tons per day via SOEC, along with an energy output of 54.3 MWh from solid oxide fuel cells (SOFC) for peak demand shaving, achieving a round-trip efficiency (RTE) of approximately 74%. From an economic standpoint, the analysis revealed that the system would reach profitability at hydrogen sales prices exceeding $2.75 per kilogram. Moreover, the incorporation of hydrogen storage for peak shaving purposes presented a highly attractive payback period, estimated to be less than two years, particularly in high-insolation regions such as Los Angeles. These findings underscore the potential of solid oxide technology, combined with concentrated solar power, to serve as a cost-effective and sustainable solution for both hydrogen production and grid stabilization in sun-rich locations.

In Chapter 4, a novel design for producing turquoise hydrogen with the minimal carbon footprint was presented, combining methane pyrolysis in molten salt with a heliostat solar field. To keep hydrogen production running smoothly during nighttime or when solar energy is

unavailable, the system was also integrated with a high-temperature thermal energy storage (HTES) unit. A detailed analysis was performed to assess the system's performance and calculate the levelized cost of hydrogen (LCOH) under different conditions. The results showed that an initial capital investment of $22 million is needed to produce approximately 9 tons of hydrogen per day. The system operates with an RTE of 49.8% and achieves an LCOH of $1.93 per kilogram, assuming a carbon price of $300 per ton and without factoring in any clean hydrogen tax incentives. If the HTES is powered by renewable energy, the capital cost and LCOH would increase to $45 million and $2.03 per kilogram, respectively. This thesis also highlighted how natural gas prices and clean hydrogen tax incentives play a crucial role in determining the LCOH. For example, as methane prices rise from $2 to $10 GJ, the base LCOH increases from $1 to $2.8 per kilogram. Moreover, the results indicate that the US Department of Energy's (DOE) target of $1 per kilogram of hydrogen could be reached by applying US hydrogen tax incentives and reducing the cost of renewable energy infrastructure by 20%.

7.2 Comparison of different technologies and case studies

Part 3, including Chapters 5 and 6, was dedicated to present a comparative analysis of various hydrogen production and consumption technologies, explored through multiple case studies. This part evaluated the performance, efficiency, and economic feasibility of different hydrogen production methods, alongside their practical applications across diverse sectors. These case studies provided a detailed examination of the strengths and limitations of each technology, offering valuable insights into their potential role in the evolving hydrogen economy.

In Chapter 5, a comparative techno-economic assessment was conducted between solar-based molten salt methane pyrolysis (SMSMP) and solar-based solid oxide electrolyzer cell (SSOEC) systems, using five cities—Edmonton, San Antonio, Auckland, Seville, and Lyon—as case

studies. The SSOEC, with both electrical and thermal inputs, produced more hydrogen at the same solar capacity, achieving an RTE of 75.2%, compared to 40.6% for SMSMP. However, SMSMP had a lower LCOH at $2.83/kg, versus $5.34/kg for SSOEC. The analysis showed that SMSMP is more cost-effective under moderate to ideal solar conditions, while SSOEC will be preferable in low solar regions, depending on grid carbon intensity and electricity prices. For instance, Edmonton, despite its low methane prices, had one of the highest LCOH for SMSMP at $4.49/kg due to poor solar conditions. San Antonio and Auckland showed the lowest LCOH for SMSMP at $2.31/kg, with Auckland also producing the cleanest hydrogen (2.01 kg CO_2/kg H_2). SSOEC was cheapest in Auckland ($5.19/kg) and Seville ($5.32/kg), with Lyon producing the cleanest hydrogen (1.84 kg CO2/kg H_2). Even with potential cost reductions in renewable infrastructure, SSOEC's LCOH is unlikely to match SMSMP or meet the $1/kg target of hydrogen production by DOE. This highlights the need for government incentives, such as clean hydrogen tax credits, to boost the viability of SSOEC systems.

In Chapter 6, first a detailed case study focusing on the University of Alberta's energy management was performed. The university's current annual expenditure for electricity and heat is over $39 million (excluding maintenance fees), contributing to over 300,000 tons of GHG emissions. In pursuit of a more sustainable campus, a detailed comparative analysis by using real operational data was conducted on SOFC-based and hydrogen internal combustion engine (HICE)-based CHPs, two leading hydrogen-based clean technologies. Results indicated that a CHP capacity of 70 MW could satisfy the university's total energy demand for both heat and electricity. Although the HICE-based CHP incurs direct NO_x emissions exceeding 4 tons and involves a lower capital cost of $140 million and annual costs of $24.25 million, the SOFC-based CHP, despite its current higher costs ($280 million for capital and $66.32 million annually), was anticipated to

achieve more favorable economic performance with ongoing development. Thus, under current economic conditions, the HICE-based CHP may be the preferred option; however, as SOFC technology advances, it is likely to become the more advantageous choice in terms of both economic and environmental impacts, solidifying its status as the optimal long-term solution for sustainable campus energy management.

In addition, a comprehensive techno-economic and environmental analyses were conducted to assess the potential of SOFC-based CHP systems for Alberta's and Canada's residential and commercial sectors. The SOFC-based CHP systems exhibit significantly greater techno-economic feasibility for large-scale applications, making them especially viable for commercial sectors. Consequently, market potential and associated job creation were projected to be substantially higher in the commercial sector than in the residential sector. Implementation timelines were thus set to commence in 2030 for commercial units and in 2035 for residential units. By 2050, projections estimated that SOFC-based CHP systems could have a market of around $2.5 billion in Alberta and $15 billion across Canada, with approximately 80% of this revenue stemming from commercial applications and the remaining 20% from residential use. Furthermore, this market expansion was anticipated to create roughly 2,300 jobs in Alberta and 13,800 jobs nationwide. Environmentally, this deployment could avoid approximately 1.6 million tons and 7.8 million tons of greenhouse gas (GHG) emissions in Alberta's and Canada's commercial sectors, respectively, while reducing emissions in the residential sectors by an estimated 700,000 tons in Canada and 380,000 tons in Alberta.

7.3 Future work

Potential avenues for extending this work in the future include:

- Enhancing the developed models for the proposed novel systems by artificial intelligence and conducting multi-objective optimization to determine the optimal operation of each novel system under various design conditions and case studies to establish a harmonious balance between the overall efficiency, economic feasibility, and sustainability.

- Investigation of the proposed novel systems using advanced assessment methodologies that can provide deeper insights into their operational viability and robustness. Specifically, employing availability and reliability analyses to evaluate system performance over time, as well as Monte Carlo simulations and Markov models to assess probabilistic behaviour and predict potential system states under varying conditions.

- Performing a comprehensive thermal analysis of the bubble-column reactor and refining system design by incorporating forthcoming advancements in methane pyrolysis (e.g., in carbon separation methods) in the near future to drive innovations in this emerging hydrogen production method.

- Designing innovative configurations that integrate high-temperature solar thermal energy with anion exchange membrane electrolyzers, while exploring further advancements in this technology. Additionally, conducting comparative analyses of this integrated system against configurations utilizing solid oxide and proton exchange membrane electrolyzers.

- Design and implementation of demo-scale systems proposed in chapters 2-5 before large-scale field studies.

- Conducting a comparative analysis of clean hydrogen tax incentives across countries to assess their impact on the economic feasibility, adoption, and innovation of water electrolysis and methane pyrolysis technologies for hydrogen production.

References

[1] Razmi AR, Sharifi S, Gholamian E, Arabkoohsar A, Shahbakhti M. 15 - Green hydrogen. Futur Grid-Scale Energy Storage Solut Elsevier 2023:573–620. doi:10.1016/B978-0-323-90786-6.00006-6.

[2] Razmi AR, Alirahmi SM, Nabat MH, Assareh E, Shahbakhti M. A green hydrogen energy storage concept based on parabolic trough collector and proton exchange membrane electrolyzer/fuel cell: Thermodynamic and exergoeconomic analyses with multi-objective optimization. Int J Hydrogen Energy 2022;47:26468–89. doi:10.1016/j.ijhydene.2022.03.021.

[3] Razmi AR, Hanifi AR, Shahbakhti M. Design, thermodynamic, and economic analyses of a green hydrogen storage concept based on solid oxide electrolyzer/fuel cells and heliostat solar field. Renew Energy 2023;215:118996. doi:10.1016/j.renene.2023.118996.

[4] Razmi AR, Hanifi AR, Shahbakhti M. Techno-economic analysis of a novel concept for the combination of methane pyrolysis in molten salt with heliostat solar field. Energy 2024;301:131644. doi:10.1016/j.energy.2024.131644.

[5] Razmi AR, Hanifi AR, Shahbakhti M. A comparative techno-economic assessment between solar-based hydrogen production by methane pyrolysis and water electrolysis methods, (Revision submitted on December 31, 2024). Renew Energy 2025.

[6] Razmi AR, Hanifi AR, Shahbakhti M. Techno-economic assessment of solid oxide fuel cells and hydrogen fuelled internal combustion engines for institutional energy management: A case study of the University of Alberta, (Submitted on January 12, 2025). Int J Hydrogen Energy 2025.

[7] Razmi AR, Hanifi AR, Shahbakhti M. The potential of the solid oxide fuel cell-based combined heat and power systems for commercial and residential applications in Alberta and Canada. Glob. Conf. Renew. Energy Clim. Chang., 2024, p. 1–6.

[8] Toub M, Reddy CR, Razmara M, Shahbakhti M, Robinett RD, Aniba G. Model-based predictive control for optimal MicroCSP operation integrated with building HVAC systems. Energy Convers Manag 2019;199:111924. doi:10.1016/j.enconman.2019.111924.

[9] Babaei SM, Nabat MH, Lashgari F, Pedram Zamani M, Arabkoohsar A. Thermodynamic analysis and optimization of an innovative hybrid multi-generating liquid air energy storage system. J Energy Storage 2021;43:103262. doi:10.1016/j.est.2021.103262.

[10] Xu Y, Zhou S, Xia C, Zhao H, Xue X. Three-dimensional thermo-mechanical analysis of abandoned mine drifts for underground compressed air energy storage: A comparative study of two construction and plugging schemes. J Energy Storage 2021;39:102696. doi:10.1016/j.est.2021.102696.

[11] Nabat MH, Zeynalian M, Razmi AR, Arabkoohsar A, Soltani M. Energy, exergy, and economic analyses of an innovative energy storage system; liquid air energy storage (LAES) combined with high-temperature thermal energy storage (HTES). Energy Convers Manag 2020;226:113486. doi:10.1016/j.enconman.2020.113486.

[12] Rohit AK, Rangnekar S. An overview of energy storage and its importance in Indian renewable energy sector: Part II – energy storage applications, benefits and market potential. J Energy Storage 2017;13:447–56. doi:10.1016/j.est.2017.07.012.

[13] Towards GD. Ren 21 - Renewable Global Futures Report. vol. 6. 2017.

[14] Moore J, Shabani B. A critical study of stationary energy storage policies in Australia in an international context: The role of hydrogen and battery technologies. Energies 2016;9:674. doi:10.3390/en9090674.

[15] Mahlia TMI, Saktisahdan TJ, Jannifar A, Hasan MH, Matseelar HSC. A review of available methods and development on energy storage; technology update. Renew Sustain Energy Rev 2014;33:532–45. doi:10.1016/j.rser.2014.01.068.

[16] Colbertaldo P, Agustin SB, Campanari S, Brouwer J. Impact of hydrogen energy storage on California electric power system: Towards 100% renewable electricity. Int J Hydrogen Energy 2019;44:9558–76. doi:10.1016/j.ijhydene.2018.11.062.

[17] Keshavarzzadeh AH, Ahmadi P, Safaei MR. Assessment and optimization of an integrated energy system with electrolysis and fuel cells for electricity, cooling and hydrogen production using various optimization techniques. Int J Hydrogen Energy 2019;44:21379–96. doi:10.1016/j.ijhydene.2019.06.127.

[18] Rohit AK, Devi KP, Rangnekar S. An overview of energy storage and its importance in Indian renewable energy sector: Part I – Technologies and Comparison. J Energy Storage 2017;13:10–23. doi:10.1016/j.est.2017.06.005.

[19] Schneider L, Sehnke F, Ohnmeiss K, Schro R, Ko E. The future electric power system: Impact of Power-to-Gas by interacting with other renewable energy components. J Energy Storage 2016;5:113–9. doi:10.1016/j.est.2015.11.012.

[20] Liu J, Duan X, Yuan Z, Liu Q, Tang Q. Experimental study on the performance, combustion and emission characteristics of a high compression ratio heavy-duty spark-ignition engine fuelled with liquefied methane gas and hydrogen blend. Appl Therm Eng 2017;124:585–94. doi:10.1016/j.applthermaleng.2017.06.067.

[21] Dawood F, Anda M, Shafiullah GM. Hydrogen production for energy: An overview. Int J Hydrogen Energy 2019;45:3847–69. doi:10.1016/j.ijhydene.2019.12.059.

[22] Hosseini SE, Wahid MA. Hydrogen production from renewable and sustainable energy resources: Promising green energy carrier for clean development. Renew Sustain Energy Rev 2016;57:850–66. doi:10.1016/j.rser.2015.12.112.

[23] Sharifi S, Razmi AR, Nabat MH, Liu JJ, Arabkoohsar A, Shahbakhti M. 16- Power-to-X. Futur Grid-Scale Energy Storage Solut Elsevier 2023:621–46. doi:10.1016/B978-0-323-90786-6.00003-0.

[24] Litti Y V. Prospects for the production of green hydrogen: Review of countries with high potential. Int J Hydrogen Energy 2022;48:4551–71. doi:10.1016/j.ijhydene.2022.10.084.

[25] Hydrogen Shot, Hydrogen and Fuel Cell Technologies Office, United States Department of Energy (DOE) “https://www.energy.gov/eere/fuelcells/hydrogen-shot, Accessed on March 4, 2024.” 2021.

[26] Pathways to Commercial Liftoff: Clean Hydrogen, US Department of Energy (DOE) “https://liftoff.energy.gov/wp-content/uploads/2023/03/20230320-Liftoff-Clean-H2-vPUB.pdf.” 2023.

[27] Carbon Intensity of Hydrogen Production Methods, Supporting the BC Hydrogen Strategy 2023.

[28] Gorski J, Jutt T, Wu KT. Carbon intensity of blue hydrogen production Accounting for technology and upstream emissions, Pembina Institute 2021.

[29] The Future of Hydrogen, Seizing today's opportunities, International Energy Agency (IEA) "https://www.iea.org/reports/the-future-of-hydrogen, Accessed on March 4, 2024." 2019.

[30] Patlolla SR, Katsu K, Sharafian A, Wei K, Herrera OE, Walter M. A review of methane pyrolysis technologies for hydrogen production. Renew Sustain Energy Rev 2023;181:113323. doi:10.1016/j.rser.2023.113323.

[31] Okeke IJ, Saville BA, Maclean HL. Low carbon hydrogen production in Canada via natural gas pyrolysis. Int J Hydrogen Energy 2022;48:12581–99. doi:10.1016/j.ijhydene.2022.12.169.

[32] Nuria S, Schl R, Ruland H. Methane Pyrolysis for Zero-Emission Hydrogen Production: A Potential Bridge Technology from Fossil Fuels to a Renewable and Sustainable Hydrogen Economy. Ind Eng Chem Res 2021;60:11855–81. doi:10.1021/acs.iecr.1c01679.

[33] Oni AO, Anaya K, Giwa T, Lullo G Di, Kumar A. Comparative assessment of blue hydrogen from steam methane reforming, autothermal reforming, and natural gas decomposition technologies for natural gas-producing regions. Energy Convers Manag 2022;254:115245. doi:10.1016/j.enconman.2022.115245.

[34] Chan YH, Chan ZP, Sow S, Lock M, Yiin CL, Foong SY, et al. Thermal pyrolysis conversion of methane to hydrogen (H2): A review on process parameters, reaction kinetics and techno-economic analysis. Chinese Chem Lett 2023:109329. doi:10.1016/j.cclet.2023.109329.

[35] Diab J, Fulcheri L, Hessel V, Rohani V, Frenklach M. Why turquoise hydrogen will Be a game changer for the energy transition. Int J Hydrogen Energy 2022;47:25831–48. doi:10.1016/j.ijhydene.2022.05.299.

[36] Incer-valverde J, Korayem A, Tsatsaronis G, Morosuk T. "Colors" of hydrogen: Definitions and carbon intensity. Energy Convers Manag 2023;291:117294. doi:10.1016/j.enconman.2023.117294.

[37] Enabling A Low-Carbon Economy, United States Department of Energy (DOE). 2020.

[38] Ochu ER, Braverman S, Smith G, Friedmann J. Hydrogen fact sheet: production of low-carbon hydrogen, Center on Global Energy Policy 2021.

[39] Cipriani G, Di V, Genduso F, La D. Perspective on hydrogen energy carrier and its automotive applications. Int J Hydrogen Energy 2014;39:8482–94. doi:10.1016/j.ijhydene.2014.03.174.

[40] Barbir F. PEM electrolysis for production of hydrogen from renewable energy sources. Sol Energy 2005;78:661–9. doi:10.1016/j.solener.2004.09.003.

[41] Dunn S. Hydrogen futures: toward a sustainable energy system. Int J Hydrogen Energy 2020;27:235–64.

[42] Kumar SS, Himabindu V. Hydrogen production by PEM water electrolysis – A review. Mater Sci Energy Technol 2019;2:442–54. doi:10.1016/j.mset.2019.03.002.

[43] Kuzel H, Wedekind E, Wedekind E, Rentschler HC, Rentschler HC, Kroll W, et al. Batteries with Solid Ion-Exchange Membrane Electrolytes. J Electrochem Soc 1960;107:3–7.

[44] Grubb WT, Niedrach LW. Batteries with Solid Ion-Exchange Membrane Electrolytes: II. Low-Temperature Hydrogen-Oxygen Fuel Cells. J Electrochem Soc 1960;107:131–5.

[45] Ju H, Badwal S, Giddey S. A comprehensive review of carbon and hydrocarbon assisted water electrolysis for hydrogen production. Appl Energy 2018;231:502–33. doi:10.1016/j.apenergy.2018.09.125.

[46] Rahim AHA, Salami A, Kamarudin SK, Hanapi S. An overview of polymer electrolyte membrane electrolyzer for hydrogen production: Modeling and mass transport. J Power Sources 2016;309:56–65. doi:10.1016/j.jpowsour.2016.01.012.

[47] Millet P, Ngameni R, Grigoriev SA, Mbemba N, Brisset F, Ranjbari A. PEM water electrolyzers : From electrocatalysis to stack development. Int J Hydrogen Energy 2010;35:5043–52. doi:10.1016/j.ijhydene.2009.09.015.

[48] Grigoriev SA, Porembsky VI, Fateev VN. Pure hydrogen production by PEM electrolysis for hydrogen energy. Int J Hydrogen Energy 2006;31:171–5. doi:10.1016/j.ijhydene.2005.04.038.

[49] Nikolaidis P, Poullikkas A. A comparative overview of hydrogen production processes. Renew Sustain Energy Rev 2017;67:597–611. doi:10.1016/j.rser.2016.09.044.

[50] Boveri B. STABILIZATION OF RuO2 BY IrO2 FOR ANODIC OXYGEN EVOLUTION IN ACID MEDIA. Electrochim Acta 1986;31:1311–6.

[51] Terezo AJ, Pereira EC. Preparation and characterization of Ti/RuO2 - Nb2O5 electrodes obtained by polymeric precursor method. Electrochim Acta 1999;44:4507–13.

[52] Liu B, Wang C, Chen Y. Surface determination and electrochemical behavior of IrO2-RuO2-SiO2 ternary oxide coatings in oxygen evolution reaction application. Electrochim Acta 2018;264:350–7. doi:10.1016/j.electacta.2018.01.141.

[53] Wu X, Tayal J, Basu S, Scott K. Nano-crystalline Rux Sn1-xO2 powder catalysts for oxygen evolution reaction in proton exchange membrane water electrolysers. Int J Hydrogen Energy 2011;6:2–10. doi:10.1016/j.ijhydene.2011.01.067.

[54] Kumar SS, Ramakrishna SUB, Devi BR, Himabindu V. Phosphorus-doped carbon nanoparticles supported palladium electrocatalyst for the hydrogen evolution reaction(HER) in PEM water electrolysis. Ionics (Kiel) 2018:3113–21.

[55] Carmo M, Fritz DL. A comprehensive review on PEM water electrolysis. Int J Hydrogen Energy 2013;38:4901–34. doi:10.1016/j.ijhydene.2013.01.151.

[56] Balat M. Potential importance of hydrogen as a future solution to environmental and transportation problems. Int J Hydrogen Energy 2008;33:4013–29. doi:10.1016/j.ijhydene.2008.05.047.

[57] Trasatti S. Water electrolysis: who first? J Electroanal Chem 1999;476:90–1.

[58] Burnat D, Schlupp M, Wichser A, Lothenbach B, Gorbar M, Züttel A, et al. Composite membranes for alkaline electrolysis based on polysulfone and mineral fillers. J Power Sources 2015;291:163–72. doi:10.1016/j.jpowsour.2015.04.066.

[59] Vermeiren P. EVALUATION OF THE ZIRFON SEPARATOR FOR USE IN ALKALINE WATER ELECTROLYSIS AND Ni-H2 BATTERIES. Int J Hydrogen Energy 1998;3199.

[60] Seetharaman S, Balaji R, Ramya K, Dhathathreyan KS. Graphene oxide modified non-noble metal electrode for alkaline anion exchange membrane water electrolyzers. Int J Hydrogen Energy 2013;38:14934–42. doi:10.1016/j.ijhydene.2013.09.033.

[61] Zeng K, Zhang D. Recent progress in alkaline water electrolysis for hydrogen production and applications. Prog Energy Combust Sci 2010;36:307–26. doi:10.1016/j.pecs.2009.11.002.

[62] Donitz W, Erdle E. High-temperature electrolysis of water vapor-status of development and perspectives for application. Int J Hydrogen Energy 1985;10:291–5.

[63] Brisse A, Schefold J, Zahid M. High temperature water electrolysis in solid oxide cells. Int J Hydrogen Energy 2008;33:5375–82. doi:10.1016/j.ijhydene.2008.07.120.

[64] Liang M, Yu B, Wen M, Chen J, Xu J, Zhai Y. Preparation of LSM–YSZ composite powder for anode of solid oxide electrolysis cell and its activation mechanism. J Power Sources 2009;190:341–5. doi:10.1016/j.jpowsour.2008.12.132.

[65] Knibbe R, Traulsen L, Hauch A, Ebbesen SD, Mogensen M. Solid Oxide Electrolysis Cells: Degradation at High Current Densities. J Electrochem Soc 2010;157:8. doi:10.1149/1.3447752.

[66] Zhou W, Zhou W, Qiu H, Li D, Zhang Y, Sajjad M, et al. Tuning the reactivity of Ni/MoS2 membrane for efficient methane pyrolysis and hydrogen production: A multi-scale study. Energy Convers Manag 2023;293:117476. doi:10.1016/j.enconman.2023.117476.

[67] Mcconnachie M, Konarova M, Smart S. Literature review of the catalytic pyrolysis of methane for hydrogen and carbon production. Int J Hydrogen Energy 2022;48:25660–82. doi:10.1016/j.ijhydene.2023.03.123.

[68] Masalani A, Hlína M, Hrabovský M, Petr K, Singh V, Fathi J, et al. Impact of natural gas composition on steam thermal plasma assisted pyrolysis for hydrogen and solid carbon production. Energy Convers Manag 2023;297:117748. doi:10.1016/j.enconman.2023.117748.

[69] Marquardt T, Bode A, Kabelac S. Hydrogen production by methane decomposition: Analysis of thermodynamic carbon properties and process evaluation. Energy Convers Manag 2020;221:113125. doi:10.1016/j.enconman.2020.113125.

[70] Pudukudy M, Yaakob Z, Zulhamizan M, Sobri M. Applied Catalysis B: Environmental One-pot sol-gel synthesis of MgO nanoparticles supported nickel and iron catalysts for undiluted methane decomposition into COx free hydrogen and nanocarbon. Appl Catal B, Environ 2017;218:298–316. doi:10.1016/j.apcatb.2017.04.070.

[71] Zhou L, Reddy L, Harb M, Saih Y, Aguilar-tapia A, Ould-chikh S, et al. Fe catalysts for methane decomposition to produce hydrogen and carbon nano materials. Appl Catal B, Environ 2017;208:44–59. doi:10.1016/j.apcatb.2017.02.052.

[72] Rastegarpanah A, Rezaei M, Meshkani F, Dai H, Arandiyan H. Thermocatalytic decomposition of methane over mesoporous Ni/xMgO·Al2O3 nanocatalysts. Int J Hydrogen Energy 2018;43:15112–23. doi:10.1016/j.ijhydene.2018.06.057.

[73] Rastegarpanah A, Rezaei M, Meshkani F, Zhang K, Zhao X. Influence of group VIB metals on activity of the Ni/MgO catalysts for methane decomposition. Appl Catal B Environ 2019;248:515–25. doi:10.1016/j.apcatb.2019.01.067.

[74] Otsuka K, Takenaka S, Ohtsuki H. Production of pure hydrogen by cyclic decomposition of methane and oxidative elimination of carbon nanofibers on supported-Ni-based catalysts. Appl Catal A Gen 2004;273:113–24. doi:10.1016/j.apcata.2004.06.021.

[75] Choudhary VR, Banerjee S, Rajput AM. Continuous Production of H2 at Low Temperature from Methane Decomposition over Ni-Containing Catalyst Followed by Gasification by Steam of the Carbon on the Catalyst in Two Parallel Reactors Operated in Cyclic Manner. J Catal 2001;198:136–41. doi:10.1006/jcat.2000.3135.

[76] Kang D, Lee JW. Enhanced methane decomposition over nickel–carbon–B2O3 core–shell catalysts derived from carbon dioxide. Appl Catal B Environ 2016;186:41–55. doi:10.1016/j.apcatb.2015.12.045.

[77] Eatemadi A, Daraee H, Karimkhanloo H, Kouhi M, Zarghami N. Carbon nanotubes: properties, synthesis, purification, and medical applications. Nanoscale Res Lett 2014;9:393.

[78] Thanh B, Ich S, Lim Y, Lee U. One-dimensional kinetic model with heat transfer and axial dispersion of molten-metal bubble column reactors for hydrogen production via methane pyrolysis. Int J Hydrogen Energy 2023;48:35821–37. doi:10.1016/j.ijhydene.2023.06.031.

[79] Paxman D, Trottier S, Nikoo M, Secanell M, Ordorica-garcia G. Initial experimental and theoretical investigation of solar molten media methane cracking for hydrogen production. Energy Procedia 2014;49:2027–36. doi:10.1016/j.egypro.2014.03.215.

[80] Geißler T, Abánades A, Heinzel A, Mehravaran K, Müller G, Rathnam RK, et al. Hydrogen production via methane pyrolysis in a liquid metal bubble column reactor with a packed bed. Chem Eng J 2016;299:192–200. doi:10.1016/j.cej.2016.04.066.

[81] Gulevich A V, Martynov PN, Gulevsky VA, Ulyanov V V. Technologies for hydrogen production based on direct contact of gaseous hydrocarbons and evaporated water with molten Pb or Pb – Bi. Energy Convers Manag 2008;49:1946–50. doi:10.1016/j.enconman.2007.12.028.

[82] Upham DC, Agarwal V, Khechfe A, Snodgrass ZR, Gordon MJ, Metiu H, et al. Catalytic molten metals for the direct conversion of methane to hydrogen and separable carbon. Science (80-) 2017;358:917–20.

[83] Ruuska T, Vinha J, Kivioja H. Measuring thermal conductivity and specific heat capacity values of inhomogeneous materials with a heat flow meter apparatus. J Build Eng 2017;9:135–41. doi:10.1016/j.jobe.2016.11.011.

[84] Zhou L, Marie J. Unsupported Ni-Pt alloy metal catalysts prepared by water-in-oil (W/O) microemulsion method for methane cracking. Fuel 2016;181:805–10. doi:10.1016/j.fuel.2016.05.067.

[85] Riedewald F, Sousa-gallagher M. Novel waste printed circuit board recycling process with molten salt. MethodsX 2015;2:100–6.

[86] Msheik M, Rodat S. Methane Cracking for Hydrogen Production: A Review of Catalytic and Molten Media Pyrolysis. Energies 2021;14:3107.

[87] https://www.energy.gov/eere/fuelcells/hydrogen-storage, Accessed on December 19, 2023.

[88] Streppel B, Hirscher M. BET specific surface area and pore structure of MOFs determined by hydrogen adsorption at 20 K. Phys Chem Chem Phys 2011:3220–2. doi:10.1039/c0cp01873b.

[89] Stergiannakos T, Tylianakis E, Klontzas E, Trikalitis PN, Froudakis GE. Hydrogen Storage in Novel Li-Doped Corrole Metal-Organic Frameworks. J Phys Chem 2012;116:8359–63.

[90] Hirscher M, Yartys VA, Baricco M, Bellosta J, Colbe V, Blanchard D, et al. Materials for hydrogen-based energy storage - past, recent progress and future outlook. J Alloys Compd 2020;827:153548. doi:10.1016/j.jallcom.2019.153548.

[91] Systems FC. Hydrogen and Fuel Cell Systems. 2014. doi:10.1016/B978-0-12-383860-5.00004-3.

[92] https://www.giacomini.com, Accessed on Nov 14, 2021.

[93] https://www.2g-energy.com, Accessed on Sep 22, 2024.

[94] Chehrmonavari H, Kakaee A, Ehsan S, Desideri U, Tsatsaronis G, Floerchinger G, et al. Hybridizing solid oxide fuel cells with internal combustion engines for power and propulsion systems: A review. Renew Sustain Energy Rev 2023;171:112982. doi:10.1016/j.rser.2022.112982.

[95] Lindqvist H, Overby P. A Literature Review of Hydrogen Internal Com- bustion Engines. Chalmers Univ Technol 2024.

[96] Badea G, Sebastian G, Giurca I, Aşchilean I, Megyesi E. Hydrogen production using solar energy - technical analysis. Energy Procedia 2017;112:418–25. doi:10.1016/j.egypro.2017.03.1097.

[97] Abdalla AM, Hossain S, Nis OB, Azad AT. Hydrogen production, storage, transportation and key challenges with applications: A review. Energy Convers Manag 2018;165:602–27. doi:10.1016/j.enconman.2018.03.088.

[98] Koumi S, Njomo D. An overview of hydrogen gas production from solar energy. Renew Sustain Energy Rev 2012;16:6782–92. doi:10.1016/j.rser.2012.07.027.

[99] Yüksel YE. Thermodynamic assessment of modified Organic Rankine Cycle integrated with parabolic trough collector for hydrogen production. Int J Hydrogen Energy 2018;43:5832–41. doi:10.1016/j.ijhydene.2017.09.164.

[100] Chitsaz A, Abdollahi M, Hosseinpour J. Thermodynamic and exergoeconomic analyses of a proton exchange membrane fuel cell (PEMFC) system and the feasibility evaluation of integrating with a proton exchange membrane electrolyzer (PEME). Energy Convers Manag 2019;186:487–99. doi:10.1016/j.enconman.2019.03.004.

[101] Chen X, Liu Q, Xu J, Chen Y, Li W, Yuan Z, et al. Thermodynamic study of a hybrid PEMFC-solar energy multi-generation system combined with SOEC and dual Rankine cycle. Energy Convers Manag 2020;226:113512. doi:10.1016/j.enconman.2020.113512.

[102] Assareh E, Mohammadi F, Azizimehr B. Simulation and Optimization of a Solar Based Trigeneration System Incorporating PEM Electrolyzer and Fuel Cell. J Sol Energy Res 2021;6:664–77. doi:https://dx.doi.org/10.22059/jser.2021.296369.1139.

[103] Naseri N, Hani S El, Aghmadi A, Mediouni H, Aboudrar I, Benbouzid M. Solar Photovoltaic Energy Storage as Hydrogen via PEM Fuel Cell for Later Conversion Back to Electricity. IECON 2019 - 45th Annu Conf IEEE Ind Electron Soc 2019;1:4549–54.

[104] Santoso D, Setiaji FD, Susilo D. Demonstration of Renewable Electrical Energy Generation based on Solar-Hydrogen Fuel Cell Technology. Int. Conf. Instrumentation, Commun. Inf. Technol. Biomed. Eng., 2011.

[105] Albarghot M, Rolland L. MATLAB/Simulink Modelling and Experimental Results of a PEM Electrolyzer Powered by a Solar Panel. IEEE Electr Power Energy Conf 2016:2–7.

[106] Yilanci A, Dincer I, Ozturk HK. A review on solar-hydrogen/fuel cell hybrid energy systems for stationary applications. Prog Energy Combust Sci 2009;35:231–44. doi:10.1016/j.pecs.2008.07.004.

[107] Lajnef T, Abid S, Ammous A. Modeling, control, and simulation of a solar hydrogen/fuel cell hybrid energy system for grid-connected applications. Adv Power Electron 2013;2013:1–9.

[108] Bilal A, Benyoucef K, Miloud TA, Ahmed K. Solar Hydrogen Production for Fuel Cell Use: Experimental Approach. Int. Symp. Environ. Energies Appl., 2012, p. 549–53.

[109] Lopes C, Watanabe EH. Experimental and theoretical development of a PEM electrolyzer model applied to energy storage systems. Brazilian Power Electron. Conf., 2009, p. 775–82.

[110] Khelfaoui N, Djafour A, Ghenai C, Laib I, Danoune MB, Gougui A. Experimental investigation of solar hydrogen production PV/PEM electrolyser performance in the Algerian Sahara regions. Int J Hydrogen Energy 2020. doi:10.1016/j.ijhydene.2020.11.193.

[111] Ahmadi P, Dincer I, Rosen MA. Transient thermal performance assessment of a hybrid solar-fuel cell system in Toronto, Canada. Int J Hydrogen Energy 2014;40:7846–54. doi:10.1016/j.ijhydene.2014.11.047.

[112] De RK, Ganguly A. Modeling and analysis of a solar thermal-photovoltaic-hydrogen-based hybrid power system for running a standalone cold storage. J Clean Prod 2021;293:126202. doi:10.1016/j.jclepro.2021.126202.

[113] Buffo G, Ferrero D, Santarelli M, Lanzini A. Energy and environmental analysis of a flexible Power-to-X plant based on Reversible Solid Oxide Cells (rSOCs) for an urban district. J Energy Storage 2020;29:101314. doi:10.1016/j.est.2020.101314.

[114] Gómez SY, Hotza D. Current developments in reversible solid oxide fuel cells. Renew Sustain Energy Rev 2016;61:155–74. doi:10.1016/j.rser.2016.03.005.

[115] Mojtaba S, Ebrahimi-moghadam A. Comparative study, working fluid selection, and optimal design of three systems for electricity and freshwater based on solid oxide fuel cell mover cycle Organic Rankine cycle. Appl Energy 2022;323:119545. doi:10.1016/j.apenergy.2022.119545.

[116] Ba L, Xiong X, Lei Z, Yang Z, Ge B. A study on solid oxide electrolyzer stack and system performance based on alternative mapping models. Int J Hydrogen Energy 2022;47:12469–86. doi:10.1016/j.ijhydene.2022.01.253.

[117] Alzahrani AA, Dincer I. Exergoeconomic analysis of hydrogen production using a standalone high-temperature electrolyzer. Int J Hydrogen Energy 2020;46:13899–907. doi:10.1016/j.ijhydene.2020.04.055.

[118] Rostami M, Dehghan M. Introducing and evaluation of a new propulsion system composed of solid oxide fuel cell and downstream cycles; usage in Unmanned Aerial Vehicles. Int J Hydrogen Energy 2022;47:13693–709. doi:10.1016/j.ijhydene.2022.02.104.

[119] Nami H, Rizvandi OB, Chatzichristodoulou C, Hendriksen V, Frandsen HL. Techno-economic analysis of current and emerging electrolysis technologies for green hydrogen production. Energy Convers Manag 2022;269:116162. doi:10.1016/j.enconman.2022.116162.

[120] Roushenas R, Zarei E, Torabi M. A novel trigeneration system based on solid oxide fuel cell-gas turbine integrated with compressed air and thermal energy storage concepts: Energy, exergy, and life cycle approaches. Sustain Cities Soc 2021;66:102667. doi:10.1016/j.scs.2020.102667.

[121] Nasser M, Hassan H. Assessment of hydrogen production from waste heat using hybrid systems of Rankine cycle with proton exchange membrane/solid oxide electrolyzer. Int J Hydrogen Energy 2022;48:7135–53. doi:10.1016/j.ijhydene.2022.11.187.

[122] Wang S, Wu X, Jafarmadar S, Kumar P, Khorasani S, Marefati M. Numerical assessment of a hybrid energy system based on solid oxide electrolyzer, solar energy and molten carbonate fuel cell for the generation of

electrical energy and hydrogen fuel with electricity storage option. J Energy Storage 2022;54:105274. doi:10.1016/j.est.2022.105274.

[123] Mohammadi A, Mehrpooya M. Thermodynamic and economic analyses of hydrogen production system using high temperature solid oxide electrolyzer integrated with parabolic trough collector. J Clean Prod 2019;212:713–26. doi:10.1016/j.jclepro.2018.11.261.

[124] Yilmaz F, Ozturk M. Design and modeling of an integrated combined plant with SOFC for hydrogen and ammonia generation. Int J Hydrogen Energy 2022;47:31911–26. doi:10.1016/j.ijhydene.2022.01.249.

[125] Zheng N, Zhang H, Duan L, Wang Q, Bischi A, Desideri U. Techno-economic analysis of a novel solar-driven PEMEC-SOFC-based multi-generation system coupled parabolic trough photovoltaic thermal collector and thermal energy storage. Appl Energy 2023;331:120400. doi:10.1016/j.apenergy.2022.120400.

[126] Wang X, Duan L, Zheng N. Thermodynamic analysis of a novel tri-generation system integrated with a solar energy storage and solid oxide fuel cell – Gas turbine. Appl Therm Eng 2023;219:119648. doi:10.1016/j.applthermaleng.2022.119648.

[127] Barelli L, Bidini G, Cinti G, Ottaviano PA. Solid oxide fuel cell systems in hydrogen-based energy storage applications: Performance assessment in case of anode recirculation. J Energy Storage 2022;54:105257. doi:10.1016/j.est.2022.105257.

[128] Bianchi FR, Bosio B, Conte F, Massucco S, Mosaico G, Natrella G, et al. Modelling and optimal management of renewable energy communities using reversible solid oxide cells. Appl Energy 2023;334:120657. doi:10.1016/j.apenergy.2023.120657.

[129] Cao Y. A solar-driven lumped SOFC/SOEC system for electricity and hydrogen production: 3E analyses and a comparison of different multi-objective optimization algorithms. J Clean Prod 2020;271:122457. doi:10.1016/j.jclepro.2020.122457.

[130] Liu H, Clausen LR, Wang L, Chen M. Pathway toward cost-effective green hydrogen production by solid oxide electrolyzer. Energy Environ Sci 2023;16:2090–111. doi:10.1039/d3ee00232b.

[131] Tyrer D. Production of hydrogen, U.S. Patent 1,803,221 1931.

[132] Steinberg M. The Carnol process for CO2 mitigation from power plants and the transportation sector 1996;37:843–8.

[133] Adinberg R, Epstein M, Karni J. Solar Gasification of Biomass: A Molten Salt Pyrolysis Study. J Sol Energy Eng 2016;126:850–7. doi:10.1115/1.1753577.

[134] Parkinson B, Tabatabaei M, Upham DC, Ballinger B, Greig C, Smart S, et al. Hydrogen production using methane: Techno- economics of decarbonizing fuels and chemicals. Int J Hydrogen Energy 2017;43:2540–55. doi:10.1016/j.ijhydene.2017.12.081.

[135] Rahimi N, Kang D, Gelinas J, Menon A, Gordon MJ, Metiu H, et al. Solid carbon production and recovery from high temperature methane pyrolysis in bubble columns containing molten metals and molten salts. Carbon N Y 2019;151:181–91. doi:10.1016/j.carbon.2019.05.041.

[136] Kang D, Rahimi N, Gordon MJ, Metiu H, Mcfarland EW. Catalytic methane pyrolysis in molten MnCl2-KCl. Appl Catal B Environ 2019;254:659–66. doi:10.1016/j.apcatb.2019.05.026.

[137] Palmer C, Tarazkar M, Gordon MJ, Mcfarland EW. Methane pyrolysis in low-cost, alkali-halide molten salts

at high temperatures. Sustain Energy Fuels 2021;5:6107–23. doi:10.1039/d1se01408k.

[138] Boo J, Ko E., Park N, Ryu C, Kim Y, Park J, et al. Methane Pyrolysis in Molten Potassium Chloride: An Experimental and Economic Analysis. Energies 2021;14:8182. doi:10.3390/en14238182.

[139] Pruvost F, Cloete S, Hendrik J, Dhoke C, Zaabout A. Techno-Economic assessment of natural gas pyrolysis in molten salts. Energy Convers Manag 2022;253:115187. doi:10.1016/j.enconman.2021.115187.

[140] Park S, Kim M, Koo Y, Kang D, Kim Y, Park J, et al. Numerical modeling of methane pyrolysis in a bubble column of molten catalysts for clean hydrogen production. Int J Hydrogen Energy 2022;48:7385–99. doi:10.1016/j.ijhydene.2022.11.068.

[141] He Y, Song B, Jing X, Zhou Y, Chang H, Yang W. Low-carbon hydrogen production via molten salt methane pyrolysis with chemical looping combustion: Emission reduction potential and techno-economic assessment. Fuel Process Technol 2023;247:107778. doi:10.1016/j.fuproc.2023.107778.

[142] Angikath F, Abdulrahman F, Yousry A, Das R, Saxena S, Behar O, et al. Technoeconomic assessment of hydrogen production from natural gas pyrolysis in molten bubble column reactors. Int J Hydrogen Energy 2023;49:246–62. doi:10.1016/j.ijhydene.2023.07.308.

[143] Antal MJ, Hofmann L, Moreira JR. Design and operation of a solar fired biomass flash pyrolysis reactor. Sol Energy 1983;30:299–312. doi:10.1016/0038-092X(83)90185-8.

[144] Abanades S, Flamant G. Production of hydrogen by thermal methane splitting in a nozzle-type laboratory-scale solar reactor. Int J Hydrogen Energy 2005;30:843–53. doi:10.1016/j.ijhydene.2004.09.006.

[145] Abanades S, Flamant G. Hydrogen production from solar thermal dissociation of methane in a high-temperature fluid-wall chemical reactor. Chem Eng Process Process Intensif 2008;47:490–8. doi:10.1016/j.cep.2007.01.006.

[146] Abanades S, Tescari S, Rodat S, Flamant G. Natural gas pyrolysis in double-walled reactor tubes using thermal plasma or concentrated solar radiation as external heating source. J Nat Gas Chem 2009;18:1–8. doi:10.1016/S1003-9953(08)60077-8.

[147] Valde´s-Parada FJ, Romero-Paredes H, Espinosa-Paredes G. Numerical simulation of a tubular solar reactor for methane cracking. Int J Hydrogen Energy 2011;36:3354–63. doi:10.1016/j.ijhydene.2010.12.022.

[148] Abanades S, Kimura H, Otsuka H. A drop-tube particle-entrained flow solar reactor applied to thermal methane splitting for hydrogen production. Fuel 2015;153:56–66. doi:10.1016/j.fuel.2015.02.103.

[149] Boretti A. A perspective on the production of hydrogen from solar-driven thermal decomposition of methane. Int J Hydrogen Energy 2021;46:34509–14. doi:10.1016/j.ijhydene.2021.07.234.

[150] Msheik M, Rodat S. Experimental comparison of solar methane pyrolysis in gas-phase and molten-tin bubbling tubular reactors. Energy 2022;260:124943. doi:10.1016/j.energy.2022.124943.

[151] Abuseada M, Fisher TS. Continuous solar-thermal methane pyrolysis for hydrogen and graphite production by roll-to-roll processing. Appl Energy 2023;352:121872. doi:10.1016/j.apenergy.2023.121872.

[152] Lehman PA, Chamberlin CE. Design of a photovoltaic-hydrogen-fuel cell energy system. Int J Hydrogen Energy 1991;16:349–52. doi:10.1016/0360-3199(91)90172-F.

[153] Lehman PA, Chamberlin CE, Pauletto G, A RM. Operating experience with a photovoltaic-hydrogen-energy system. Int J Hydrogen Energy 1997;22:465–70. doi:10.1016/S0360-3199(96)00127-9.

[154] Gibson TL, Kelly NA. Optimization of solar powered hydrogen production using photovoltaic electrolysis devices. Int J Hydrogen Energy 2008;33:5931–40. doi:10.1016/j.ijhydene.2008.05.106.

[155] Saeed F, Alsyouri HM, Al-ghandoor A, Al-husban Y, Abdelhadi A. Developing an Integrated Solar Powered System to Generate Hydrogen from Sea Water. Int J Electrochem Sci 2013;8:6311–20. doi:10.1016/S1452-3981(23)14763-8.

[156] Alzahrani AA, Dincer I. Design and analysis of a solar tower based integrated system using high temperature electrolyzer for hydrogen production. Int J Hydrogen Energy 2016;41:8042–56. doi:10.1016/j.ijhydene.2015.12.103.

[157] Yadav D, Banerjee R. Economic assessment of hydrogen production from solar driven high-temperature steam electrolysis process Steam generator. J Clean Prod 2018;183:1131–55. doi:10.1016/j.jclepro.2018.01.074.

[158] Wang H, Kong H, Pu Z, Li Y, Hu X. Feasibility of high efficient solar hydrogen generation system integrating photovoltaic cell/photon-enhanced thermionic emission and high-temperature electrolysis cell. Energy Convers Manag 2020;210:112699. doi:10.1016/j.enconman.2020.112699.

[159] Niaz H, Liu JJ. Dynamic optimization of a stand-alone alkaline water electrolyzer for future operation using a predicted solar forecast. vol. 50. Elsevier Masson SAS; 2021. doi:10.1016/B978-0-323-88506-5.50197-2.

[160] Roy D, Samanta S. A solar-assisted power-to-hydrogen system based on proton-conducting solid oxide electrolyzer cells. Renew Energy 2024;220:119562. doi:10.1016/j.renene.2023.119562.

[161] Dorregaray-oyaregui S. Installation of fuel cells in building in use: Technical, regulatory, and economic feasibility. Energy Convers Manag X 2024;22. doi:10.1016/j.ecmx.2024.100536.

[162] Ademollo A, Mati A, Pagliai M, Carcasci C. Exploring the role of hydrogen in decarbonizing energy-intensive industries: A techno-economic analysis of a solid oxide fuel cell cogeneration system. J Clean Prod 2024;469:143254. doi:10.1016/j.jclepro.2024.143254.

[163] Elmer T, Worall M, Wu S, Riffat SB. Emission and economic performance assessment of a solid oxide fuel cell micro-combined heat and power system in a domestic building. Appl Therm Eng 2015;90:1082–9. doi:10.1016/j.applthermaleng.2015.03.078.

[164] Marocco P, Gandiglio M, Santarelli M. Evaluation of the environmental sustainability of SOFC-based cogeneration systems in commercial buildings. Energy Reports 2023;9:433–8. doi:10.1016/j.egyr.2023.09.032.

[165] Gandiglio M, Marocco P, Nieminen A, Santarelli M, Kiviaho J. Energy and environmental performance from field operation of commercial-scale SOFC systems. Int J Hydrogen Energy 2024;85:997–1009. doi:10.1016/j.ijhydene.2024.08.332.

[166] Alns A, Sleiti AK. Combined heat and power system based on Solid Oxide Fuel Cells for low energy commercial buildings in Qatar. Sustain Energy Technol Assessments 2021;48:101615. doi:10.1016/j.seta.2021.101615.

[167] Roy D, Samanta S, Roy S, Smallbone A. Techno-economic analysis of solid oxide fuel cell-based energy systems for decarbonising residential power and heat in the United Kingdom. Green Chem R Soc Chem 2024:3979–94. doi:10.1039/d3gc02645k.

[168] Lago R, Fogue A, Monsalve J, Cleary D, T CMTM. Techno-economic assessment of hydrogen as a fuel for internal combustion engines and proton exchange membrane fuel cells on long haul applications. Energy Convers Manag 2024;311:118522. doi:10.1016/j.enconman.2024.118522.

[169] Kistner L, Schubert FL, Minke C, Bensmann A, Hanke-rauschenbach R. Techno-economic and Environmental Comparison of Internal Combustion Engines and Solid Oxide Fuel Cells for Ship Applications. J Power Sources 2021;508:230328. doi:10.1016/j.jpowsour.2021.230328.

[170] Habib MA, Abdulrahman GAQ, Alquaity ABS, Qasem NAA. Hydrogen combustion, production, and applications: A review. Alexandria Eng J 2024;100:182–207. doi:10.1016/j.aej.2024.05.030.

[171] Ihsan M, Rao A, Farhan M, Liu Y, Ahmad H, Chen T, et al. Hydrogen production techniques and use of hydrogen in internal combustion engine: A comprehensive review. Fuel 2024;378:132769. doi:10.1016/j.fuel.2024.132769.

[172] Heng Y, Geok H, Danh T, Tho H, Lin D, Rashid T, et al. A review on production and implementation of hydrogen as a green fuel in internal combustion engines. Fuel 2023;333:126525. doi:10.1016/j.fuel.2022.126525.

[173] Goyal H, Jones P, Bajwa A, Parsons D, Akehurst S, Davy MH, et al. Design trends and challenges in hydrogen direct injection (H2DI) internal combustion engines – A review. Int J Hydrogen Energy 2024;86:1179–94. doi:10.1016/j.ijhydene.2024.08.284.

[174] Englander JG, Bharadwaj S, Brandt A. Historical trends in greenhouse gas emissions of the Alberta oil sands (1970–2010). Environ Res Lett 2013. doi:10.1088/1748-9326/8/4/044036.

[175] Yu S, Fan Y, Shi Z, Li J, Zhao X. Hydrogen-based combined heat and power systems: A review of technologies and challenges. Int J Hydrogen Energy 2023;48:34906–29. doi:10.1016/j.ijhydene.2023.05.187.

[176] Inci M. Future vision of hydrogen fuel cells: A statistical review and research on applications, socio-economic impacts and forecasting prospects. Sustain Energy Technol Assessments 2022;53. doi:10.1016/j.seta.2022.102739.

[177] https://www.edmonton.ca/city_government/city_vision_and_strategic_plan/energy-transition, Accessed on May 2, 2024.

[178] https://www.calgary.ca/environment/climate/net-zero-by-2050.html, Accessed on May 2, 2024.

[179] Champier D. Thermoelectric generators: A review of applications. Energy Convers Manag 2017;140:167–81. doi:10.1016/j.enconman.2017.02.070.

[180] Kalogirou SA. Solar energy engineering: processes and systems, chapter 3. Academic Press; 2013.

[181] Alirahmi SM, Rahmani S, Ahmadi P, Wongwises S. Multi-objective design optimization of a multi-generation energy system based on geothermal and solar energy. Energy Convers Manag 2020;205:112426. doi:10.1016/j.enconman.2019.112426.

[182] Alirahmi SM, Assareh E. Energy, exergy, and exergoeconomics (3E) analysis and multi-objective optimization of a multigeneration energy system for day and night time power generation - Case study: Dezful city. Int J Hydrogen Energy 2020;45:31555–73. doi:10.1016/j.ijhydene.2020.08.160.

[183] Dincer I, Rosen MA, Ahmadi P. Optimization of energy systems, chapter 7. Wiley Online Library; 2017.

[184] Saeed EW, Warkozek EG. Modeling and Analysis of Renewable PEM Fuel Cell System. Energy Procedia 2015;74:87–101. doi:10.1016/j.egypro.2015.07.527.

[185] Zhao P, Wang J, Gao L, Dai Y. Parametric analysis of a hybrid power system using organic Rankine cycle to recover waste heat from proton exchange membrane fuel cell. Int J Hydrogen Energy 2012;37:3382–91. doi:10.1016/j.ijhydene.2011.11.081.

[186] Sarma U, Ganguly S. Determination of the component sizing for the PEM fuel cell-battery hybrid energy system for locomotive application using particle swarm optimization. J Energy Storage 2018;19:247–59. doi:10.1016/j.est.2018.08.008.

[187] Assareh E, Alirahmi SM, Ahmadi P. Geothermics A Sustainable model for the integration of solar and geothermal energy boosted with thermoelectric generators (TEGs) for electricity, cooling and desalination purpose. Geothermics 2021;92:102042. doi:10.1016/j.geothermics.2021.102042.

[188] Xi Z, Eshaghi S, Sardari F. Energy, exergy, and exergoeconomic analysis of a polygeneration system driven by solar energy with a thermal energy storage tank for power, heating, and freshwater production. J Energy Storage 2021;36:102429. doi:10.1016/j.est.2021.102429.

[189] Razmi AR, Soltani M, Ardehali A, Gharali K, Dusseault MB, Nathwani J. Design, thermodynamic, and wind assessments of a compressed air energy storage (CAES) integrated with two adjacent wind farms: A case study at Abhar and Kahak sites, Iran. Energy 2021;221:119902. doi:10.1016/j.energy.2021.119902.

[190] Razmi A, Soltani M, Tayefeh M, Torabi M, Dusseault MB. Thermodynamic analysis of compressed air energy storage (CAES) hybridized with a multi-effect desalination (MED) system. Energy Convers Manag 2019;199:112047. doi:10.1016/j.enconman.2019.112047.

[191] Nabat MH, Soltani M, Razmi AR, Nathwani J, Dusseault MB. Investigation of a green energy storage system based on liquid air energy storage (LAES) and high-temperature concentrated solar power (CSP): Energy, exergy, economic, and environmental (4E) assessments, along with a case study for San Diego, US. Sustain Cities Soc 2021;75:103305. doi:doi.org/10.1016/j.scs.2021.103305.

[192] Soltani M, Nabat MH, Razmi AR, Dusseault MB, Nathwani J. A comparative study between ORC and Kalina based waste heat recovery cycles applied to a green compressed air energy storage (CAES) system. Energy Convers Manag 2020;222:113203. doi:10.1016/j.enconman.2020.113203.

[193] Pourrahmani H, Moghimi M. Exergoeconomic analysis and multi-objective optimization of a novel continuous solar-driven hydrogen production system assisted by phase change material thermal storage system. Energy 2019;189:116170. doi:10.1016/j.energy.2019.116170.

[194] Houshfar E. Thermodynamic analysis and multi-criteria optimization of a waste-to-energy plant integrated with thermoelectric generator. Energy Convers Manag 2020;205:112207. doi:10.1016/j.enconman.2019.112207.

[195] Wolf E. Large-Scale Hydrogen Energy Storage. Electrochem. Energy Storage Renew. Sources Grid Balanc., Elsevier Inc.; 2015, p. 129–42. doi:10.1016/B978-0-444-62616-5.00009-7.

[196] Oruc ME, Desai A V, Kenis PJA, Nuzzo RG. Comprehensive energy analysis of a photovoltaic thermal water electrolyzer. Appl Energy 2016;164:294–302. doi:10.1016/j.apenergy.2015.11.078.

[197] Calise F, Damian R, Massarotti N, Mauro A, Vanoli L. Polygeneration system based on PEMFC, CPVT and electrolyzer: Dynamic simulation and energetic and economic analysis. Appl Energy 2017;192:530–42. doi:10.1016/j.apenergy.2016.08.018.

[198] Ni M, Leung MKH, Leung DYC. Energy and exergy analysis of hydrogen production by a proton exchange membrane (PEM) electrolyzer plant. Energy Convers Manag 2008;49:2748–56. doi:10.1016/j.enconman.2008.03.018.

[199] Ahmadi P, Dincer I, Rosen MA. Energy and exergy analyses of hydrogen production via solar-boosted ocean thermal energy conversion and PEM electrolysis. Int J Hydrogen Energy 2013;38:1795–805. doi:10.1016/j.ijhydene.2012.11.025.

[200] Alirahmi SM, Rostami M, Hamzeh A. Multi-criteria design optimization and thermodynamic analysis of a novel multi-generation energy system for hydrogen, cooling, heating, power, and freshwater. Int J Hydrogen Energy 2020;45:15047–62. doi:10.1016/j.ijhydene.2020.03.235.

[201] Li D, Guo J, Zhang J, Zhan L, Alizadeh M. Numerical assessment of a hybrid energy generation process and energy storage system based on alkaline fuel cell, solar energy and Stirling engine. J Energy Storage 2021;39:102631. doi:10.1016/j.est.2021.102631.

[202] Khanmohammadi S, Saadat-Targhi M, Ahmed FW, Afrand M. Potential of thermoelectric waste heat recovery in a combined geothermal, fuel cell and organic Rankine flash cycle (thermodynamic and economic evaluation). Int J Hydrogen Energy 2020;45:6934–48. doi:10.1016/j.ijhydene.2019.12.113.

[203] Azad A, Fakhari I, Ahmadi P, Javani N. Analysis and optimization of a fuel cell integrated with series two-stage organic Rankine cycle with zeotropic mixtures. Int J Hydrogen Energy 2021. doi:10.1016/j.ijhydene.2021.02.061.

[204] Baniasadi E, Toghyani S, Afshari E. Exergetic and exergoeconomic evaluation of a trigeneration system based on natural gas-PEM fuel cell. Int J Hydrogen Energy 2017;42:5327–39. doi:10.1016/j.ijhydene.2016.11.063.

[205] Ghorbani B, Mehrpooya M, Ardehali A. Energy and exergy analysis of wind farm integrated with compressed air energy storage using multi-stage phase change material. J Clean Prod 2020;259:120906. doi:10.1016/j.jclepro.2020.120906.

[206] Roushenas R, Razmi AR, Soltani M, Torabi M, Dusseault MB. Thermo-environmental analysis of a novel cogeneration system based on solid oxide fuel cell (SOFC) and compressed air energy storage (CAES) coupled with turbocharger. Appl Therm Eng 2020;181:115978. doi:10.1016/j.applthermaleng.2020.115978.

[207] Razmi A, Soltani M, Aghanaja C, Torabi M. Thermodynamic and economic investigation of a novel integration of the absorption-recompression refrigeration system with compressed air energy storage (CAES). Energy Convers Manag 2019;187:262–73. doi:10.1016/j.enconman.2019.03.010.

[208] Razmi AR, Arabkoohsar A, Nami H. Thermoeconomic analysis and multi-objective optimization of a novel hybrid absorption/recompression refrigeration system. Energy 2020;210:118559. doi:10.1016/j.energy.2020.118559.

[209] Nami H, Anvari-Moghaddam A, Arabkoohsar A, Razmi AR. 4E Analyses of a Hybrid Waste-Driven CHP–ORC Plant with Flue Gas Condensation. Sustainability 2020;12:9449. doi:10.3390/su12229449.

[210] Razmi AR, Janbaz M. Exergoeconomic assessment with reliability consideration of a green cogeneration system based on compressed air energy storage (CAES). Energy Convers Manag 2020;204:112320. doi:https://doi.org/10.1016/j.enconman.2019.112320.

[211] Cavalcanti EJC. Exergoeconomic and exergoenvironmental analyses of an integrated solar combined cycle system. Renew Sustain Energy Rev 2017;67:507–19. doi:https://doi.org/10.1016/j.rser.2016.09.017.

[212] Ahmadi F, Chavoshi M, Sabeti V. Multi-generation system incorporated with PEM electrolyzer and dual ORC based on biomass gasi fi cation waste heat recovery: Exergetic , economic and environmental impact optimizations. Energy 2018;145:38–51. doi:10.1016/j.energy.2017.12.118.

[213] Habibollahzade A, Gholamian E, Ahmadi P. Multi-criteria optimization of an integrated energy system with thermoelectric generator, parabolic trough solar collector and electrolysis for hydrogen production Organic Rankine cycle. Int J Hydrogen Energy 2018;43:14140–57. doi:10.1016/j.ijhydene.2018.05.143.

[214] Behzadi A, Gholamian E, Ahmadi P, Habibollahzade A. Energy , exergy and exergoeconomic (3E) analyses and multi-objective optimization of a solar and geothermal based integrated energy system. Appl Therm Eng 2018;143:1011–22. doi:10.1016/j.applthermaleng.2018.08.034.

[215] Ioroi T, Yasuda K, Siroma Z, Fujiwara N, Miyazaki Y. Thin film electrocatalyst layer for unitized regenerative polymer electrolyte fuel cells. J Power Sources 2002;112:583–7.

[216] Al-sulaiman FA. Exergy analysis of parabolic trough solar collectors integrated with combined steam and organic Rankine cycles. ENERGY Convers Manag 2014;77:441–9. doi:10.1016/j.enconman.2013.10.013.

[217] Hameed IA, Bye RT, Osen OL. Grey wolf optimizer (GWO) for Automated Offshore Crane Design. IEEE Symp. Ser. Comput. Intell., 2016, p. 16670343.

[218] Macchi E, Astolfi M. Organic rankine cycle (ORC) power systems: technologies and applications. Woodhead Publishing; 2016.

[219] Shahin MS, Orhan MF, Uygul F. Thermodynamic analysis of parabolic trough and heliostat field solar collectors integrated with a Rankine cycle for cogeneration of electricity and heat. Sol Energy 2016;136:183–96. doi:10.1016/j.solener.2016.06.057.

[220] Tehrani SSM, Taylor RA. Off-design simulation and performance of molten salt cavity receivers in solar tower plants under realistic operational modes and control strategies. Appl Energy 2016;179:698–715. doi:10.1016/j.apenergy.2016.07.032.

[221] Mehrpooya M, Dehghani H, Moosavian SMA. Optimal design of solid oxide fuel cell, ammonia-water single effect absorption cycle and Rankine steam cycle hybrid system. J Power Sources 2016;306:107–23. doi:10.1016/j.jpowsour.2015.11.103.

[222] Aghaie M, Mehrpooya M, Pourfayaz F. Introducing an integrated chemical looping hydrogen production, inherent carbon capture and solid oxide fuel cell biomass fueled power plant process configuration. Energy Convers Manag 2016;124:141–54. doi:10.1016/j.enconman.2016.07.001.

[223] Sadeghi M, Jafari M, Hajimolana YS, Woudstra T, Aravind P V. Size and exergy assessment of solid oxide fuel cell-based H2-fed power generation system with alternative electrolytes: A comparative study. Energy Convers Manag 2021;228:113681. doi:10.1016/j.enconman.2020.113681.

[224] Bafekr SH, Chitsaz A, Ghazanfari S. Thermo-electrochemical modeling of oxygen ion-conducting solid oxide fuel cells with internal steam reforming in the water-energy nexus. Energy Nexus 2022;5:100057. doi:10.1016/j.nexus.2022.100057.

[225] Nabat MH, Sharifi S, Razmi AR. Thermodynamic and economic analyses of a novel liquid air energy storage (LAES) coupled with thermoelectric generator and Kalina cycle. J Energy Storage 2022;45:103711. doi:10.1016/j.est.2021.103711.

[226] Momeni M, Fartaj A. Numerical thermal performance analysis of a PCM-to-air and liquid heat exchanger

implementing latent heat thermal energy storage. J Energy Storage 2023;58:106363. doi:10.1016/j.est.2022.106363.

[227] Rivero RÃ, Garfias M. Standard chemical exergy of elements updated. Energy 2006;31:3310–26. doi:10.1016/j.energy.2006.03.020.

[228] Momeni M, Askar S, Fartaj A. Thermal performance evaluation of a compact two-fluid finned heat exchanger integrated with cold latent heat energy storage. Appl Therm Eng 2023;230:120815. doi:10.1016/j.applthermaleng.2023.120815.

[229] Roodbari M, Abbasi M, Arabha S, Gharedaghi A, Rajabpour A. Interfacial thermal conductance between TiO2 nanoparticle and water: A molecular dynamics study. J Mol Liq 2022;348:118053. doi:10.1016/j.molliq.2021.118053.

[230] Razmi A, Soltani M, M. Kashkooli F, Garousi Farshi L. Energy and exergy analysis of an environmentally-friendly hybrid absorption/recompression refrigeration system. Energy Convers Manag 2018;164:59–69. doi:10.1016/j.enconman.2018.02.084.

[231] Habibi H, Zoghi M, Chitsaz A, Javaherdeh K, Ayazpour M, Bellos E. Working fluid selection for regenerative supercritical Brayton cycle combined with bottoming ORC driven by molten salt solar power tower using energy–exergy analysis. Sustain Energy Technol Assessments 2020;39:100699. doi:10.1016/j.seta.2020.100699.

[232] Abbasi HR, Pourrahmani H, Yavarinasab A, Ali M, Hoorfar M. Exergoeconomic optimization of a solar driven system with reverse osmosis desalination unit and phase change material thermal energy storages. Energy Convers Manag 2019;199:112042. doi:10.1016/j.enconman.2019.112042.

[233] Li X, Kong W, Wang Z, Chang C, Bai F. Thermal model and thermodynamic performance of molten salt cavity receiver. Renew Energy 2010;35:981–8. doi:10.1016/j.renene.2009.11.017.

[234] Mosaffa AH, Ghaffarpour Z, Garousi Farshi L. Thermoeconomic assessment of a novel integrated CHP system incorporating solar energy based biogas-steam reformer with methanol and hydrogen production. Sol Energy 2019;178:1–16. doi:10.1016/j.solener.2018.12.011.

[235] Benammar S, Khellaf A, Mohammedi K. Contribution to the modeling and simulation of solar power tower plants using energy analysis. Energy Convers Manag 2014;78:923–30. doi:10.1016/j.enconman.2013.08.066.

[236] Roodbari M, Alimoradi H, Shams M, Aghanajafi C. An experimental investigation of microstructure surface roughness on pool boiling characteristics of TiO2 nanofluid. J Therm Anal Calorim 2021;c. doi:10.1007/s10973-021-10666-w.

[237] Polimeni S, Binotti M, Moretti L, Manzolini G. Comparison of sodium and KCl-MgCl2 as heat transfer fluids in CSP solar tower with sCO2 power cycles. Sol Energy 2018;162:510–24. doi:10.1016/j.solener.2018.01.046.

[238] Wang J, Heng TY. Techno-economic and thermodynamic analysis of solid oxide fuel cell combined heat and power integrated with biomass gasification and solar assisted carbon capture and energy utilization system. Energy Convers Manag 2023;280:116762. doi:10.1016/j.enconman.2023.116762.

[239] Yang S, Chen T, Wang Y, Peng Z, Wang WG. Electrochemical Analysis of an Anode-Supported SOFC. Int J Electrochem Sci 2013;8:2330–44. doi:10.1016/S1452-3981(23)14312-4.

[240] Xu Y, Lin Z, Ma T, She C, Xing S, Qi L, et al. Optimization of a biomass-driven Rankine cycle integrated

with multi-effect desalination, and solid oxide electrolyzer for power, hydrogen, and freshwater production. Desalination 2022;525. doi:10.1016/j.desal.2021.115486.

[241] Habibollahzade A, Gholamian E, Behzadi A. Multi-objective optimization and comparative performance analysis of hybrid biomass-based solid oxide fuel cell/solid oxide electrolyzer cell/gas turbine using different gasification agents. Appl Energy 2019;233–234:985–1002. doi:10.1016/j.apenergy.2018.10.075.

[242] Alirahmi SM, Fateme S, Ahmadi P, Arabkoohsar A. Soft computing analysis of a compressed air energy storage and SOFC system via different artificial neural network architecture and tri- objective grey wolf optimization. Energy 2021;236:121412. doi:10.1016/j.energy.2021.121412.

[243] Chuahy FDF, Kokjohn SL. Solid oxide fuel cell and advanced combustion engine combined cycle: A pathway to 70% electrical efficiency. Appl Energy 2019;235:391–408. doi:10.1016/j.apenergy.2018.10.132.

[244] Ghaebi H, Parikhani T, Rostamzadeh H, Farhang B. Thermodynamic and thermoeconomic analysis and optimization of a novel combined cooling and power (CCP) cycle by integrating of ejector refrigeration and Kalina cycles. Energy 2017;139:262–76. doi:10.1016/j.energy.2017.07.154.

[245] Alirahmi SM, Behzadi A, Ahmadi P, Sadrizadeh S. An innovative four-objective dragonfly-inspired optimization algorithm for an efficient, green, and cost-effective waste heat recovery from SOFC. Energy 2023;263:125607. doi:10.1016/j.energy.2022.125607.

[246] Najafi A, Jafarian A, Darand J. Thermo-economic evaluation of a hybrid solar-conventional energy supply in a zero liquid discharge wastewater treatment plant. Energy Convers Manag 2019;188:276–95. doi:10.1016/j.enconman.2019.03.059.

[247] Arabkoohsar A, Nami H. Thermodynamic and economic analyses of a hybrid waste-driven CHP – ORC plant with exhaust heat recovery. Energy Convers Manag 2019;187:512–22. doi:10.1016/j.enconman.2019.03.027.

[248] Razmi AR, Janbaz M. Exergoeconomic assessment with reliability consideration of a green cogeneration system based on compressed air energy storage (CAES). Energy Convers Manag 2019:112320. doi:10.1016/j.enconman.2019.112320.

[249] Ebbesen SD, Graves C, Mogensen M. Production of Synthetic Fuels by Co-Electrolysis of Steam and Carbon Dioxide. Int J Green Energy 2009;6:646–60. doi:10.1080/15435070903372577.

[250] Zhao F, Virkar A V. Dependence of polarization in anode-supported solid oxide fuel cells on various cell parameters. J Power Sources 2005;141:79–95. doi:10.1016/j.jpowsour.2004.08.057.

[251] Li X, Zhang Q, Li X. A Kalina cycle with ejector. Energy 2013;54:212–9. doi:10.1016/j.energy.2013.03.040.

[252] https://meteonorm.com, Accessed on Dec 5, 2022.

[253] Nezamoddini N, Wang Y. Real-time electricity pricing for industrial customers: Survey and case studies in the United States. Appl Energy 2017;195:1023–37. doi:10.1016/j.apenergy.2017.03.102.

[254] Kandezi MS, Mojtaba S, Naeenian M. Thermodynamic and economic analysis of a novel combination of the heliostat solar field with compressed air energy storage (CAES); a case study at San Francisco, USA. J Energy Storage 2022;49:104111. doi:10.1016/j.est.2022.104111.

[255] Houssainy S, Janbozorgi M, Ip P, Kavehpour P. Thermodynamic analysis of a high temperature hybrid compressed air energy storage (HTH-CAES) system. Renew Energy 2018;115:1043–54. doi:10.1016/j.renene.2017.09.038.

[256] Houssainy S, Janbozorgi M, Kavehpour P. Thermodynamic performance and cost optimization of a novel hybrid thermal-compressed air energy storage system design. J Energy Storage 2018;18:206–17. doi:10.1016/j.est.2018.05.004.

[257] Zaghloul N, Kodama S, Sekiguchi H. Hydrogen Production by Methane Pyrolysis in a Molten-Metal Bubble Column 2021:1–9. doi:10.1002/ceat.202100210.

[258] Reddy CR, Shahbakhti M, Robinett RD, Razmara M. Exergy-wise predictive control framework for optimal performance of MicroCSP systems for HVAC applications in buildings. Energy Convers Manag 2020;210:112711. doi:10.1016/j.enconman.2020.112711.

[259] Wu C, Wang Q, Wang X, Sun S, Cui D, Pan S, et al. Thermodynamic calculations and experimental studies of ternary molten salts for high-temperature thermal energy storage. J Energy Storage 2023;73:109220. doi:10.1016/j.est.2023.109220.

[260] Marculescu C. Comparative analysis on waste to energy conversion chains using thermal-chemical processes. Energy Procedia 2012;18:604–11. doi:10.1016/j.egypro.2012.05.073.

[261] Msheik M, Rodat S, Abanades S. Enhancing molten tin methane pyrolysis performance for hydrogen and carbon production in a hybrid solar/electric bubbling reactor. Int J Hydrogen Energy 2024;49:962–80. doi:10.1016/j.ijhydene.2023.08.068.

[262] Mu R, Liu M, Zhang P, Yan J. System design and thermo-economic analysis of a new coal power generation system based on supercritical water gasification with full CO2 capture. Energy 2023;285:129384. doi:10.1016/j.energy.2023.129384.

[263] Asgari A, Yari M, Mahmoudi SMS. Exergy and exergoeconomic analyses and multi- objective optimization of a novel cogeneration system for hydrogen and cooling production. Int J Hydrogen Energy 2021;47:26114–34. doi:10.1016/j.ijhydene.2021.11.037.

[264] Clean Hydrogen Production Tax Credit (45V) Resources "https://www.energy.gov/articles/clean-hydrogen-production-tax-credit-45v-resources" 2023.

[265] Sep V. Title I — Committee on finance subtitle A — deficit reduction. Public Law 117th Congr 2022:1–274.

[266] https://www.canada.ca/en/department-finance, Accessed on Oct 16, 2022.

[267] https://www.hydrogeninsight.com/policy/canada-unveils-details-of-its-hydrogen-tax-credits-and-promises-future-contracts-for-difference-subsidy-scheme/2-1-1427954 2023.

[268] https://www.irena.org, Accessed on Jan 19, 2024.

[269] Razmi AR, Sharifi S, Vafaeenezhad S, Hanifi AR, Shahbakhti M. Modeling and microstructural study of anode-supported solid oxide fuel cells: Experimental and thermodynamic analyses. Int J Hydrogen Energy 2024;54:613–34. doi:10.1016/j.ijhydene.2023.08.296.

[270] https://www.globalpetrolprices.com/natural_gas_prices/, Accessed on April 17, 2024.

[271] https://www.globalpetrolprices.com/data_natural_gas, Accessed on April 17, 2024.

[272] https://ec.europa.eu/eurostat/statistics-explained/index.php?title=Natural_gas_price_statistics#Natural_gas_prices_for_non-household_consumers,

Accessed on April 17, 2024.

[273] https://tradingeconomics.com/spain/electricity-price, Accessed on April 17, 2024.

[274] https://hayaenergy.com/spanish-markets-analysis-2/, Accessed on April 17, 2024.

[275] https://figure.nz/chart/, Accessed on April 17, 2024.

[276] https://www.hydroquebec.com/data/documents-donnees/pdf/comparison-electricity-prices.pdf, Accessed on April 17, 2024.

[277] https://www.eia.gov/dnav/ng/NG_PRI_SUM_A_EPG0_PIN_DMCF_M.htm, Accessed on April 17, 2024.

[278] https://economicdashboard.alberta.ca/dashboard/natural-gas-price/, Accessed on April 17, 2024.

[279] https://www.statista.com, Accessed on April 17, 2024.

[280] https://nsrdb.nrel.gov/data-viewer, Accessed on April 17, 2024.

[281] Littlefield J, Rai S, Skone TJ. Life Cycle GHG Perspective on U.S. Natural Gas Delivery Pathways. Environ Sci Technol 2022;56:16033–42. doi:10.1021/acs.est.2c01205.

[282] Measuring emissions: A guide for organisations, Ministry for the Environment, New Zealand Government, ME 1764. 2023.

[283] Whitehouse S. Greenhouse Gas Intensity of Natural Gas, Natural & Bio Gas Vehicle Association (NGVA) Europe, V1.0, 2017.

[284] https://app.electricitymaps.com, Accessed on April 17, 2024.

[285] https://www.canada.ca/en/environment-climate-change/services/managing-pollution/fuel-life-cycle-assessment-model/pre-publication-proposed-update-carbon-intensity-natural-gas-early-notice.html, Accessed on April 17, 2024.

[286] https://www.ualberta.ca, Accessed on Nov 7, 2024.

[287] https://www.ualberta.ca/en/university-services-operations-finance/initiatives/our-district-energy-system.html, Accessed on Nov 7, 2024.

[288] https://www.edmonton.ca, Accessed on Nov 7, 2024.

[289] Envision Energy Reduction Master Plan (2022-2030), University of Alberta, https://www.ualberta.ca/en/campus-operations-services/media-library/ualberta_envision_energy_reduction_plan_november-2021.pdf, November 2021.

[290] Energy and climate action, envision phase 5, “https://www.ualberta.ca/en/governance/media-library/documents/member-zone/board-of-governors/item-10d-envision-attachment-1-06-16-23.pdf” 2023.

[291] https://erh2.ca/ Accessed on November 4, 2024.

[292] https://www.futureenergysystems.ca, Accessed on October 7, 2024.

[293] https://www.fuelcellenergy.com, Accessed on Sep 27, 2024.

[294] https://www.bchydro.com/news/conservation/2022/cold-weather-heat-pumps. Accessed on Oct 19, 2024.

[295] Heating and cooling with a heat pump, "https://natural-resources.canada.ca/energy-efficiency/energy-star-canada/about/energy-star-announcements/publications/heating-and-cooling-heat-pump/6817", Accesses on Oct 6, 2024.

[296] https://heatpump.ca/service/mitsubishi-heat-pumps. Accessed on Oct 6, 2024.

[297] Labbé S, Heat pumps outperform gas even in coldest temperatures, https://www.biv.com/news/economy-law-politics/heat-pumps-outperform-gas-even-coldest-temperatures-finds-canadian-researcher-8273254. Accesses on Oct 7, 2024.

[298] Hewitt NJ. Coming in from the cold: Heat pump efficiency at low temperatures. Joule 2023;7:1939–42. doi:10.1016/j.joule.2023.08.005.

[299] Bernath S, Heat pump price guide: how much you will pay for a new heat pump installed in Canada (2024), https://www.furnaceprices.ca/heat-pumps/heat-pump-prices. Accessed on Oct 6, 2024.

[300] Edmonton temperatures: averages by month, https://www.currentresults.com/Weather/Canada/Alberta/Places/edmonton-temperatures-by-month-average.php, Accessed on Oct 6, 2024.

[301] Ghenai C, Bettayeb M. Modelling and performance analysis of a stand-alone hybrid solar PV/Fuel Cell/Diesel Generator power system for university building. Energy 2019;171:180–9. doi:10.1016/j.energy.2019.01.019.

[302] Al-shara A, Sahin AZ, Ayar T, Yilbas BS. Techno-economic analysis and optimization of solar and wind energy systems for power generation and hydrogen production in Saudi Arabia 2017;69:33–49. doi:10.1016/j.rser.2016.11.157.

[303] Marocco P, Gandiglio M, Santarelli M. When SOFC-based cogeneration systems become convenient? A cost-optimal analysis. Energy Reports 2022;8:8709–21. doi:10.1016/j.egyr.2022.06.015.

[304] Scataglini R, Mayyas A, Wei M, Chan SH, Lipman T, Gosselin D, et al. A total cost of ownership model for solid oxide fuel cells in combined heat and power and power- only applications. Berkeley Natl Labratoty, Environ Energy Technol Div 2015.

[305] https://oee.nrcan.gc.ca/corporate/statistics/neud/dpa/showTable.cfm?type=CP&sector, Accessed on Oct 4, 2024.

[306] Aliramezani M, Koch CR, Shahbakhti M. Modeling, diagnostics, optimization, and control of internal combustion engines via modern machine learning techniques: A review and future directions. Prog Energy Combust Sci 2022;88:100967. doi:10.1016/j.pecs.2021.100967.

[307] Hydrogen Program Plan, United States Department of Energy, https://www.hydrogen.energy.gov/docs/hydrogenprogramlibraries/pdfs/hydrogen-program-plan-2020.pdf?Status=Master, Accessed on December 20, 2024.

[308] Liso V, Zhao Y, Brandon N, Pagh M. Analysis of the impact of heat-to-power ratio for a SOFC-based mCHP system for residential application under different climate regions in Europe. Int J Hydrogen Energy 2011;36:13715–26. doi:10.1016/j.ijhydene.2011.07.086.

[309] Alberta Hydrogen Roadmap, Ministry of Energy. Gov Alberta 2021.

[310] Zarabi S, Imran M, Lund PD. A review on solid oxide fuel cell durability: Latest progress, mechanisms, and study tools. Renew Sustain Energy Rev 2022;161:112339. doi:10.1016/j.rser.2022.112339.

[311] August C. Report on the Status of the Solid Oxide Fuel Cell Program. US Dep Energy 2019.

[312] https://www.epi.org/publication/updated-employment-multipliers-for-the-u-s-economy, Accessed on Feb 8, 2024.

[313] https://oee.nrcan.gc.ca/corporate/statistics/neud/dpa/showTable.cfm, Accessed on Feb 11, 2024.

Appendix A: Ph.D. Publications

A.1 Peer Reviewed Journal Papers

A.1.1 Published

1. **A.R. Razmi**, S.M. Alirahmi, M.H. Nabat, E. Assareh, M. Shahbakhti, A green hydrogen energy storage concept based on parabolic trough collector and proton exchange membrane electrolyzer/fuel cell: Thermodynamic and exergoeconomic analyses with multi-objective optimization, *International Journal of Hydrogen Energy* 2022;47:26468-26489.

2. **A.R. Razmi**, A.R. Hanifi, M. Shahbakhti, Design, thermodynamic, and economic analyses of a green hydrogen storage concept based on solid oxide electrolyzer/fuel cells and heliostat solar field, *Renewable Energy* 2023;215:118996.

3. **A.R. Razmi**, Sh. Sharifi, S. Vafaeenezhad, A.R. Hanifi, M. Shahbakhti, Modeling and microstructural study of anode-supported solid oxide fuel cells: Experimental and thermodynamic analyses, *International Journal of Hydrogen Energy* 2024;54:613-634.

4. **A.R. Razmi**, A.R. Hanifi, M. Shahbakhti, Techno-economic analysis of a novel concept for the combination of methane pyrolysis in molten salt with heliostat solar field, *Energy* 2024;301:131644.

A.1.2 Accepted

1. **A.R. Razmi**, A.R. Hanifi, M. Shahbakhti, A comparative techno-economic investigation between solar-based hydrogen production by methane pyrolysis and water electrolysis methods, *Renewable Energy*, 47 pages, Accepted for publication on January 24, 2025.

A.1.3 Under Review

1. **A.R. Razmi**, A.R. Hanifi, M. Shahbakhti, Techno-economic assessment of solid oxide fuel cells and hydrogen internal combustion engines for institutional energy management: A case study of the University of Alberta, *International Journal of Hydrogen Energy*. Submitted on Jan 10, 2025.

A.2 Book Chapters

1. **A.R. Razmi**, Sh. Sharifi, E. Gholamian, A. Arabkoohsar, M. Shahbakhti, Green Hydrogen, *Future Grid-Scale Energy Storage Solutions, Elsevier* 2023:573-619.

2. Sh. Sharifi, **A.R. Razmi**, M.H. Nabat, J. Jay Liu, A. Arabkoohsar, M. Shahbakhti, Power-to-X, *Future Grid-Scale Energy Storage Solutions, Elsevier* 2023:621-646.

3. M.H. Nabat, **A.R. Razmi**, Sh. Sharifi, A. Arabkoohsar, M. Shahbakhti, Liquid Air Energy Storage, *Future Grid-Scale Energy Storage Solutions, Elsevier* 2023:345-408.

A.3 Peer Reviewed Conference Papers

1. A.K. ElKashat, **A.R. Razmi**, S. Vafaeenezhad, A.R. Hanifi, T.H. Etsell, M. Shahbakhti, Experimental and thermodynamic analyses of a novel anode supported solid oxide fuel cell, *Proceedings of the Canadian Society for Mechanical Engineering (CSME) International Congress*, Edmonton, Canada, Jun 2022.

2. **A.R. Razmi**, A.R. Hanifi, M. Shahbakhti, Potential of solid oxide fuel cell-based combined heat and power systems for commercial and residential applications in Alberta and Canada, *Global Conference on Renewable Energy and Climate Change*, Ottawa, Canada, Nov 2024.

A.4 Technical Posters

1. S. Vafaeenezhad, A.R. Hanifi, M. Cugliette, **A. R. Razmi**, A.K. ElKashat, M. Shahbakhti, P. Sarkar, T.H. Etsell, High-efficiency and Stable Solid Oxide Fuel Cells and Electrolysis Cells, *Canadian Hydrogen Convention*, Edmonton, Canada, May 2022.

2. **A. R. Razmi**, S. Vafaeenezhad, Sh. Sharifi, A.R. Hanifi, C.R. Koch, M. Shahbakhti, Stable and efficient solid oxide fuel cells/electrolyzer combined with heliostat solar system for green hydrogen production, *University of Alberta - Denmark Workshop*, University of Alberta, Edmonton, Canada, May 2023.

Appendix B: Thesis Files

B.1 Chapter 1 source files

Table B. 1. Source files of chapter 1.

File name	File description
Energy Storage technologies.ai	Figure 1.1
15-Green Hydrogen.pdf	Figure 1.2
Hydrogen price and carbon intensity.xlsx	Figure 1.3
PEM.eddx	Figure 1.4
AWE.eddx	Figure 1.5
SOEC.eddx	Figure 1.6
Hydrogen storage.eddx	Figure 1.7
15-Green Hydrogen.pdf	Figure 1.8
15-Green Hydrogen.pdf	Figure 1.9
2g-energy.com.jpg	Figure 1.10
Solar-based PEME-PEMFC.ai	Figure 1.11
Solar-based SOEC-SOFC.eddx	Figure 1.12
Molten_salt_methane_pyrolysis.pptx	Figure 1.13
Electrolysis_vs_pyrolysis.pptx	Figure 1.14
Thesis outline.pptx	Figure 1.17

B.2 Chapter 2 source files

Table B. 2. Source files of chapter 2.

File name	File description
Solar-based PEME-PEMFC code.EES	System modeling code
Solar-based PEME-PEMFC optimization.rar	System optimization
Solar-based PEME-PEMFC cycle.ai	Figure 2.1
T-S diagram.ai	Figure 2.2
Fig. 2.3.rar	Figure 2.3
ANN diagram.ai	Figure 2.4
Fig. 2.5.fig	Figure 2.5
Solar-based PEME-PEMFC optimization.rar	Figure 2.6
TOPSIS.fig	Figure 2.7
Fig. 2.8.fig	Figure 2.8
Exergy.sankey	Figure 2.9
Exergoeconomic.sankey	Figure 2.10
Cost rates.ai	Figure 2.11
Fig. 2.12.rar	Figure 2.12
Bar.rar	Figure 2.13
Bar.rar	Figure 2.14
Fig. 2.15.png	Figure 2.15
Fig. 2.16.png	Figure 2.16

B.3 Chapter 3 source files

Table B. 3. Source files of chapter 3.

File name	File description
Solar-based SOEC-SOFC code.EES	System modeling code
Solar-based SOEC-SOFC cycle.eddx	Figure 3.1
System flowchart.ai	Figure 3.2
Fig. 3.3.rar	Figure 3.3
Sankey diagram.sankey	Figure 3.4
Capital cost diagram.ai	Figure 3.5
Fig. 3.6.rar	Figure 3.6
Fig. 3.7.rar	Figure 3.7
Fig. 3.8.rar	Figure 3.8
Fig. 3.9.rar	Figure 3.9
Fig. 3.10.rar	Figure 3.10
Hourly DNI.fig	Figure 3.11
DNI&Annual hydrogen graphs.rar	Figure 3.12
Fig. 3.13.rar	Figure 3.13
Fig. 3.14.rar	Figure 3.14
Fig. 3.15.rar	Figure 3.15

B.4 Chapter 4 source files

Table B. 4. Source files of chapter 4.

File name	File description
Solar-based methane pyrolysis code.EES	System modeling code
Solar-based methane pyrolysis cycle.eddx	Figure 4.1
Fig. 4.2.rar	Figure 4.2
Fig. 4.3.rar	Figure 4.3
Capital cost.ai	Figure 4.4
Fig. 4.5.rar	Figure 4.5
Fig. 4.6.rar	Figure 4.6
Fig. 4.7.rar	Figure 4.7
Fig. 4.8.rar	Figure 4.8
Fig. 4.9.rar	Figure 4.9
Fig. 4.10.rar	Figure 4.10
Fig. 4.11.rar	Figure 4.11
Fig. 4.12.rar	Figure 4.12
Fig. 4.13.rar	Figure 4.13
Fig. 4.14.rar	Figure 4.14
Fig. 4.15.rar	Figure 4.15

B.5 Chapter 5 source files

Table B. 5. Source files of chapter 5.

File name	File description
SMSMP code.EES	SMSMP modeling code
SSOEC code.EES	SSOEC modeling code
SMSMP cycle.eddx	Figure 5.1
SSOEC cycle.eddx	Figure 5.2
Fig. 5.3.rar	Figure 5.3
Fig. 5.4.rar	Figure 5.4
Fig. 5.5.rar	Figure 5.5
Fig. 5.6.rar	Figure 5.6
Fig. 5.7.rar	Figure 5.7
Fig. 5.8.rar	Figure 5.8
Fig. 5.9.rar	Figure 5.9
Fig. 5.10.rar	Figure 5.10
Fig. 5.11.rar	Figure 5.11
Fig. 5.12.rar	Figure 5.12
Fig. 5.13.rar	Figure 5.13
Fig. 5.14.rar	Figure 5.14
Fig. 5.15.rar	Figure 5.15
Fig. 5.16.rar	Figure 5.16
Fig. 5.17.rar	Figure 5.17
Fig. 5.18.rar	Figure 5.18
Fig. 5.19.rar	Figure 5.19

B.6 Chapter 6 source files

Table B. 6. Source files of chapter 6.

File name	File description
UofA.eddx	Figure 6.1
Heat pumps in cold temperatures.pdf	Figure 6.2
Methodology.pptx	Figure 6.3
Calculations for SOEC and HICE-based CHP.xlsx	Figure 6.4 to 6.10
Comparison.rar	Figure 6.11
Alberta Innovates presentation.pptx	Figures 6.12 to 6.17
Residential Alberta.xlsx	Figure 6.18
Commercial Alberta.xlsx	Figure 6.19
Residential Canada.xlsx	Figure 6.20
Commercial Canada.xlsx	Figure 6.21